Lomnitz, Michael R. Ph.D., NUCLEAR PHYSICS

MEASUREMENT OF CHARMED MESON AZIMUTHAL ANISOTROPY IN AU+AU COLLISIONS AT $\sqrt{s_{NN}}$ = 200 GEV AT RHIC (189 pp.)

Director of Dissertation: Spyridon Margetis and Xin Dong (Lawrence Berkeley National Laboratory)

Heavy ion collisions at RHIC provide a unique environment to probe into the understanding of nuclear matter under extreme high temperature and density conditions. Among the many insights that can be provided is the further understanding of the QCD (Quantum Chromo Dynamics) phase diagram and equation of state, as well as search for evidence of the QCD critical point and chiral symmetry restoration.

Production of heavy quarks in high-energy nuclear collisions at RHIC occurs mainly through gluon fusion and quark anti-quark annihilation; and while heavy flavor production may be somewhat enhanced due to final state interactions via thermal processes these channels are greatly suppressed due to the heavy quark masses.

Thus heavy flavor provides an ideal probe in the study of the hot and dense medium created in high-energy collisions as it is produced early in the evolution of the collision, and hence is sensitive to the collision dynamics of the partonic matter at early stages.

Previous measurements of collective motion (flow) in light quarks (u,d,s) at RHIC suggest that partonic collectivity has been achieved in the collisions. These results also seem to suggest that the dense matter produced during collisions thermalizes at very high temperatures and form a strongly coupled Quark Gluon Plasma (QGP)

whose behavior is compatible with viscous hydrodynamic models with a low *shear*-viscosity-to-entropy-density (η/s) ratio. The question remains as to whether or not this collective behavior applies to heavy flavor and a detailed description of the behavior of heavy flavor is essential to understand the underlying dynamics, distinguish between different energy loss mechanisms, and constrain theoretical models. In particular, if the elliptic flow of charm quarks is found to be comparable to that of lighter matter this would be indicative of frequent interactions between all quarks and would strongly support the discovery of QGP at RHIC. Understanding how this collective behavior emerges from the individual interactions between partonic matter as well as the differences between quarks species will need to be investigated further to understand this new state of matter and is at the center of the RHIC scientific program.

However, precise measurements of open heavy flavor are difficult to obtain due to the low yields and short lifespan of heavy hadrons. One approach to reduce this combinatorial background and reconstruct open heavy flavor in heavy ion collisions involves distinguishing between an event's primary vertex and a hadron's decay vertex through direct topological reconstruction from the decay products.

The Heavy Flavor Tracker (HFT) silicon vertex upgrade for the STAR experiment, which made its debut during the 2014 year's run together with the Muon Telescope Detector (MTD), has vastly improved the experiment's heavy flavor capabilities making STAR an ideal detector to study the hot and dense matter created in heavy ion collisions. Taking advantage of the greatly improved pointing resolution from a dedicated micro-vertex detector, it is possible to directly track and reconstruct weak decay products from hadrons comprised of heavy "charm" and "bottom" quarks. The HFT consists of three sub-detectors: PIXEL (PXL), the Intermediate Silicon

Tracker (IST) and the Silicon Strip Detector (SSD) with 4 separate layers of silicon to guide tracks reconstructed in the Time Projection Chamber down to a pointing resolution of around 30 μm for one GeV/c pions, a requirement to distinguish between an event's primary vertex and the position of a hadron's decay.

This dissertation is centered on using the HFT to reconstruct charmed mesons in Au+Au collisions at $\sqrt{s_{NN}}$ = 200 GeV through their hadronic channels ($D^{\pm} \rightarrow K^{\mp} + 2\pi^{\pm}$, $D^0 \rightarrow K^- + \pi^+$).

In order to achieve the precision of the HFT for physics analysis, careful calibration of the detector is essential to ensure the quality of the processed data and, as a consequence, any measured observables. As such, details related to the identification of bad channels in the PXL subsystem as well as the internal alignment of the HFT detector are presented in this dissertation. In-depth studies of the detector's response were performed in simulations and, together with comparisons to data, were used to verify our understanding of the detector's delivered efficiency and tracking performance.

As motivated above, a sizable sample of charmed meson candidates was obtained and used to study the flow patterns employing the event plane method, whose simple interpretation allows for immediate comparison to theoretical models. The thesis presents the first measurement of D-meson v_2 and v_3 at RHIC energy, and the result shows D-meson v_2 is finite indicating charm quarks are participating the collective behavior with the medium. The results are compared to lighter particle species and appear to follow the same Number of Constituent Quarks (NCQ) scaling as is observed for other hadrons. The measured v_3 is found to be non-zero within large uncertainties, indicating the importance of considering fluctuations in the initial conditions of the collision. These results are then compared to a series of model calculations in an

attempt to extract information related to the transport properties of the bulk matter formed in the collision. In particular, the measured elliptic flow for D^0 is found to favor a scenario where charm quarks flow with the medium and compatible with a (3+1)D viscous hydrodynamics. The comparisons were used to extract a range of compatible values for the charm spatial diffusion coefficient $2\pi TD_s$ in the QGP medium.

Once processed, the dataset collected in 2016 (2 billion MinBias events) will provide a further factor 2-4 in the D^0 significance. This dataset will allow STAR to study the centrality dependence of charm hadron v_2 in more detail as well as the production of open bottom at RHIC in order to further constrain the transport properties of the medium.

MEASUREMENT OF CHARMED MESON AZIMUTHAL ANISOTROPY IN AU+AU COLLISIONS AT $\sqrt{s_{NN}} = 200$ GEV AT RHIC

A dissertation submitted to
Kent State University in partial
fulfillment of the requirements for the
degree of Doctor of Philosophy

by

Michael R. Lomnitz

December, 2016

© Copyright

All rights reserved

Except for previously published materials

Dissertation written by

Michael R. Lomnitz

B.S., Universidad Nacional Autónoma de México (UNAM), 2010

M.A., Kent State University, 2012

Ph.D., Kent State University, 2016

Approved by

_____ , Chair, Doctoral Dissertation Committee
Dr. Spyridon Margetis

_____ , Members, Doctoral Dissertation Committee
Dr. Xin Dong

_____ ,
Dr. Declan Keane

_____ ,
Dr. Michael Strickland

_____ ,
Dr. Robert Twieg

_____ ,
Dr. Mietek Jaroniec

Accepted by

_____ , Chair, Department of Physics
Dr. James T. Gleeson

_____ , Dean, College of Arts and Sciences
Dr. James L. Blank

Table of Contents

List of Figures vii

List of Tables xvi

Acknowledgements xvii

1 **Introduction and research objectives** 1

1.1 The Standard Model 3

1.1.1 Quantum Chromodynamics 5

1.1.2 Chiral symmetry 8

1.2 Heavy Ion Collisions 9

1.2.1 Collectivity 12

1.2.2 Energy loss 14

1.2.3 Heavy quarks 16

2 **Experimental set-up** 22

2.1 RHIC facility 22

2.2 STAR experiment 24

2.2.1 Time Projection Chamber 25

2.2.2 Time-of-Flight detector 30

2.2.3 Vertex Position Detector 31

2.2.4 Heavy Flavor Tracker 33

3 **HFT calibrations and performance** . . . 37
3.1 HFT Calibrations . . . 37
3.2 HFT Perfomance . . . 39

4 **Event, track and decay reconstruction** . . . 48
4.1 Event reconstruction . . . 48
4.1.1 Centrality definition . . . 50
4.1.2 Track selection and PID . . . 51
4.2 Topological selection with HFT . . . 52
4.2.1 D^0 topological cuts . . . 54
4.2.2 $D^{\pm}$ topological cuts . . . 55
4.3 Background description . . . 55
4.3.1 Event mixing . . . 59
4.3.2 Correlated background - $K\pi$ foreground "bump" . . . 61

5 *D* **meson azimuthal anisotropy** . . . 66
5.1 Event plane determination . . . 67
5.2 Event Plane Resolution . . . 68
5.3 Azimuthal Anisotropy . . . 70
5.4 Systematic studies . . . 89
5.5 Non-flow estimation . . . 90
5.6 Feed-down . . . 93

6 **Experimental Results and discussion** . . . 99
6.0.1 D-meson v_2 . . . 99
6.0.2 D^0 v_3 . . . 101

6.1 Comparison to data . . . 102
6.2 Theory Overview . . . 107
6.2.1 Second-order hydrodynamics (CCNU-LBNL) . . . 109
6.2.2 Non-perturbative T-matrix in a parametrized hydrodynamic background (TAMU) . . . 110
6.2.3 pQCD with viscous hydrodynamics (DUKE) . . . 112
6.2.4 pQCD + HTL in a fluid dynamic medium (SUBATECH) . . . 113
6.3 Comparison to models . . . 115
6.3.1 D^0 v_2 . . . 115
6.3.2 D^0 v_3 . . . 116

7 **Summary and outlook** . . . 119
7.1 Summary . . . 119
7.2 Outlook . . . 121

Appendices . . . 124

A **PXL Detector masking** . . . 125
A.1 Introduction . . . 125
A.2 Physics Data Masking . . . 127
A.2.1 Definitions and criteria . . . 129
A.2.2 Performance . . . 132
A.3 Cosmic Data Masking . . . 133
A.3.1 Performance and results . . . 138
A.4 Table structure . . . 141
A.5 Package contents and read me . . . 144

B **Composite Structure Track Based Alignment** 150

B.1 General χ^2 algorithm 151

B.2 Geometry Transformations and conventions 152

B.3 Method performance: simulations 154

B.4 Relative alignment for full PXL system 157

B.5 Calculation of Jacobian matrix elements 158

C **Event Plane Detector Prototype** 161

C.1 Silicon photomultipliers 162

C.2 Fiber preparation 163

C.3 Tile design 164

C.4 Fiber coupling 166

C.5 Radiation hardness of optical cement 167

C.6 EPD prototype design and assembly 169

C.7 Prototype installation 171

List of Figures

1.1.1 Summary of the Standard Model of fundamental particles (Credit: CERN). 3

1.1.2 QCD vacuum diagrams. 5

1.1.3 Summary of the measurements of α_s as a function of the energy scale Q. The degree of perturbation theory used in the extraction of α_s is indicated in the brackets(NLO: next-to leading order, NNLO:next-to-NLO, etc.) Figure reprinted from [28] with permission from the American Physical Society. 7

1.1.4 Quark masses coming from QCD vacuum and the Higgs vacuum. A large fraction of the light quark masses are due to chiral symmetry breaking the QCD vacuum. Figure reprinted from [88] with permission from Elsevier. 10

1.2.1 A cartoon illustrating the space-time evolution of a heavy ion collision generated at LHC. The panel on the right shows the evolution in the lab frame. Figure reprinted from [79] with permission from the author. 11

1.2.2 Non-central versus central collisions. The participants in the shaded overlap region will experience pressure leading to the momentum anisotropy illustrated by the arrows. 12

1.2.3 Time evolution of the spatial eccentricity ϵ_x and momentum anisotropy ϵ_p for an equation of state with a phase transition (solid) and ideal massless gas at very high temperature (dashed). Figure reprinted from [54] with permission from Elsevier. 14

1.2.4 v_2 for identified particles in Au+Au $\sqrt{s_{NN}}$ =200 GeV collisions recorded at STAR. Figure reprinted from [4] with permission from the American Physical Society. 15

1.2.5 Average of D^0, $D^{\pm}$ and D^{*+} v_2 as a function of p_T compared to charged particle v_2 from ALICE. Figure taken from [2]. 18

1.2.6 Nuclear modification factor for most central collisions 0-10%. Left: Comparison between light (π^0) [11] and heavy (D) [5, 10] at LHC and RHIC energies. Right: Comparison to several theoretical calculations [9, 77]. 19

1.2.7 Schematic of charm quark hadronizing to neutral D meson and then decaying through hadronic and semi-leptonic channels. Taken from [76]. 20

2.1.1 The RHIC accelerator complex (credit:BNL). 23

2.2.1 Schematic showing STAR experiment and important detector systems. 25

2.2.2 Schematic showing the structure of the STAR TPC detector taken from [78]. 26

2.2.3 Schematic cutaway of MWPC design showing pad plane and the three wire planes :anode, grounding and gating grid. Figure reprinted from [18] with permission from Elsevier. 27

2.2.4 TPC dE/dx measured in 200GeV AuAu collisions collected in 2014 at RHIC. 29

2.2.5 TOF particle identification from $1/\beta$ measured in 200GeV AuAu collisions collected in 2014 at RHIC. 32
2.2.6 34
2.2.7 DCA resolution for TPC tracks with hits in IST and both PXL layers vs. p_{T} in Au-Au collisions at $\sqrt{s_{NN}} = 200$GeV. 36
3.1.1 SSD QA plots for a single run taken in 2016 showing (clockwise starting from upper left): The number of reconstructed hits in each SSD wafer, digital signal matching between both sides of the SSD, reconstructed hit position in the beam direction and reconstructed hit position in the transverse (xy) plane. 38
3.1.2 Summary of IST performance in year 2016 showing on the left the percentage of flagged (bad, hot or cold) chips and the hit occupancy per chip on each ladder on the right. 39
3.1.3 Summary of PXL detector performance in 2016 showing the number of sensors of different qualities on the inner layer (top) and outer layer (bottom) of the detector. 40
3.2.1 (a), (b)TPC track $\eta - \phi$ distributions from data (left) and simulation (right). (c), (d) HFT matched track $\eta - \phi$ distributions from data (left) and simulation (right). 43
3.2.2 HFT ratio as a function of particle p_{T} from data and simulation. . . . 44
3.2.3 Single track distance of closest approach (DCA) to the primary vertex in the transverse plain for low (left) and intermediate (right) p_{T} from simulations and data. 45

3.2.4 Mean, width and DCA ratio from data and simulation distributions in the xy-plane. 46
4.1.1 Invariant mass spectrum of $K\pi$ pairs using primary vertex determined using KF (left) and MINUIT (right) from min-bias trigger in run14. Unlike-sign combinations are shown in black symbols while the like-sign background is shown in blue. 50
4.1.2 Run 14 centrality definition and associated track multiplicity measured in the TPC. 51
4.2.1 Illustration of $D^0 \rightarrow K^-\pi^+$(left) and $D^\pm \rightarrow K^\mp 2\pi^\pm$(right) decay topology and topological variables. 53
4.2.2 Signal efficiency, lowest background efficiency, significance and so on vs. signal efficiency. Top: First iteration, Bottom: Fourth iteration. . 56
4.2.3 Invariant mass of $K\pi$ with D^0 signals after topological cut for different p_T bins. The red histograms are like-sign pair and blue histograms are mixed event. 57
4.3.1 Invariant mass distribution for foreground and three descriptions of combinatorial background in four p_{T} bins. 60
4.3.2 Simulated contribution to the invariant mass spectrum from reconstructed $K\pi$ pairs without (top) and with (bottom) HFT topological cuts. 63
4.3.3 Comparison of combinatorial background+toy Monte Carlo versus foreground from data for two p_{T} ranges. 65
5.1.1 Event plane recentering correction. 69
5.2.1 70

5.3.1 D^0 reconstruction efficiency vs p_T for different centrality classes obtained. 71

5.3.2 Corrected invariant mass distributions in $\phi - \Psi_2$ bins for $0.5 < p_T < 1$ GeV/c and v_2^{obs} calculation. 74

5.3.3 Corrected invariant mass distributions in $\phi - \Psi_2$ bins for $1 < p_T < 1.5$ GeV/c and v_2^{obs} calculation. 75

5.3.4 Corrected invariant mass distributions in $\phi - \Psi_2$ bins for $1.5 < p_T < 2$ GeV/c and v_2^{obs} calculation. 76

5.3.5 Corrected invariant mass distributions in $\phi - \Psi_2$ bins for $2 < p_T < 2.5$ GeV/c and v_2^{obs} calculation. 77

5.3.6 Corrected invariant mass distributions in $\phi - \Psi_2$ bins for $2.5 < p_T < 3$ GeV/c and v_2^{obs} calculation. 78

5.3.7 Corrected invariant mass distributions in $\phi - \Psi_2$ bins for $3 < p_T < 3.5$ GeV/c and v_2^{obs} calculation. 79

5.3.8 Corrected invariant mass distributions in $\phi - \Psi_2$ bins for $3.5 < p_T < 4$ GeV/c and v_2^{obs} calculation. 80

5.3.9 Corrected invariant mass distributions in $\phi - \Psi_2$ bins for $4 < p_T < 5$ GeV/c and v_2^{obs} calculation. 81

5.3.10 Corrected invariant mass distributions in $\phi - \Psi_2$ bins for $5 < p_T < 10$ GeV/c and v_2^{obs} calculation. 82

5.3.11 Corrected invariant mass distributions in $\phi - \Psi_3$ bins for $1 < p_T < 1.5$ GeV/c and v_3^{obs} calculation. 83

5.3.12 Corrected invariant mass distributions in $\phi - \Psi_3$ bins for $1.5 < p_T < 2$ GeV/c and v_3^{obs} calculation. 84

5.3.13 Corrected invariant mass distributions in $\phi - \Psi_3$ bins for $2 < p_T < 2.5$ GeV/c and v_3^{obs} calculation. 85
5.3.14 Corrected invariant mass distributions in $\phi - \Psi_3$ bins for $2.5 < p_T < 3$ GeV/c and v_3^{obs} calculation. 86
5.3.15 Corrected invariant mass distributions in $\phi - \Psi_3$ bins for $3 < p_T < 4$ GeV/c and v_3^{obs} calculation. 87
5.3.16 Corrected invariant mass distributions in $\phi - \Psi_3$ bins for $4 < p_T < 10$ GeV/c and v_3^{obs} calculation. 88
5.4.1 Studies of D^0 v_2 systematic uncertainties versus $p_{\rm T}$ in three centrality classes, clockwise from top left: 0-10%, 10-40%, 40-80% and 0-80%. . 91
5.4.2 Studies of D^0 v_3 systematic uncertainties versus $p_{\rm T}$ in 10-40% (left) and 0-80% (right) central events. 92
5.5.1 $D^{*\pm}$-hadron azimuthal correlation in pp 200 GeV collisions, with different trigger D^* p_T and η gaps. 95
5.5.2 $D^{*\pm}$-hadron correlation $\langle\cos(2(\Delta\phi))\rangle$ vs. p_T in pp 200 GeV collisions, with different η gaps. The left panel sums up correlations for the whole 2π range and the right panel is for the near side only. 96
5.5.3 $D^{*\pm}$-hadron correlation $\langle\Sigma_i \cos 2(\phi(p_T) - \phi_i)\rangle$ vs. p_T for $D^{*\pm}$-hadron, $D^{*\pm}$-hadron from decay feed-down only, D^0-hadron from feed-down only, and the deduced D^0-hadron correlation. Only the near side correlation is summed. The left panel shows the result with no η gap and the right panel shows result with the same η gap of 0.15 as v_2 calculation. 96
5.5.4 D^0-hadron correlation and the estimated non-flow effect on D^0 v_2. . 97

5.6.1 (a) B and D^0 meson p_T spectra in AuAu 200GeV, (b) the input B^+/D^0 ratio as a function of p_T. 97

5.6.2 FONLL-based simulation of the ratio of D^0 from B decay over inclusive D^0 as a function of p_T. The red square represents ratio without any cuts, the blue square is ratio with all topology cuts. 98

6.0.1 D^0 v_2 measured in 0-10%, 10-40%, 40-80% and 0-80% central events. 100

6.0.2 v_2 vs p_{T} for two charmed mesons D^0 and $D\pm$ in 10-40%(left) and 0-80%(right) central Au+Au collisions. the non-flow estimation has been removed from this comparison since it should apply to both species. . 101

6.0.3 D^0 v_3 measured in 10-40% and 0-80% central events. 102

6.1.1 v_2 vs p_{T} (top) and v_2/NCQ vs $(m_T - m_0)/NCQ$ for D^0 (bottom) compared to other particle species [3, 4] in 0-80% central events with m_0 the mass of the particle and $m_T = \sqrt{p_T^2 + m_0^2}$. 103

6.1.2 v_2 vs p_{T} (top) and v_2/NCQ vs $(m_T - m_0)/NCQ$ (bottom) for D^0 compared to other particle species [3] in 0-10% central events with m_0 the mass of the particle and $m_T = \sqrt{p_T^2 + m_0^2}$. 104

6.1.3 v_2 vs p_{T} (top) and v_2/NCQ vs $(m_T - m_0)/NCQ$ (bottom) for D^0 compared to other particle species [3] in 10-40% central events with m_0 the mass of the particle and $m_T = \sqrt{p_T^2 + m_0^2}$. 105

6.1.4 v_2 vs p_{T} (top) and v_2/NCQ vs $(m_T - m_0)/NCQ$ (bottom) for D^0 compared to other particle species [3] in 40-80% central events with m_0 the mass of the particle and $m_T = \sqrt{p_T^2 + m_0^2}$. 106

6.3.1 D^0 v_2 as a function p_{T} in 0-80% central events compared to the different model calculations discussed in section 6.2 116

6.3.2 Diffusion coefficient extracted from a series of model calculations together with the inferred range of compatible values obtained from the comparisons done to the measured result. 117
6.3.3 v_3 vs p_{T} for D^0 in 10-40% central events compared to model calculations in two centralities. 118
A.1.1Schematic showing pixel sensor layout 126
A.1.2Example of faulty sensors from run Au+Au Low luminosity run 15077043128
A.2.1Sample raw hit map for two unmasked sensors 133
A.2.2Sample raw hit map for two sensors after masking 134
A.2.3Number of hot pixels for all Au-Au runs obtained during year 2014. . 136
A.3.1Raw PXL hit distribution Sector 1 Ladder 4 Sensor 2, run 15050257 . 139
A.3.2Masked PXL hit distribution Sector 1 Ladder 4 Sensor 2, run 15050257 140
A.3.3PXL Hits per subarray Sector 4 run 15050257 141
A.3.4Masked PXL hits per subarray Sector 4 run 15050257 142
A.3.5Raw hits per event for all sensors and all runs 143
A.3.6Comparison between hot and good sensor from run 15092071 143
A.5.1Example of sense status plot produced by makePlot macro 148
A.5.2Example of run summary produced by makePlots.C macro 149
B.3.1Calculated and introduced misalignments. Angles are reported in mrad and shifts in microns 155
B.3.2Raw and corrected residuals vs. z for simulations 156
B.3.3Calculated corrections as a function of algorithm iteration 157
B.3.4Raw and corrected residuals for run 2013 data for PXL sectors 2 and 4. 158
B.3.5Raw and corrected residuals for run 2013 data forXL sector 7. 159

C.2.1Kuraray Y-11(200) wavelength shifting fibers before (left) and after polishing (right). 164
C.3.1Test tiles for the EPD. The upper right tile shows the sigma groove. The upper left shows a tile design that was discarded. The lower right shows a tile wrapped in mylar, and the lower left shows a tile wrapped in mylar and then covered with black tape. 165
C.4.1WLS to clear fiber connector (left) and fiber to SiPM connector (right) used for the EPD Prototype 166
C.5.1One of 12cm×5.5cm×0.5cm EJ-200 scintillator with a triple layer of Kuraray Y-11 WLS fibers glued with EJ-500 optical cement 167
C.5.2Measured efficiency vs. dose of the assembled detector tiles compared to reported observations in Y-11 WLS and 3HF clear fibers 169
C.6.1SolidWorks model of the EPD prototype showing dimensions in centimeters. 170
C.6.2Tile designs showing σ and straight line groves to accommodate the wavelength shifting fibers. 170
C.7.1On the left is the light test done for the assembled prototype, where light was shined into the fiber optics. On the right is the finished EPD prototype. 172
C.7.2The installation of the EPD prototype in 2016. The blue lines are drawn into the photograph in order to guide the eye. 173

List of Tables

3.2.1 Integrated hit densities from pile-up sources on each PXL layer used simulations. 41

4.2.1 Standard geometrical cuts for different D^0 p_T. 55

4.2.2 Tight geometrical cuts for different D^0 p_T. 58

4.2.3 Loose geometrical cuts for different D^0 p_T. 59

4.2.4 Topological cuts for different $D^{\pm}$ p_T ranges. 61

4.3.1 Summary of information saved to the event buffer for mixing. 62

C.5.1 Doses deposited per tile and measured efficiency 168

Acknowledgements

First and foremost I would like to express my gratitude towards my family for all of their support. In particular I would like to mention my mother, Gale Lynn, and grandmother, Larissa Adler, for all of the help and encouragement over the years. Their selflessness, hard work and love has provided for all of my needs and engendered all of the opportunities in life that have finally led me to this accomplishment.

I would also like to express my gratitude to my advisors, Prof. Spiridon Margetis and Dr. Xin Dong, for their guidance and supervision throughout my doctoral research. I am indebted to them for providing me with many opportunities to explore and grow as a scientist.

Finally, I would like to mention Mustafa Mustafa for his time and our many discussions, which dramatically sped up the development of this work.

This material is based upon work supported by the U.S. Department of Energy, Office of Science, Office of Workforce Development for Teachers and Scientists, Office of Science Graduate Student Research (SCGSR) program. The SCGSR program is administered by the Oak Ridge Institute for Science and Education for the DOE under contract number DE-AC05-06OR23100.

Chapter 1

Introduction and research objectives

In our current understanding, it is believed that the universe sprang out of existence roughly 13.8 billion years ago from an infinitely hot and dense "singularity" and then cooled and expanded to the size and temperature of our current universe. It is believed that the high temperatures and densities experienced during the first microseconds of this expansion were enough to "melt" normal matter into its constituents, quarks and gluons, forming a novel state of matter dubbed the quark-gluon plasma (QGP). It has been posited that ultra-relativistic heavy ion collisions can deposit sufficient energy into a finite volume of matter replicating the conditions necessary for the formation of QGP.

Creating and understanding the QGP is one of the primary aims of the ongoing nuclear collision programs at the Relativistic Heavy Ion Collider (RHIC) in Brookhaven N.Y. and the Large Hadron Collider (LHC) at CERN. Consequently, measurements at RHIC [8, 22, 23, 12] seem to suggest that the matter produced in the collisions behaves like a nearly perfect liquid whose bulk properties are predominantly governed by light quarks and gluons. However, heavy quarks (charm and bottom) provide ideal probes in understanding the properties of the QGP: due to their large mass they are predominantly formed early in hard scattering processes and hence experience the entire evolution of the system. Furthermore, as the heavy quarks traverse the QGP and interact with the medium their distributions are modified and can reveal crucial information about the properties of the medium though physical observables. Finally,

due to flavor conservation heavy quarks are tagged by their flavor and can be uniquely reconstructed, even after hadronization.

This dissertation will focus on the azimuthal anisotropy of charm mesons in Au+Au collisions at center of mass energy 200 GeV per nucleon pair using data collected during 2014 with the newly installed Heavy Flavor Tracker (HFT) at the STAR experiment at RHIC. The state of the art vertex detector is employed to directly reconstruct charm mesons from the decay fragments of the hadronic channels. The dissertation is organized as follows: Chapter 1 provides a brief outline of the physics behind relativistic heavy-ion physics with an emphasis on heavy quark production, the collective dynamics of the partonic medium as well as introducing previous measurements of charm mesons. Chapter 2 will introduce the experimental set-up with particular attention to the detectors used for tracking and particle identification in this analysis.

Chapter 3 provides some details on the data set used, event and track reconstruction, the centrality definition and the use of the HFT to identify charm meson candidates through reconstruction of the decay topology. Chapter 4 presents the invariant mass of reconstructed charm mesons as well as details on the event plane determination and azimuthal anisotropy calculations. The results, together with comparison to other particle species and model calculations, are presented in Chapter 5. Chapter 6 summarizes the results and conclusions together with a brief outlook.

Several appendices are included to discuss other activities, such as service work, that have been part of my doctoral studies but do not have an immediate impact on the physics discussed in the main body of this dissertation.

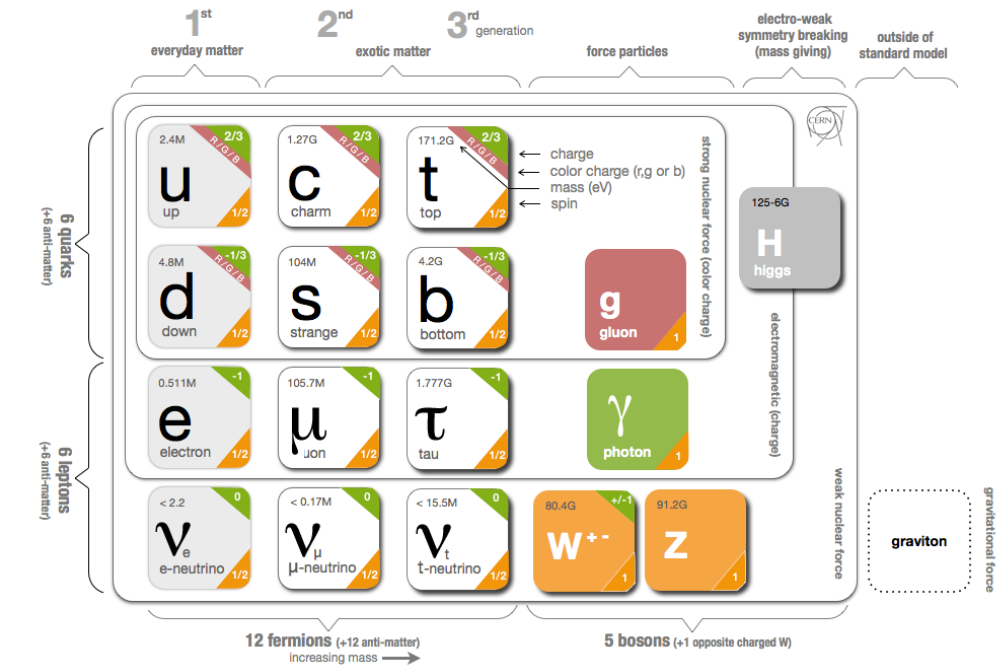


Figure 1.1.1: Summary of the Standard Model of fundamental particles (Credit: CERN).

1.1 The Standard Model

The Standard Model of particle physics is the theory concerning the electromagnetic, weak and strong nuclear interactions and classifies all known subatomic particles (Figure 1.1.1): fermions, gauge bosons and the Higgs boson. In the Standard Model, particles interact by exchanging a gauge boson associated with a particular charge, manifesting macroscopically as a force influencing both particles. The gauge bosons have integer spin and hence follow Bose-Einstein statistics and are unconstrained by the Pauli exclusion principle.

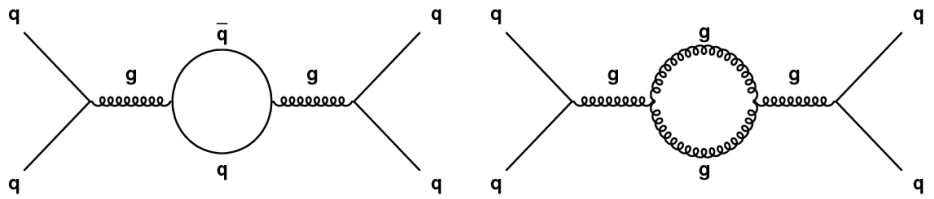
The photon mediates the electromagnetic interaction between electrically charged particles and is successfully described by Quantum Electrodynamics (QED). It is both

massless and charge neutral. The Z and $W^{\pm}$ are massive bosons associated with the weak interaction between particles of different flavors (all fermions), however the W boson also carries an electric charge and can hence couple to the electromagnetic interaction. Finally, gluons mediate the strong force between color charged particles, the quarks. Unlike photons, gluons carry a color charge and, as such, can interact with each other with important implications. The theory that describes the strong interaction is known as quantum chromodynamics (QCD).

The Standard model classifies the 12 known fundamental fermions (carry spin $\hbar/2$) according to the interactions that can influence them, or in other words the types of charge they carry. While quarks carry both electric and color charge and hence can interact by exchanging any of the gauge bosons, the leptons can only interact through electroweak interactions.

There are three color charges a quark can carry, *red*, *green* and *blue*, as well as the three corresponding anti-colors for anti-quarks. Quarks bind together through the strong interaction to form color neutral bound-states known as hadrons, which can also be classified according to their quark content: mesons are formed by combining a quark anti-quark pair while (anti)baryons are formed from a combination of three (anti)quarks of different color charge.

The last ingredient in the Standard Model, the Higgs boson, was originally theorized in 1967 and is necessary to explain why the elementary particles, other than the gluon and photon, have masses. The Higgs particle has spin 0 and hence is classified as a boson, and is believed to have been observed with a mass of 125 GeV at CERN experiments [36, 1].



(a) Screening. (b) Antiscreening.

Figure 1.1.2: QCD vacuum diagrams.

1.1.1 Quantum Chromodynamics

As mentioned in the previous section, QCD is the theory that describes the strong interaction between color charged particles. Although similar in some aspects to QED, the strong force has several defining features, in particular it is worth noting that the assumption of a self interacting gluon field leads to what is referred to as confinement and asymptotic freedom, which can be qualitatively understood in terms of the action of the field on virtual particles, illustrated in the vacuum diagrams 1.1.2a and 1.1.2b.

As in the case of QED, the vacuum polarization of color charge (1.1.2a) has the effect of screening the associated charge among interacting particles and in consequence a reduced effective charge and a diminishing interaction at large distances. However, the fact that gluons carry color charge and couple to themselves implies the existence of virtual gluonic loops (1.1.2b) with the opposite effect, i.e. anti-screening. Furthermore, since there are more types of gluons (8 color combinations) than quarks, the contribution of the gluonic loops is greater and antiscreening dominates, essentially leading to a weakening of the coupling constant $\alpha_s(Q)$ for decreasing distances (large momentum transfers).

Although the exact value of the coupling constant can not be predicted by QCD, the theory can provide a functional form [29] whose magnitude can then be determined

experimentally. At one loop order, one finds:

$$\alpha_s(Q^2) = \frac{12\pi}{(33 - 2N_f)\ln Q^2/\Lambda^2_{QCD}} \tag{1.1}$$

where N_f is the number of quark flavors and Λ_{QCD} is a parameter that essentially sets the energy scale where $\alpha_s(Q)$ diverges to infinity ($Q^2 \to \Lambda^2_{QCD}, \alpha_s \to \infty$). Moreover, the strength of the interaction becomes vanishingly small for large momentum transfer ($Q >> \Lambda_{QCD}$) and the quarks and gluons that make up the hadrons can exist almost freely in a state dubbed the Quark Gluon Plasma (QGP). For energy scales above 1 GeV the value of $\alpha_s < 1$ and QCD can be treated perturbatively. Figure 1.1.3, taken from [28], shows a summary of the measurements of the coupling constant α_s as a function of the energy scale Q together with the global fit evaluated at the Z boson mass. As a consequence, the bound states of quarks and gluons within hadrons are expected to exist freely, or nearly so, for very high temperatures and densities.

However, as α_s approaches unity the problem can no longer be tackled using the perturbative approach (pQCD) and so low energy scale problems are solved using numerical methods such as lattice gauge theory, or lQCD. In these conditions the QCD potential can be approximated with:

$$V(r) \approx \lambda r \tag{1.2}$$

The strength of this interaction does not diminish as the distance between them is increased, such that in attempting to separate a quark from a bound state the energy in the gluon fields is eventually enough to produce another quark-anti-quark pair and hence the quarks are always bound, known as confinement.

The gauge invariant Lagrangian that describes the the dynamics of quarks and gluons

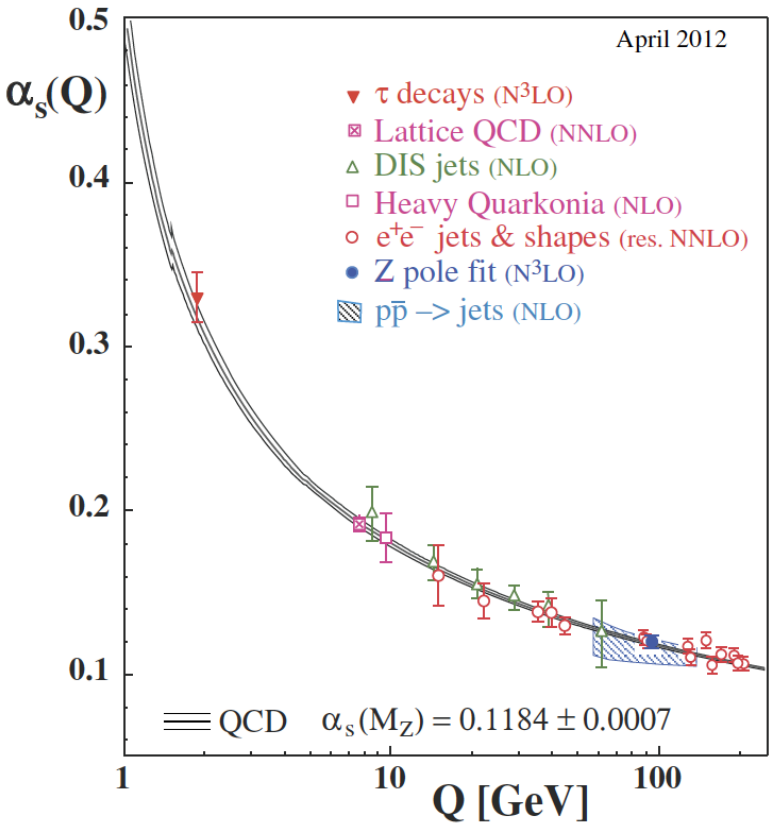


Figure 1.1.3: Summary of the measurements of α_s as a function of the energy scale Q. The degree of perturbation theory used in the extraction of α_s is indicated in the brackets(NLO: next-to leading order, NNLO:next-to-NLO, etc.) Figure reprinted from [28] with permission from the American Physical Society.

in a color field is:

$$\mathcal{L}_{QCD} = \overline{\psi}_i(i(\gamma^\mu D_\mu)_{ij} - m\delta_{ij})\psi_j - \frac{1}{4}G^a_{\mu\nu}G^{\mu\nu}_a \tag{1.3}$$

where ψ_i is the quark field, γ_μ are the Dirac matrices and $G^a_{\mu\nu}$ the gluonic field-strength tensors:

$$G^a_{\mu\nu} = \partial_\mu A^a_\nu - \partial_\nu A^a_\mu + g f^{abc} A^b_\nu A^c_\nu \tag{1.4}$$

Above, f^{abc} are the structural constant of the SU(3) symmetry group, g and m control the quark mass and coupling in the theory, and $D_\mu := \partial_\mu - ieA_\mu$ is the covariant derivative responsible for the interaction between the quarks and the gauge potentials A^a_μ.

1.1.2 Chiral symmetry

The Lagrangian discussed in the previous section has several global symmetries as well as the local SU(3) associated to the color gauge, however there is an additional, approximate symmetry associated to chirality. This can be introduced in the QCD Lagrangian by projecting the Dirac operators into their right and left handed components:

$$\psi_L \equiv \frac{1-\gamma^5}{2}\psi \qquad \psi_R \equiv \frac{1-\gamma^5}{2}\psi \tag{1.5}$$

This symmetry is explicitly broken in the QCD Lagrangian due to the term $m\overline{\psi}\psi$ and as such, massive fermions will not exhibit chiral symmetry. However, for small masses compared to Λ_{QCD} (up, down and to a lesser extent strange quarks), the previous term has near negligible contribution and $\mathcal{L}_{QCD}$ becomes invariant under

$SU(3)_R \times SU(3)_L$.

There is an important consequence that follows from spontaneous symmetry breaking, proven as part of Goldstone's theorem. In short, the theorem states that the spectrum of physical particles must include at least one particle of zero mass for every symmetry that is spontaneously broken, known as Goldstone bosons. Chiral symmetry is only approximate in QCD, and so the associated psuedo-Goldstone bosons have finite mass, the pions. Thus, the masses of the quarks confined in hadrons have two distinct contributions: a mass generated from the Higgs mechanism as well as a contribution caused by interactions with the pions due to chiral symmetry breaking, known as the QCD mass. In the case of the lighter quarks (up down and to a lesser extent strange) the QCD mass can account for up to 99% of the observed mass which is in stark contrast with heavy flavor (charm, bottom and top), shown in Figure 1.1.4.

Furthermore, as the medium created in a heavy ion collision transits to the QGP state, more and more quark pairs can form and eventually can surpass the binding energy of the $\psi_R\overline{\psi}_L$ states and the chiral condensate ceases to exist, known as Chiral Symmetry Restoration. In a QGP where Chiral symmetry has been restored, the light quarks will exhibit, in essence, only their bare masses while the heavy quark masses will remain for the most part unchanged.

1.2 Heavy Ion Collisions

In order to study the nuclear phase diagram and test the hypothesis of deconfinement, it is necessary to reproduce the high density/temperature environment envisioned to have occurred moments after the big bang. The Relativistic Heavy Ion Collider was built to study the formation of QGP by colliding Au atoms at a center of mass energy $\sqrt{s_{NN}} = 200$ GeV, and is described in detail in the following chapter.

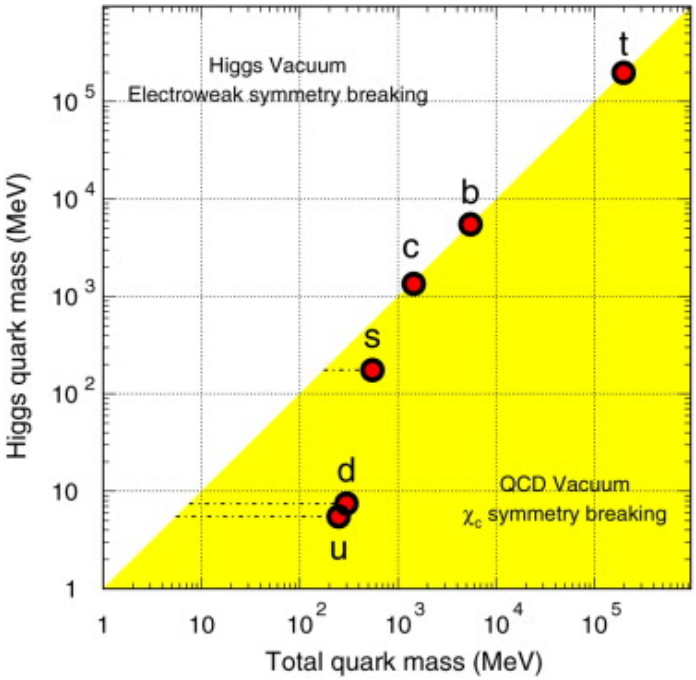


Figure 1.1.4: Quark masses coming from QCD vacuum and the Higgs vacuum. A large fraction of the light quark masses are due to chiral symmetry breaking the QCD vacuum. Figure reprinted from [88] with permission from Elsevier.

In this section we will focus on evolution of a heavy ion collision, some expected signatures of the QGP and heavy quark production.

Figure 1.2.1 shows, schematically, the different stages in the space-time evolution of a heavy ion collision. The incoming nuclei move at relativistic speeds and hence appear flat in lab frame due to Lorentz contraction. Once the nuclei collide, the partons interact through hard processes from which both heavy flavor and high p_T jets can form.

As the nuclei continue passing through each other the energy density increases as more quark anti-quark pairs are formed. As the temperature approaches the critical value the quarks and gluons become de-confined and the QGP is formed, eventually reaching equilibrium. The equilibrated QGP continues expanding due to the pressure

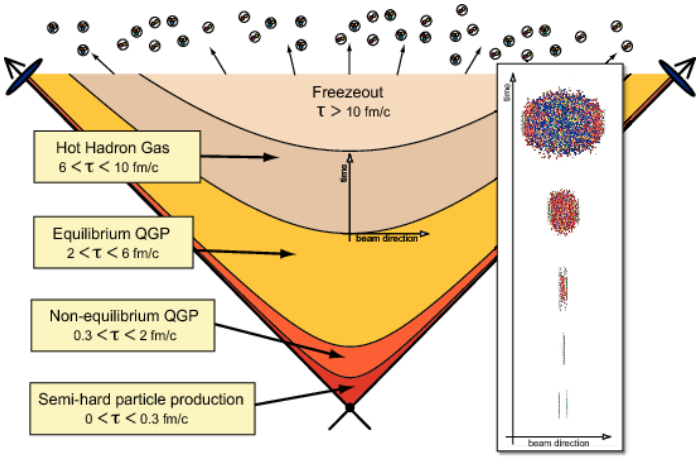


Figure 1.2.1: A cartoon illustrating the space-time evolution of a heavy ion collision generated at LHC. The panel on the right shows the evolution in the lab frame. Figure reprinted from [79] with permission from the author.

in the system eventually cooling enough for confinement to set in again, known as hadronization. As the system continues to expand, the hadrons continue to interact with each other through both elastic and inelastic collisions. Eventually, the system has cooled and expanded enough that the hadrons can only interact through elastic collisions consequently fixing the particle ratios, this stage is known as chemical freeze-out. Finally, the hadrons will reach kinematic freeze-out once the hadrons have drifted far enough from each other and can no longer interact, fixing the particle momenta which is later observed in the detectors.

Lattice calculations seem to suggest that the onset of QGP should occur at temperatures $T_c = 155$ MeV or a Bjorken energy density $\epsilon_c \sim 1$ GeV/fm^3 [53], whereas the value at RHIC for $\sqrt{s_{NN}} = 200$ GeV was measured [14] to be 5.4 GeV/fm^3 in the most central collisions, well above the requirement for de-confinement.

The times indicated in Figure 1.2.1 are only estimates, however it is clear that the QGP is extremely short lived and as such, impossible to probe externally. The following sections will focus on useful observables and probes that may carry signatures

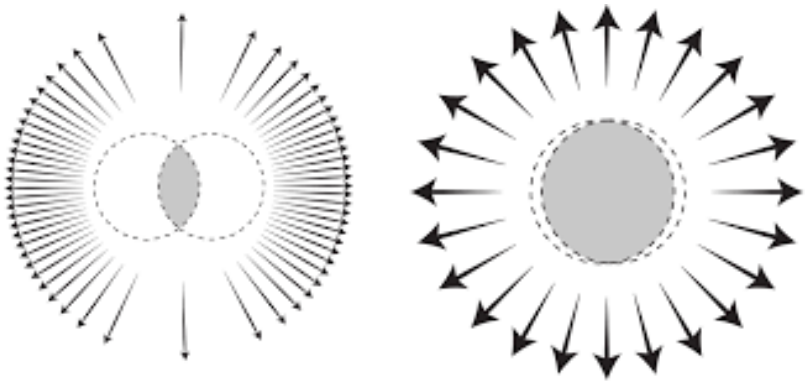


Figure 1.2.2: Non-central versus central collisions. The participants in the shaded overlap region will experience pressure leading to the momentum anisotropy illustrated by the arrows.

of the QGP that can be disentangled from the effects of later stages in the collision.

1.2.1 Collectivity

When the two colliding heavy ions are off center, i.e. have a finite impact parameter, the fireball produced in the overlapping region will have an eccentricity that is different from 0. This spatial anisotropy will produce pressure gradients in the expanding medium, boosting particles in the direction of the pressure gradients and transforming into anisotropies the particle momenta, as is illustrated in Figure 1.2.2. These anisotropies, caused by the collective motion of the particles in the fireball, are generally referred to as $flow$ and can be naturally studied by decomposing the azimuthal distribution of the particles, relative to the reaction plane Ψ_r defined by the vector joining the centers of the ions and the beam direction, in a Fourier series:

$$E\frac{d^3N}{dp^3} = \frac{1}{2\pi}\frac{d^2N}{p_T dp_T dy}\left(1 + \sum_{n=1}^{\infty} 2v_n \cos(n(\phi - \Psi_r))\right) \tag{1.6}$$

Chapter 4 will discuss the study of azimuthal anisotropies in more detail, however it is worth mentioning in passing that by drawing an analogy to hydrodynamics we can connect the observed flow patterns to fundamental properties of the fluid-like

medium produced in the collision. In particular, the first two harmonics have been traditionally studied, the directed flow v_1 and the elliptic flow v_2; though recently higher harmonics have also become of interest and are associated with fluctuations in the initial condition in an event.

The phase transition to the QGP is expected to have noticeable effects on the flow patterns through two important mechanisms. At low p_T the elliptic flow, v_2, results from interactions with the medium and therefore develops over time. Figure 1.2.3 shows the time evolution of both the spatial eccentricity and the momentum anisotropy of the fireball [54]. In particular, the solid curves show the results from a hydrodynamic calculation with a first order phase transition. The spatial eccentricity is large at the beginning of the evolution and continuously decreases while driving the momentum anisotropy which saturates around 6 fm/c, suggesting that the majority of the v_2 is generated in the early stages and is sensitive tho the dynamics of the QGP phase. The second mechanism that can influence the v_2 is the path dependence of the in-medium energy loss, which is expected to lead to a positive value for the elliptic flow for hadrons up to high p_T. In the ideal hydrodynamics picture, the observed final state hadrons freeze out from fluid cells that are in local equilibrium but have local transverse velocity relative to the lab frame. Although this is not true in the case of viscous hydrodynamics, for small values of η/s the departures from equilibrium are relatively small and may be neglected. Since all these are boosted with the same velocity, this should result in a mass ordering of the particle transverse momentum spectra and hence in the flow patterns, as seen in Figure 1.2.4.

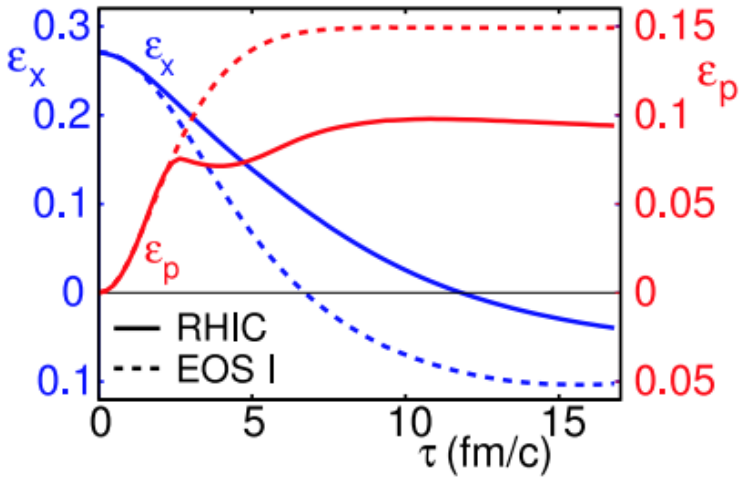


Figure 1.2.3: Time evolution of the spatial eccentricity ϵ_x and momentum anisotropy ϵ_p for an equation of state with a phase transition (solid) and ideal massless gas at very high temperature (dashed). Figure reprinted from [54] with permission from Elsevier.

1.2.2 Energy loss

Another signature of phase transition to the QGP state would be a difference (relative to p+p collisions) in the produced particle p_T spectra due to the effects of medium-induced energy loss. This energy loss is expected to occur both through elastic (collisional) and inelastic (radiative) processes and theoretical studies have an established history. A simple estimate can be obtained by considering an average energy transfer $v_{el} \approx q_\perp^2/2\omega$ between the jet parton and a thermal parton with energy ω and transverse momentum transfer $q_\perp$, the resulting elastic energy loss [84] is:

$$\frac{dE_{el}}{dx} = C_2 \frac{3\pi\alpha^2}{2} T^2 \log\left(\frac{3ET}{2\mu^2}\right) \tag{1.7}$$

Where μ is the Debye screening mass and C_2 is the Casimir factor of the propagating parton in its fundamental representation. It is clear that the elastic energy loss is sensitive to the temperature in the medium however it's effect is, in general, small when compared the radiative energy loss.

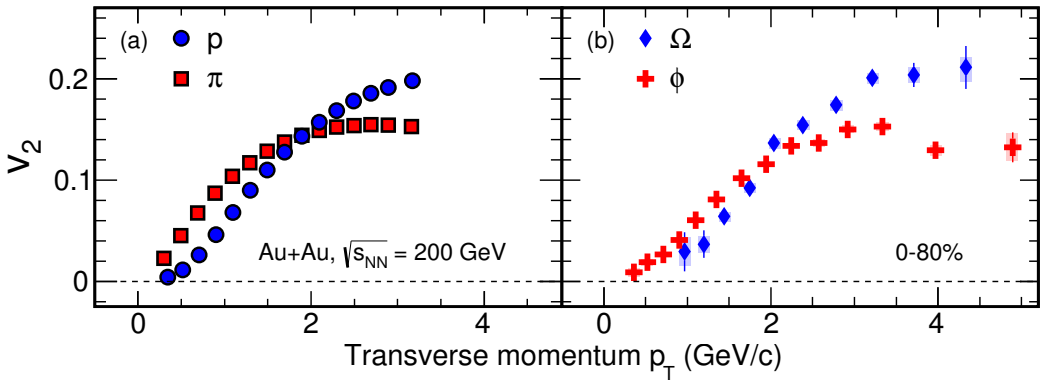


Figure 1.2.4: v_2 for identified particles in Au+Au $\sqrt{s_{NN}}$ =200 GeV collisions recorded at STAR. Figure reprinted from [4] with permission from the American Physical Society.

An upper bound for the radiative energy loss was first estimated using the uncertainty principle [32] and has been modeled in ever more complex schemes. The first theoretical study of QCD radiative energy loss [86] modeled the multiple scattering occurring in the medium in terms of a screened Coulomb potential and found interference effects between adjacent scattering sites, suppressing Bremsstrahlung and pair production at high energies or matter densities, an effect known as the Landau-Pomeranchuk-Migdal (LPM) effect.

Another interesting property of gluon emission in a QCD medium, known as the dead cone effect [81], introduces a suppression in the probability for gluon emission for quarks with a large mass to transverse momentum ratio. Hence, heavy flavor is expected to show a reduced energy loss at lower p_T when compared to light quarks. These studies have been followed by more recent work, however a unique feature of radiative energy loss in QCD is the non linear dependence on the path-length which arises from the non-Abelian nature of QCD.

Given that the QGP is not expected to form in small systems (i.e. p+p), the effects of

in-medium energy loss in heavy ion collisions should provide strong evidence for the phase transition to this state of matter. The suppression is measured experimentally in the observable known as the nuclear modification factor R_{AB} for the system A+B relative to p+p, defined as:

$$R_{AB} = \frac{1}{N_{bin}} \frac{\frac{d^2N_{AB}(p_T,y)}{dp_T dy}}{\frac{d^2N_{p+p}(p_T,y)}{dp_T dy}} \tag{1.8}$$

where N_{bin} is the average number of binary collisions in the A+B system, usually obtained together with the centrality form Glauber model fits, and $d^2N_{p+p}(p_T)/dp_T dy$ $d^2N_{AB}(p_T)/dp_T dy$ are the invariant yields in p+p and A+B respectively. Figure 1.2.6a shows the measured [11, 5, 10] R_{AA} for light flavor π^0 at RHIC versus that of heavy flavor at both the LHC and RHIC. A significant suppression is observed in the π^0 spectra over the entire region, suggesting a strong modification in the denser Au+Au system.

1.2.3 Heavy quarks

The lifetime of the hot and dense matter produced in heavy ion collisions at RHIC is expected to last on the order of a few fm/c and it has an initial transverse radius of roughly 6 fm. Because of this short-lived nature, studying the QGP must rely on probes that are produced in the collision itself. In particular, energetic probes are especially useful as they will penetrate the bulk matter. However, these high p_T partons can not be directly measured and so, one can either reconstruct clusters of correlated hadrons, known as *jets* or reconstruct hadrons consisting of at least one heavy quark.

Due to their large mass, heavy quark production through thermal processes is considerably suppressed relative to lighter flavors and as such they are predominantly

produced in early stages in hard scatterings. Furthermore if we consider that the minimum momentum exchange Q needed to create a quark anti-quark pair is $2m_q$, this translates to a space-time scale of the order $1/2m_q \sim 0.1$ fm/c for charm and an order of magnitude lower for bottom, so production is expected to occur before the onset of QGP. Finally, interactions with the QGP will not change the quark flavor so measured heavy flavor can be traced back to initial hard scattering in the collision.

The measurement of heavy flavor elliptic flow provides further insight into the transport properties of the medium given that the final state heavy quarks at all transverse momenta experience the whole evolution of the system. At low p_T, charmed hadron v_2 can test whether quarks with large mass participate in the collective dynamics and thermalize in the medium. Because of their large mass, charm quarks are expected to have a longer relaxation time with respect to that of lighter quarks [63]. At mid and low momentum the elliptic flow of D mesons is sensitive to the charm quark hadronization mechanism. In particular, low and mid momentum heavy quarks could hadronize via recombination, in which case the azimuthal anisotropy for charm hadrons should be greater than that of open heavy flavor. Finally, at high p_T the D meson v_2 can constrain, together with the R_{AA}, the path dependence of the in medium energy loss.

Figure 1.2.5 [2] shows the azimuthal anisotropy for D mesons versus charged particles at LHC energies in semi central collisions. It is observed that the v_2 for D mesons in the range $2 < p_T < 6$ GeV/c is finite and comparable to that obtained for light flavor, and indication that low momentum charm quarks are interacting with the medium and partaking in the collective flow. The finite value for the v_2 at high p_T most likely originates from the path length dependence of energy loss in the QGP,

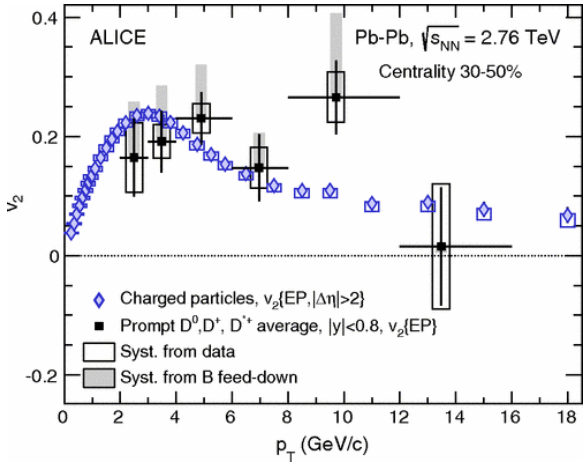
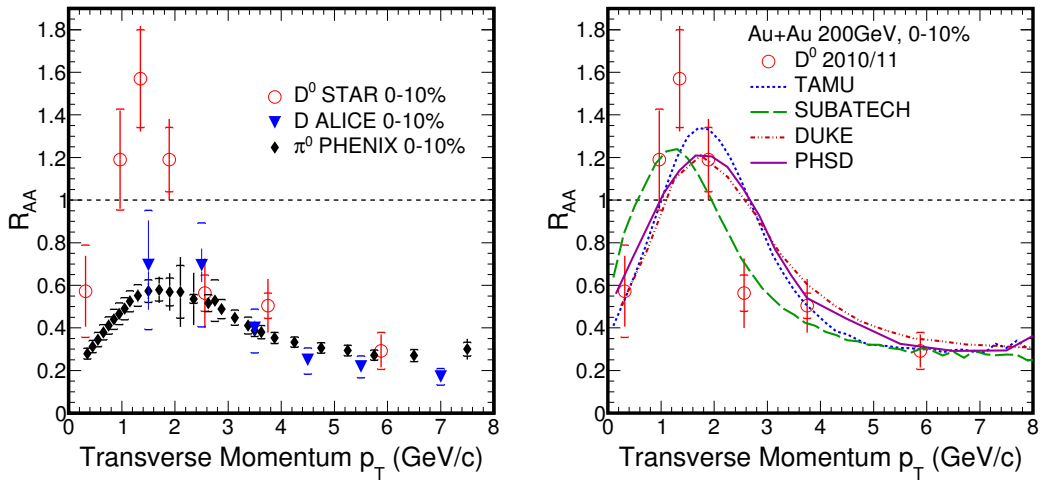


Figure 1.2.5: Average of D^0, $D^{\pm}$ and D^{*+} v_2 as a function of p_T compared to charged particle v_2 from ALICE. Figure taken from [2].

and together with the R_{AA} should be able to provide constraints on model calculations. The measurement of nuclear modification of heavy flavor from STAR shows a series of interesting features. First of all, strong suppression for $p_T > 3$ GeV/c is in agreement with the ALICE result and again is indicative of large energy loss of heavy quarks in the medium. It is worth noting that this agreement does not necessarily imply the same degree of energy loss at both energies since the R_{AA} is also sensitive to the particle spectra in p+p. In other words, the combined effect of a denser and harder p_T spectra at LHC could results in a similar value of the R_{AA}.

At low-mid p_T, the two different collider energies show a much more striking difference with a considerable enhancement measured by STAR in the D^0 R_{AA}. This effect can be explained by models including parton energy loss, collective flow and the contribution of recombination to the charm quark hadronization, a sample of which [9, 77] are shown in Figure 1.2.6b.

Although uncertainties are still too large to draw firm conclusions, the features



(a) Species comparison.

(b) Comparison to models.

Figure 1.2.6: Nuclear modification factor for most central collisions 0-10%. Left: Comparison between light (π^0) [11] and heavy (D) [5, 10] at LHC and RHIC energies. Right: Comparison to several theoretical calculations [9, 77].

observed at the two different collider energies could be explained due to the different role of initial-state effects and radial flow at the different energies. For one, the momentum broadening (Cronnin) effect that gives rise to the enhancement at intermediate p_T is known to be more pronounced at lower energies [85]. On the other hand, in the final state the radial flow may be altering the p_T distribution by transferring momentum to low momentum charm quarks that partake in the collective motion, pushing them towards higher momenta.

Experimentally, heavy quark reconstruction is carried out through measured leptons from semi-leptonic decays or from the hadronic decays (illustrated in Figure 1.2.7) both with their respective advantages and disadvantages.

While electrons from semi-leptonic decays, referred to as non-photonic electrons, tend to have relatively high branching ratios and are easily triggered by detectors, the measurement relies on careful interpretation to disentangle the contribution from

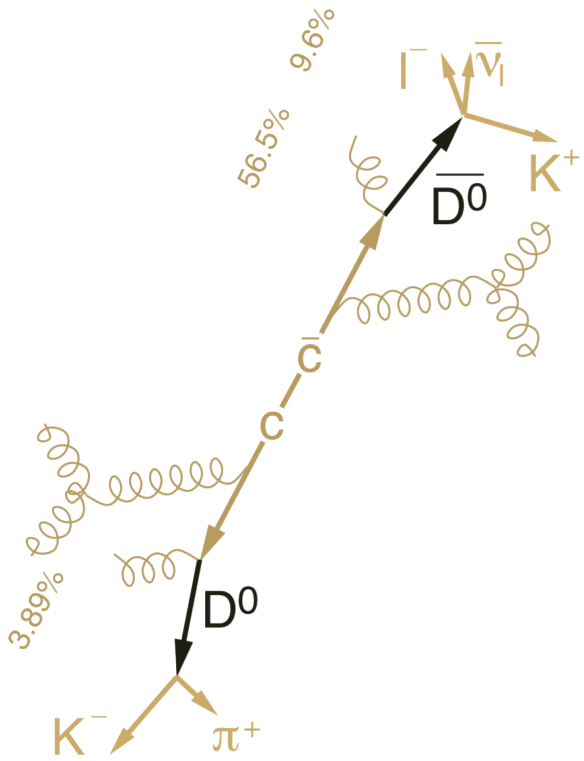


Figure 1.2.7: Schematic of charm quark hadronizing to neutral D meson and then decaying through hadronic and semi-leptonic channels. Taken from [76].

the various charmed and bottom decays. Furthermore, due to decay-smearing the p_T of measured leptons can come from a wide kinematic region.

On the other hand, the hadronic channels allow to fully reconstruct the charmed hadrons and so do not suffer from the complications in the semi-leptonic decays, however the measurement can be challenging due to large combinatorial backgrounds and lower branching ratios. One approach is to use the decay topology to reduce this background by distinguishing between tracks that come from the collision itself (primary vertex) and those that come from a secondary decay vertex. This, however, places stringent requirements on the detectors as they must be able to resolve differences on the order of tens of microns. The Heavy Flavor Tracker at STAR was designed with this specific purpose and will be discussed in more detail in following sections.

Chapter 2

Experimental set-up

2.1 RHIC facility

The Relativistic Heavy Ion Collider (RHIC) accelerator facility, located at Brookhaven National Laboratory, is one of two operating heavy-ion colliders and the only spin-polarized proton collider ever built. RHIC was first turned on in 2000 and was, until 2010, the highest energy collider ever built.

The collider consists of two independent rings with radii 3.8 km used to accelerate and store heavy ions and protons. The RHIC storage rings employ ∼1.7k niobium-titanium superconducting magnets, cooled to about 4.2 K, to focus the beams. There are six interaction regions where the two rings intersect out which four originally housed experiments: PHOBOS, BRAHMS, PHENIX and STAR (only the latter 2 continue to operate today). The layout of the RHIC facility and location of the six interaction regions is shown in Figure 2.1.1.

The rings are versatile enough to permit storing and colliding particles ranging from protons to the heaviest stable nuclei, and due to their independence can be used to study asymmetric collisions such as p+A or d+A. The top collision energy for the heaviest nuclei is $\sqrt{s_{NN}} = 200$ GeV/c center of mass energy per nucleon pair, and $\sqrt{s} = 500$ GeV for protons. Heavy ion beams originate in a pulsed spitter source and are accelerated successively by a Tandem van der Graaf generator, Booster synchrotron and Alternating Gradient Synchrotron (AGS) where they are fully stripped of electrons and then injected into RHIC with an energy of 10.8 GeV per nucleon.

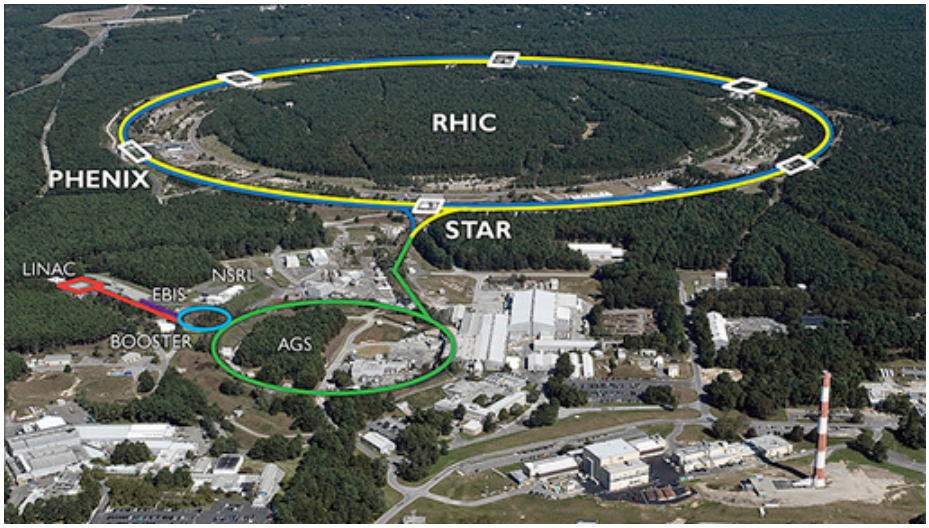


Figure 2.1.1: The RHIC accelerator complex (credit:BNL).

Protons originate in a 200 MeV linear accelerator and then fed to the Booster and AGS for further acceleration prior being injected into RHIC with an energy of 24.3 GeV.

Two separate radio frequency systems (RF) are used at RHIC: a system running at 28 MHz captures and accelerates the bunches received from AGS while a second system, at 197 MHz, focuses the beams to a small collision diamond to fully take advantage of the luminosity. The current average luminosity for top energy Au+Au beams is $50 \times 10^{26}\text{cm}^{-2}\text{s}^{-1}$ which is roughly 25 times the original design goal.

To date, RHIC has collided a number of different systems: p+p, p+Al, p+Au, d+Au, h(helium-3)+Au, Cu+Cu, Cu+Au, Au+Au and U+U. This dissertation will focus on recent results from the STAR experiment, obtained during 2014 Au+Au collisions, and the following sections will provide further detail on the experimental set-up.

2.2 STAR experiment

The Solenoidal Tracker At RHIC (STAR) experiment is one of the two remaining large detector systems constructed to obtain measurements at the interaction regions at the Relativistic Heavy Ion Collider (RHIC), located in Brookhaven, N.Y.

STAR was originally commissioned in order to investigate the behavior of strongly interacting matter present at high energy density, in particular looking to understand the phase diagram of nuclear and search for signatures of the creation of Quark Gluon Plasma (QGP).

In order to accomplish this, STAR was primarily designed to obtain measurements of hadrons over a large solid angle, and as a consequence was built with full azimuthal coverage over two units of pseudo rapidity ($|\eta| < 1$), featuring high precision tracking and particle identification at the center of mass of the collisions. The STAR experiment consists of a large, room temperature solenoidal magnet as well as an array of detectors used for charged particle identification, tracking and timing. Figure 2.2.1 shows an overview of the STAR experiment and the main detector systems.

Momentum determination using the Time Projection Chamber (TPC) requires a powerful magnetic field in order to measure the curvature of high momentum tracks, while the position resolution in TPC is strongly sensitive to in-homogeneities in the magnetic field. As a consequence, the solenoid at STAR has been optimized to produce reasonably uniform magnetic fields for 0.25 T $< |B_z| <$0.5 T with a uniformity below 1 mm in the azimuth, and 2.3 mm in the radial direction over the entirety of the TPC volume.

The magnet consists of 10 main coils and two space trim coils, all connected in series and drawing a maximum of over 5000 A at full field. Space trim coils are also included

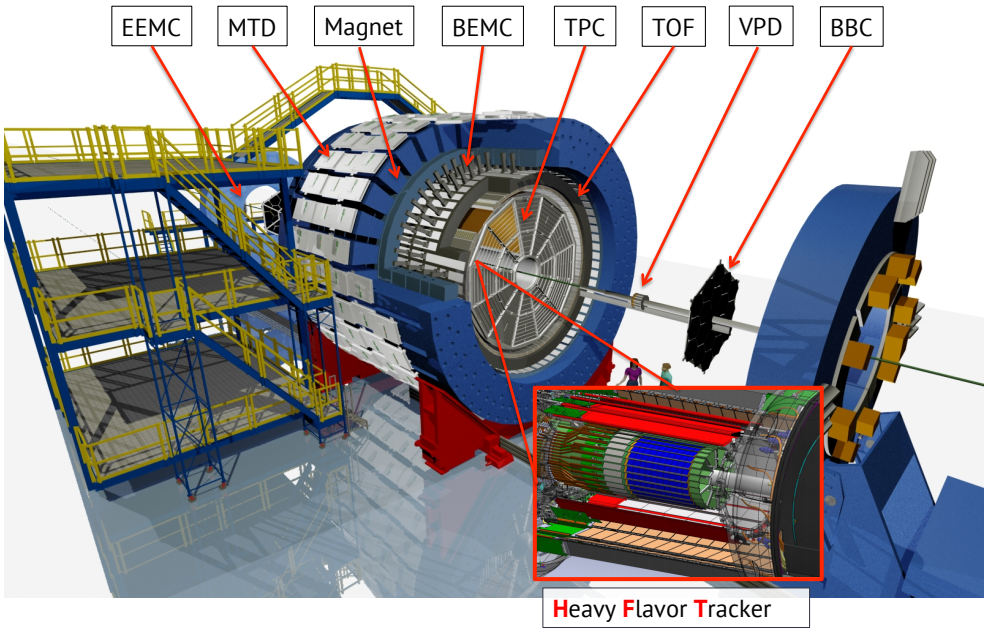


Figure 2.2.1: Schematic showing STAR experiment and important detector systems.

in the magnet pole tips to aid in maintaining the field uniformity. The magnet operates at roughly room temperature (29° C), and is water-cooled with a closed, internal loop dissipating roughly 3.5MW of power to an external loop via heat exchangers. The following section will briefly describe the relevant detectors to the analysis and research project presented in this dissertation.

2.2.1 Time Projection Chamber

The Time Projection Chamber (TPC) is the main detector at STAR measuring 4.2 m in length and 4 m in diameter, it provides full azimuthal coverage out to ± 1.8 units of rapidity and particle identification down to transverse momenta of 100 MeV/c. The TPC is separated in two halves by a central membrane (CM) and both chambers are filled with P10 gas (90% Argon, 10% Methane) regulated to 2 mbar

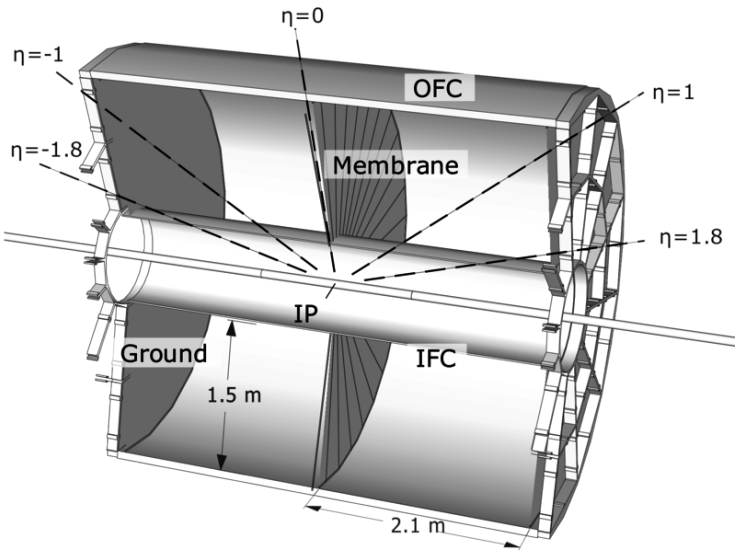


Figure 2.2.2: Schematic showing the structure of the STAR TPC detector taken from [78].

above atmospheric pressure. As charged particles travel through the gas, molecules are ionized and the electrons are accelerated with a uniform electric field established by grounding the endcaps and holding the central membrane at -31 kV. The drifting electrons can continue ionizing gas, producing an avalanche that is then collected in pad planes at the end of the TPC.

P10 gas has been traditionally selected for TPCs because of the fast drift velocity that peaks at low electric fields, permitting use of low voltage in the field cage and greatly simplifying the design. Furthermore, methane acts as a quencher/absorber for energetic photons that may be emitted by excited gas molecules falling to their ground state, ensuring that avalanches measured by the TPC are coming from the electron released from a charged particle produced in the collision.

Readout is performed using two pad planes at opposite ends of the TPC, with each segmented in 12 sectors with 45 rows of pads. Each sector in itself is divided into:

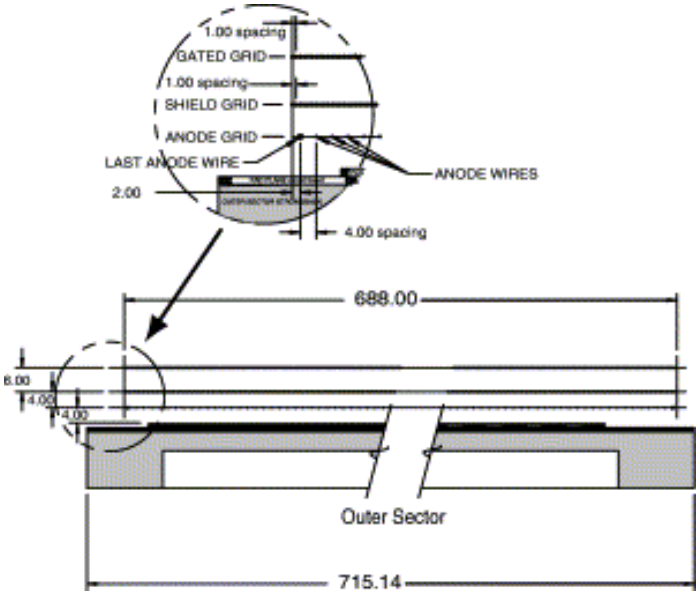


Figure 2.2.3: Schematic cutaway of MWPC design showing pad plane and the three wire planes :anode, grounding and gating grid. Figure reprinted from [18] with permission from Elsevier.

- Inner sector ($60 < R < 127$ cm) with pad spacing of 3.35 mm along a row and 50 mm between padrows

- Outer sector ($127 < R < 189$ cm) with pad spacing of 6.75 mm along a row and 20 mm between padrows

The measurements are done using MultiWire Proportional Chambers (MWPCs) which consist of three sets of wire grids and the pad plane, schematically shown in 2.2.3.

As the drifting electrons enter the vicinity of the anode grid, they avalanche and the resulting positive ions produce a temporary image charge on the pad plane which is then measured by a preamplifier/shaper/waveform digitizer system.

The ground grid plane of 75 μm wires completes the sector structure and is primarily

used to terminate the high intensity field in the avalanche region and provide additional rf shielding for the pads. A final layer of wires, the gating grid, is located 6mm from the ground grid and functions as a shutter to control the entry of electrons from the TPC into the MWPCs as well as blocking positive ions produced in the MWPC from returning into the TPC drift volume where they would heavily distort the drift field. Given that electrons can travel up to 2 m before being collected in a MWPC, the field homogeneity is fundamental for track reconstruction and particle identification.

The total charge deposited in the MWPCs is proportional to the ionization produced in the drift volume and as such, can be related to the energy loss (dE/dx) incurred by the particle as it traverses the TPC. As the ionization itself is proportional to the velocity of the particle, not the momenta, the energy loss can be used to distinguish between particle species as long as the as the momenta does not exceed the mass, that is roughly $v > 0.7$c. Figure 2.2.4 shows the track energy loss measured in TPC in Au-Au collisions collected during 2014 with the different particle species associated to the observed bands.

The TPC can provide three dimensional information by determining the z-position according to the arrival time of the electrons. Information is gathered in 512 time bins corresponding to roughly 1 cm in the average drift field. In the $r - \phi$ direction the maximum resolution, determined by the number and spacing of the pads, is about 0.4 mm in the inner sector and 0.6 mm in the outer, however this deteriorates for tracks that cross the pad at large angles [18].

In the z-direction the arrival time of electrons from an ionization cluster are usually

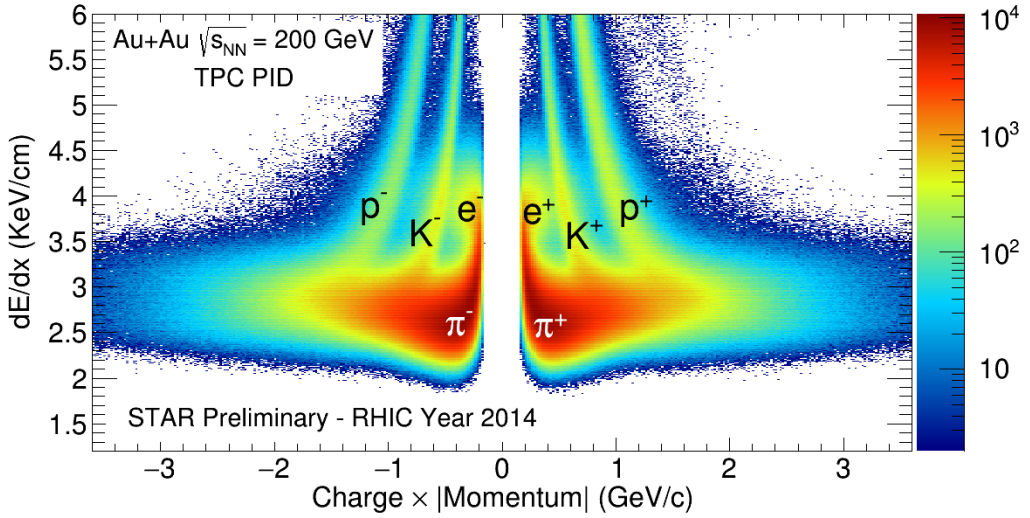


Figure 2.2.4: TPC dE/dx measured in 200GeV AuAu collisions collected in 2014 at RHIC.

spread over several time bins due to electron diffusion as well as the track dip angle itself, and so the resolution can vary between ∼0.5-2 mm.

2.2.2 Time-of-Flight detector

As was discussed in previous sections, the STAR particle identification (PID) was initially done using energy loss in the TPC. This approach, however, has some shortcomings at high transverse momentum, $p_{\mathrm{T}} > 0.7$ GeV/c where the distinguishing power of dE/dx in the TPC is no longer enough to separate between charged hadrons. As such, roughly half of the charged hadrons in top energy Au-Au collision at RHIC could not be directly identified.

The TOF system was designed and commissioned to fill in these "gaps" in PID. With a total timing resolution of 100 ps, and given the TPC's tracking resolution, the TOF detector can provide direct PID $p : \pi : K$ up to transverse momenta $\sim 1.7 - 1.9$ GeV/c and $(\pi + K) : p$ up to $\sim 2.9 - 3.1$ GeV/c [57]. Timing information from TOF, together with dE/dx from TPC, can be combined to provide high efficiency particle identification for $\sim 98\%$ of the charged hadron spectra. The use of TOF to exclude "slow" tracks also allows a clean separation, together with TPC, between pions and electrons as well as some rejection for pile-up tracks.

The STAR TOF is based on multi-gap resistive plate chambers originally developed at CERN by the ALICE group and constructed in China . Consisting of a stack of resistive plates (0.54 mm float glass) with five 220 μm gas gaps, graphite electrodes (1.1 mm thick) are applied to the outermost glass layers and held at a voltage differential of ~ 14 kV and the gas chambers are filled with 5% isobutane and 95% Freon R-134a gas. As a particle crosses the MRPC and ionizes the gas in the chambers,

the resulting electrons are accelerated by the intense electric field established by the voltage differential and avalanche amplifying the signal. Due to their large resistivity, both the glass and electrodes are transparent to the avalanche charge such that the image charge in the copper readout plates (outside the electrodes) can be collected. The total signal, proportional to the summed avalanche charge in the MRPC chambers, is generally quite small, requiring careful pre-amplification and rf shielding in the mechanical design. The typical dark count for a STAR MRPC is $\sim$ 20 Hz/pad. The TOF detector, fully installed in STAR since 2010, consists of 120 trays arranged in two adjoining rings immediately outside the STAR TPC. Each tray covers a pseudo rapidity interval of $\sim$ 0.9 and 1/60th of the azimuth and each tray has 32 MRPC's arranged nearly projectively for collisions at the center of STAR. In total the TOF system consists of 3840 MRPC's and 23,040 read-out channels with an occupancy of around 12% for central Au-Au collisions at top RHIC energy. Figure 2.2.5 shows an example of particle identification with TOF from 2014 Au-Au collisions at top RHIC energy.

2.2.3 Vertex Position Detector

The STAR Vertex Position Detector (VPD) [58] provides the primary detector input to the STAR minimum-bias trigger in A+A collisions. It consists of two identical assemblies at the east and west ends of the STAR experiment and each assembly consists of 19 detectors housing 0.25 inch lead converters followed by a 1 cm thick fast plastic scintillator which are, in turn, coupled to a mesh dynode photomultiplier tube (PMT) with optically transparent silicon adhesive.

The two assemblies are mounted symmetrically around the center of STAR at a distance of 5.7 m from the interaction region covering a pseudo rapidity range of

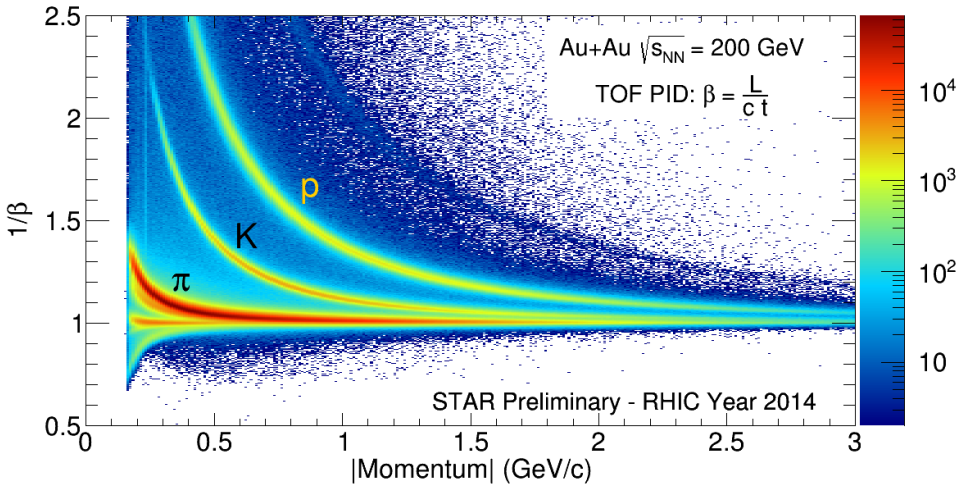


Figure 2.2.5: TOF particle identification from $1/\beta$ measured in 200GeV AuAu collisions collected in 2014 at RHIC.

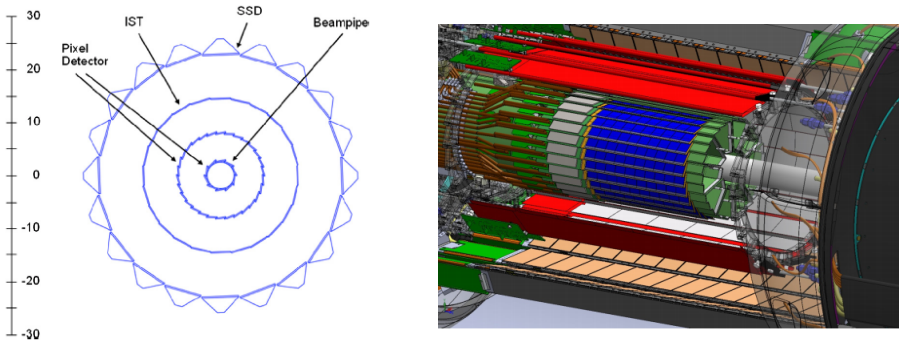
$4.24 \leq |\eta| \leq 5.1$. The minimum-bias triggers generally use timing information from both ends of the VPD to set constraints on the position of the primary vertex to enhance the rate of recorded collisions in the center of STAR. The single-detector timing resolution of the VPD is roughly 95 ps in Au+Au collisions and degrades to $\sim$ 150 ps in p+p and can measure the location of the primary vertex to within $\sim$ 1 cm and $\sim$ 2.5 cm in full energy Au+Au and p+p collisions, respectively.

2.2.4 Heavy Flavor Tracker

The Heavy Flavor Tracker (HFT) [70] upgrade for the STAR experiment was commissioned in order to boost the study heavy flavor production in the busy environment created in top energy collisions at RHIC through direct reconstruction from their hadronic decay fragments. Given the small lifetimes of these heavy particles, this sets a stringent requirement for the HFT tracking resolution. For instance, the channel $D^0(\bar{c}u) \rightarrow K^-\pi^+$ has decay length $c\tau \sim 120$ μm and tracking with HFT must be able to distinguish between particles coming from the collision's primary vertex and those coming from these displaced vertices.

The HFT, shown schematically in 2.2.6a and 2.2.6b, consists of four layers of silicon in three sub-detectors arranged to incrementally guide tracks from TPC to the innermost layers with improved resolution: the Silicon Strip Detector (SSD), the Intermediate Silicon Tracker (IST) and, innermost, the Pixel (PXL) detector.

- The SSD was originally commissioned together with the Silicon Vertex Detector in 2005 and removed from STAR after 2006. The existing silicon strips [20] were refurbished with faster readout electronics and repurposed as the outermost



(a) Schematic of the HFT cross section. (b) 3D model of HFT detector as it sits inside the STAR TPC.

Figure 2.2.6

layer of the HFT. The SSD detector sits at a radius of 22 cm and consists of two clamshells with 10 fiber ladders each. The ladders contain 16 wafers of double sided silicon strip sensors with 95 μm pitch providing a position resolution of 20 μm in $r \times \phi$ and 740 μm along the beam axis (z).

The ladders, measuring 1060 mm long, are built out of carbon fiber due to its low material budget and good rigidity, while the triangular cross-section allows for airflow in the ladder to cool the detector. The SSD has full azimuthal coverage in $|\eta| < 1.2$ and has a thickness of roughly 1% radiation length.

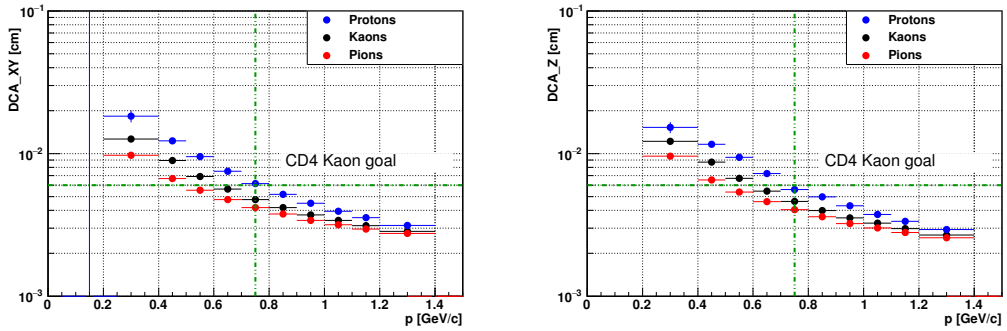
- The IST has single-sided double-metal silicon pad sensors with pad size 600 μm $\times$ 6 mm. It can provide position resolution of 170 μm in $r \times \phi$ and 1.8 mm in z. The IST consists of 24 staves that sit at a radius of 14 cm, each consisting of carbon fiber support structure, 6 silicon pad sensors, readout chips and an aluminum tube for liquid cooling.

  In order to be compatible with the TPC, the IST has full coverage in the azimuth in $|\eta| < 1.2$ and an overall thickness of roughly 1.5% radiation length.

- The PXL detector is the core of the HFT upgrade and consists of two layers of ultra-thin (50 μm) state of the art CMOS Monolithic Active Pixel Sensors (MAPS)[48]. It is divided into 10 sectors which sit on one of two halves for easy removal and installation. Each sector contains one inner ladder, at a radius of 2.8 cm, and three outer ladders 8.0 cm away from the beam. Each ladder has 10 MAPS sensors with 928 $\times$ 960 pixels distributed on the 2 cm $\times$ 2 cm sensor. In total there are about 360M pixels on 0.16 m^2 of silicon with a total hit resolution of 6.3 μm, including the effects of the detector vibration. Given the closeness to the primary vertex, a low material budget was fundamental in the design of the PXL detector. Air cooling, together with the thinned silicon sensors and carbon fiber support limit the thickness of PXL to 0.4% radiation length for Al-cable ladders and 0.5% for Cu-cables. In Run14 only 2 out 10 of the inner ladders were equipped with Al-cables, the rest being replaced for Run16.

  The PXL detector is the first implementation of MAPS technology in a collider experiment and is based on CMOS technology where electrons, released by a traversing particle, are allowed to diffuse in the low-doped epitaxial layer until they are collected in a large E-field depleted collection diode. The signals are then passed to the discriminator and digitizers at the edges of the circuits and rolling shutter read out (sequencing over the rows) records hits for particles that pass through a pixel in between interrogations, leading to an integration time of 186 μs.

The purpose of IST and SSD is to improve the track reconstruction efficiency by guiding the TPC tracks down to PXL with sufficient resolution to select the correct



(a) (b)

Figure 2.2.7: DCA resolution for TPC tracks with hits in IST and both PXL layers vs. p_{T} in Au-Au collisions at $\sqrt{s_{NN}} = 200$GeV.

hit in a high hit-density environment. Furthermore, as fast detectors (unlike TPC or PXL) both IST and SSD can also provide important pile-up protection to reject reconstructed tracks that arrive at the wrong time. SSD and IST are redundant and either one can provide sufficient leverage to guide tracks to PXL.

Figures 2.2.7a and 2.2.7b show the distance of closest approach (DCA) resolution for pions, kaons and protons for TPC tracks with hits in IST and both layers of PXL from Au-Au collisions at RHIC top energy collected in 2014. The green line shows the design goal for the HFT system for Kaons at $p_{\mathrm{T}} = 750$ MeV/c, the results for both the z and xy directions exceed this goal.

Chapter 3

HFT calibrations and performance

While preparing the physics results presented in this research project, I was personally tasked with several calibration and software tasks related to the PXL detector. This section will briefly discuss calibration as well as studies on the performance of the Heavy Flavor Tracker.

3.1 HFT Calibrations

Careful calibration of the HFT detector is essential in order to ensure the quality of data taken, optimize its performance and fully incorporate the subsystem into the rest of the STAR experiment. In broad terms, calibrating the detector consists of two important activities:

- The quality of the data acquired by each one of the subsystems must be verified. Both "hot" (or noisy) channels, as well as underperforming or dead areas in each of the subsystems must be identified. This serves the double purpose of ensuring the veracity of recorded hits to remove issues that might result from recording fake hits as well as allowing an accurate determination of the reliable acceptance of the detector.

  Given that the technology used in each of the three subsystems (SSD, IST and PXL) is different, the procedures followed for quality assurance (QA) also vary, however the details will not be covered in this section. Nevertheless, due to my own involvement appendix A provides a detailed explanation of the masking

procedures implemented for PXL. Figure 3.1.1 shows a series of SSD QA plots obtained from a single recorded run in 2016 while figures 3.1.2 and 3.1.3 provide a summary of the IST and PXL subsystems during 2016.

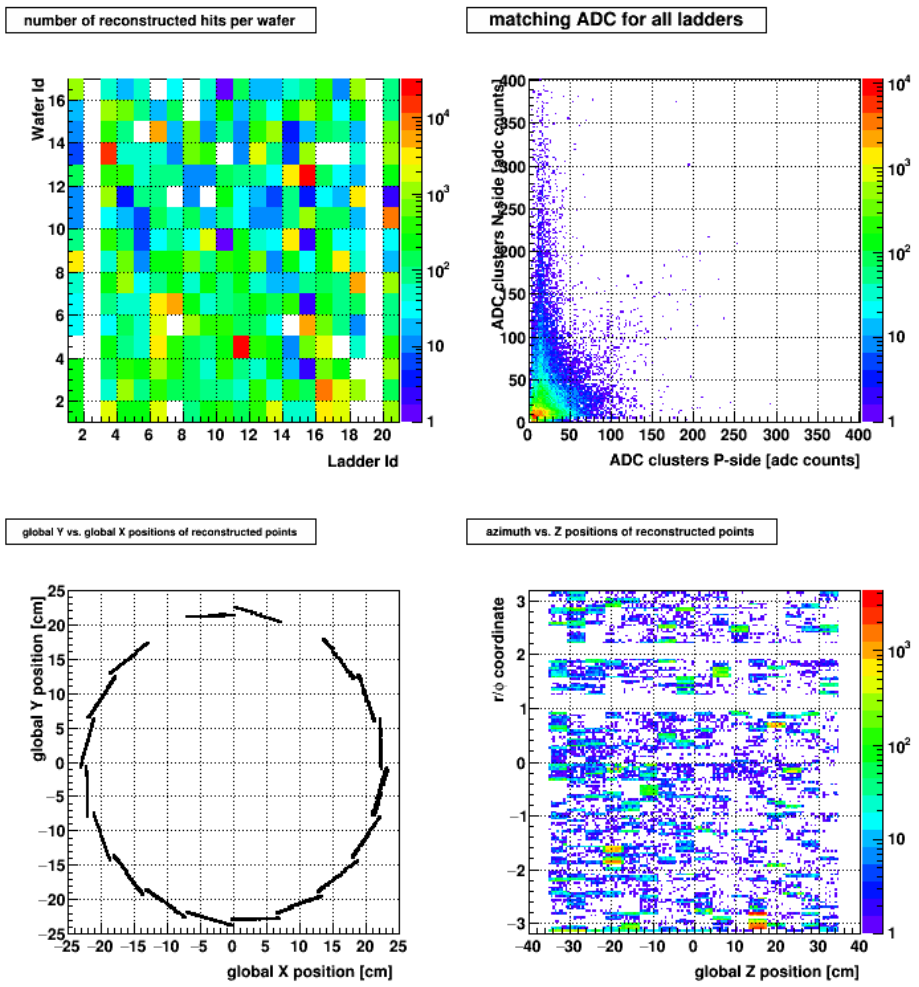


Figure 3.1.1: SSD QA plots for a single run taken in 2016 showing (clockwise starting from upper left): The number of reconstructed hits in each SSD wafer, digital signal matching between both sides of the SSD, reconstructed hit position in the beam direction and reconstructed hit position in the transverse (xy) plane.

- A second important calibration activity is that of alignment. To fully take advantage of the HFT upgrade, it is important to accurately determine the

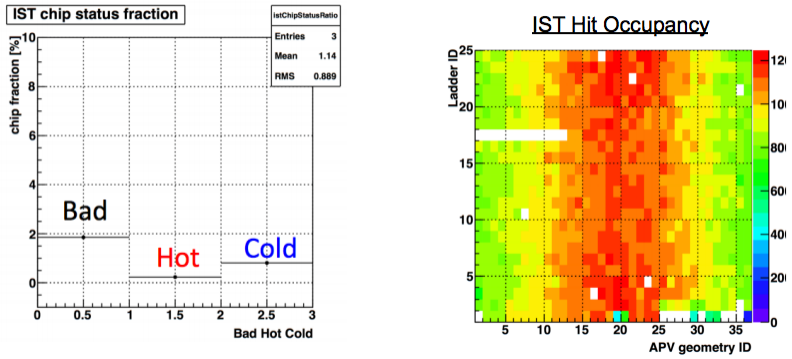


Figure 3.1.2: Summary of IST performance in year 2016 showing on the left the percentage of flagged (bad, hot or cold) chips and the hit occupancy per chip on each ladder on the right.

position of the different subsystems relative to both each other and the rest of the STAR experiment, in particular the TPC. Without accurate alignment, the TPC tracks will fail to find the correct associated hits within the expected error windows, leading to stark drops in the number of TPC tracks matched to HFT as well as increasing the number of mis-associated hits. Given that the expected resolution from HFT greatly exceeds that of the TPC, tracks reconstructed from the HFT alone are first used to obtain the internal alignment and these are then matched to the TPC to obtain the position of the detector within STAR. Appendix B covers, in depth, one of the procedures that was developed and employed for the alignment.

3.2 HFT Perfomance

In order to fully understand the HFT's performance, a detailed set of studies comparing simulation to data were undertaken. Au+Au events generated using the HIJING Monte Carlo model (version 1.382) [46, 84] were reconstructed in STAR using a full GEANT environment to simulate the detector response. Given the high

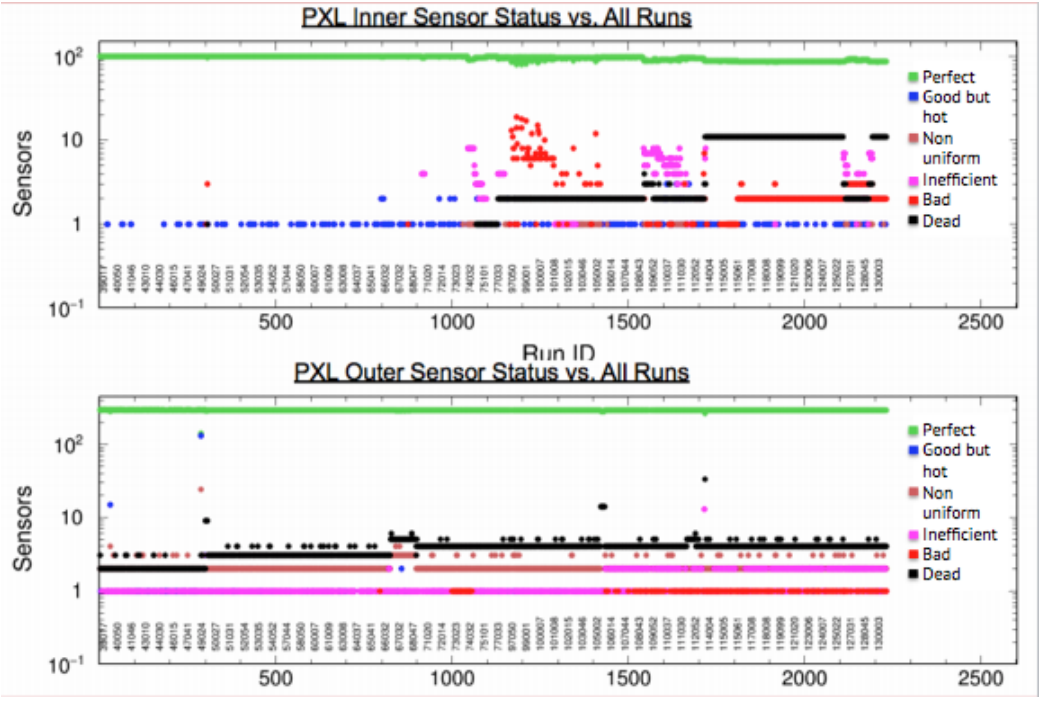


Figure 3.1.3: Summary of PXL detector performance in 2016 showing the number of sensors of different qualities on the inner layer (top) and outer layer (bottom) of the detector.

luminosity environment at RHIC together with the large integration time for the PXL subsystem, multiple events/vertices may be recorded during a single triggered event. As such, pile-up tracks are simulated to more realistically describe the performance in data by mixing the electron tracks from ultra-periferal collisions (UPC) and Au+Au minimum bias events from data into the simulated events. The hit densities used in the simulations from these two sources are shown in table 3.2.1.

To accurately describe the detector's acceptance in data, a single run from year 2014 was selected and the status of the individual sensors for both of the subsystems included in the reconstruction (PXL and IST) were used to define the probability of losing a hit on a given sensor in the case of non ideal detectors.

	PXL inner layer	PXL outer layer
Radius	2.9 cm	8 cm
Integrated MinBias collisions(pile-up)	7 cm^2	2.4 cm^2
UPC electrons	21 cm^2	3.4 cm^2
Total (average)	28 cm^2	5.8 cm^2

Table 3.2.1: Integrated hit densities from pile-up sources on each PXL layer used simulations.

The following are the criteria used for event selection when comparing these studies to the data sampled:

- Events in the top 10% centrality class (see section 4.1.1) from data are compared to simulated events with impact parameter between 0 and 4.5 fm.
- The location of the primary vertex determined by TPC (V_z) should be within 6 cm of STAR origin ($|V_z| < 6$ cm). The V_z distribution from data is sampled to produce simulated events V_z.
- The z-position of the primary vertex determined by TPC and the trigger detector VPD ($V_z^{\rm vpd}$) should be within 3 cm of each other ($|V_z - V_z^{\rm vpd}| < 3$ cm). The VPD was not included in the simulation and therefore this criterion is only available for data.

"Good" TPC tracks are determined according to the following:

- Number of reconstructed TPC hits associated to the track $nHitsFit > 20$
- All charged particle tracks
- Within HFT acceptance $|\eta| < 1$
- Distance of closest approach (DCA) to the primary vertex DCA < 1.5 cm

In addition, tracks are considered to be matched to the HFT if they satisfy the following:

- Hit in IST and both layers of PXL
- Distance of closest approach to primary vertex in xy and z less than 1cm respectively

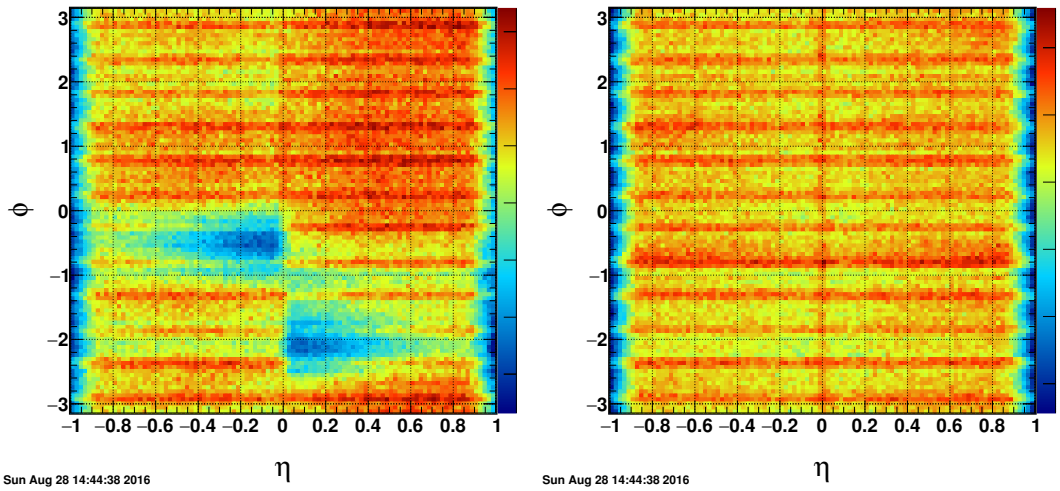
Given that the TPC performance is well understood by embedding simulated tracks in real events, there was no need to accurately describe the acceptance in this detector in this set of simulations. Instead, HFT performance is studied in terms of the the TPC track matching efficiency to the HFT by considering the ratio of "good" TPC tracks with associated hits in IST and PXL versus all "good" TPC tracks.

(3.1)

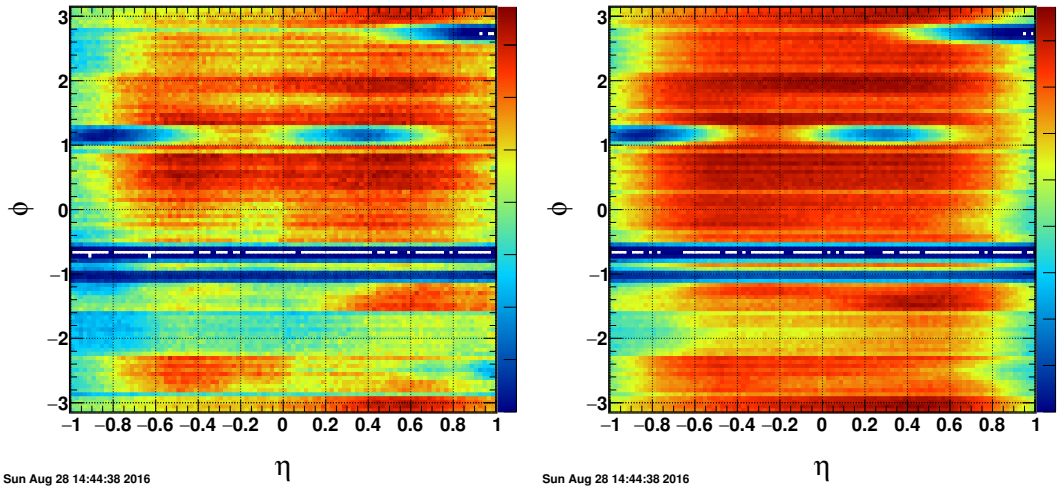
$$\text{HFTMatchingRatio} = \frac{\text{Good TPC tracks with hits in both layers of PXL and IST}}{\text{All good TPC tracks}}$$

Figure 3.2.1 shows a comparison of acceptance in $\eta - \phi$ for TPC tracks (top) and tracks matched to HFT (bottom) from data (left) and simulation (right). The large differences between simulations and data observed in the TPC distributions are factored out by looking at the HFT ratio (3.1) and a reasonably good description of the HFT acceptance is obtained by using the relevant masking tables.

The top panel in figure 3.2.2 shows the same HFT ratio as a function of the particle transverse momenta p_{T} obtained from the distributions in data and simulations, and the ratio between data and simulation is shown in the bottom panel. The agreement between data and the simulations, within 5%, is quite remarkable and suggests an overall good understanding of the detector performance. However, slight differences are visible once the comparison is done with further detail. Figure 3.2.3 shows the



(a) (b)



(c) Data (d) HIJING

Figure 3.2.1: (a), (b)TPC track $\eta - \phi$ distributions from data (left) and simulation (right). (c), (d) HFT matched track $\eta - \phi$ distributions from data (left) and simulation (right).

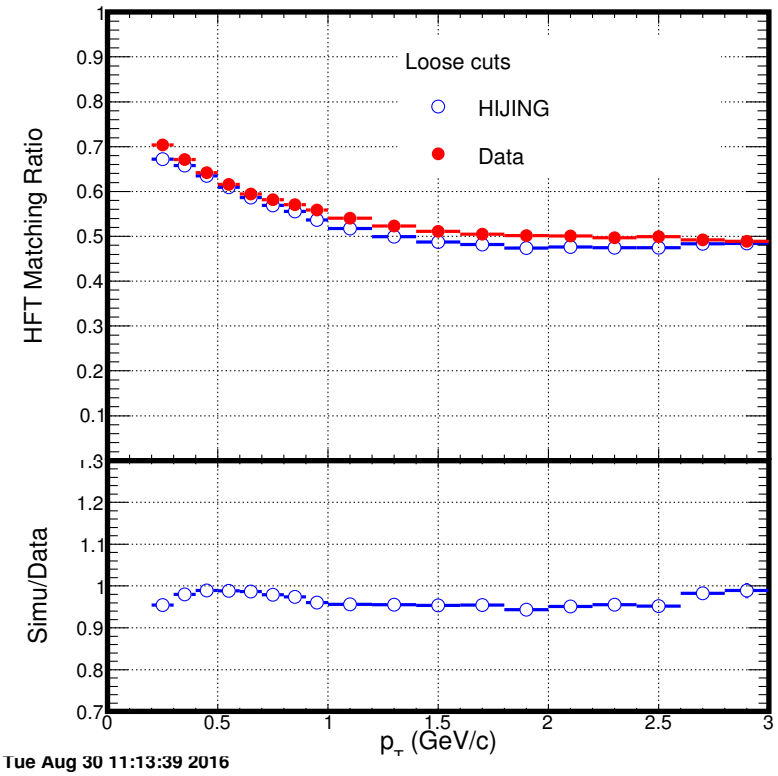
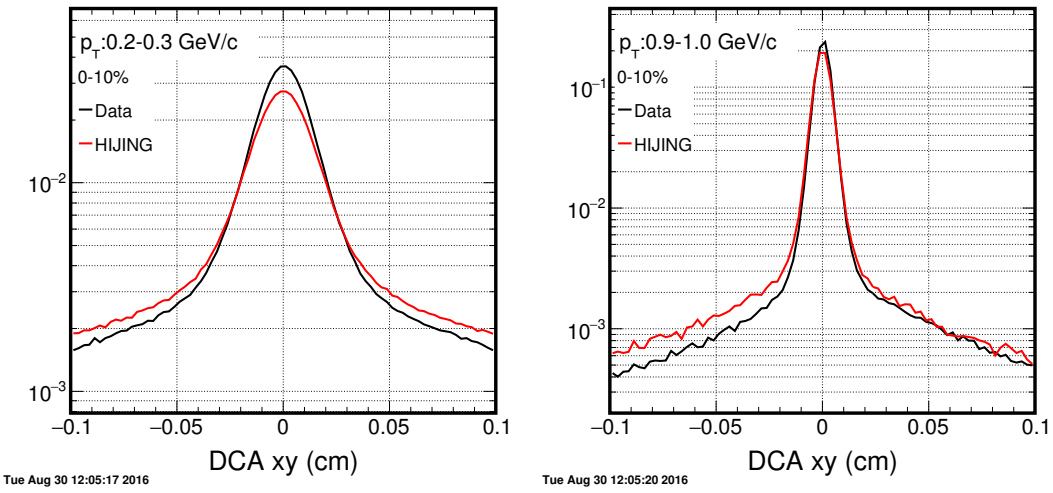


Figure 3.2.2: HFT ratio as a function of particle p_{T} from data and simulation.



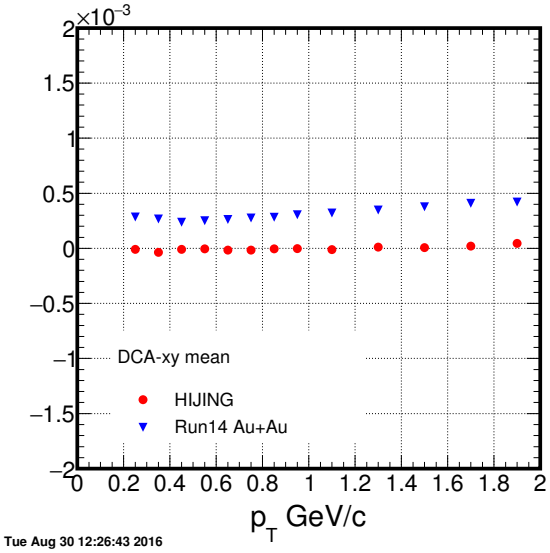
(a) (b)

Figure 3.2.3: Single track distance of closest approach (DCA) to the primary vertex in the transverse plain for low (left) and intermediate (right) p_{T} from simulations and data.

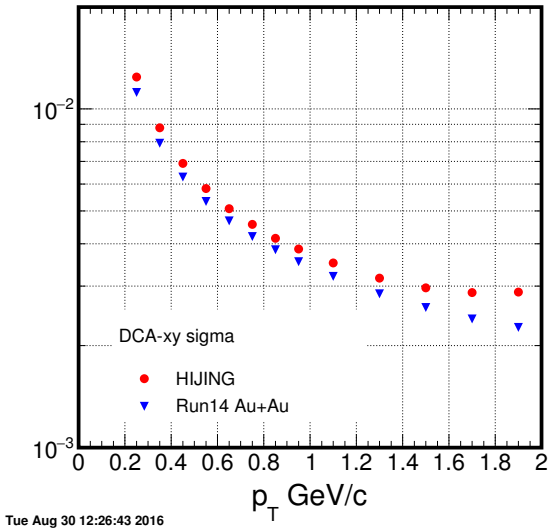
single track distance of closest approach to the primary vertex in the transverse plane (xy) for two p_{T} intervals for both simulation and data. The distributions in simulations are normalized to the distributions from data to simplify the comparison by scaling the area under the curves in the plotted range $(-0.1, 0.1)$ cm so that they are equal. In both p_{T} ranges, the distribution from simulation is slightly broader and has larger tails at larger values of |DCA|. These differences suggests slightly larger contributions from mismatched tracks which have picked up an incorrect hit in one of the layers of the HFT. To illustrate the differences between these distributions, the central peak of the DCA distributions have been fit to a Gaussian function and the mean, width(σ) and following ratio:

$$\frac{\text{counts in } \pm 3\sigma}{\text{counts in } \pm 0.1cm} \tag{3.2}$$

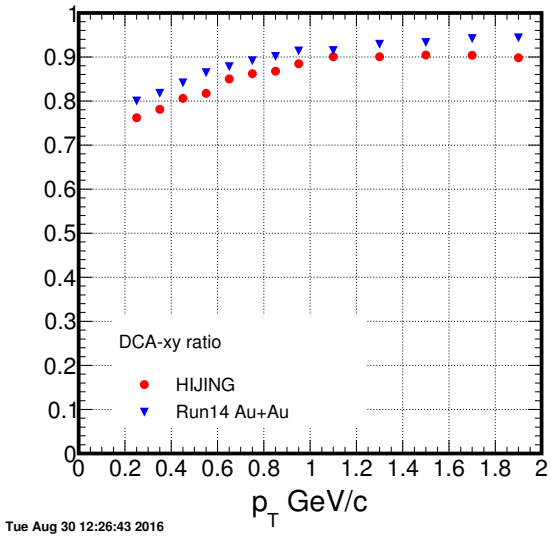
are plotted as a function of p_{T} in figure 3.2.4. These quantities in essence reflect what



(a) Mean.



(b) Width.



(c) DCA ratio.

Figure 3.2.4: Mean, width and DCA ratio from data and simulation distributions in the xy-plane.

is visible by eye in the naked distributions, that is, the central peak is described by a narrower Gaussian in data when compared to the HIJING simulations while the broader tails at high DCA observed in simulations lead to slightly lower DCA ratios, again pointing towards slight discrepancies in the degree of mismatch observed in the single tracks.

Chapter 4

Event, track and decay reconstruction

4.1 Event reconstruction

The trajectory of particles inside STAR are initially reconstructed by finding ionization clusters in the TPC. As discussed previously, the hit position in reconstructed separately in the x-y plane (given by the position of the padrows that collected the charge) and along z where timing information in the drift field is used. In general a track traversing the TPC will produce clusters recorded in the pad planes. In the case of single tracks, the centroid is taken as the position of the hit. Corrections that could affect the reconstructed hits, for example the space-charge or grid leak correction, are applied and the clusters and converted into TPC hits (in STAR software infrastructure) with their 3D position and associated dE/dx information.

Once hits in TPC have been reconstructed, tracks are formed using a simple physics model (helix) as an assumption of the expected pattern to identify hits that are coming from the same particle track. The standard STAR tracking algorithm begins track reconstruction in the outer most region of TPC where the hit density is lowest. TPC hits that are close to each other are joined to form track seeds which are propagated inwards, assuming a helical trajectory, in search of further hits that may be associated to the track.

Once all possible hits have been added to this preliminary track, they are refitted using the physics model (including effects such as coulomb multiple scattering, energy loss, etc.) to extract physical information of the track, such as momentum and

energy loss. These tracks form the pool we refer to as *global tracks*.

With the addition of HFT in 2014, the tracking software at STAR was expanded to search for associated hits in the four silicon layers. The TPC track candidates, and their errors, are propagated to the HFT where the hits in the vicinity of the TPC projection are associated to the track.

The reconstructed TPC tracks are the used to determine the collision's primary vertex. Each track is projected back from the TPC to their point distance of closest approach to the beam-line, and the position of the primary vertex is fixed by minimizing the track DCA's. In order to improve the efficiency in peripheral collisions, where the standard MINUIT algorithm [50] can fail due to the reduced number of tracks used in the minimization. To improve in these events the vertex is refit using the Kalman Filter (KF) algorithm [41, 42] with global tracks that satisfy:

- DCA to MINUIT primary vertex below 3 cm ($|\text{DCA(PV)}| < 3$ cm).
- Track has at least 20 hit points (out of a maximum of 45) in the TPC .

Figure 4.1.1 shows the comparison invariant mass spectra of $K\pi$ pairs using primary vertex determined using MINUIT and KF algorithms for min-bias triggered Au-Au collisions recorded during 2014 running with the HFT. As can be seen, the significance and number of raw counts for $D^0(\overline{D^0})$ candidates.

Once the primary vertex has been determined, global tracks with DCA to the primary vertex below 3 cm are refitted using the primary vertex as an additional constraint and considering track projection errors. These tracks are referred to as *primary tracks*.

For the results shown in this dissertation Au-Au collisions at center of mass energy

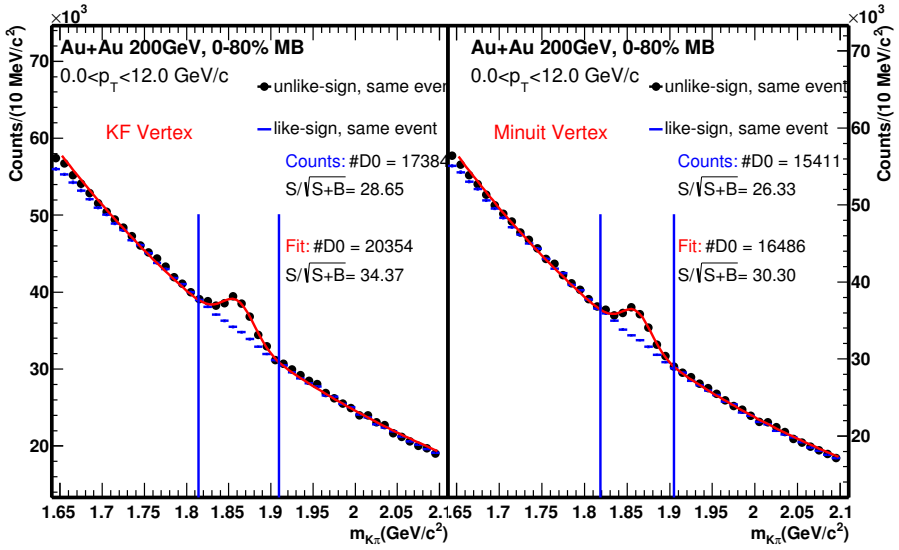


Figure 4.1.1: Invariant mass spectrum of $K\pi$ pairs using primary vertex determined using KF (left) and MINUIT (right) from min-bias trigger in run14. Unlike-sign combinations are shown in black symbols while the like-sign background is shown in blue.

$\sqrt{s_{NN}} = 200$ GeV collected during year 2014 at the STAR and including, for the first time, the HFT detector. A minimum-bias trigger is used together with the following criteria to ensure that the events are near the center of HFT acceptance:

- The location of the primary vertex determined by TPC (V_z) should be within 6 cm of STAR origin ($|V_z| < 6$ cm).
- The z-position of the primary vertex determined by TPC and the trigger detector VPD ($V_z^{\rm vpd}$) should be within 3 cm of each other ($|V_z - V_z^{\rm vpd}| < 3$ cm)

Slightly over 1 billion events are analyzed after these quality cuts are imposed.

4.1.1 Centrality definition

In order to approximate the impact parameter of a collision it is common practice to map an event's multiplicity to different centrality classes on a statistical basis. A

centrality %	multiplicity	centrality %	multiplicity
80-100	<10	35-40	116-145
75-80	10-14	30-35	145-179
70-75	14-21	25-30	179-218
65-70	21-29	20-25	218-263
60-65	29-40	15-20	263-315
55-60	40-54	10-15	315-373
50-55	54-71	5-10	373-441
45-50	71-92	0-5	>441
40-45	92-116		

Figure 4.1.2: Run 14 centrality definition and associated track multiplicity measured in the TPC.

Glauber Monte Carlo simulation [62] is matched to the number of observed global tracks at STAR in $|\eta| < 0.5$. Table 4.1.2 shows the centrality definition used for run14 after correcting for z-position of the vertex as well as the luminosity:

4.1.2 Track selection and PID

D-mesons were studied using the HFT to directly reconstruct the decay from the daughter particles in the channels [66]:

- $D^0(\overline{D^0}) \rightarrow K^{\mp}\pi^{\pm}$, B.R. $(3.93 \pm 0.04)\%$, $c\tau = 122.9$ μm
- $D^{\pm} \rightarrow K^{\mp}2\pi^{\pm}$, B.R. $(9.46 \pm 0.24)\%$, $c\tau = 311.8$ μm

Global tracks are used to reconstruct charm meson candidates given that these daughter tracks should appear to come from a displaced vertex relative to the primary. The following criteria were used to select and assure the quality of daughter candidates in the analysis:

- Transverse momentum $p_{\mathrm{T}} > 0.2$ GeV/c.
- Within HFT acceptance $|\eta| < 1$.

- Number of TPC hits used in track fit $nHitsFit > 20$.
- At least one hit on each layer of PXL and IST.

Hybrid particle identification is done using energy loss measured in TPC together with timing information from TOF (Figures 2.2.5) when available. Given that the TOF has finite timing resolution ($\delta t < 100$ ps) the measured $1/\beta$ is allowed to be within 0.03 the expected $1/\beta$ (assuming the track travels the full length of the TPC in a straight line $c \times \frac{\delta t}{2} = 0.015$, we allow for deviations twice as large).

Pion PID:

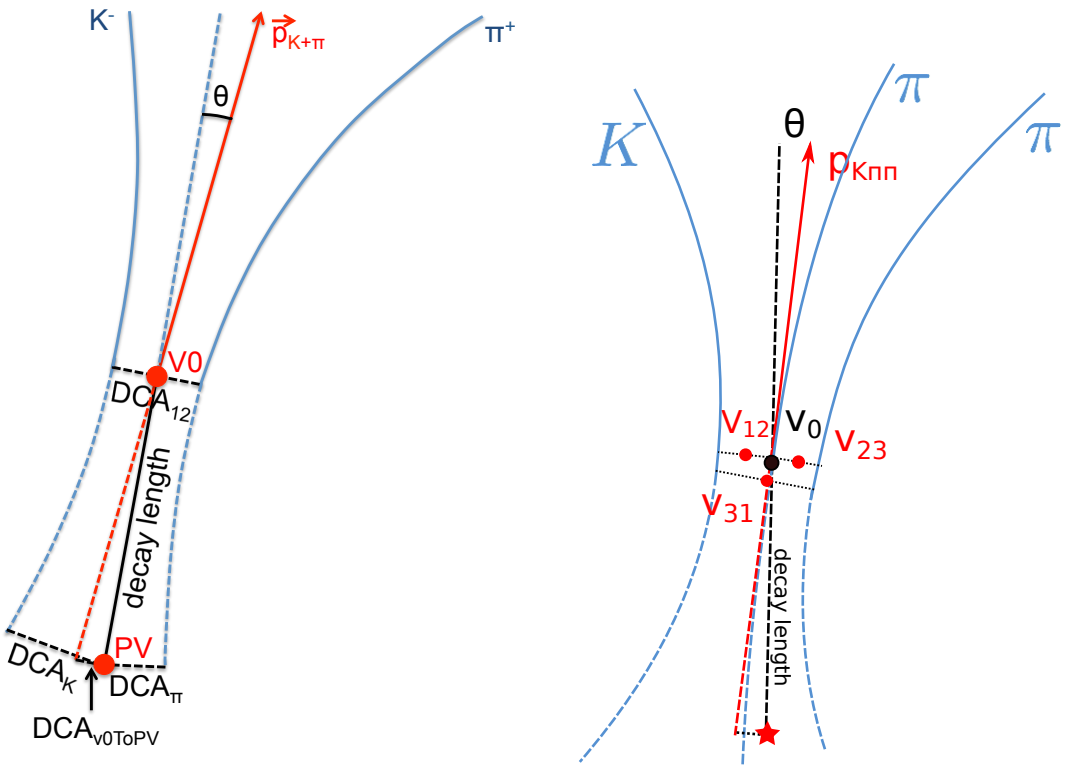
- TPC dE/dx within 3 standard deviations(σ) of the expected value $|n\sigma_\pi| < 3$.
- TOF $1/\beta$ within ± 0.03 of expected value for particle species $|1/\beta - 1/\beta_{exp}| < 0.03$.

Kaon PID:

- TPC dE/dx within 2 standard deviations(σ) of the expected value $|n\sigma_K| < 2$.
- TOF $1/\beta$ within ± 0.03 of expected value for particle species $|1/\beta - 1/\beta_{exp}| < 0.03$.

4.2 Topological selection with HFT

Once daughter candidates have been identified, the decay vertex can be reconstructed. In the case of two body decays, e.g. $D^0(\overline{D^0})$, the secondary vertex is reconstructed at the mid point of their distance of closest approach (DCA), where as for three body decays, such as $D^\pm$, the average between the midpoints of pairwise DCA's is taken as the decay position.



(a) (b)

Figure 4.2.1: Illustration of $D^0 \to K^-\pi^+$(left) and $D^\pm \to K^\mp 2\pi^\pm$(right) decay topology and topological variables.

4.2.1 D^0 topological cuts

The topological cuts used to select for D^0 mesons were obtained by H. Qiu using the Toolkit for Multivariate Analysis (TMVA) package to optimize for the significance. The package must be first trained using a sample background and signal. The signal was produced using a Monte Carlo simulation to decay the D^0 and smear the daughter particle momenta in accordance to the detector response. The background was taken directly from data, using reconstructed like-sign pairs under the D^0 invariant mass window and unlike-sign pairs in the sidebands. Loose topological cuts were applied in the pair selection, rejecting the majority of the background and improving the sensitivity of the optimization.

The "cuts" option was employed in TMVA. This mode randomly samples different cut sets in variable space and then selects the set with lowest background efficiency for a given 1% signal efficiency bin. Five topological variables were included in the optimization:

- Decay length: Calculated as the distance between the reconstructed decay vertex and the primary vertex(PV).
- Distance of closest approach (DCA) between the 2 daughter tracks.
- DCA between reconstructed D^0 and the PV.
- DCA between the π and the PV.
- DCA between the K a the PV

The procedure was applied in different D^0 candidate p_T bins, and in many cases further improvement was obtained by repeating the procedure 2-3 times. Figure

4.2.2 shows the result of the cut tuning after the first (left) and the fourth (right) iteration with TMVA and the cuts with greatest significance $S/\sqrt{S+B}$. These cuts are summarized in table 4.2.1.

Figure 4.2.3 shows the D^0 signals obtained using the cuts from optimization with TMVA in different p_T intervals. Two more sets of topological cuts were considered as part of the study of systematic uncertainties int he v_2 measurement. These were selected to have 50% and 150% signal efficiency relative to the standard or optimal cuts used. These two sets are summarized in tables 4.2.2 and 4.2.3.

4.2.2 $D^{\pm}$ topological cuts

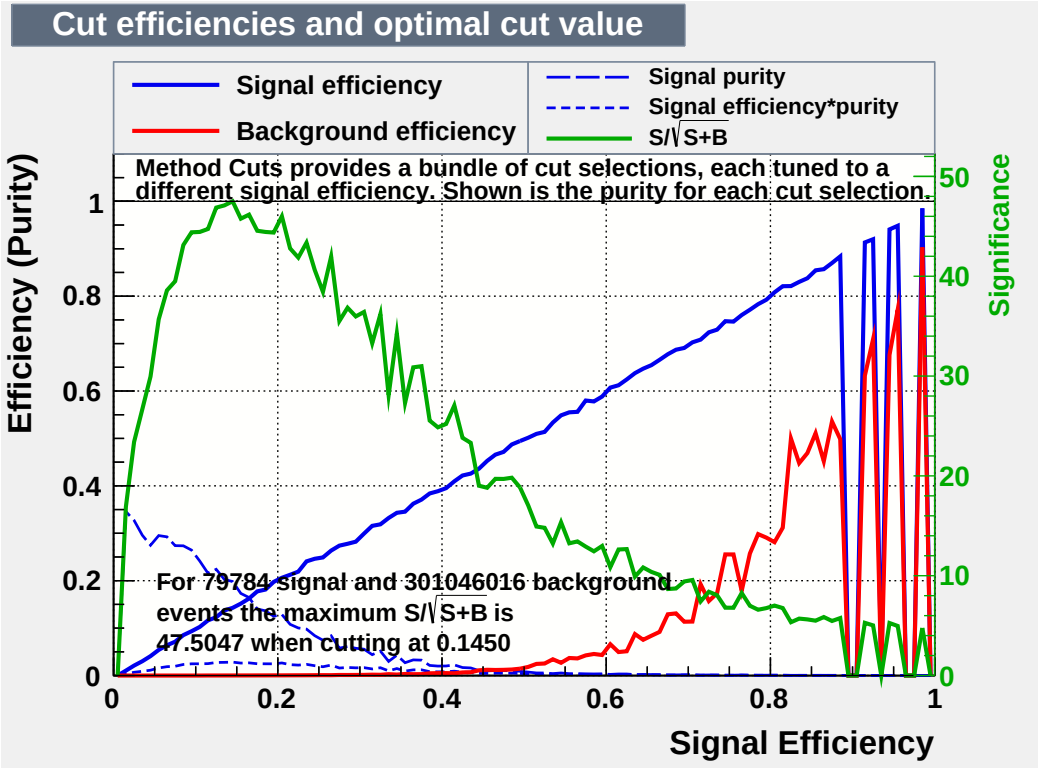
Table 4.2.4 shows the set of topological cuts used at the time of writing this dissertation for a preliminary study of the $D^{\pm}$ azimuthal anisotropy in parallel to the results obtained for D^0. Following the same procedure described in section 4.2.1, these cuts were optimized for $D^{\pm}$ by G. Xie, however due to time constraints this was the only set of cuts used in this analysis.

4.3 Background description

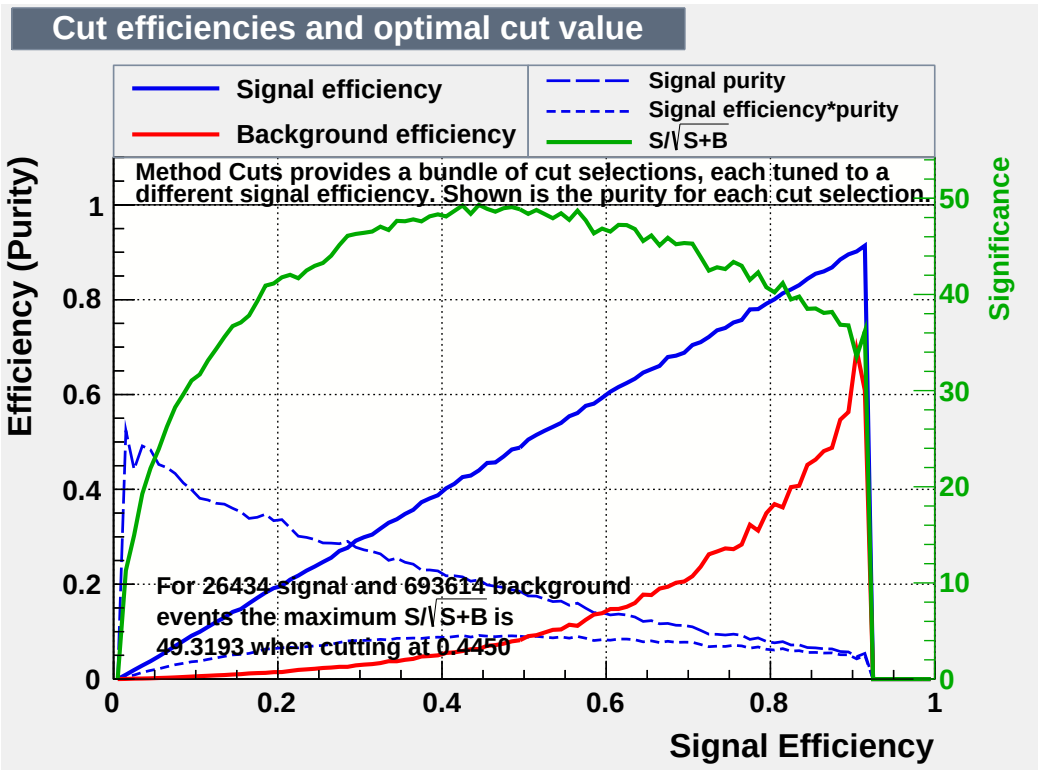
There are several established procedures to statistically describe the contribution of the uncorrelated background to the foreground when studying particle reconstruction. In the particular, all correlations between particles can be broken by mixing

Table 4.2.1: Standard geometrical cuts for different D^0 p_T.

D^0 p_T (GeV/c)	0-1	1-2	2-3	3-5	5-10
decay length (μm) >	145	181	212	247	259
DCA between 2 daughters (μm) <	84	66	57	50	60
DCA between D^0 and PV (μm) <	61	49	38	38	40
DCA between π and PV (μm) >	110	111	86	81	62
DCA between K and PV (μm) >	103	91	95	79	58



(a)



(b)

Figure 4.2.2: Signal efficiency, lowest background efficiency, significance and so on vs. signal efficiency. Top: First iteration, Bottom: Fourth iteration.

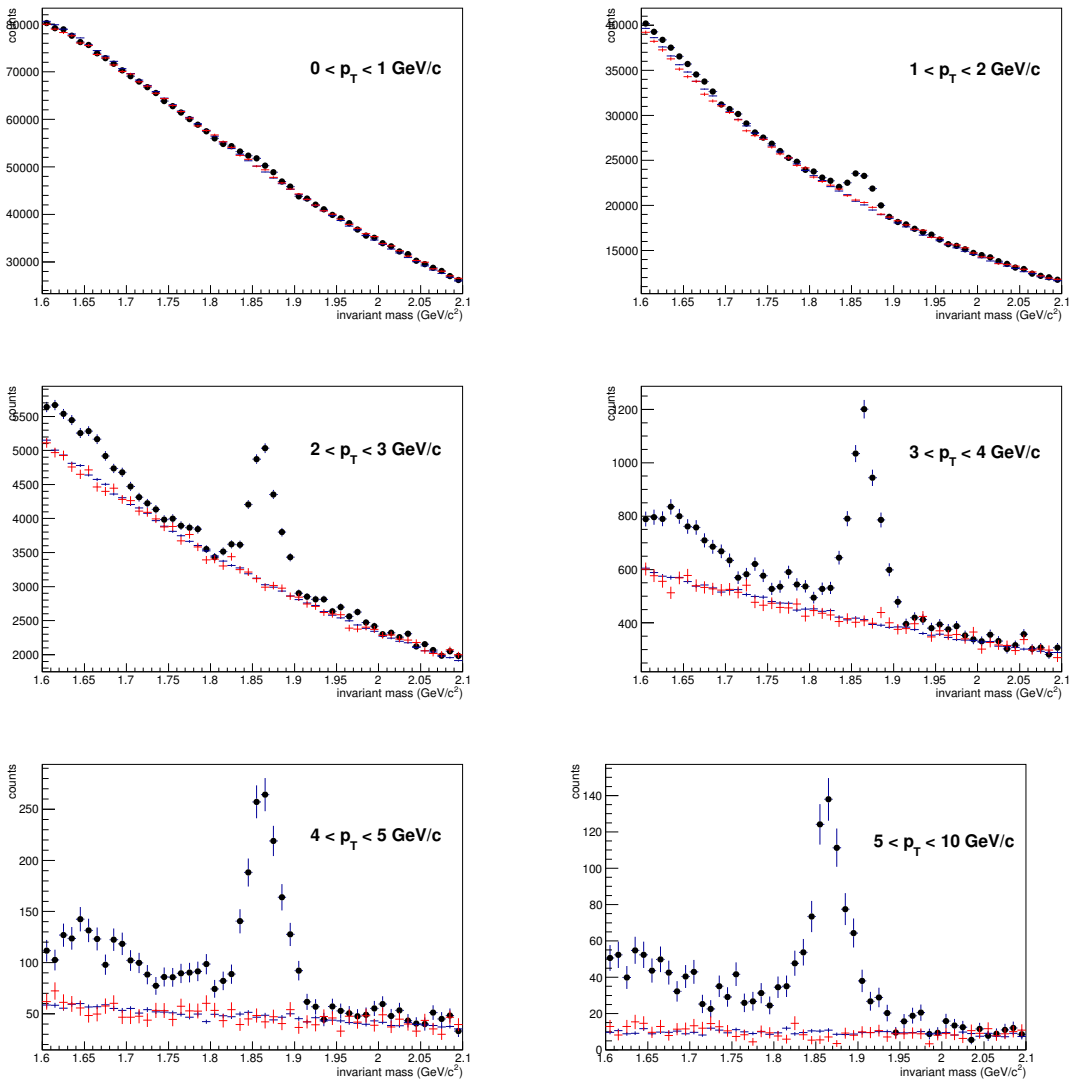


Figure 4.2.3: Invariant mass of $K\pi$ with D^0 signals after topological cut for different p_T bins. The red histograms are like-sign pair and blue histograms are mixed event.

tracks from different events with the added benefit of improved statistical precision as a single event can be mixed with many others.

To construct the mixed event background it is important to combine events with some degree of similarity, and as such events are classified according to the position of the primary vertex (PV) along the beam-line, their centrality class and the orientation of the event plane. Ten bins of equal width were used for both the event plane ($\Psi \in [-\pi, \pi]$) and the position of the primary vertex ($V_z \in [-6, 6]$), as well as nine centrality classes between 0-80%, for a total of 900 event "categories". Given that events must be read and mixed over several files, each event is saved to an associated buffer after being categorized, and due to memory and speed considerations only the relevant information from a given event and its associated tracks are saved. Table 4.3.1 summarizes the important information saved to the event buffers.

Each mixer track, as they were dubbed, occupies roughly 90 bytes of memory and contains the necessary information to reconstruct the track, its orientation relative to the event plane (used for the v_2 analysis) as well as other track information such as charge, PID according to different detectors, etc. which is encoded in the binary representation of a short variable.

In the current implementation studying $D^0 \rightarrow K\pi$ reconstruction, only pions and kaons were identified and the position of their associated tracks in the array of mixer

Table 4.2.2: Tight geometrical cuts for different D^0 p_T.

D^0 p_T (GeV/c)	0-1	1-2	2-3	3-5	5-10
decay length (μm) >	144	204	242	245	300
DCA between 2 daughters (μm) <	69	48	44	49	47
DCA between D^0 and PV (μm) <	44	36	31	26	32
DCA between π and PV (μm) >	120	102	118	109	96
DCA between K and PV (μm) >	119	110	109	106	80

tracks is saved to reduce the time required during the mixing.

4.3.1 Event mixing

Once the buffer has been filled, the pions from the first event are combined with kaons from the rest of the events in the buffer, considering both like-sign and unlike-sign combinations. In the first iteration, the pions and kaons from the same event are combined to produce the foreground (unlike-sign) as well the same event like-sign background.

In order to apply the topological cuts to the background, the second event is moved during the mixing such that the position of the primary vertex in both coincides. Once the mixing has been completed, the first event is removed from the buffer leaving space for another event to be added at the end. Figure 4.3.1 shows the invariant mass distribution for the foreground and three different uncorrelated backgrounds: same event like-sign, mixed event like-sign and mixed event unlike-sign in three p_{T} bins. Both mixed event backgrounds have been scaled to the foreground using the integration range $m_{K\pi} \in [2, 2.1]$ GeV/c^2.

There is good agreement between the three descriptions of the combinatorial background and they appear to provide an adequate description in the vicinity of the D^0 signal and, as was to be expected, the mixed event backgrounds have improved

Table 4.2.3: Loose geometrical cuts for different D^0 p_T.

D^0 p_T (GeV/c)	0-1	1-2	2-3	3-5	5-10
decay length (μm) >	110	168	187	199	180
DCA between 2 daughters (μm) <	77	78	74	68	66
DCA between D^0 and PV (μm) <	72	53	47	42	62
DCA between π and PV (μm) >	92	78	86	65	47
DCA between K and PV (μm) >	105	68	80	66	41

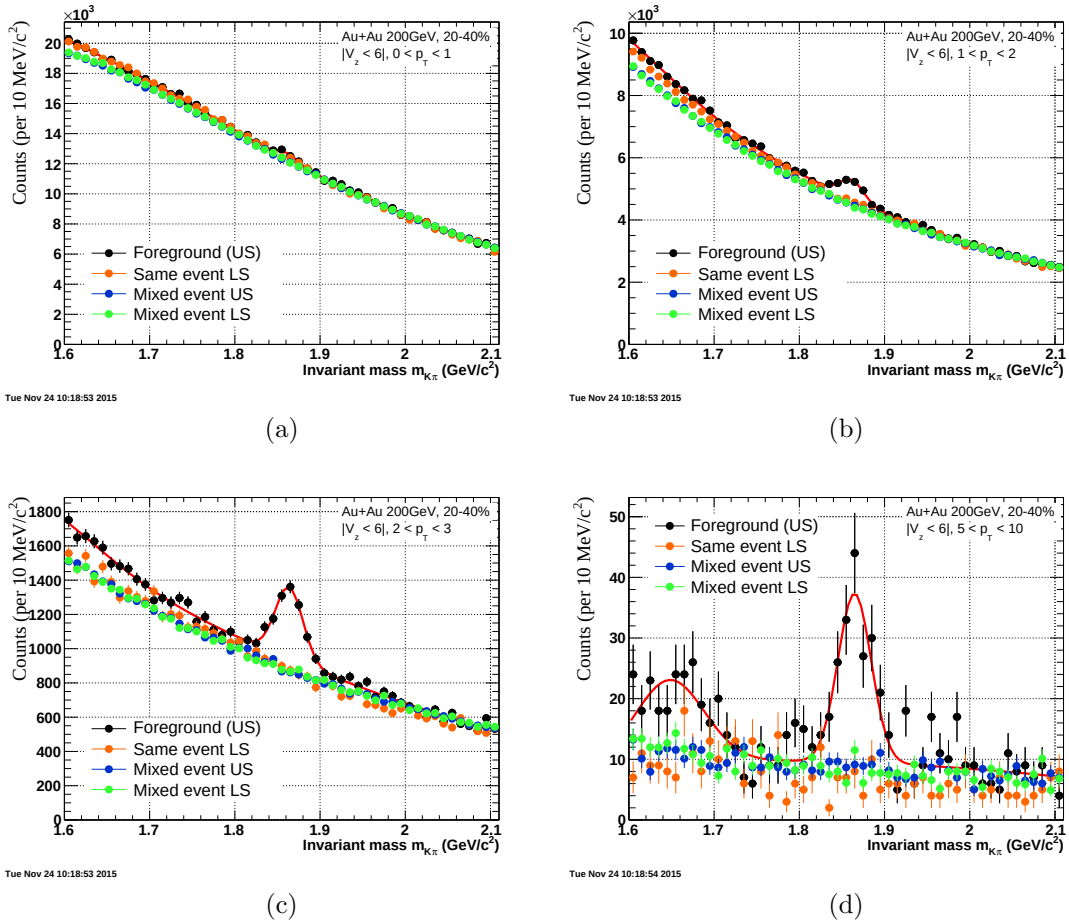


Figure 4.3.1: Invariant mass distribution for foreground and three descriptions of combinatorial background in four p_{T} bins.

statistical precision.

It is interesting to observe the presence of an "excess" in the foreground, relative to all of the background curves, below roughly 1.75 GeV/c^2. This so called bump was investigated using the Data Driven Fast Simulator, and will be discussed briefly in the following section.

4.3.2 Correlated background - $K\pi$ foreground "bump"

In order to study other possible contributions to the observed D^0 background, a cocktail of particle decays were generated with realistic p_{T} distributions (from published D^0 data) and flat η and ϕ distributions, which were then decayed using a simple Monte Carlo simulation and sampling distributions obtained from data and embedding.

Once the particles are decayed, the daughter momentum and the distance of closest approach (DCA) to the primary vertex (PV) are smeared according to distributions obtained from data.

Pion-kaon pairs are formed from the decays using the topological cuts optimized for D^0 reconstruction to study the contributions that fall within the invariant mass spectrum studied. The finite probability of double mis-PID, where a pion is confused with

Table 4.2.4: Topological cuts for different $D^{\pm}$ p_T ranges.

$D^{\pm}$ p_T (GeV/c)	0-1	1-2	2-3	3-5	5-15
decay length (μm) >	300	300	300	247	259
Maximum DCA between 2 daughters (μm) <	84	66	57	50	60
DCA between $D^{\pm}$ and PV (μm) <	61	49	38	38	40
DCA between π and PV (μm) >	110	111	86	81	62
DCA between K and PV (μm) >	103	91	95	79	58

StMixerTrack	StMixerEvent
Origin	PV Origin
Momentum	Magnetic Field
Q-Vector	Event Plane
Track information	Array of mixer tracks
	Array of indices to identified pions
	Array of indices to identified kaons

Table 4.3.1: Summary of information saved to the event buffer for mixing.

a kaon and vice a versa, was also included in this study by sampling TPC dE/dx distributions from data.

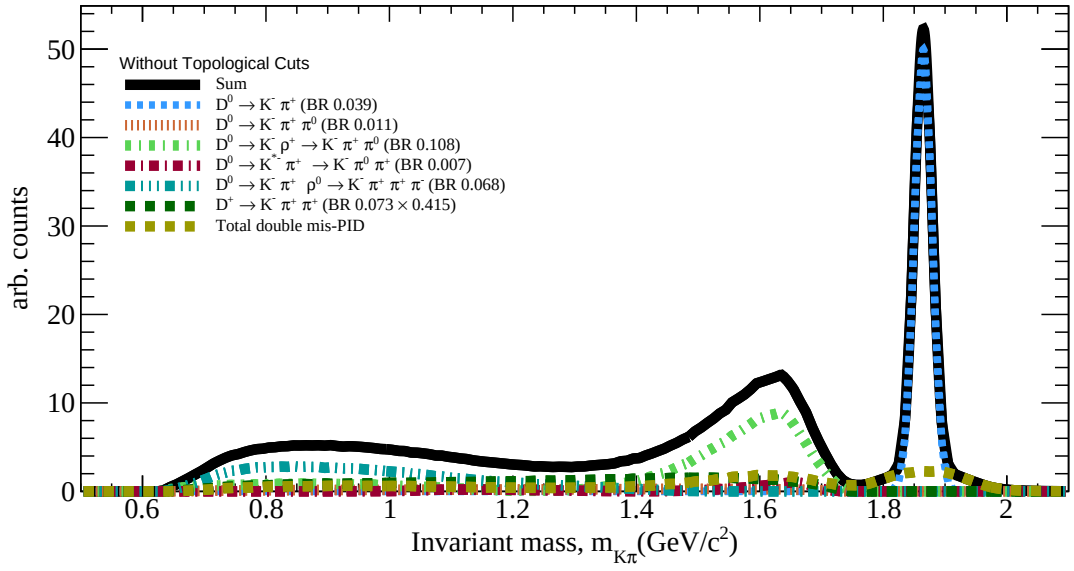
The contributions to the invariant mass spectrum from the following D^0 and $D^{\pm}$ decays were included in a qualitative study of the correlated background:

- $D^0 \to K^-\pi^+$ (B.R. 0.039)
- $D^0 \to K^-\pi^+\pi^0$ (B.R. 0.011)
- $D^0 \to K^-\rho^+ \to K^-\pi^+\pi^0$ (B.R. 0.108)
- $D^0 \to K^{*-}\pi^+ \to K^-\pi^+\pi^0$ (B.R. 0.007)
- $D^+ \to K^-\pi^+\pi^+$ (B.R. 0.073 $\times$ 0.415)

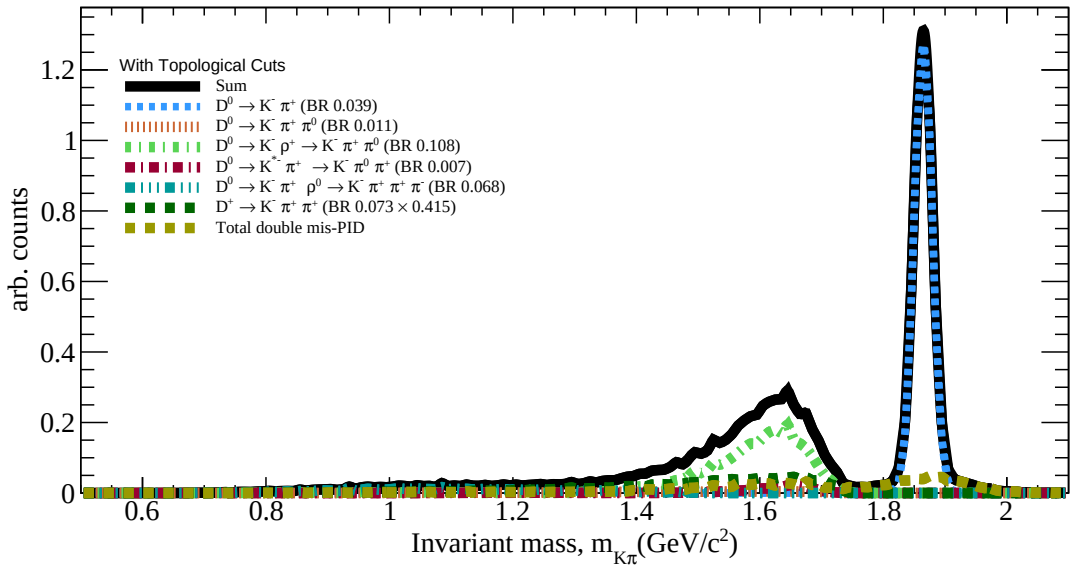
Figure 4.3.2 shows the invariant mass spectrum obtained from the cocktail after scaling by the branching ratio for different decays as well as the fragmentation function for the different charmed meson species.

The spectrum is shown before and after the $D^0 \to K\pi$ topological cuts have been applied. It is clear that the contributions from correlated background can, at least in part, account for the enhancement observed below roughly 1.7 GeV/c^2.

The cocktail simulation was then scaled by fitting the amplitude of the D^0 peak obtained from fast simulator to the signal observed in data, and the cocktail was then



(a)



(b)

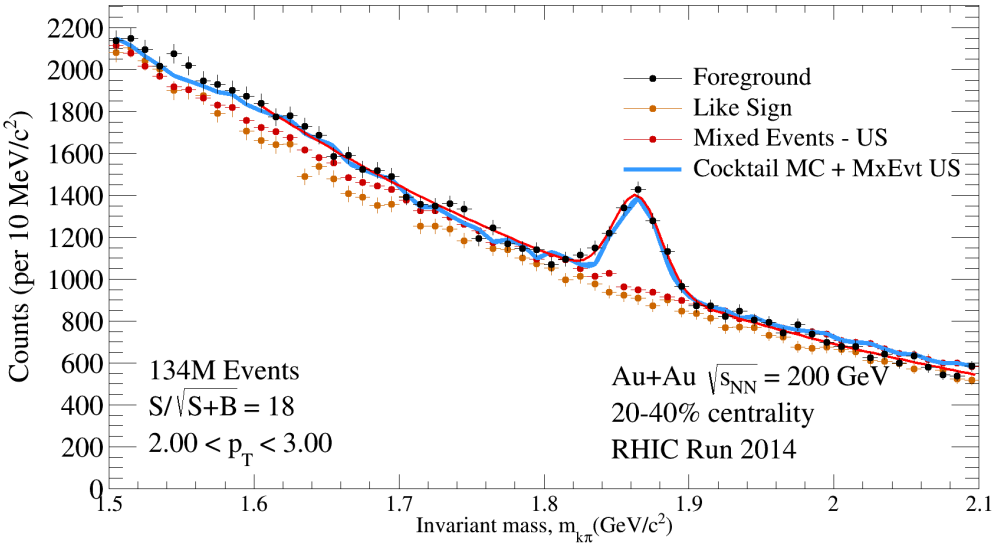
Figure 4.3.2: Simulated contribution to the invariant mass spectrum from reconstructed $K\pi$ pairs without (top) and with (bottom) HFT topological cuts.

added to the mixed event background. Figure 4.3.3 shows a comparison between the invariant mass distribution obtained from data and the spectrum obtained by combining the mixed event background and the results from the data driven fast simulator.

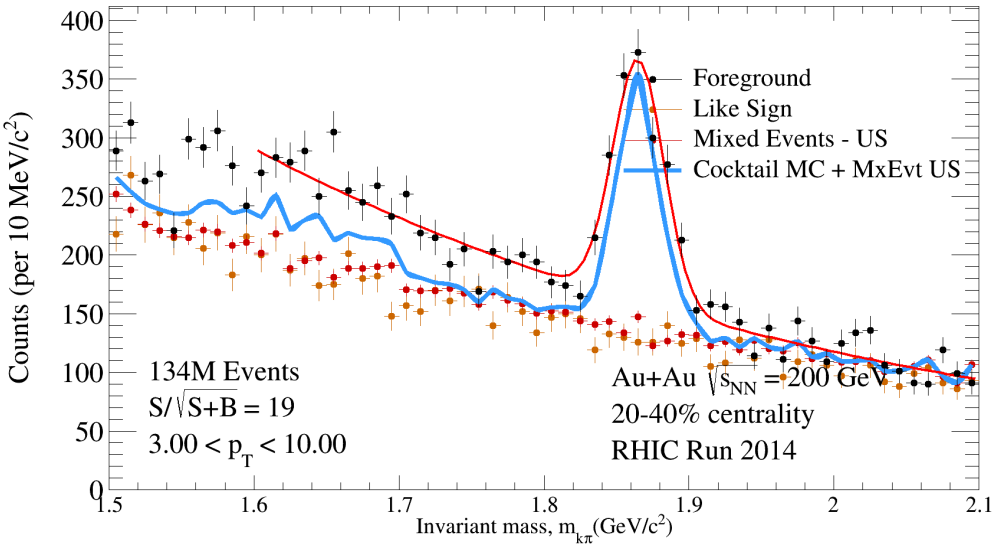
The inclusion of correlated background sources can qualitatively describe the foreground observed, reproducing the location of the bump structure albeit underestimating the degree of enhancement itself. Furthermore, there is likely a finite contribution to the observed bump originating from jet correlations which should be included to improve on the description of the background

It should also be noted that the studies presented here were done with an early version of the fast simulator which only included the p_{T} and centrality dependence of sampled distributions, revisiting the studies with more differential distributions should improve on these results.

Nonetheless, the results provide confidence in a qualitative understanding of the sources of the correlated background and, what is more, suggest that the contribution from these sources in the D^0 signal range are dominated by double mis-PID (dashed olive green in figure 4.3.3), and is nearly negligible.



(a)



(b)

Figure 4.3.3: Comparison of combinatorial background+toy Monte Carlo versus foreground from data for two p_{T} ranges.

Chapter 5

D meson azimuthal anisotropy

As two heavy nuclei are compressed and heated in a relativistic nuclear collision, flow patterns emerge in the subsequent expansion of the medium. Classically we can draw an analogy to hydrodynamics where one can connect conservation laws to fundamental properties of the fluid in question: such as the equation of state and the transport properties of the medium. This collective motion can be observed experimentally by studying anisotropies in the azimuthal distributions of generated particles, as has been been discussed at length [68].

A natural description to study azimuthal distributions is given in terms of a Fourier decomposition, where the different kinds of anisotropies can be characterized by the different harmonics:

$$E\frac{d^3N}{d^3p} = \frac{1}{2\pi}\frac{d^2N}{p_{\mathrm{T}}dp_{\mathrm{T}}dy}\left(1+\sum_{n=1}^{\infty}2v_n\cos(n(\phi-\Psi_r))\right) \tag{5.1}$$

Where Ψ_r is the true reaction plane angle for a collision and the odd(sin) terms vanish due to the symmetry around the reaction plane.

This procedure allows one to correct for the finite event plane resolution caused by the finite multiplicity of event, with out which the observed anisotropies always underestimate the true value. Furthermore, in this particular choice for the expansion the coefficients have a tangible interpretation where the coefficients $v_n = \langle\cos(n(\phi-\Psi_r))\rangle$

follow from equation 5.

5.1 Event plane determination

Experimentally, the reaction plane can be approximated by using the anisotropic flows themselves. For a given harmonic n the associated event plane Ψ_n can be determined independently from the rest and described by the the event flow vector Q_n :

$$Q_n \cos(n\Psi_n) = X_n = \sum_i w_i \cos(n\phi_i) \tag{5.2}$$

$$Q_n \sin(n\Psi_n) = Y_n = \sum_i w_i \sin(n\phi_i) \tag{5.3}$$

and

$$\Psi_n = \left(\tan^{-1} \frac{\sum_i w_i \sin(n\phi_i)}{\sum_i w_i \cos(n\phi_i)} \right) / n \tag{5.4}$$

where $\sum_i$ indicates sum of all particles to be used in the event plane determination and w_i the associated weights. The particular choice for w_i is usually made to optimize for the event plane resolution. In the case of studying the flow in the transverse plane at low p_{T} a common choice is to select $w_i = p_{\mathrm{T}}$ to maximize the event plane resolution. It is important to note that given a Fourier harmonic, n, the corresponding coefficient v_n can be determined by using the reaction plane determined by any harmonic m with $n \geq m$ and n a multiple of m.

As was mentioned previously, detector acceptance can contribute to the observed azimuthal anisotropies and must be corrected for in the laboratory. To this end there

are several procedures available, each with its strength and weaknesses. The simplest (re-centering) involves subtracting the event average of distributions (X_n, Y_n) from the distributions themselves. The greatest disadvantage to this particular procedure is the possibility of higher harmonic anisotropies introduced by the detector itself, which would need to be removed using alternate methods, which are discussed in further detail in [27, 26].

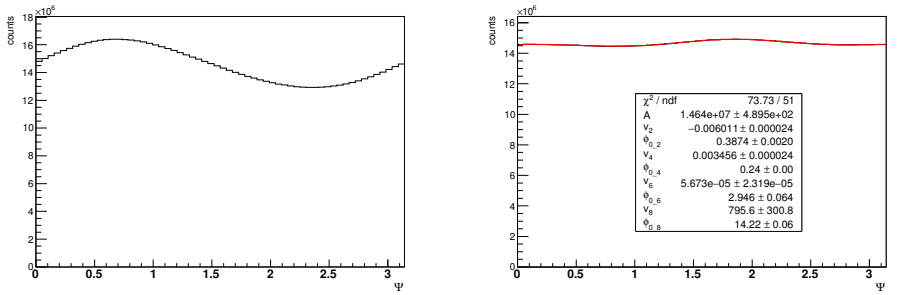
In the current analysis, TPC primary tracks were used in the determination of the event planes, with the following quality selection cuts:

- At least 15 TPC points used in tracking
- $0.2 < p_T < 2$ GeV/c
- $|\eta| < 1$

The D^0 daughter tracks are excluded from the event plane reconstruction in order to remove self-correlations, and to correct for detector acceptance, re-centering is applied separately for both halves of TPC ($\eta < 0$ and $\eta > 0$) on a run by run basis. Figures 5.1.1a and 5.1.1b show the 2nd order event plane before and after the re-centering correction is applied.

5.2 Event Plane Resolution

Once the particle azimuthal distributions are expanded in terms of the Fourier harmonics for a given event plane, we can obtain the coefficients that would be obtained when measuring with respect to the reaction plane by dividing by the event plane resolution, i.e.:



(a) Ψ_2 Event plane before recentering (b) Ψ_2 Event plane after recentering

Figure 5.1.1: Event plane recentering correction.

$$v_n = v_n^{obs} / < \cos(km(\Psi_m - \Psi_r) > \tag{5.5}$$

The event plane resolution is a function of both the event plane used in the determination, m, as well as the particular harmonic to be determined, $n = km$. It is generally the case that the best accuracy for determination of v_n is achieved when the event plane associated to the harmonic is being used, that is $k = 1$.

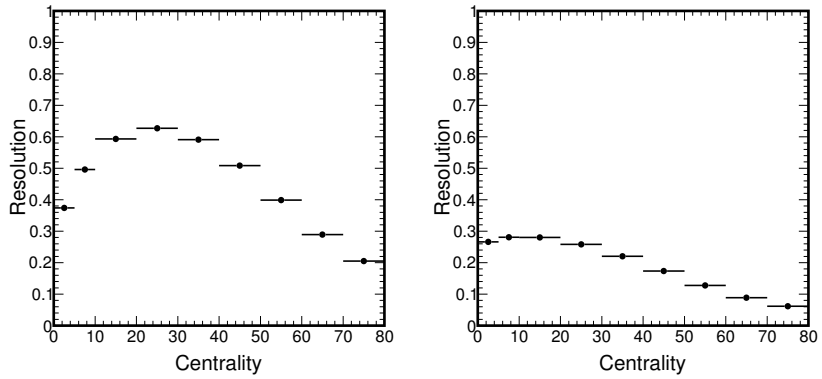
To calculate the resolution one can begin by expressing the $m(\Psi_m - \Psi_r)$ distribution as follows:

$$\frac{dP}{d(m(\Psi_m - \Psi_r))} = \int \frac{v'_m dv'_m}{2\pi\sigma^2} \exp(-\frac{v_m^2 + v_m'^2 - 2v_m v'_m \cos(m(\Psi_m - \Psi_r))}{2\sigma^2}) \tag{5.6}$$

where σ is as follows:

$$\sigma^2 = \frac{1}{2N} \frac{< w^2 >}{< w >^2} \tag{5.7}$$

The integral (5.2) can be obtained analytically and hence the resolution can be written:



(a) Second event plane resolution Ψ_2. (b) Third event plane resolution Ψ_3.

Figure 5.2.1

$$< \cos(km(\Psi_m - \Psi_r)) >= \frac{\sqrt{\pi}}{2\sqrt{2}} \chi_m \exp(\chi_m^2/4) \left(I_{\frac{k-1}{2}}(\chi_m^2/4) + I_{\frac{k+1}{2}}(\chi_m^2/4) \right) \tag{5.8}$$

where $\chi_m \equiv v_m/\sigma$ and I_v are the modified Bessel functions. Figures 5.2.1a and 5.2.1b show the obtained resolutions for the second and third harmonic event planes observed at STAR as a function of the centrality class.

5.3 Azimuthal Anisotropy

Once the event plane has been determined, one can study the particle distributions with respect to the event plane. Assuming the event plane has been determined using the m-th harmonic, the Fourier expansion can be written as:

$$\frac{d(wN)}{d(\phi - \Psi_m)} = \frac{< wN >}{2\pi} \left(1 + 2 \sum_{k=1}^{\infty} v_{km}^{obs} \cos(km(\phi - \Psi_m) \right) \tag{5.9}$$

Therefore a given coefficient v_n can be computed experimentally by averaging over the distributions $\langle \cos(n(\phi - \Psi_m)) \rangle$. It is worth noting that for a given event plane, m, negative entries in the distributions can be shifted to positive ones by adding 2π

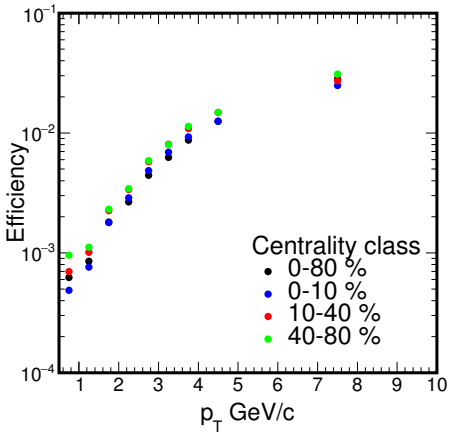


Figure 5.3.1: D^0 reconstruction efficiency vs p_T for different centrality classes obtained.

and folding in the distribution with the correct periodicity, $2\pi/m$.

Experimentally the invariant mass distributions of $K\pi$ pairs, selected using HFT as discussed in section 4.2, are plotted in ten $\phi - \Psi_m$ bins between 0 and $2\pi/m$ and scaled by $1/(R_m\epsilon)$ where R_m is the event plane resolution and ϵ the relative D^0 reconstruction efficiency, both of which are centrality dependent. The efficiency, shown in figure 5.3.1, is obtained using the raw yields from Run14 including the HFT and the expected yield obtained from the fit from published 2010 and 2011 results [6] scaled by the number of events analyzed. The uncorrelated background is estimated by scaling the mixed event, unlike-sign distribution to the same event like-sign distribution and is then subtracted from the $K\pi$ foreground before the yields are extracted. The mixed event background is primarily used used to reduce the the statistical error on the combinatorial background to obtain a measurement in $p_{\mathrm{T}} < 1$ GeV/c.

Once the mixed event background has been subtracted, the yields themselves are obtained using the two following procedures:

- The sidebands are fit using a first order polynomial in the ranges $m_{K\pi} \in (1.71, 1.8)$ and $(1.93, 2.02)$ GeV/c^2. The resulting polynomial is then fit, together with a Gaussian (signal), in the whole range (1.71,2.02) GeV/c^2 and the Gaussian is integrated in $\pm 2.5\sigma$ around the mean to obtain the yield.

- After following the same fit procedure (described in the previous bullet), the counts in sidebands are scaled to the signal range ($\pm 2.5\sigma$ around the Gaussian mean) and subtracted from the signal counts.

The results from this "bin counting" method are reported as the central value while yields obtained by integrating the fit function are used to study the systematic uncertainties. Two symmetric bins around π/m are merged and the corrected yields are then plotted versus $\phi - \Psi_m$. The resulting distribution is then fit with:

$$f(\phi) = N\left[1 + v_m^{obs}\cos(m(\phi - \Psi_m))\right] \tag{5.10}$$

where N and v_m^{obs} are two free parameters used to obtain the observed value for the m-harmonic coefficient v_m^{obs}.

Figures 5.3.2 through 5.3.10 show the corrected signals and yields obtained in $\phi - \Psi_2$ for the 0-80% central events in the nine p_{T} ranges studied in this analysis together with the fit used to calculate the value of v_2^{obs}. Similar calculations are obtained in 0-10% and 10-40% central events though the details are not shown.

Figures 5.3.11 through 5.3.16 show the same corrected yields in 0-80% central events relative to the third event plane $\phi - \Psi_3$ used to extract the observed v_3^{obs}. Though not shown, the same procedure is followed in order to calculate the v_3 in 10-40% central events. Finally, the observed anisotropy v_m^{obs} is scaled to account for the wide centrality ranges used [61] using the average event plane resolution weighted

by the D^0 yield to obtain the physical value v_m.

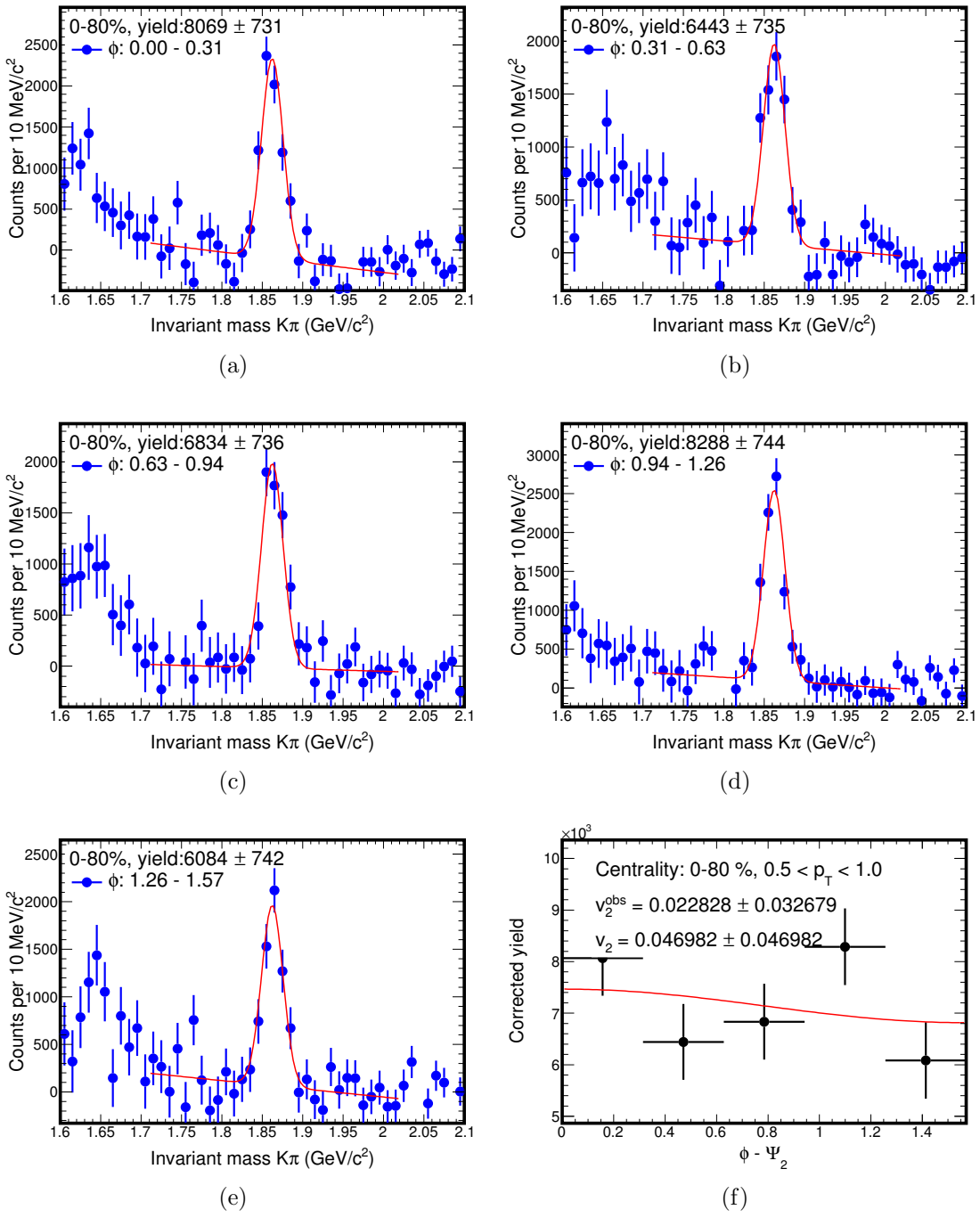


Figure 5.3.2: Corrected invariant mass distributions in $\phi - \Psi_2$ bins for $0.5 < p_T < 1$ GeV/c and v_2^{obs} calculation.

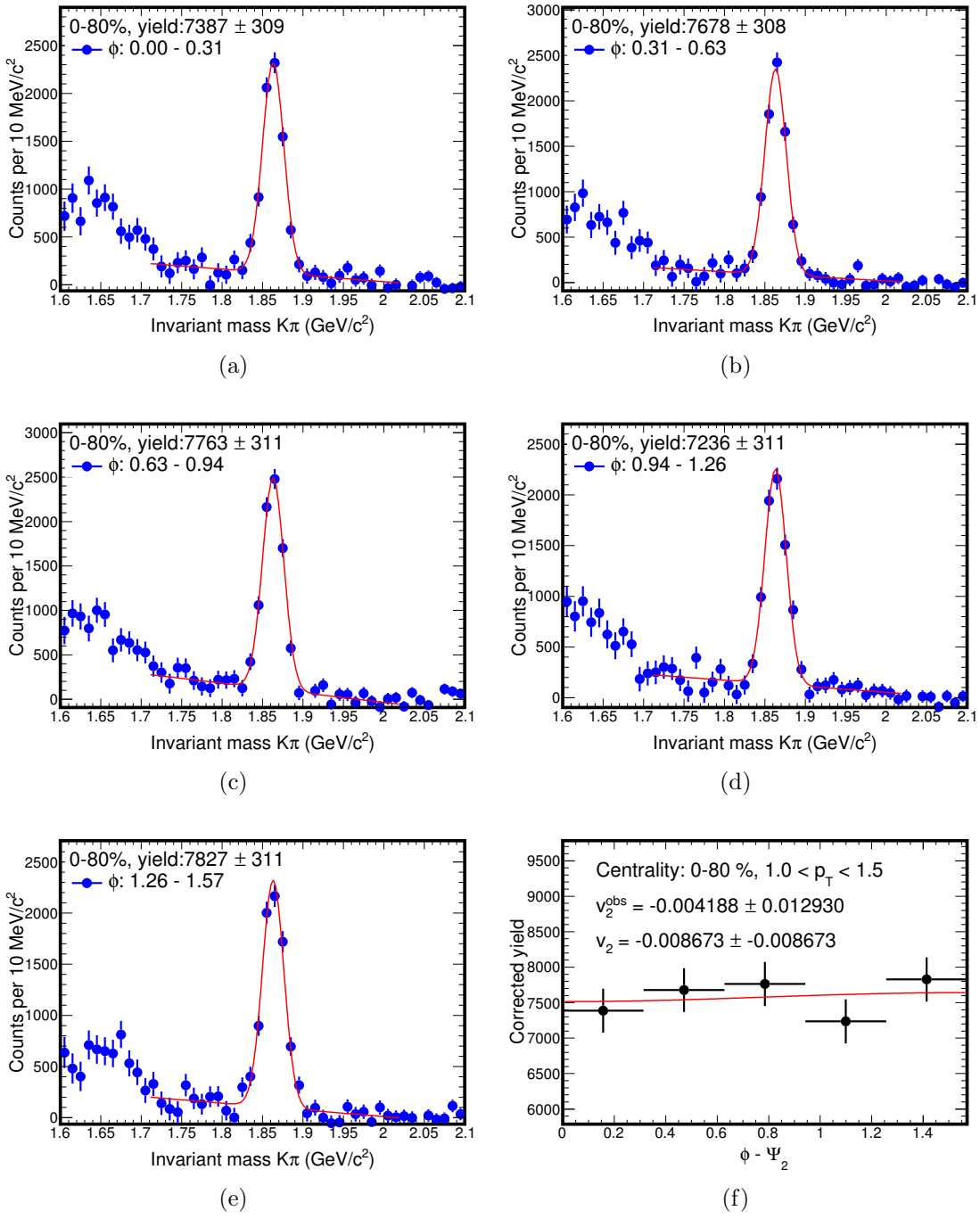


Figure 5.3.3: Corrected invariant mass distributions in $\phi - \Psi_2$ bins for $1 < p_T < 1.5$ GeV/c and v_2^{obs} calculation.

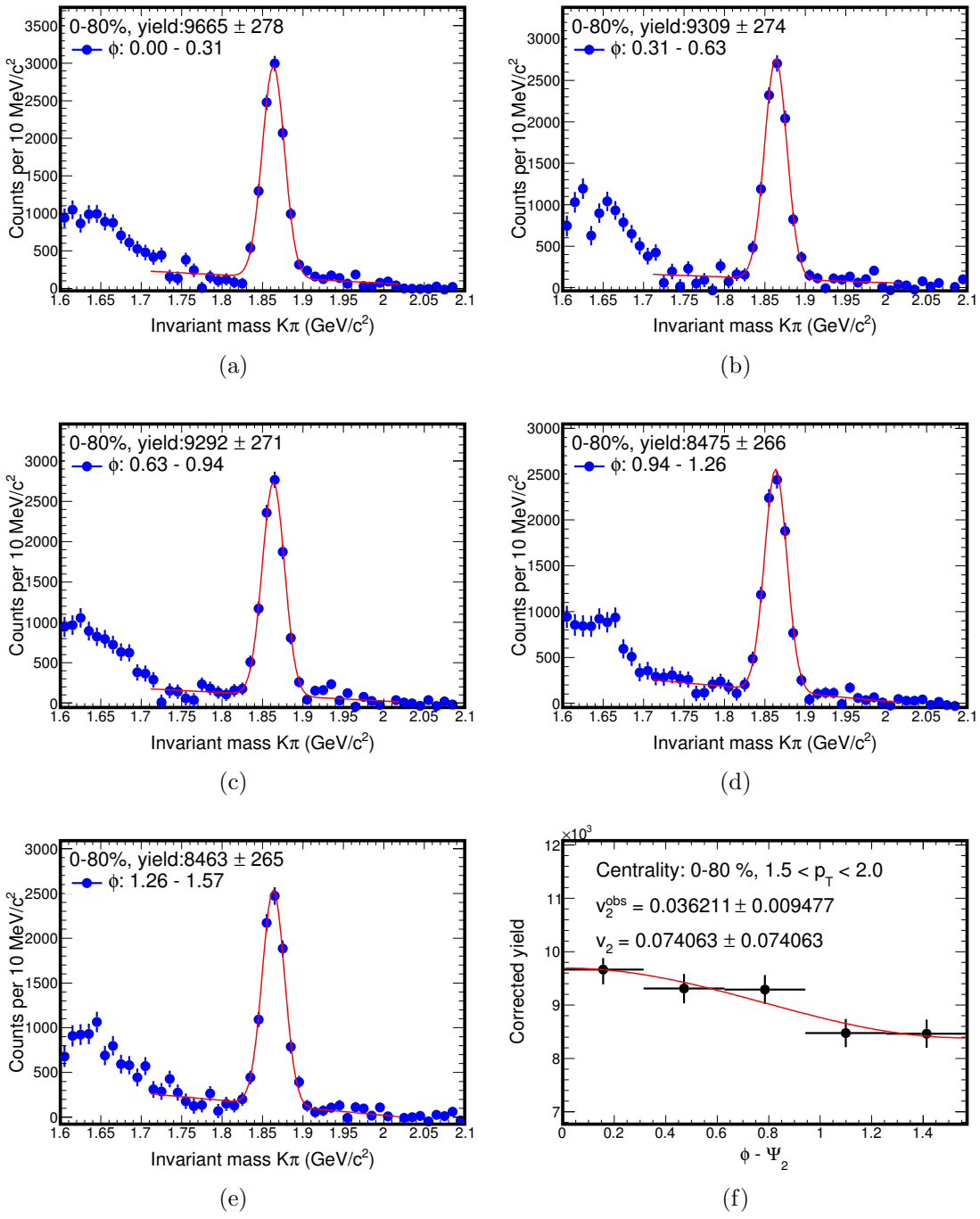


Figure 5.3.4: Corrected invariant mass distributions in $\phi - \Psi_2$ bins for $1.5 < p_T < 2$ GeV/c and v_2^{obs} calculation.

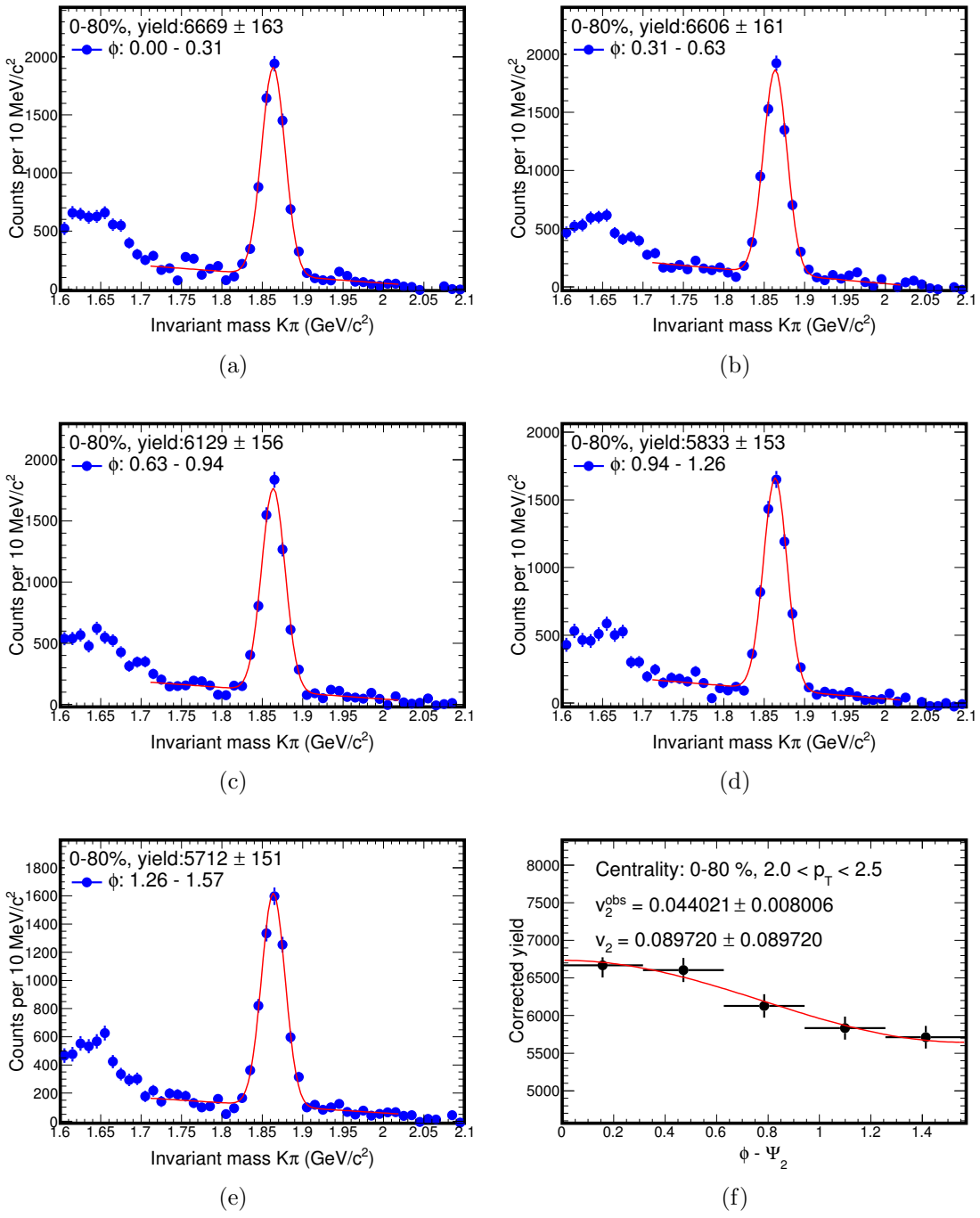


Figure 5.3.5: Corrected invariant mass distributions in $\phi - \Psi_2$ bins for $2 < p_T < 2.5$ GeV/c and v_2^{obs} calculation.

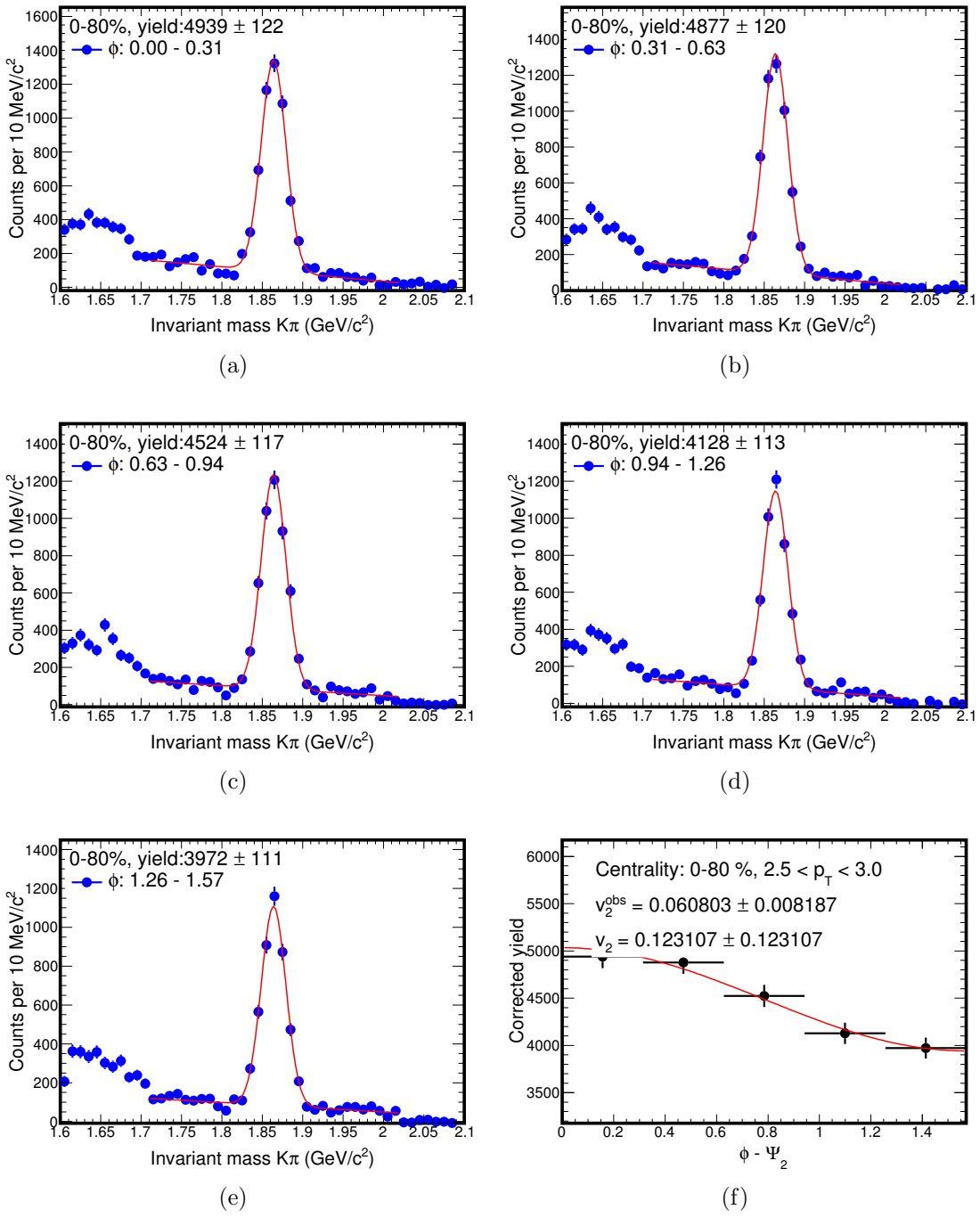


Figure 5.3.6: Corrected invariant mass distributions in $\phi - \Psi_2$ bins for $2.5 < p_T < 3$ GeV/c and v_2^{obs} calculation.

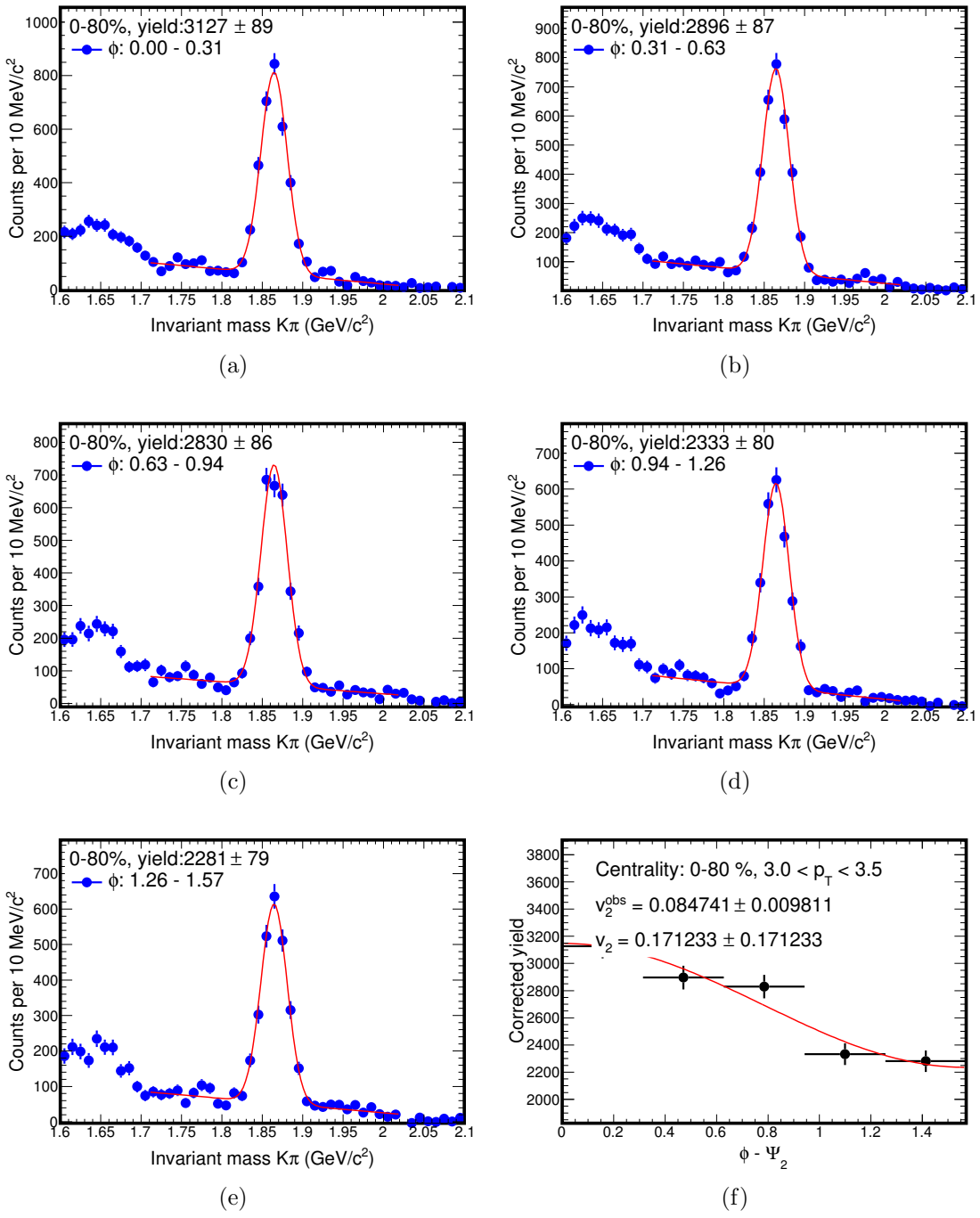


Figure 5.3.7: Corrected invariant mass distributions in $\phi - \Psi_2$ bins for $3 < p_T < 3.5$ GeV/c and v_2^{obs} calculation.

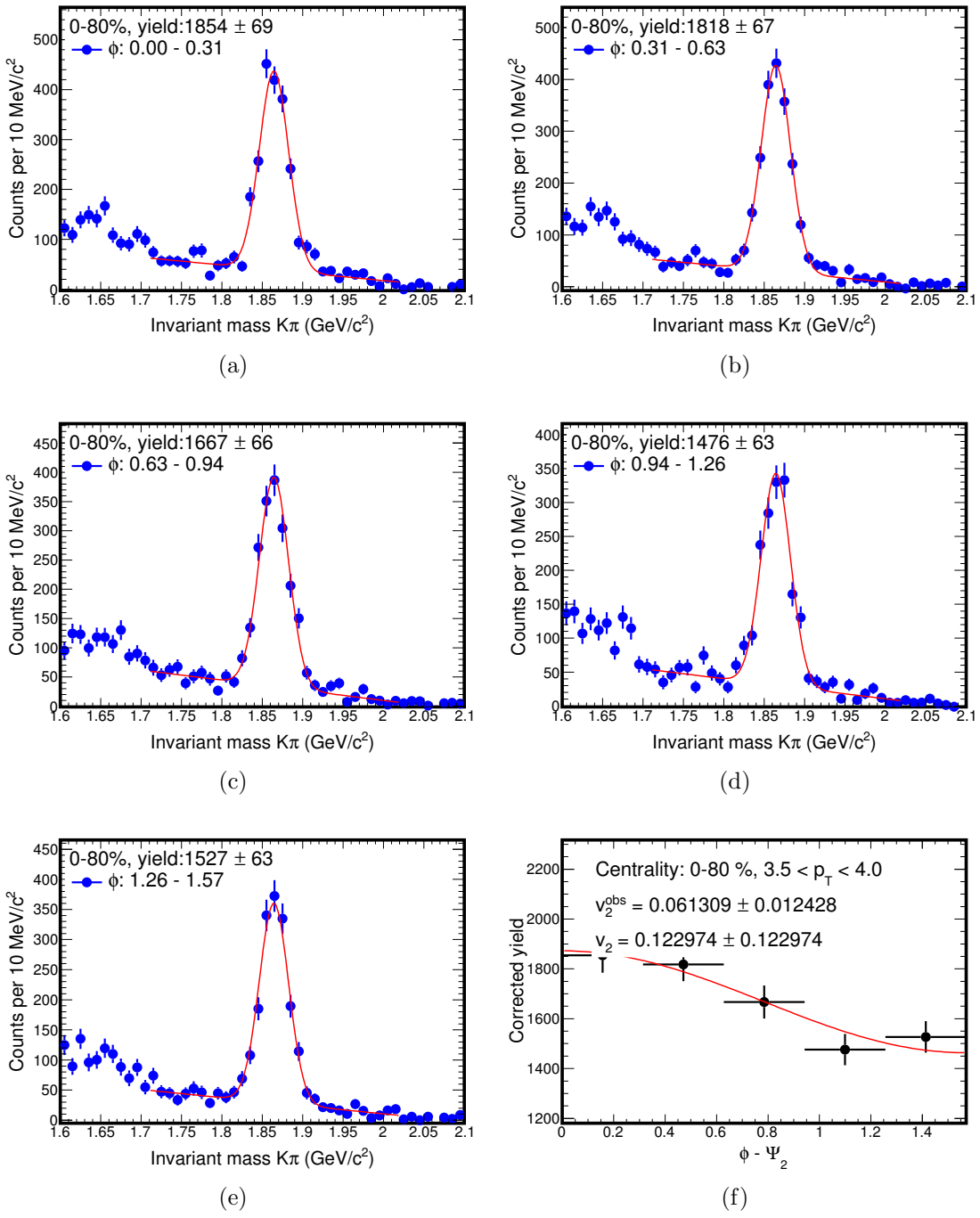


Figure 5.3.8: Corrected invariant mass distributions in $\phi - \Psi_2$ bins for $3.5 < p_T < 4$ GeV/c and v_2^{obs} calculation.

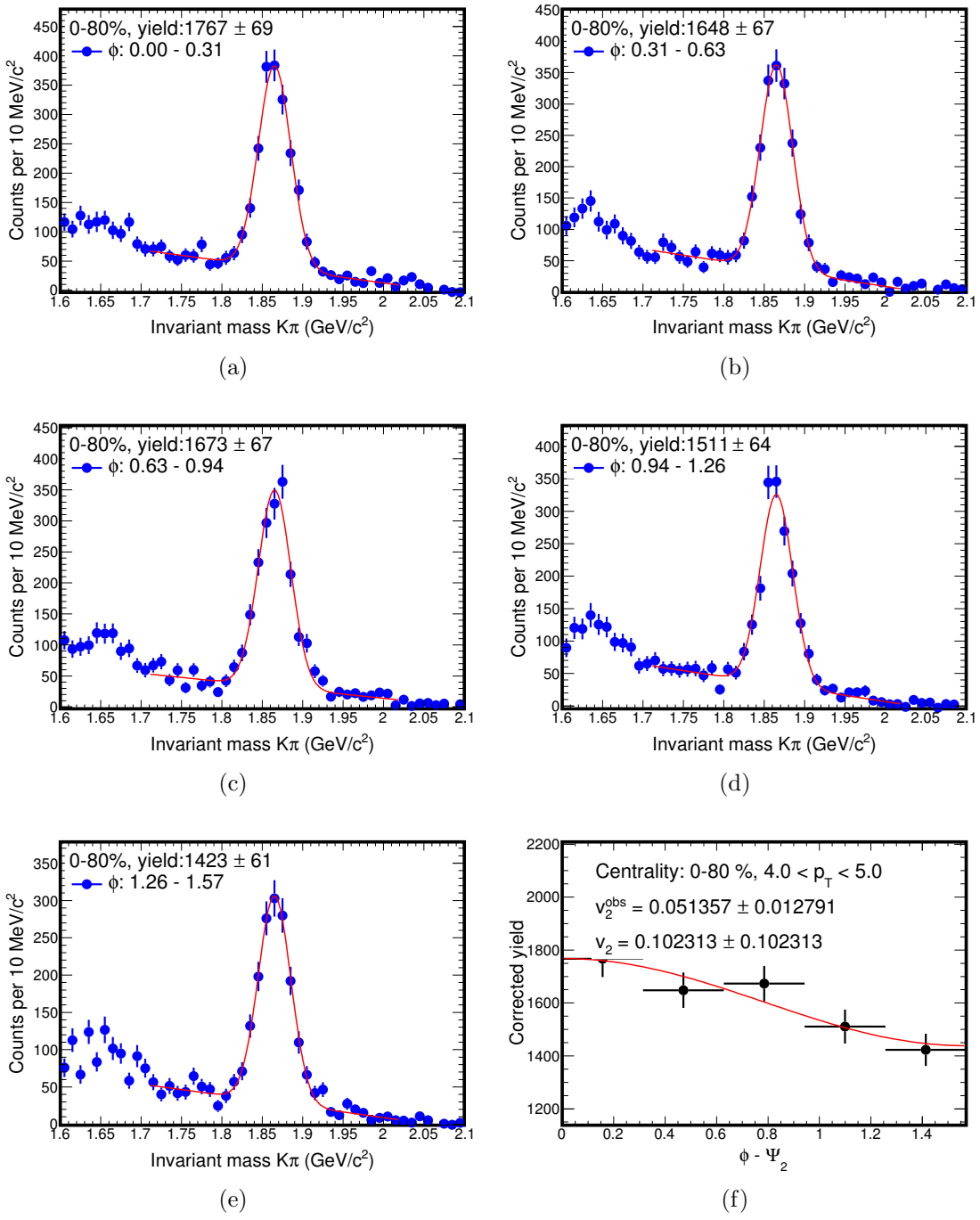


Figure 5.3.9: Corrected invariant mass distributions in $\phi - \Psi_2$ bins for $4 < p_T < 5$ GeV/c and v_2^{obs} calculation.

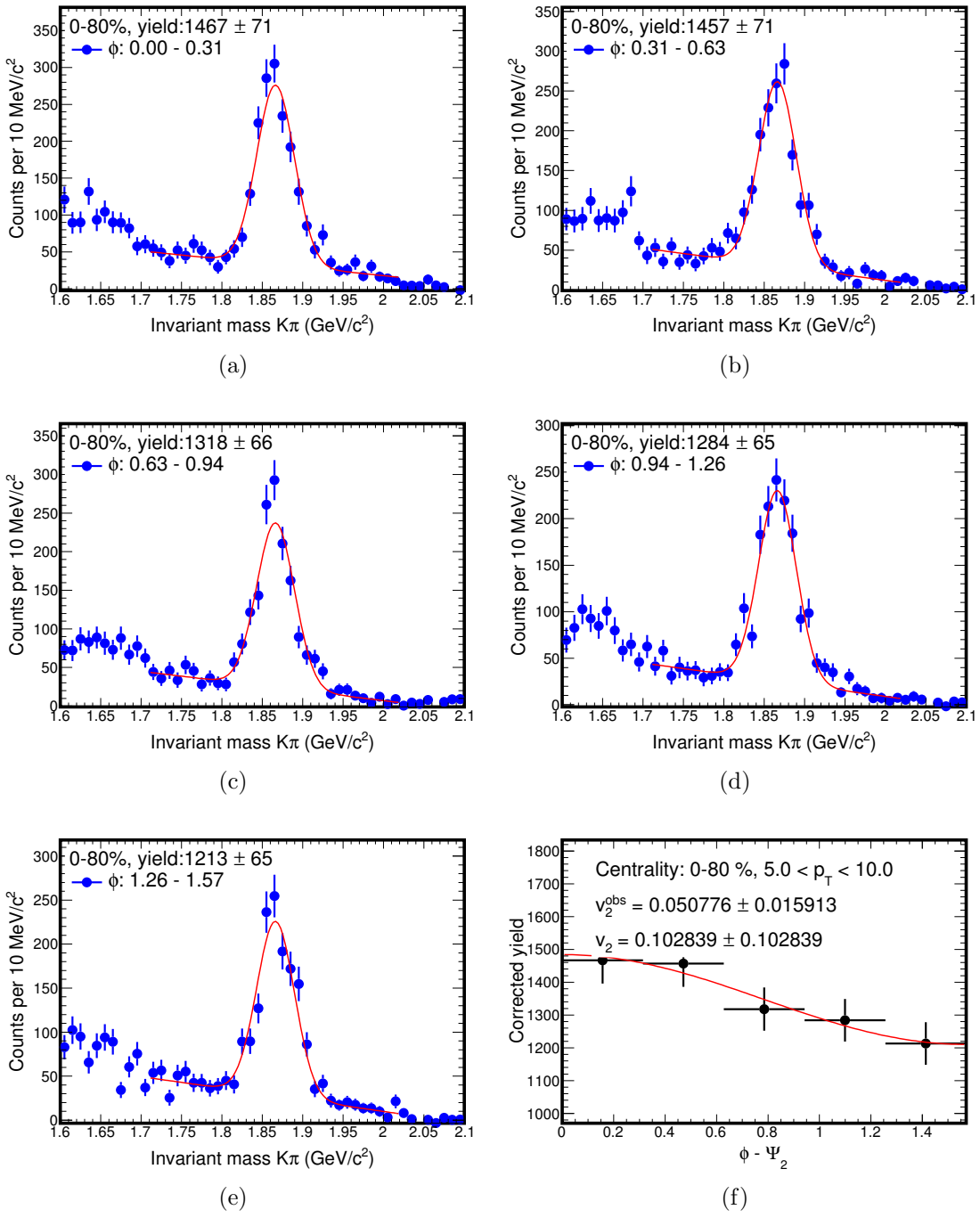


Figure 5.3.10: Corrected invariant mass distributions in $\phi - \Psi_2$ bins for $5 < p_T < 10$ GeV/c and v_2^{obs} calculation.

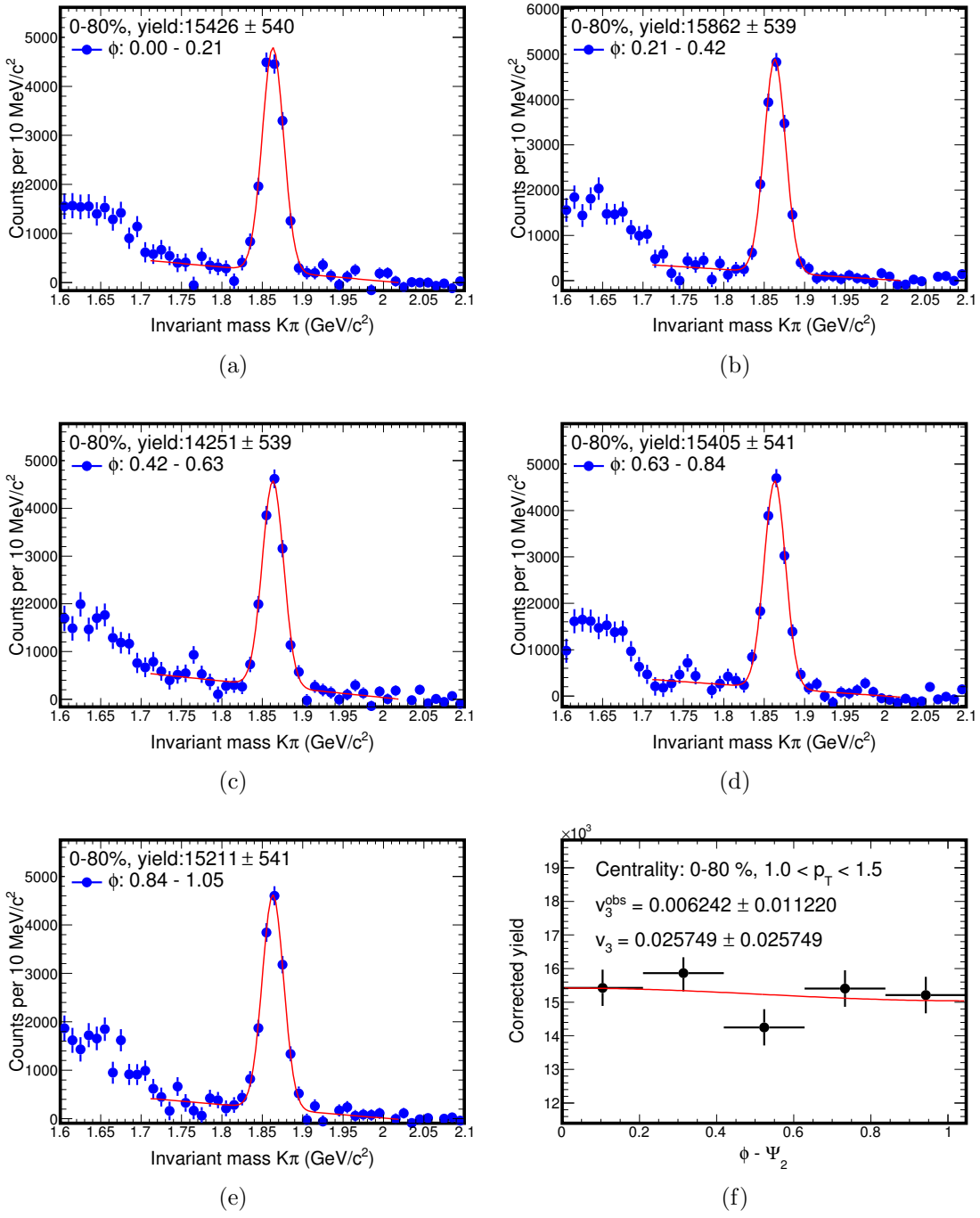


Figure 5.3.11: Corrected invariant mass distributions in $\phi - \Psi_3$ bins for $1 < p_T < 1.5$ GeV/c and v_3^{obs} calculation.

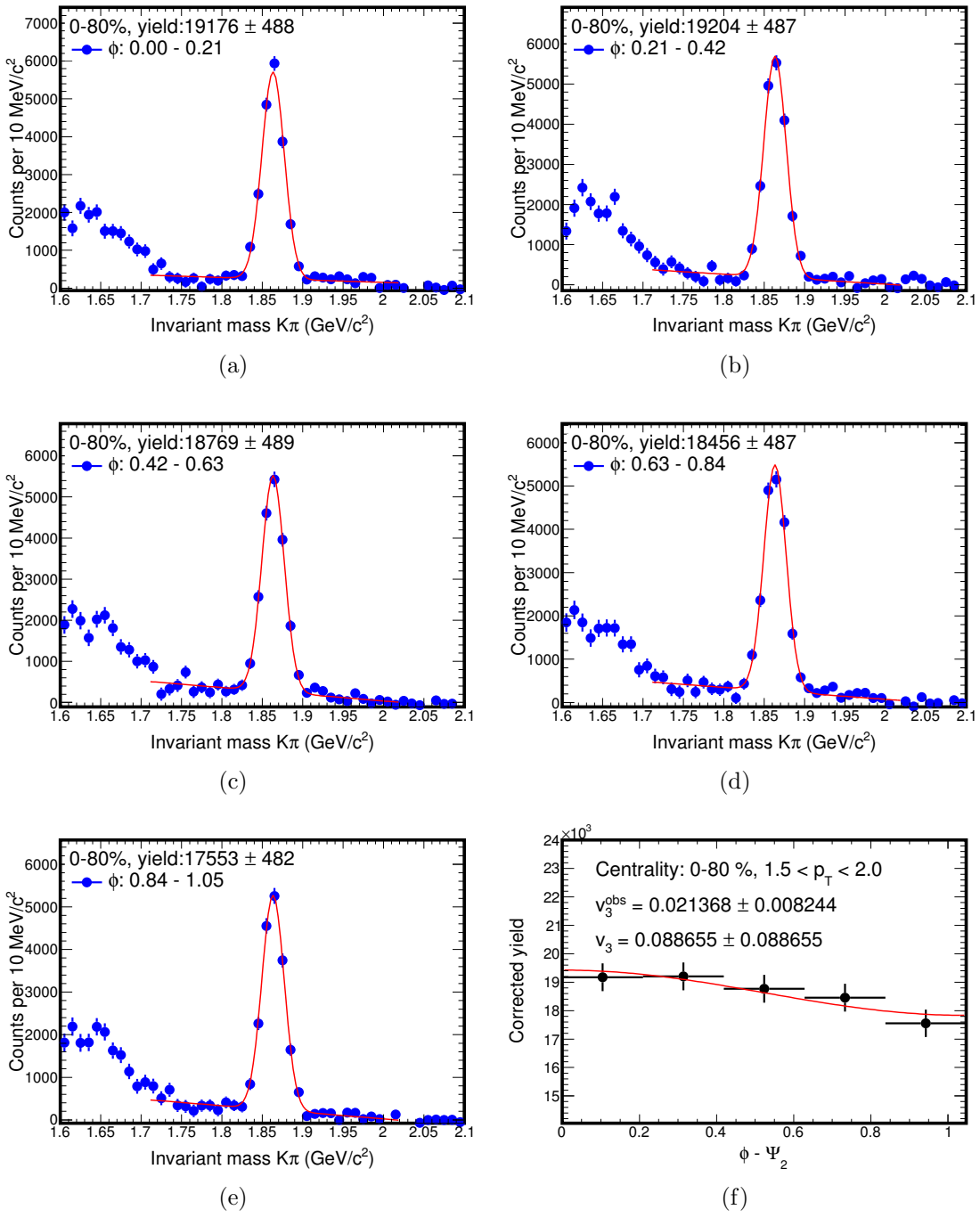


Figure 5.3.12: Corrected invariant mass distributions in $\phi - \Psi_3$ bins for $1.5 < p_T < 2$ GeV/c and v_3^{obs} calculation.

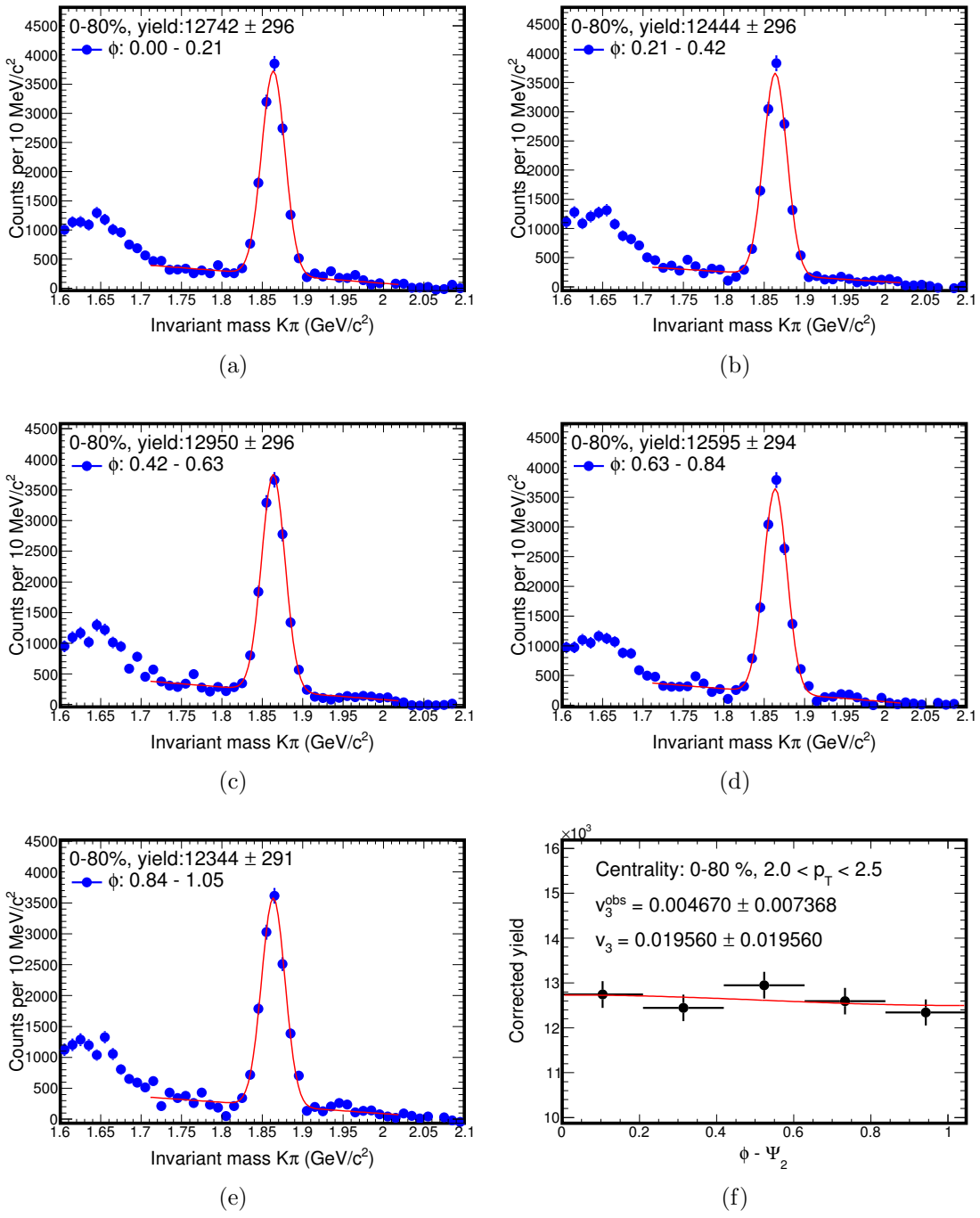


Figure 5.3.13: Corrected invariant mass distributions in $\phi - \Psi_3$ bins for $2 < p_T < 2.5$ GeV/c and v_3^{obs} calculation.

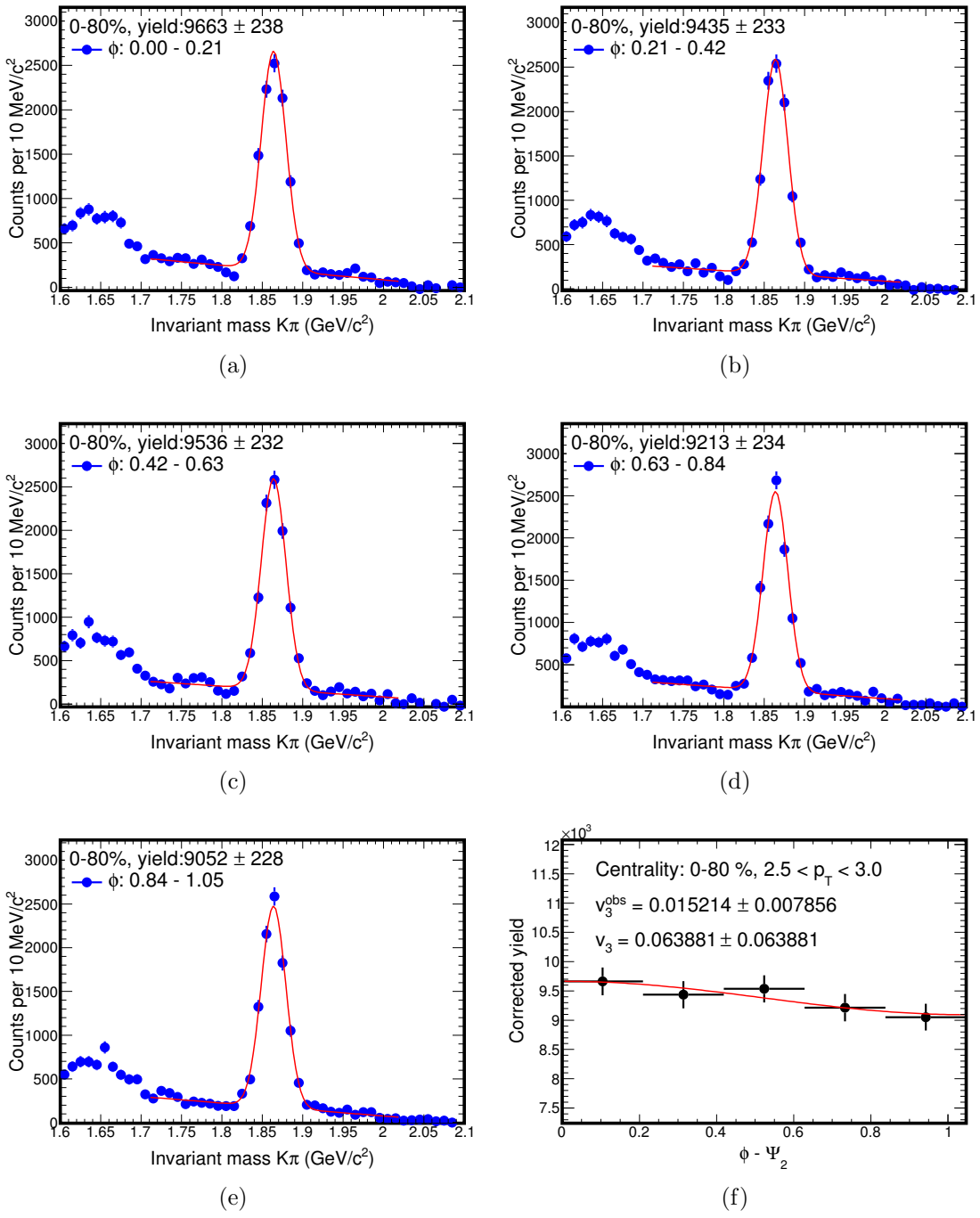


Figure 5.3.14: Corrected invariant mass distributions in $\phi - \Psi_3$ bins for $2.5 < p_T < 3$ GeV/c and v_3^{obs} calculation.

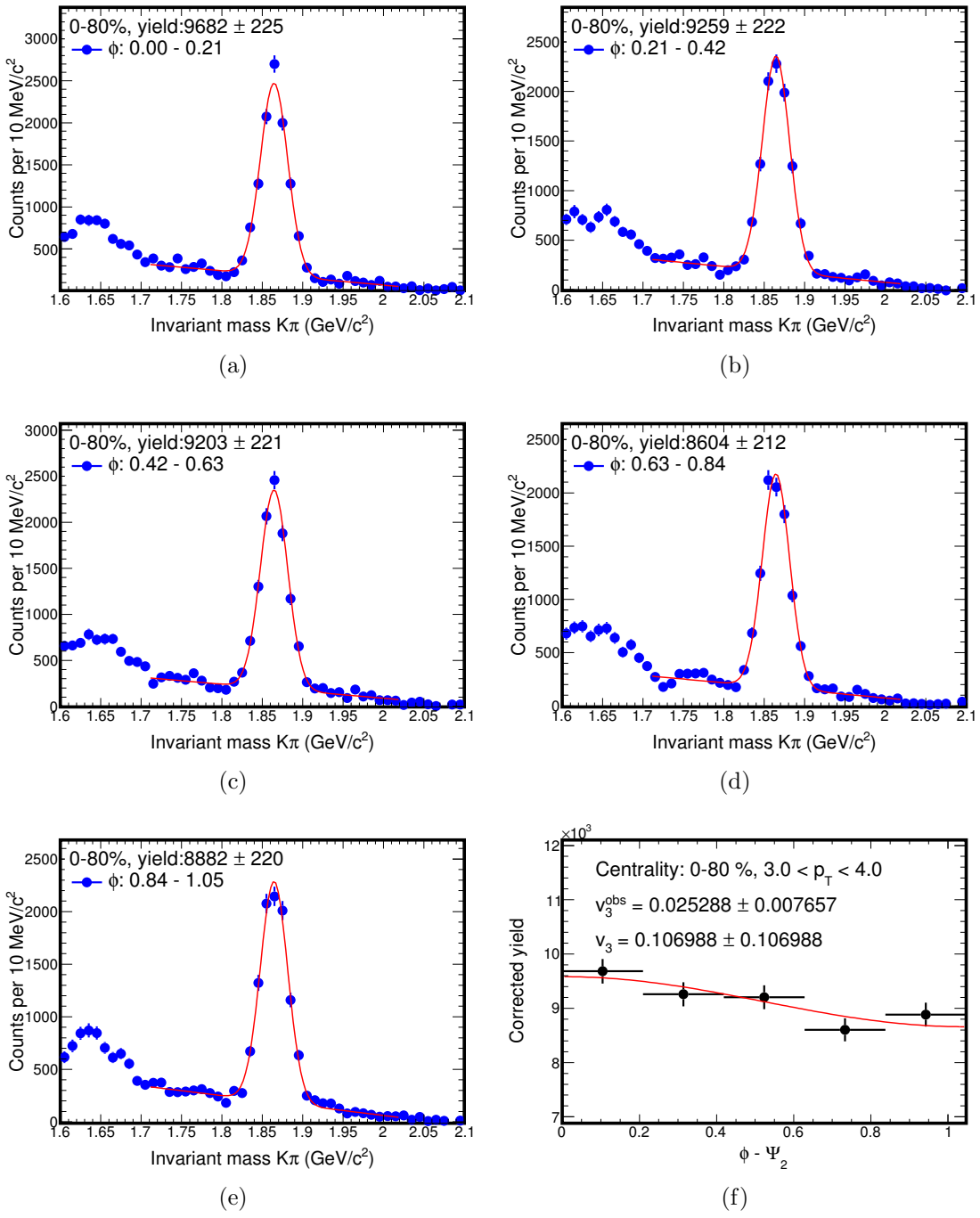


Figure 5.3.15: Corrected invariant mass distributions in $\phi - \Psi_3$ bins for $3 < p_T < 4$ GeV/c and v_3^{obs} calculation.

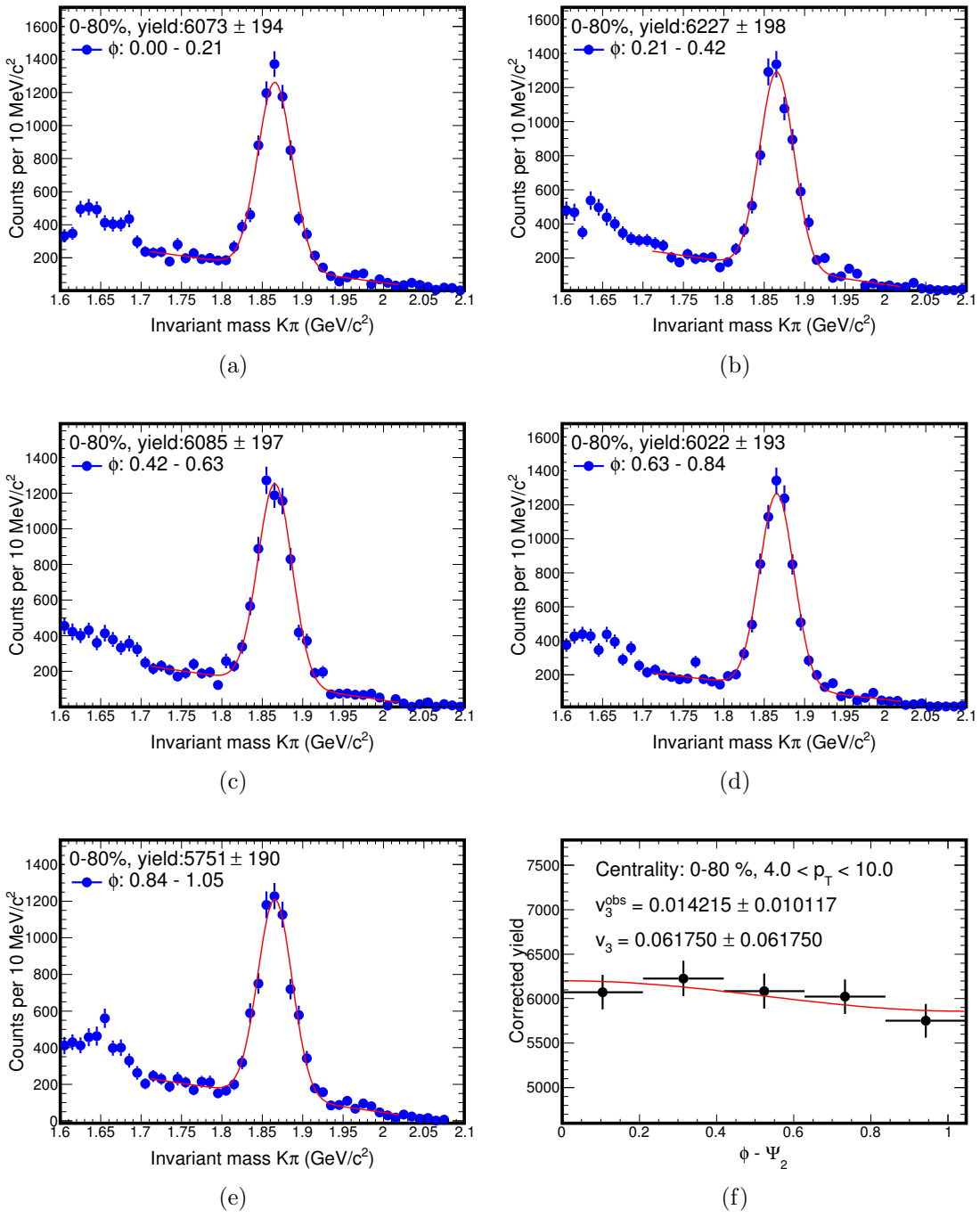


Figure 5.3.16: Corrected invariant mass distributions in $\phi - \Psi_3$ bins for $4 < p_T < 10$ GeV/c and v_3^{obs} calculation.

5.4 Systematic studies

The most dominant contributions to the systematics in this analysis come from the yield extraction and hence, the treatment of the background remaining under the D meson peak. The relative D^0 reconstruction efficiency, used to merge combine large centrality classes, should also introduce systematics due to the uncertainty in the published D^0 spectra versus p_{T} that was used. Finally, both the feed-down from B decays in the D^0 channel and the contribution from other non-flow effects is also considered and described in more details in sections 5.5 and 5.6.

In the yield extraction it is assumed that the background is linear in the vicinity of the reconstructed open heavy signals. However, as was discussed in sections 4.3.2 candidates were both daughters are erroneously identified will have a small and broad contribution below the D^0 mass while the effect of correlated background from three and four body decays produces a visible bump below the D^0 mass peaking at roughly 1.7 GeV/c. Both of these contributions to the background should have second order effects on the measured v_2, and so we estimate the systematics from the different v_2 obtained by varying the regions used to describe the background for the yields obtained from either the fit or the "bin counting" methods.

The result from fitting the background in the ranges $(1.71, 1.80)$ and $(1.93, 2.02)$ GeV/c^2 and the Gaussian in $(1.80, 1.93)$ with the "bin counting" procedure was used for the central value. A second set of intervals $(1.73, 1.78)$ and $(1.95, 2.00)$ GeV/c^2 was used to estimate the systematics from the description of the background as well as the interval $(1.78, 1.95)$ for the signal. All four possible combinations were considered for each yield extraction procedure.

The effect of the topological cuts was also taken into consideration and were varied

to have 50% and 150% relative to the yield used as the baseline. These cuts were also obtained using TMVA to optimize for the best significance for a given efficiency. The three sets of topological cuts in different p_{T} bins are shown in section 4.2.1 in the tables 4.2.1 and 4.2.2 and 4.2.3. Assuming that the v_n from all these combinations follow a normal distribution, the mean square error can be obtained as the maximum difference between any 2 results divided by $\sqrt{12}$. Figure 5.4.1 shows the results from studying the v_2 systematic errors in four centrality classes while figure 5.4.2 show the results obtained for the D^0 triangular flow in 10-40% (left) and 0-80% (right) central events. The different open (closed) symbols correspond the bin counting (fit integral) yield extraction procedure and the different colors represent different combinations of the ranges used for the yield extraction. The different shaped markers represent the results obtained for the different sets of topological cuts. For both the v_2 and v_3 the dominant contribution towards the systematic errors is the variation on the topological cuts, suggesting that these fluctuations are mostly driven by statistical fluctuations and indicating that these errors are most likely over estimating the true systematic uncertainties.

5.5 Non-flow estimation

There are other sources of azimuthal correlations that are unrelated to the reaction plane that may complicate the interpretation of the measured v_2. Collectively referred to as non-flow, examples include correlations caused by jets, resonance decays, final state interactions, etc [13]. The contribution from these other sources can be reduced by eliminating particles in the vicinity of the measured D^0 when correlating to the event plane. However, even though an η-gap is applied around the D^0 candidate in the analysis non-flow effects could still remain and contribute towards the measured

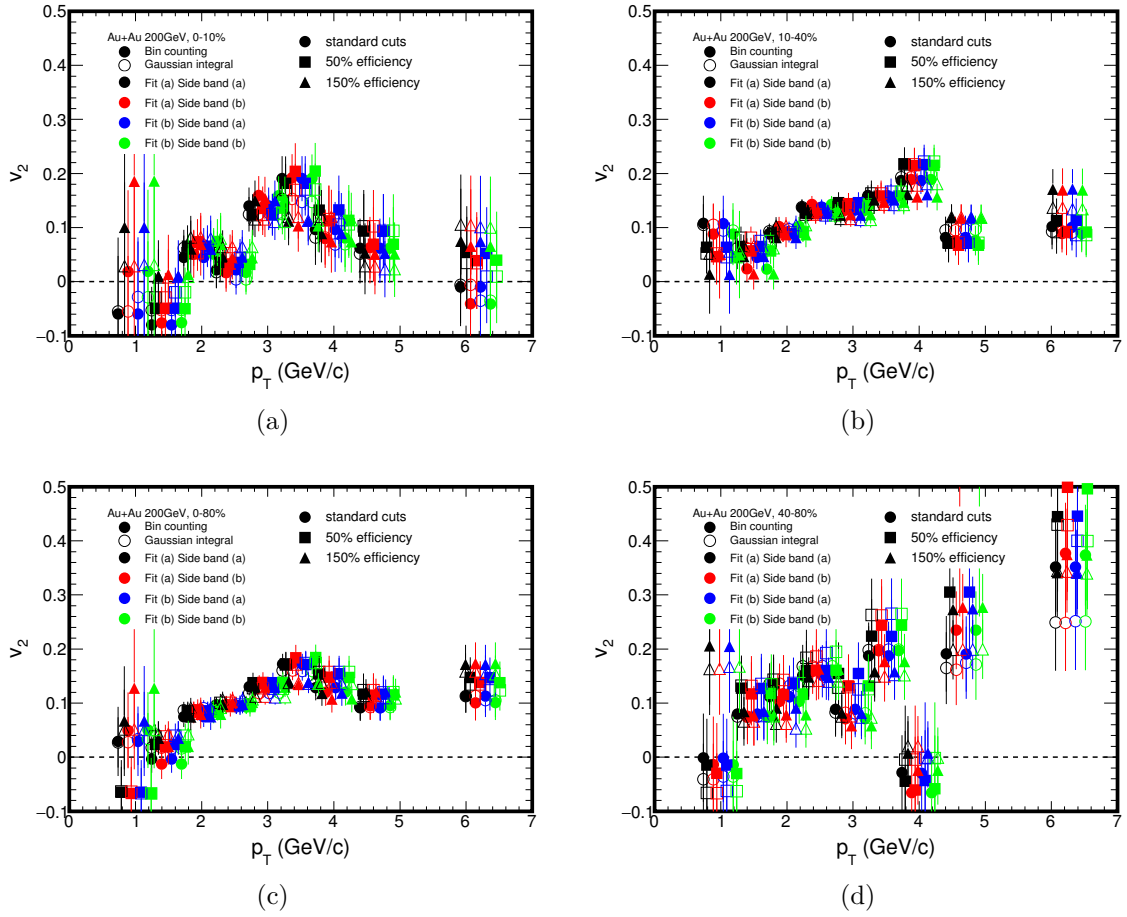
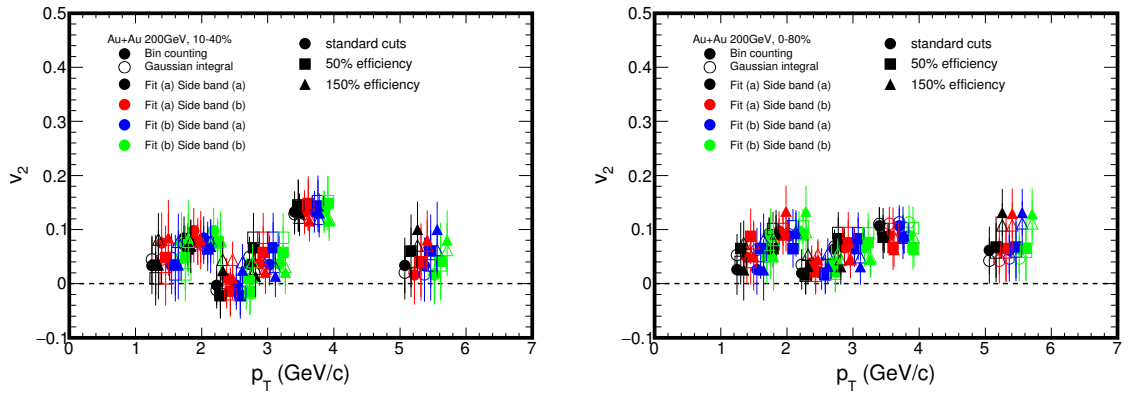


Figure 5.4.1: Studies of D^0 v_2 systematic uncertainties versus p_{T} in three centrality classes, clockwise from top left: 0-10%, 10-40%, 40-80% and 0-80%.

v_n. The non-flow contribution to the measured v_2 was estimated using the D -hadron correlations measured in p+p 200 GeV collisions at RHIC. Due to the limited D^0 signal obtained from p+p at 200 GeV at STAR, and given that charm fragmentation into D^0 is quite similar to that of $D^{*\pm}$ these were used as a proxy in the non-flow studies. Figure 5.5.1 shows the $D^{*\pm}$-hadron azimuthal correlation obtained form Run 12 p+p 200 GeV collisions with different sets of η gaps.

Figure 5.5.2 shows the $D^{*\pm}$-hadron correlation $< \sum_i \cos(2(\phi(p_{\mathrm{T}}) - \phi_i)) >$ vs p_{T} obtained with different η gaps for both the whole 2π range as well as the near side



(a) (b)

Figure 5.4.2: Studies of D^0 v_3 systematic uncertainties versus $p_{\rm T}$ in 10-40% (left) and 0-80% (right) central events.

only. Given that the charm fragmentation into D^0 is quite similar to that of $D^{*\pm}$, the calculated D-hadron correlation should provide a good substitute, however the decay feed-down to these two particle species is considerably different. For instance, the D^0 themselves may come from $D^{*\pm}$ decays and be strongly correlated with the $D^{*\pm}$ daughter. The effects of the correlation due to feed-down were estimated using HIJING simulations. Figure 5.5.3 shows the near side $< \sum_i \cos(2(\phi(p_{\rm T}) - \phi_i)) >$ as a function of transverse momenta for $D^{*\pm}$-hadron and $D^{*\pm}$-hadron correlation coming solely from feed-down, D^0-hadron from feed-down and the deduced D^0-hadron correlation for no η gap and an η gap of $|\Delta\eta| = 0.15$.

Following the procedure set forth in [7] we can estimate the correlation from a particle at a given $p_{\rm T}$ and azimuthal angle $\phi(p_{\rm T})$ as follows:

$$\left\langle \sum_i \cos\left(2(\phi(p_{\rm T}) - \phi_i)\right) \right\rangle \geq M v_2^{n.f.}(p_{\rm T})\overline{v_2} + \text{non} - \text{flow} \tag{5.11}$$

where $v_2(p_{\rm T})$ is the elliptic flow of the particles in the given $p_{\rm T}$ bin, $\overline{v_2}$ is the average flow of the particles used and M is the multiplicity of particles contributing to the

sum. Assuming that the non-flow correlations in Au+Au are the same as those in p+p collisions and that there is no flow in p+p collisions, then the non-flow contribution to the D^0 v_2 in Au+Au can be estimated as [7]:

$$v_2^{n.f.} = \frac{\langle \sum_i \cos\left(2(\phi(p_{\mathrm{T}}) - \phi_i)\right)\rangle}{M\overline{v_2}} \tag{5.12}$$

Figure 5.5.4 shows the estimated D^0-hadron correlation and calculated non-flow effect on the D^0 v_2 measured. Due to limited statistics, the study has been done in 3 wide p_{T} ranges and the non-flow as a function of p_{T} is obtained from interpolating between these 3 points.

5.6 Feed-down

Another important source to consider is the effect of reconstructed charm mesons coming from B decays. Because of the B lifetime, the topological cuts should serve to reduce the number of reconstructed D^0 mesons coming from these decays. To determine the size of this contribution, FONLL calculations [33] were used to calculate the B and D^0 spectra in Au+Au collisions at 200 GeV. Figure 5.6.1 shows the input B and D^0 spectra (left) and, as an example, the B^+/D^0 ratio (right) obtained from the FONLL calculations as function of p_{T}. A large sample of B and D^0 particles are then simulated using the FONLL spectra to provide a realistic p_T distribution for the particles. The B are then forced to decay in the channel $B \to D^0(\overline{D^0}) + X$ using the PYTHIA event generator, and all of the $D^0(\overline{D^0})$ are then decayed with 100% probability in the πK channels. The daughter tracks are then smeared using the distributions from data in different p_T, ϕ and η bins.

These daughters are then used to reconstruct $D^0(\overline{D^0})$ candidates and the same set of topology cuts as were used in the analysis were applied. Figure 5.6.2 shows the

ratio of D^0's coming from B decays versus all D^0 candidates reconstructed from the sample. There are two sets of markers in the figure. In red the ratio obtained without applying the topological cuts and in blue the same ratio with the topological cuts. As we can see, after all topological cuts are applied, the B-feed-down contribution can be reduced to less that 4% in the whole p_{T} range. As an illustration, we can consider the extreme case where the v_2 of B mesons is zero. The value of the measured inclusive D^0 v_2 will be reduced by 4% relative to that of the prompt D^0. Assuming the D^0 v_2 has a maximum value of 0.15, the effect from B feed-down will be less than 0.006 which is, for all purposes, negligible.

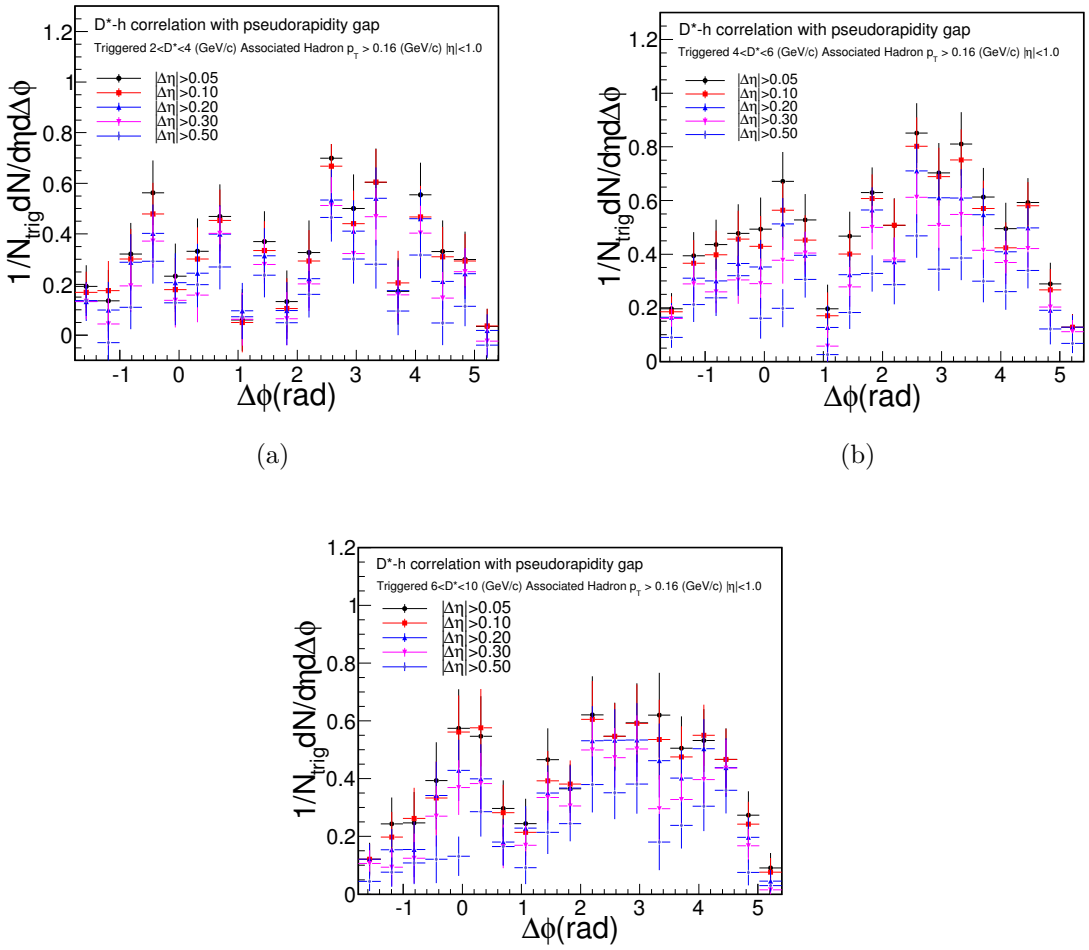
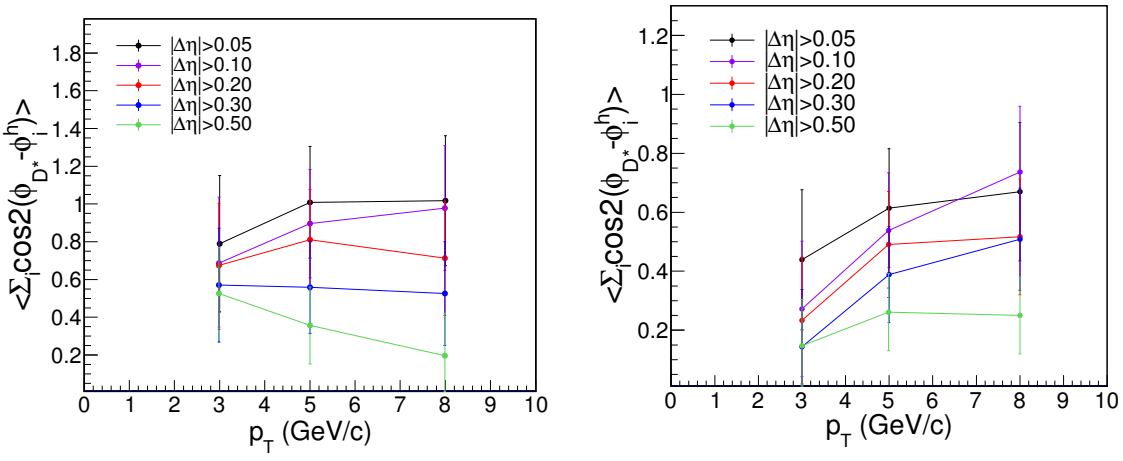
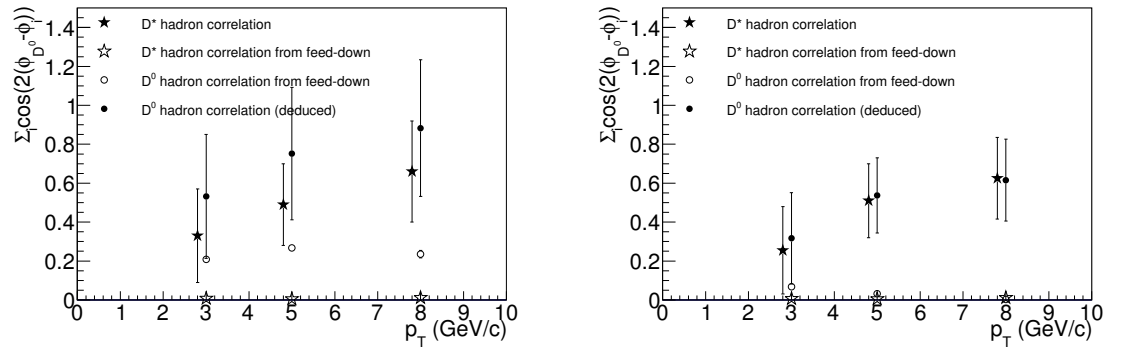


Figure 5.5.1: $D^{*\pm}$-hadron azimuthal correlation in pp 200 GeV collisions, with different trigger D^* p_T and η gaps.



(a) (b)

Figure 5.5.2: $D^{*\pm}$-hadron correlation $\langle\cos(2(\Delta\phi))\rangle$ vs. p_T in pp 200 GeV collisions, with different η gaps. The left panel sums up correlations for the whole 2π range and the right panel is for the near side only.



(a) (b)

Figure 5.5.3: $D^{*\pm}$-hadron correlation $\langle\Sigma_i \cos 2(\phi(p_T) - \phi_i)\rangle$ vs. p_T for $D^{*\pm}$-hadron, $D^{*\pm}$-hadron from decay feed-down only, D^0-hadron from feed-down only, and the deduced D^0-hadron correlation. Only the near side correlation is summed. The left panel shows the result with no η gap and the right panel shows result with the same η gap of 0.15 as v_2 calculation.

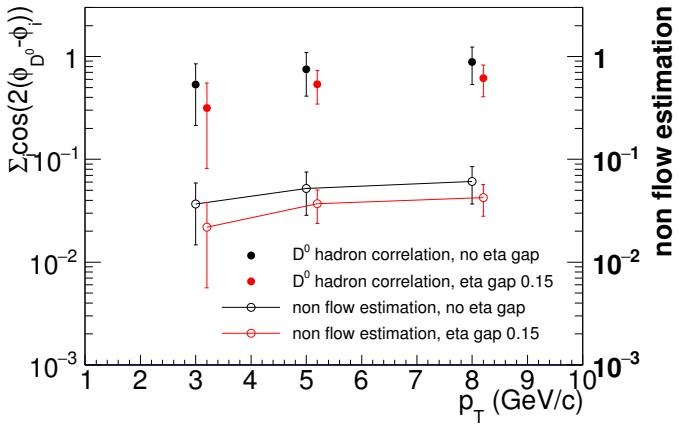


Figure 5.5.4: D^0-hadron correlation and the estimated non-flow effect on D^0 v_2.

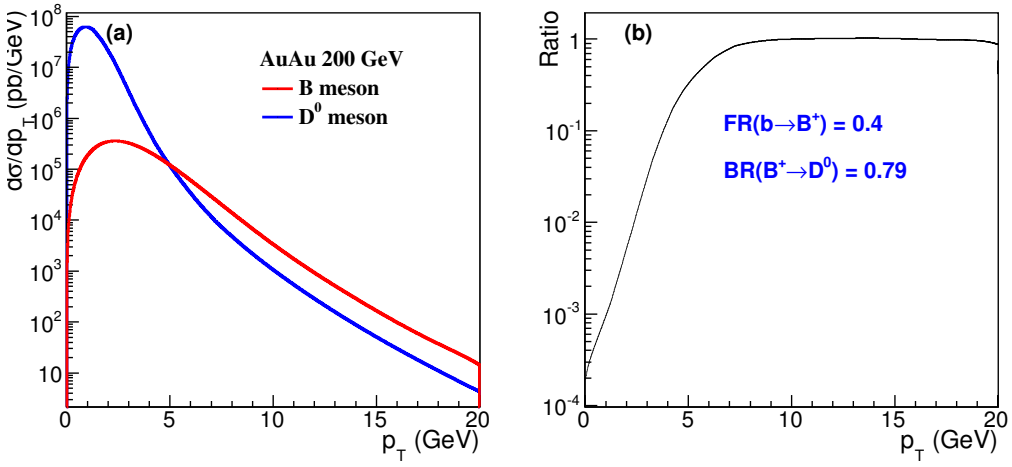


Figure 5.6.1: (a) B and D^0 meson p_T spectra in AuAu 200GeV, (b) the input B^+/D^0 ratio as a function of p_T.

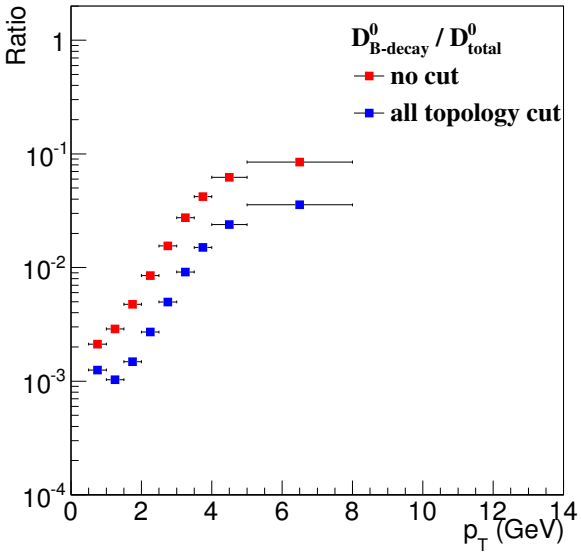


Figure 5.6.2: FONLL-based simulation of the ratio of D^0 from B decay over inclusive D^0 as a function of p_T. The red square represents ratio without any cuts, the blue square is ratio with all topology cuts.

Chapter 6

Experimental Results and discussion

The following sections will show the results obtained from studying roughly 1 billion MinBias events of the processed dataset obtained during Run 14 together with a brief introduction to model comparisons and discussion related to the physics impact of the measurements on our understanding of the QGP.

6.0.1 D-meson v_2

Figure 6.0.1 shows the measured D^0 v_2 in four centrality classes (0-10%, 10-40%, 40-80% and 0-80%) using the event plane method. As discussed, to reduce the contributions of non-flow effects, only tracks in the opposite side of the TPC (relative to the D-meson candidate) were used for the event plane determination. An additional gap $|\eta| < 0.05$ is always removed in order to account for cases when the reconstructed D-meson is close to midrapididty. An immediate observation that can be made from these results is the fact that the D^0 elliptic flow is finite in the four centrality bins studied. The results in 0-10% and 40-80% centralities are shown with coarser binning and the lowest p_{T} (0.5-1 GeV/c) is suppressed due to limited statistics.

The results obtained for $D^{\pm}$, using roughly 75% (700 million MinBias events) are preliminary for two important reasons: a) without published results, the relative reconstruction efficiency can not be accounted for and b) the major source of systematic uncertainties, i.e. the variation of the geometrical cuts, is not available at the time of

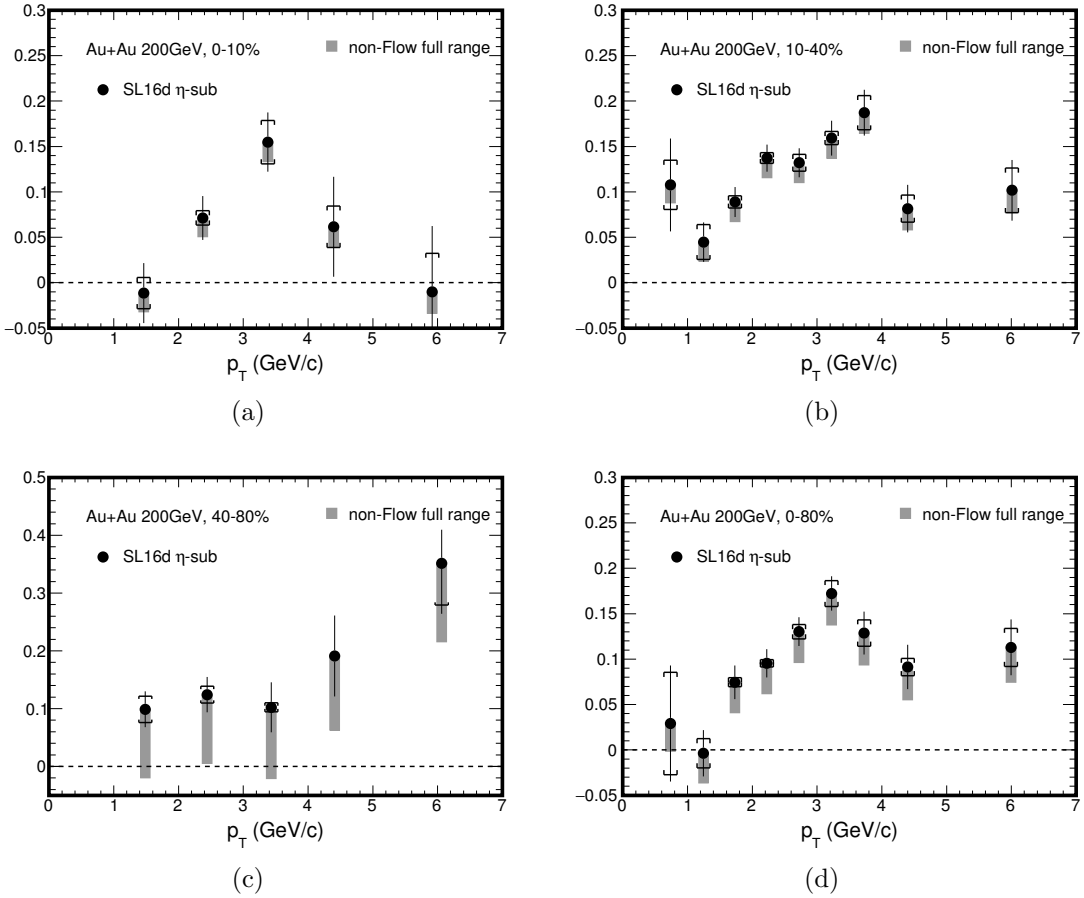
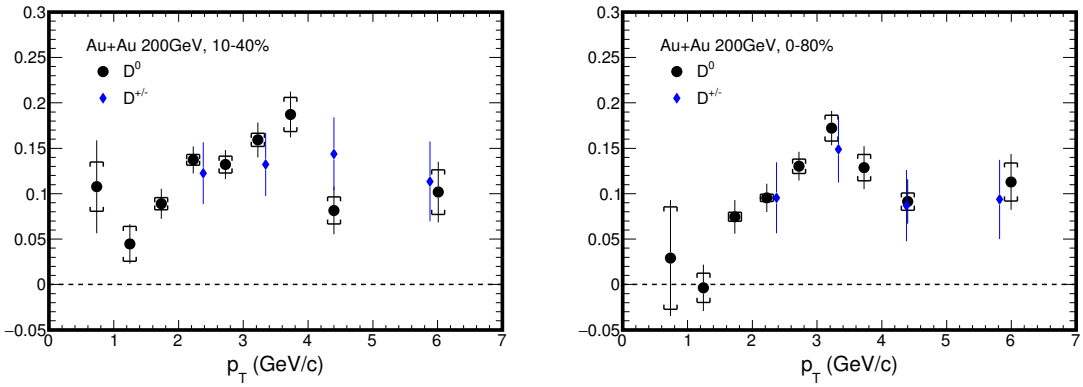


Figure 6.0.1: D^0 v_2 measured in 0-10%, 10-40%, 40-80% and 0-80% central events.

writing this dissertation (and as such the systematics have not been included). However, it is interesting to compare the results with those obtained for D^0. Given that $D^{\pm}$ the reconstruction efficiency is further reduced by the presence of a third track, the significance of the reconstructed signal is reduced. For this reason, we present the result in 0-80% and 10-40% central events for $p_{\mathrm{T}} > 2$ GeV/c only. Figure 6.0.2 shows the comparison between the results obtained for the two charmed meson species. As was expected from their similar masses ($D^{\pm} - D^0 = 4.77 \pm 0.08$ MeV/c^2 [51]) and quark content, the measured v_2 for both charmed mesons studied is in good agreement across the p_{T} range. Due to the preliminary nature of the $D^{\pm}$ measurement and reduced statistical significance, we will focus on D^0 for the following sections.



(a) (b)

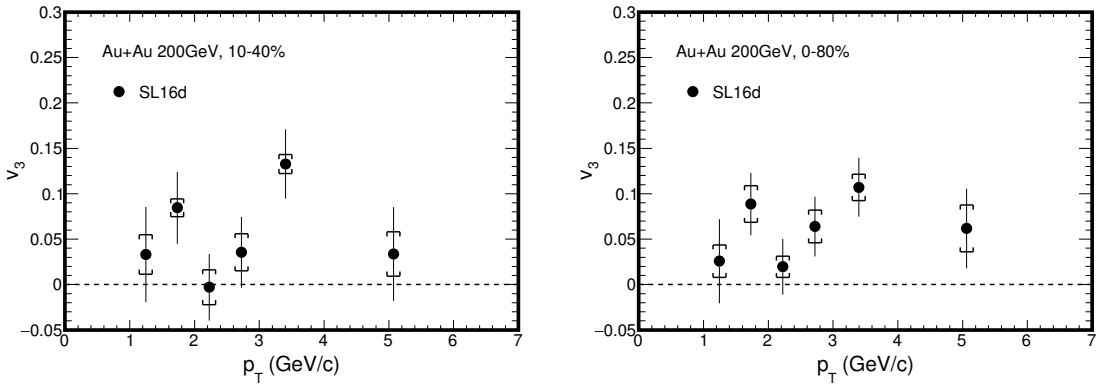
Figure 6.0.2: v_2 vs p_{T} for two charmed mesons D^0 and $D\pm$ in 10-40%(left) and 0-80%(right) central Au+Au collisions. the non-flow estimation has been removed from this comparison since it should apply to both species.

6.0.2 D^0 v_3

Some model calculations [64] including fluctuations in the initial conditions of the colliding nuclei together with the interactions with the medium have predicted that this might lead to a finite value for the D^0 triangular flow v_3. Figure 6.0.3 shows the

measured D^0 triangular flow v_3 in 10-40% and 0-80% central events obtained from the same data sample. The contribution from non-flow has not been estimated in this case since the effect should have a much less significant effect on the measurement.

These results, however, suggest a finite value of the v_3 and given that the triangular



(a) (b)

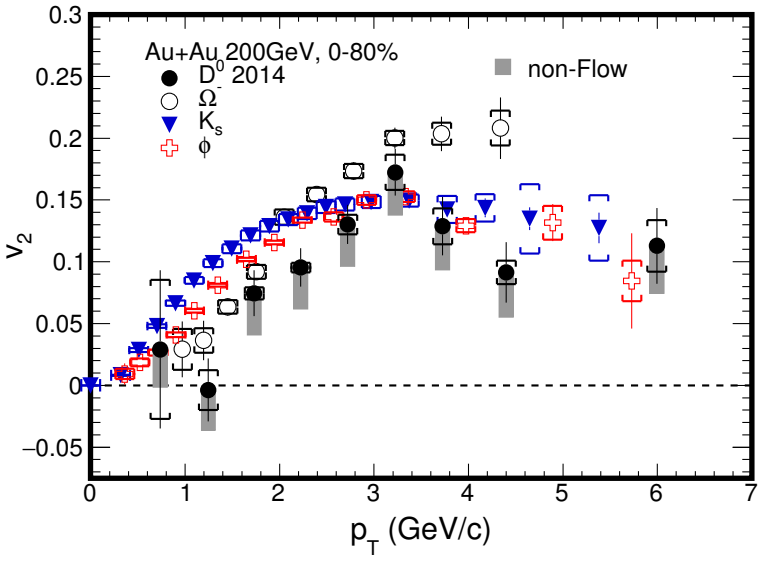
Figure 6.0.3: D^0 v_3 measured in 10-40% and 0-80% central events.

flow should depend less strongly on the initial eccentricity of the collision (versus v_2), the centrality dependence of the v_3 can provide insight into the properties of the QGP, especially when compared to light quarks.

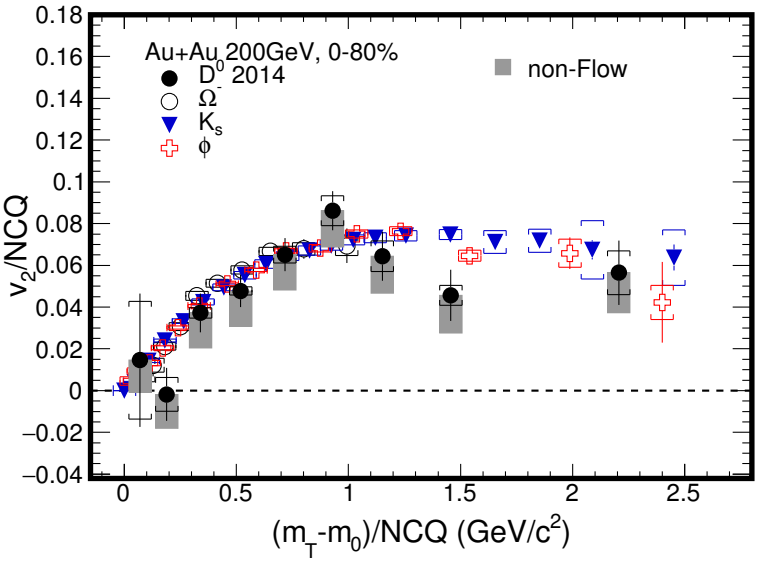
6.1 Comparison to data

Figures 6.1.1, 6.1.2, 6.1.3 and 6.1.4 show the comparison between D^0 v_2 and other particle species measured at 200 GeV [3, 4] versus p_{T}(top) in different centrality classes. Furthermore, in order to account for the different particle masses and Number of Constituent Quarks (NCQ), the comparison is done(bottom) by plotting v_2/NCQ vs $(m_T - m_0)/NCQ$ where $m_T = \sqrt{p_T^2 - m_0^2}$.

Given that charm production is skewed towards more central events when compared to light quark production, the comparison in a wide centrality range, i.e. 0-80%, is

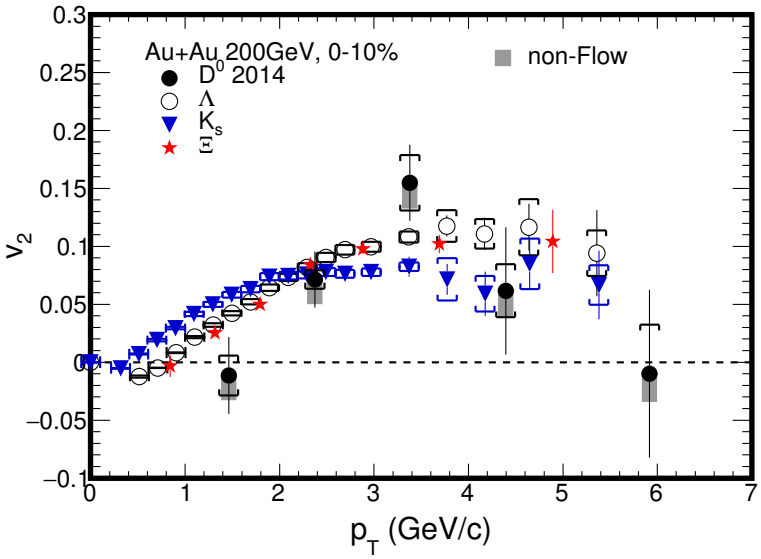


(a)

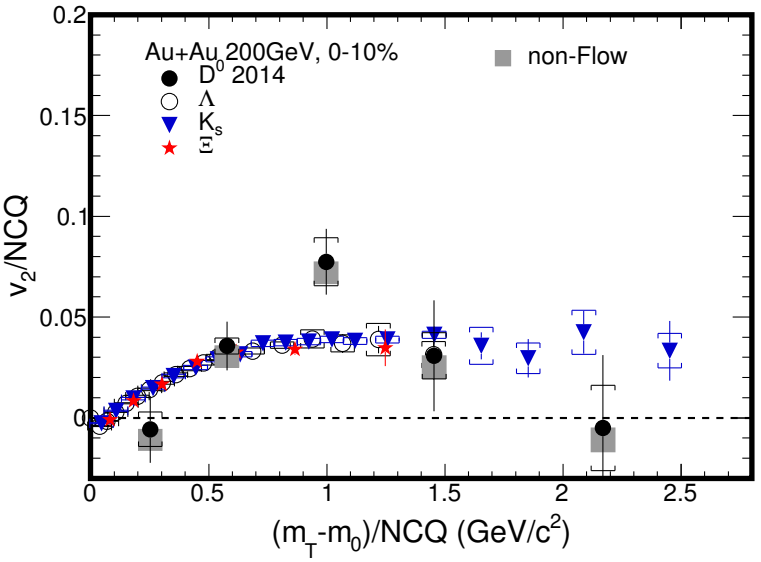


(b)

Figure 6.1.1: v_2 vs p_{T} (top) and v_2/NCQ vs $(m_T - m_0)/NCQ$ for D^0 (bottom) compared to other particle species [3, 4] in 0-80% central events with m_0 the mass of the particle and $m_T = \sqrt{p_T^2 + m_0^2}$.

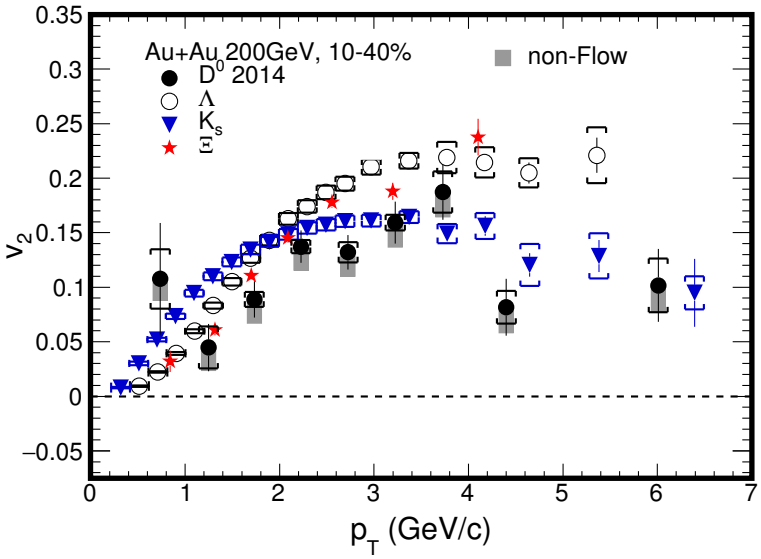


(a)

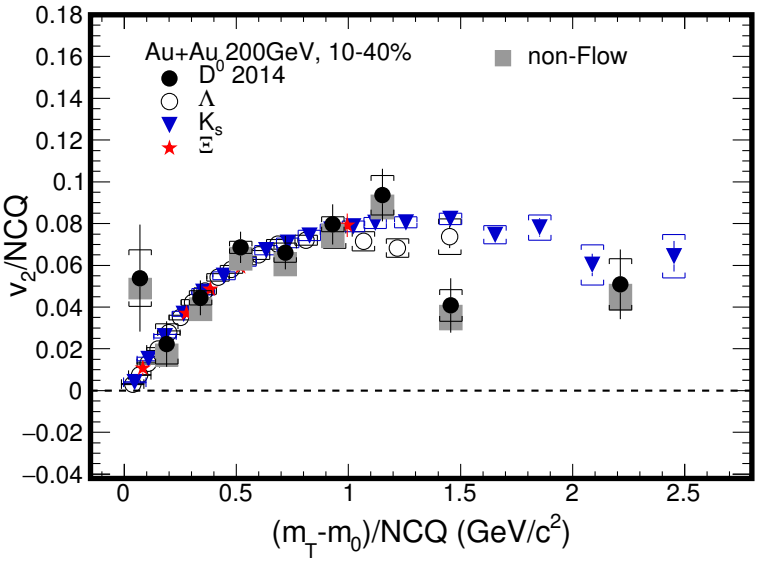


(b)

Figure 6.1.2: v_2 vs p_{T} (top) and v_2/NCQ vs $(m_T - m_0)/NCQ$ (bottom) for D^0 compared to other particle species [3] in 0-10% central events with m_0 the mass of the particle and $m_T = \sqrt{p_T^2 + m_0^2}$.

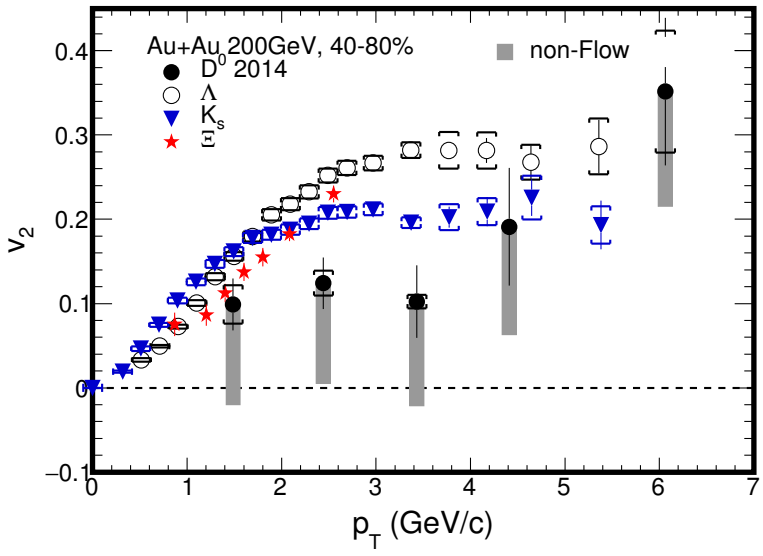


(a)

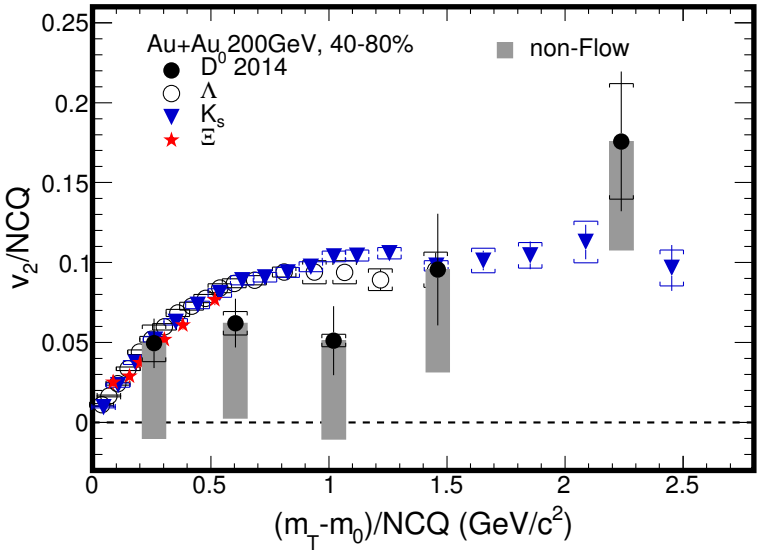


(b)

Figure 6.1.3: v_2 vs p_{T} (top) and v_2/NCQ vs $(m_T - m_0)/NCQ$ (bottom) for D^0 compared to other particle species [3] in 10-40% central events with m_0 the mass of the particle and $m_T = \sqrt{p_T^2 + m_0^2}$.



(a)



(b)

Figure 6.1.4: v_2 vs p_{T} (top) and v_2/NCQ vs $(m_T - m_0)/NCQ$ (bottom) for D^0 compared to other particle species [3] in 40-80% central events with m_0 the mass of the particle and $m_T = \sqrt{p_T^2 + m_0^2}$.

not very informative. However, from the bottom figures in 6.1.2, 6.1.3 and 6.1.4 we can see that all of the particle species, including D^0, follow the same trend. This is a strong indication that charm quarks are flowing with a thermalized medium where the partons are the relevant degrees of freedom.

6.2 Theory Overview

In this section we will briefly discuss the theoretical approaches describing the heavy flavor interaction in the QGP medium. In essence, the objective of the different approaches is to determine the probability that a heavy quark (Q) with initial 4-momentum p_Q^{in} will escape the medium as a heavy flavor hadron (H) with final momentum p_H^{out}, that is $P_{Q\to H}(p_Q^{in}, p_H^{out})$. This problem is often tackled by assuming that the previous probability function can be taken to be a convolution of the probability that a heavy quark will loose $\Delta E = p_Q^{in} - p_Q^{out}$ energy in the medium $P_{Q\to Q'}(p_Q^{in}, p_Q'^{out})$ with the unmodified fragmentation function. Hadronization through recombination as well as other late stage interactions between the heavy hadrons and the partonic/hadronic medium have also been considered in some treatments.

In the ultra-relativistic limit ($p_Q \gg m_Q$), it is generally agreed that the dominant contribution to the in-medium energy loss can be attributed to radiative processes resulting from scattering off of light partons (q). In all treatments of radiative energy loss, this process proceeds through long formation times, and as such several consecutive scatterings contribute coherently and the energy loss must be evaluated at the end of the in medium path length, L, when the heavy quark has exited the QGP. For lower energy quarks, merely in the relativistic scheme ($p_Q <\sim 10 m_Q$) the contribution from collisional energy loss also has an important contribution.

The in medium energy loss is dependent on: the mean free path $\lambda = 1/(\sigma\rho)$ related to the medium's density ρ and the cross section of the parton-medium interaction σ; the Debye mass m_D, the inverse of the screening length of the color electric fields in the medium; and the transport coefficients that describe the momentum transfers with the medium.

In the relativistic scheme, the gluon formation time becomes small enough that the probability for energy loss $P(\Delta E)$ can be obtained as a result of a local transport equation, such as the Boltzman equation, in terms of the local cross sections. This same simplification can be applied in the treatment of collisional energy loss. The transport model can be reduced further in the case where the average momentum transfer is below the quark mass. In this situation the Boltzman equation can be reduced to the Fokker-Plank equation which is often further simplified to the Langevin equation. These equations describe the time evolution of the heavy quark momentum distributions, and the medium properties are encoded in three transport coefficients:

- The drift coefficient η_D, also called drag or friction coefficient, which represents the fractional energy loss per unit time in fluctuation-less medium.
- The longitudinal and transverse diffusion coefficients B_L and B_T encode the increase of the variance of the heavy quark momentum distribution per unit time. For small momentum the diffusion and drift coefficients are related through the Einstein relation $B = m_Q\eta_Q T$.
- The spatial diffusion coefficient D_s represents the spread of the distributions in space-time.

The following sections will describe, in more detail, a particular subset of theoretical

approaches that will ultimately be compared to our experimental results.

6.2.1 Second-order hydrodynamics (CCNU-LBNL)

Relativistic hydrodynamics has been one of the most successful and essential tools in studying the collective phenomena that emerges in Heavy Ion collisions. Good agreement has generally been found between hydrodynamic simulations and data shown both at RHIC and the LHC providing strong evidence for the local equilibration at early times in the evolution of the fireball ($\tau < 1$ fm/c) after which the system evolves in accordance to the laws of viscous hydrodynamics. Furthermore, sensitivity to the initial conditions in the calculations favors a scenario where de-confinement has been achieved when compared to data at RHIC, as is thoroughly discussed in [49].

A picture in which the QGP behaves as a nearly ideal fluid has emerged from ongoing advances in viscous hydrodynamic simulations with a small shear viscosity to entropy ratio (η_ν/s) approaching the quantum limit $1/4\pi$ [59] computed in super-Yang-Mills theory using the conjectured AdS/CFT correspondence.

More recently, there has been important advances in solving relativistic ideal and viscous hydrodynamic equations with both ideal and numerical approaches, for instance an exact solution to the first order viscous hydrodynamic equations (the Navier-Stokes equation) has been found [45]. This solution, however, shows unphysical behavior (such as negative energy densities at early times) exposing the need for more complete solutions. For instance in [67] the ideal 3+1 dimensional hydrodynamic model is extended, in absence of external currents, by solving the equation $\nabla_\mu T^{\mu\nu} = 0$ with

the energy-momentum tensor:

$$T^{\mu\nu} = \epsilon u^{\mu} u^{\nu} - p\Delta^{\mu\nu} + \Pi^{\mu\nu} \tag{6.1}$$

where ϵ is the energy density, p the pressure, u^{μ} is the normalized flow 4-velocity ($u^{\mu}u_{\mu} = 1$), and $\Delta^{\mu\nu} = g^{\mu\nu} - u^{\mu}u^{\nu}$ is the projection operator orthogonal to the flow velocity. The viscous pressure tensor $\pi^{\mu\nu}$ represents the deviation from ideal hydrodynamic picture, and local equilibrium.

The numerical solution to second-order hydrodynamic equations is obtained by solving the the previous equations for $T^{\mu\nu}$ and $\pi^{\mu\nu}$ with the conformal equation of state $\epsilon = 3p$ in Minkoski space-time.

6.2.2 Non-perturbative T-matrix in a parametrized hydrodynamic background (TAMU)

The thermodynamic T-matrix approach has been widely employed in the description of electromagnetic plasmas and nuclear many-body problems. It is a first-principles framework to self-consistently calculate one and two body correlations in a hot and dense medium. In this approach, the main assumption is that a basic two body interaction can be described in terms of a potential $V(t)$ as a function of an approximate momentum transfer $t = q^2 = \vec{q_0}^2 - \vec{q}^2 \sim -\vec{q}^2$. The large mass of heavy quarks($Q = c, b$) implies $\vec{q_0}^2 \simeq (\vec{q}^2/2m_Q)^2 \ll \vec{q}^2$, such that this approximation should hold true for a QGP with temperatures up to two or three times the critical temperature T_c.

The T-matrix approach can be systematically constrained using lattice data and implemented to calculate heavy flavor observables for both open and hidden heavy flavor states in heavy-ion collisions. However, the modification to the potential V due to

interactions with the medium is still an open question. Two limiting cases, employing the heavy quark internal (U) and free (F) energy potentials computed using lQCD have been studied [75]. It was found that the internal energy produces a stronger interaction with the medium and provides a better description for several quantities that can also be computed on the lattice. Furthermore, the resulting quark relaxation rates for both c and b quarks are observed to be enhanced relative to their counterparts obtained in the perturbative regime. This enhancement is predominantly caused by the presence of D/B-meson and di-quark states which emerge as T_c is approached from above. These states naturally provide channels for heavy quark coalescence in the hadronization process, i.e.: the same interactions behind the non-perturbative diffusion are responsible for hadronization. After coalescence into open heavy flavor, the approach can also account for for the diffusion of heavy flavor mesons in the hadronic gas.

This T-matrix approach has been implemented [74, 75] into a 2+1 dimensional hydrodynamic background [56, 71] with some modifications to improve on the description of bulk-hadron observables at RHIC and LHC. First of all the quasi-particle equation of state (EoS) for the QGP is replaced by a lQCD EoS which provides nearly smooth matching to the hadronic-resonance gas. Second, a kick in the transverse momentum of the hadrons is applied on the thermalized distributions to account for a non-trivial flow field, in particular in the directed flow, to better match to experimental data [55]. Finally, the initial energy density profile is chosen in a more compact form resembling the initial states obtained from a saturation picture. The result of all three amendments is a much more violent transverse expansion and an important step in solving the discrepancy between hydrodynamic predictions and the measured

Hanbury-Brown-Twiss (HBT) radii [69].

Heavy flavor diffusion is implemented into the hydrodynamic background through relativistic Langevin simulations of the Fokker-Plank equation and the initial heavy quark momentum distributions are taken from FONLL pQCD calculations which can describe p+p spectra with the correct choice of the fragmentation functions. After diffusion in the QGP, coalescence is modeled using a resonance recombination model (RRM) [73], and the remaining heavy flavor is then hadronized using the unmodified fragmentation functions from p+p. The resulting charm meson distributions are then evolved through the hadronic phase until kinetic freeze-out.

6.2.3 pQCD with viscous hydrodynamics (DUKE)

In the weak coupling approach the interaction of heavy flavor with the medium can be described in terms of uncorrelated scatterings with light quarks and gluons belonging to the de-confined medium. If one neglects radiative processes one can evaluate the heavy flavor transport coefficients that arise form the $2 \rightarrow 2$ elastic scattering processes. The approach, developed in [15, 16], is to simulate the propagation of the heavy quarks in the medium with a relativistic stochastic Langevin equation:

$$\frac{\Delta\vec{p}}{\Delta t} = \eta_D(p)\vec{p} + \vec{\xi}(t) \quad \text{with} \quad \langle \xi^i(t)\xi^j(t)\rangle = b^{ij}(\vec{p})\delta_{tt'}/\Delta t \tag{6.2}$$

where the right side of the equation is given by the sum of the deterministic friction and the stochastic noise, and:

$$b_{ij}(\vec{p}) = B_L(p)\hat{p}^i\hat{p}^j + B_T(p)(\delta^{ij} - \hat{p}^i\hat{p}^j) \tag{6.3}$$

encodes information related to the interaction with the medium in the two transport coefficients $B_{L/T}$ previously discussed. In the DUKE model [35, 34] this Langevin

approach is generalized by including the contribution due to radiative energy loss, and the generalized Langevin equation takes the form:

$$\frac{\Delta\vec{p}}{\Delta t} = \eta_D(p)\vec{p} + \vec{\xi}(t) + \vec{f}_g \tag{6.4}$$

where the last term $\vec{f}_g$ is the recoil force exerted on the heavy quark due to radiative energy loss. In practice, the associated (discretized) recoil momentum $\Delta\vec{p}_g$ is obtained at each time step Δt of the simulations by sampling the radiated gluon spectrum $dN_s/(dxdk_\perp^2 dt)$ according to the probability of radiation. In this treatment the stochastic forces $\vec{\xi}$ are chosen to be auto-correlated in time, i.e. $\langle \xi^i(t)\xi^j(t)\rangle = \kappa\delta^{ij}\delta_{tt'}/\Delta t$ and the value of the diffusion coefficient $(2\pi T)D_s$ is chosen to be around 5-6, consistent with the values extracted by the JET collaboration from experimental data and various jet energy loss models. The gluon radiation term is computed using the pQCD using the higher-twist approach.

The space-time evolution of the medium temperature profile and collective flow profiles are described using (2+1)d viscous hydrodynamics [56, 71] and hadronization is modeled with a hybrid scenario with both fragmentation and recombination processes. Fragmentation is simulated using PYTHIA 6.4 [82] while heavy quark coalescence is treated using the sudden recombination approach developed in [65].

6.2.4 pQCD + HTL in a fluid dynamic medium (SUBATECH)

In the Monte Carlo Boltzman propagation of Heavy Quarks (MC@sHQ) scheme heavy quarks loose and gain energy through interactions with light partons from the thermalized medium according to rates that include the contribution of both elastic and radiative processes. For the collisional energy loss, the elements of the transition matrix are calculated from the pQCD Born approximation, supplemented by a

running coupling constant $\alpha_s(Q^2)$ computed according to the 1-loop renormalisation for $|Q^2| \ll \Lambda^2_{QCD}$ and chosen to saturate at low Q^2 so as to satisfy the universality relation:

$$\alpha_s(Q^2) = \frac{4\pi}{\beta_0} \begin{cases} L_-^{-1} & Q^2 < 0 \\ \frac{1}{2} - \frac{1}{\pi}\arctan(L_+/\pi) & Q^2 > 0 \end{cases} \tag{6.5}$$

where $\beta_0 = 11 - \frac{2}{3}n_f$, $L_\pm = \ln(\pm Q^2/\Lambda^2)$ with $\Lambda = 200$ MeV and $n_f = 3$. Infrared regulation is required for a complete description of the elastic collisions and is achieved by using the the Hard Thermal Loop (HTL) [31] approach to describe the gluon propagators at low Mandelstam t, and the bare propagators for large momentum transfers [43, 44]. The model is simplified further by using an effective scalar propagator $\alpha(t - \kappa m_D^2(T))^{-1}$ for exchanged thermal gluons, where m_D is the Debye mass $m_D^2 = \frac{Nc}{3}\left(1 + \frac{1}{6}n_F\right)4\pi\alpha_s T^2$ and κ is selected such that the calculated energy loss can reproduce the results obtained from Born pQCD calculations.

Radiative energy loss in this model focusses on intermediate energies where the coherence effects have a minimal role. In this approach, the cross section $d\sigma(Qq \to Qqg)$ can be factorized as the product of of the elastic cross section $d\sigma(Qq \to Qq)$ and the conditional probability of radiating a gluon per collision P_g. In practice, the calculation involves explicitly obtaining the collisional energy loss and then sampling the probability distribution P_g as a function of the radiated gluon momentum and its transverse momentum.

More recently, efforts have been made to include the effect of coherent gluon radiation [19] by interpolating between single and multiple scatterings matched to the BDMPS [24] result. This approach neglects the effects of the path-length dependence in thin plasmas, i.e. the "LPM" effect.

The space-time evolution of the medium is done using the EPOS3 event generator based on a 3+1D hydrodynamic starting from flux-tube initial conditions [87].

6.3 Comparison to models

6.3.1 D^0 v_2

One of the main motivations for measuring the charm quark flow is that of constraining the properties of the QGP medium, for instance the transport properties discussed earlier in this section. Figure 6.3.1 shows the comparison to the different models introduced in 6.2.

Two calculations from the TAMU model are included in this comparison, the blue line assuming charm quark diffusion in the medium agrees well with the data while the second calculation without charm diffusion, in magenta, underestimates the measured v_2 at mid p_{T} further supporting the conclusions that charm quarks are experiencing frequent interactions and flowing with the medium. The results from the SUBATECH model can also qualitatively describe the data in the studied p_T range, however the calculation seems to under-predict the magnitude of the observed v_2 in the range $3 < p_{\mathrm{T}} < 4$ GeV/c. The hydrodynamic model presented here has been tuned to describe the v_2 measured for light quarks and describes the data well in the range where the calculations are provided, strengthening the conclusion that charm quarks are fully thermalized with the medium. Finally, the DUKE model shown here has been tuned to describe the measured R_{AA} at LHC energies with a fixed value for the dimensionless diffusion coefficient $(2\pi TD_s) = 7$ and underestimated the magnitude of the observed v_2.

The values of the diffusion coefficient extracted from a series of model calculations

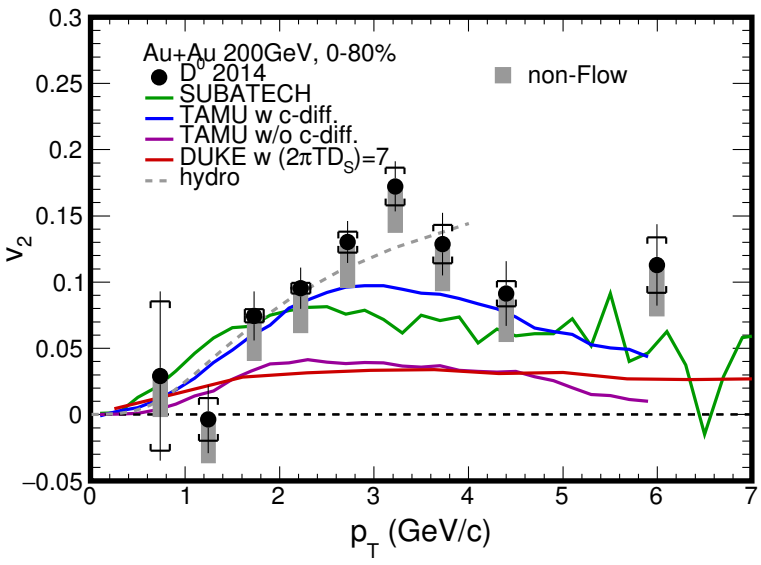


Figure 6.3.1: D^0 v_2 as a function p_{T} in 0-80% central events compared to the different model calculations discussed in section 6.2

are shown in figure 6.3.2 together with the range of values that are compatible with the measured results as shown in 6.3.1. It is interesting to note that the values obtained from lattice calculations [38, 25] are consistent, albeit with large uncertainties, with those obtained from other models shown here and the range inferred from STAR data. However more work will be needed from theory in order to differentiate between the scenarios and further constrain the transport properties of the QGP.

6.3.2 D^0 v_3

Figure 6.3.3 shows the v_3 compared to model calculations from the SUBATECH group in two different centrality bins. The agreement between theory and experiment is very encouraging, indicating that charm quarks are flowing with the system as well as heightening the importance of considering fluctuations in the initial conditions when describing the QGP. Improving on this measurement with a larger data set to study finer centrality classes, as well as comparing to light quarks will be important

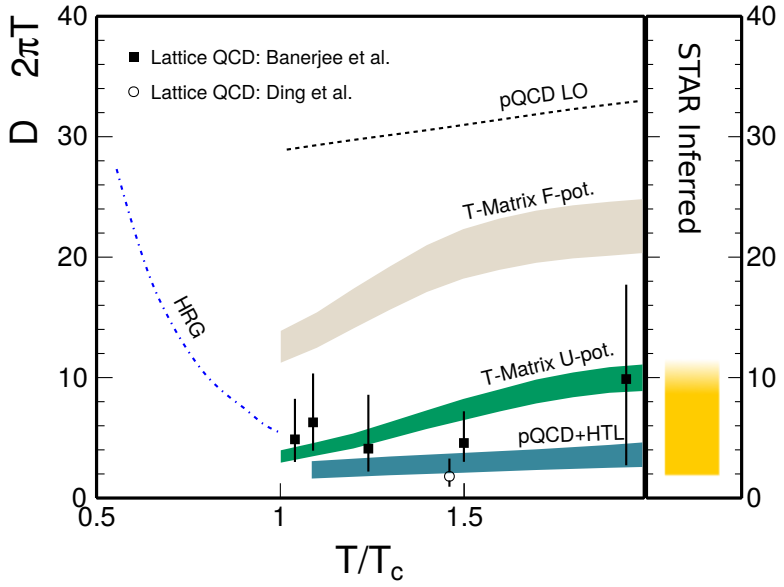


Figure 6.3.2: Diffusion coefficient extracted from a series of model calculations together with the inferred range of compatible values obtained from the comparisons done to the measured result.

in making further conclusions.

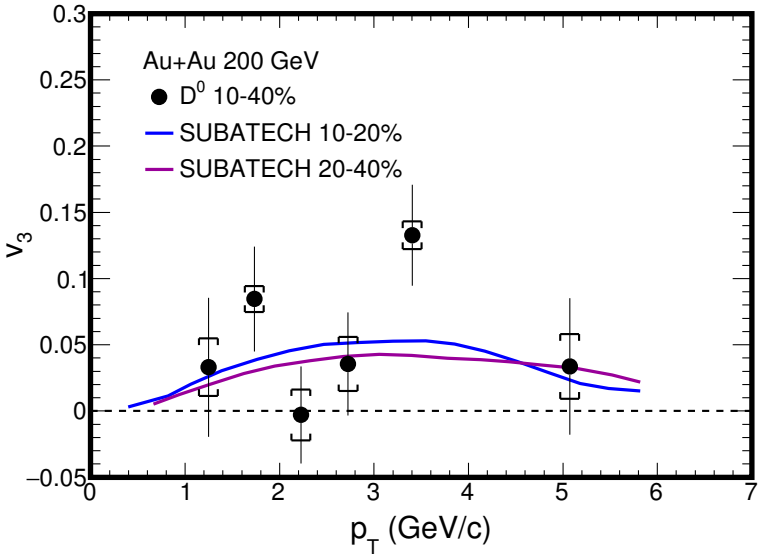


Figure 6.3.3: v_3 vs p_{T} for D^0 in 10-40% central events compared to model calculations in two centralities.

Chapter 7

Summary and outlook

7.1 Summary

With strong evidence for the discovery of the QGP at RHIC, describing its properties is an essential next step in completing our understanding of the behavior of nuclear matter under extreme conditions. Heavy flavor, with its large mass and early production though hard scattering processes, provides a unique opportunity to probe the entire evolution of the fireball created in heavy ion collisions. In particular, by studying the diffusion of heavy flavor in the QGP, one can gather insights about the underlying medium, as was first described by Einstein in 1905 when he analytically solved the problem of Brownian motion.

However, the measurement of open heavy flavor in heavy ion collisions, and in particular at low momenta, is complicated by the busy environment produced in the collisions as well as the short lifetime of these exotic particles. The Heavy Flavor Tracker has proven to be the first successful implementation of a MAPS-based vertex detector at a collider experiment and has provided STAR with the capability to distinguish between particles coming from the primary vertex and those coming from heavy flavor decays, with an impressive single track pointing resolution below 50 μm for 750 MeV/c kaons.

Employing the HFT and fully incorporating the detector into the STAR experiment was not without its challenges as the very precision of the detector sets much stricter

requirements on the calibrations and alignment in order to fully exploit the capabilities. I have presented a series of tests using full GEANT simulations showing the depth of our understanding of the detector's performance. The success of HFT is an important motivation for future upgrades in other experiments that will employ similar technology with similar goals, such as the Inner Tracker System (ITS) for the ALICE experiment and the tracking system for the planned sPHENIX experiment to be built at RHIC.

In this dissertation analysis, I have shown one of the first measurements of open heavy flavor through direct topological reconstruction in the hadronic decay channels using the capabilities provided by the HFT at STAR. A dramatic reduction in the combinatorial background is achieved with the HFT. In consequence we observe an improvement of over an order of magnitude in the D^0 significance per billion events when compared to previously published results from STAR, permitting the measurement of charm observables with unprecedented precision. Using 75% of the dataset obtained in the detector's first year of running (2014) I have shown the first measurement of charm quark elliptic flow in Au+Au at top RHIC energy in 0-80%, 0-10%, 10-40% and 40-80% central events. The observed v_2 is found to be non-zero, indicating that charm quarks are in fact taking part in the collective expansion of the produced QGP medium. The elliptic flow was then compared to previously published results for a series of light hadrons (K_s, Ω, Λ, Ξ and ϕ) at the same energy. Though charm v_2 appears to be systematically below that of light hadrons, it appears to follow the same trend in 0-10% and 10-40% central events once the mass of the particles and number of constituent quarks are taken into account. This NCQ scaling is a strong indication that charm is indeed fully thermalized with the medium, a conclusion that

is further supported by the agreement with hydrodynamic calculations tuned to describe the v_2 of light hadrons.

Comparison to different model calculations has also been presented, showing that various models are able to simultaneously describe a series of observables measured by experiments. The agreement in these comparisons was used to infer a range of compatible values for the diffusion coefficient, an important transport parameter that can be used to describe the dynamics of the QGP.

The first measurement of charm quark triangular flow (v_3) has also been presented in this dissertation. As was the case for v_2, the results for v_3 obtained in 0-80% and 10-40% central events are found to be non-zero, indicating the importance of considering fluctuations in the initial conditions of the colliding nuclei. Comparison to a transport model assuming the presence of these fluctuations as well as frequent interactions with the medium show good agreement in the p_{T} range, strengthening our understanding of the dynamics at play.

7.2 Outlook

At the time of writing this dissertation, the HFT has been removed from STAR in order to prepare for a second phase of Beam Energy Scan (BES-II). Nonetheless, the HFT has accumulated a significant data set that will further improve the results shown here, with a total of roughly 4-5 times more Au+Au minimum bias collisions (relative to the results presented here) will be available with the combined 2014 and 2016 datasets. Furthermore, in 2016 the ladders on the inner layer of the PIXEL detector have been replaced with upgraded ladders using aluminum cables to reduce the material budget and improve the HFT's performance at low p_{T}. This will, in essence, translate to a further factor 2-3 improvement in the measured significance

for measured D^0 and, hence, the statistical uncertainties presented in these analysis. Precision measurements with the combined HFT data sets will have an important role in deepening our understanding of the dynamics at play by placing strong constraints on the available model calculations as well as opening the doors for many other heavy flavor measurements that will help to complete the picture that is already beginning to form. For instance, the observation of fully thermalized charm quarks at RHIC top energy now brings into question the degree to which bottom quarks, with a mass roughly 4 times that of charm quarks, are interacting with the QGP. Although bottom production is much lower at RHIC, the large datasets with the HFT could provide sufficient to obtain such measurements.

What is more, the heavy flavor program is only one part of the STAR physics program. In the upcoming years, the RHIC facility will undergo important upgrades to increase the luminosity at lower BES-II energies. Similarly, the STAR experiment has also planned upgrades to achieve the physics goals of the program. By far the largest planned upgrade, the inner TPC (iTPC) will strengthen the experiment's tracking at low p_{T}, improve the particle identification and increase the experiment's acceptance. A forward Time of Flight will also be installed to improve the particle identification in the forward direction and, finally, an Event Plane Detector (EPD) has been planned to provide an independent measure of the collisions centrality and the event plane angle itself. Appendix C covers some of the details of my own work in constructing and installing the prototype Event Plane Detector tested in STAR 2016.

In closing, this dissertation has covered details on the calibration and characterization of the HFT as well as one of the flagship measurements for which it has been built. The results shown are an important step towards understanding the properties and

dynamics of the medium created in heavy ion collisions with unprecedented precision placing strong constraint on theory to further drive our understanding of nuclear matter.

Appendices

Appendix A

PXL Detector masking

Calibration of the PXL detector, the innermost two layers of the HFT upgrade for the STAR experiment, is essential to assure the quality of data as well as to improve its performance. Among the many activities that fall within this broad set of activities it is necessary to characterize the performance of the individual sensors as well as flag and remove channels that are underperforming or overly active.
To this end, masking software was implemented and tested throughout run 14. In this document we will discuss the final version of the masking software as well as some studies on the performance of the algorithms.

A.1 Introduction

The PXL detector is a low mass detector designed with the goal of delivering high-precision heavy flavor measurements over a broad p_T range. It consists of 2 tracking layers located very close to the beam (r=2.9 and 8cm) with a total of 400 MAPS (Monolithic Active Pixel Sensors) silicon pixel sensors developed by the IPHC group at Strasbourg.
The use of MAPS sensors permitted satisfying important design requirements:

- They can be thinned (50μm) to reduce multiple Coulomb scattering.
- Both amplifier and capacitor storage for Correlated Double Sampling (CDS) on each pixel, allowing use of a single on-chip discriminator at the end of each

column to record hits and eliminate the need of for an additional silicon read out layer.

- They are relatively low power, allowing for air cooling of the system to further reduce the radiation length of the detector.
- The sensors have a a high radiation tolerance, necessary to survive in the extreme environment.

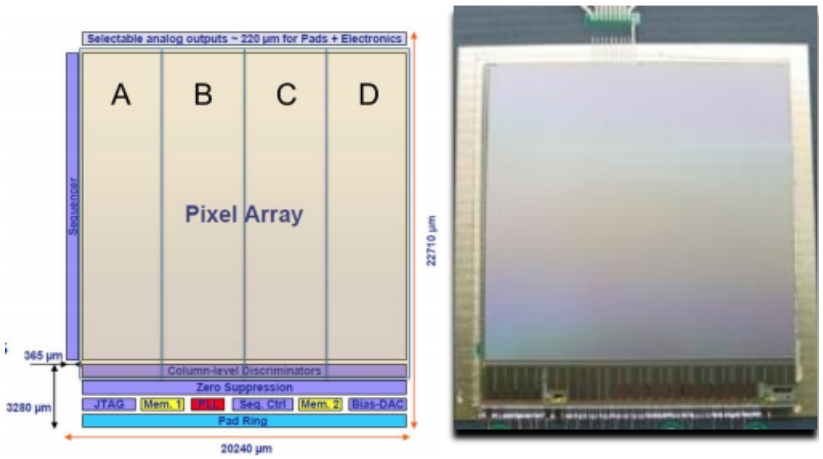


Figure A.1.1: Schematic showing pixel sensor layout

Rolling shutter readout involves sequencing through the rows of a given sensor. Once a row is selected, the pixels are connected to their columns and the discriminator at the end of the column identifies whether or not the pixel contained a hit before moving ahead to the next row. Hits are recorded for particles that pass through the sensors between interrogations.

The readout time for the 400 sensors used on PXL is 186 μs and they are arranged in 40 ladders (30 in the outer layer and 10 in the inner) providing full azimuthal coverage for $|\eta| < 1$. Each of the sensors contains 960 columns and 928 rows of square pixels

measuring 20μm $\times$ 20μm and is further subdivided into 4 subarrays of 240 columns with shared thresholds characterizing the noise. Taking into account that there are small variations in the performance of individual pixels or entire columns and rows is an essential step in calibrating the detector for optimal response.

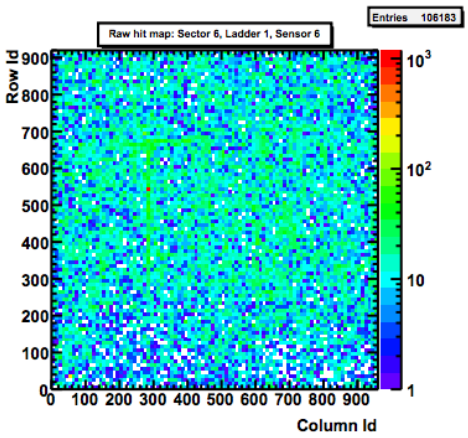
Figure A.1.2 shows the raw hit map (obtained from commissioning QA plots during year 2014) for three sensors requiring masking of individual pixels (a), columns (b) or rows (c), illustrating the need to mask these three distinct contributions. These features might be permanent defects or might be due to a single event upset that can later be remedied by restarting the detector.

Using information from the PXL detector raw hit maps, the offline masking procedure was implemented at three distinct levels: flagging individual pixels, flagging entire rows/columns, and characterizing the performance of each of the 400 sensors and is intended to be implemented on a run by run basis, producing three sets of tables for each.

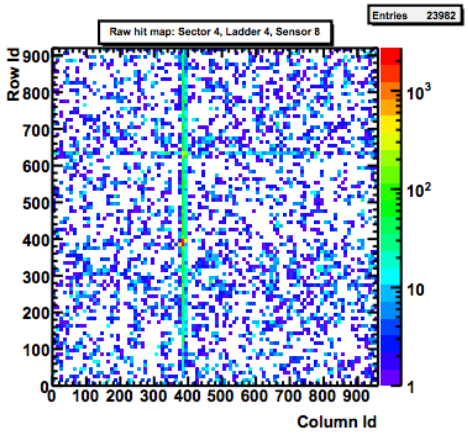
Furthermore, given the very distinct running conditions that exist during physics running and cosmic ray data taking, the algorithm was optimized for these two situations and the sets of cuts used to define the hot channels and sensor status were refined using data taken during year 2014. The following sections will detail the different criteria that were established for both.

A.2 Physics Data Masking

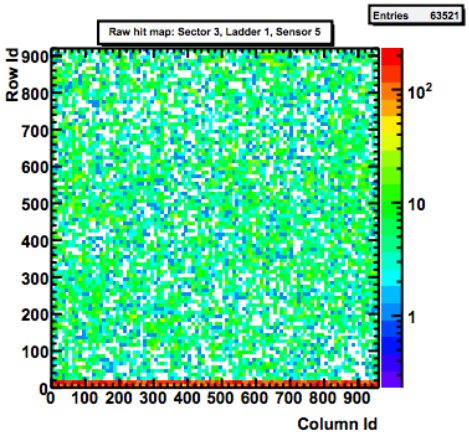
The following section will document the definitions and criteria used in masking during regular physics running. These quantities were refined throughout 2014 running period using mid to low luminosity gold gold collisions at 200GeV.



(a) PXL sensor with single bad pixel near (row,column) = (540,280)



(b) PXL sensor with an array of bad columns



(c) PXL sensors with single bad row

Figure A.1.2: Example of faulty sensors from run Au+Au Low luminosity run 15077043

When applicable, the name of the constants, defined in StPxlMaskConstants.h (see section 5), have been included to clarify their usage in the masking procedure.

A.2.1 Definitions and criteria

Hot Pixels

- Pixel content per event is greater than 0.1

$$\frac{\text{Pixel content}}{\text{No. Events}} \quad > \quad 0.1 = \text{hPix}$$

Bad Columns

After masking individual pixels, the following criteria are used to flag either hot or missing columns as a whole:

- Column contains more than 200 hot pixels ($\sim 20\%$ of column)

- Column content is roughly 100 times greater than average column content in sensor:

$$\text{Col. content} \quad > \quad 100 \times \frac{\text{Sensor entries}}{1000} = \frac{\text{Sensor entries}}{10} = \frac{\text{Sensor entries}}{\text{hCol}}$$

- In order to account for changes in luminosity throughout each fill of the RHIC rings, the following criteria were established with respect to the average over the whole detector. Furthermore, two separate averages are used for inner and outer layers, given that the likelihood of a track crossing a sensor in the outer layer of PXL is roughly a third (not accounting for ghosting or pileup) of the probability of it crossing a given sensor on the inner layer (there are three times as many sensors on the outer layer compared to the inner). A column is flagged as hot if the content is 10 times greater than the average in that layer (dead

sensors were ignored):

$$\begin{aligned} \text{Col. Content} &> 10 \times \text{sAverage}_{1,2} \\ \text{sAverage}_{1,2} &= \sum_{\text{layer}=1,2} \frac{\text{Sensor entries}}{960 \times (\text{No. sensors in layer})} \end{aligned}$$

- In order to study the efficiency of sensors, missing or low efficiency columns were also flagged. Only blocks with at least 50 consecutive missing columns were flagged and a single column is considered missing if its content is less than 10 times the average column content in the sensor after masking individual sensors and rows (hot columns are ignored for obvious reasons):

$$\text{Col. content} \leq \frac{1}{10} \times \frac{\text{Sensor entries (after mask)}}{960}$$

Bad Rows

After masking individual pixels and entire columns, the following criteria are used to flag hot rows:

- Row content is roughly 100 times greater than average column content in sensor:

$$\text{Row content} > 100 \times \frac{\text{Sensor entries}}{1000} = \frac{\text{Sensor entries}}{10} = \frac{\text{Sensor entries}}{\text{hRow}}$$

- In order to account for changes in luminosity throughout each fill of the RHIC rings, the following criteria were established with respect to the average over the whole detector. Furthermore, two separate averages were used for inner and outer layers given that the likelihood of a track crossing a sensor in the outer layer of PXL is roughly a third(not accounting for ghosting or pileup) of the probability of it crossing a given sensor on the inner layer (there are three times as many sensors on the outer layer compared to the inner). A row is flagged as

hot if the content is 10 times greater than the average in that layer(dead sensors were ignored):

$$\begin{aligned} \text{Row. Content} &> 10 \times \text{sAverage}_{1,2} \\ \text{sAverage}_{1,2} &= \sum_{\text{layer}=1,2} \frac{\text{Sensor entries}}{928 \times (\text{No. sensors in layer})} \end{aligned}$$

Sensor Status

Once masking is performed for individual pixels and entire columns/rows, each sensor is classified according with the area of the sensor that was hot/missing. A status between 1 and 10 are used for sensors of varying quality that are to be included in reconstruction while a status above 10 denotes sensors that are rejected for one reason or another. The classification scheme is as follows:

- Good sensor (Flag 1 or status G):

$$0 < \text{No. of hot columns and rows} < 5 \ (\sim 0.5\% \text{ of sensor})$$

- Good but hot sensor (Flag 2 or status H):

$$5 < \text{No. of hot columns and rows} < 50 \ (\sim 5\% \text{ of sensor})$$

- Non-uniform sensor (Flag 3 or status U):

$$50 < \text{No. of hot columns and rows} < 720 \ (\sim 75\% \text{ of sensor})$$

- Low efficiency sensor (Flag 11 or status L):

  After masking hot col/rows, the number of entries per event for the sensor is very low (less than 1). In other words:

$$\frac{\text{No. entries (after masking)}}{\text{No. events}} < 1 \tag{A.1}$$

- Bad sensor (Flag 12 or status B):

  1. The number of entries per event is very high after masking:

$$\frac{\text{No. entries (after masking)}}{\text{No. events}} > 1000$$

  2. Roughly 3/4 of sensor masked out:

$$\text{No. of hot columns and rows} > 720 \ (\sim 75\% \text{ of sensor})$$

- Dead sensor (Flag 0 or status D):

  Sensor on active sector with no hits.

A.2.2 Performance

Masking tables for the Au+Au collisions obtained during the 2014 running period were produced on a run by run basis using the raw hit maps produced from a subsample of the collected events, and the output tables have been uploaded to STAR database. The cuts mentioned in the previous section were all refined for use with gold gold collisions and take into account the luminosity changes that occur during a fill. Figure A.2.1 shows the raw hit map for two sensors showing a cluster of hot pixels on the left and an array of hot columns on the right. The same sensors can be seen in A.2.2 after masking is applied. The distribution of raw hits is visibly more homogeneous and the scale is no longer dominated by the contributions of these hot channels. Figure A.2.3a shows the number of masked columns and rows for the whole PXL detector for all runs obtained using set of fixed cuts (details can be found in: [60]). A sizable variation was found in the number of flagged columns within individual RHIC fills, suggesting the importance of taking into account the luminosity in individual runs. These variations are undesirable given that they make estimation

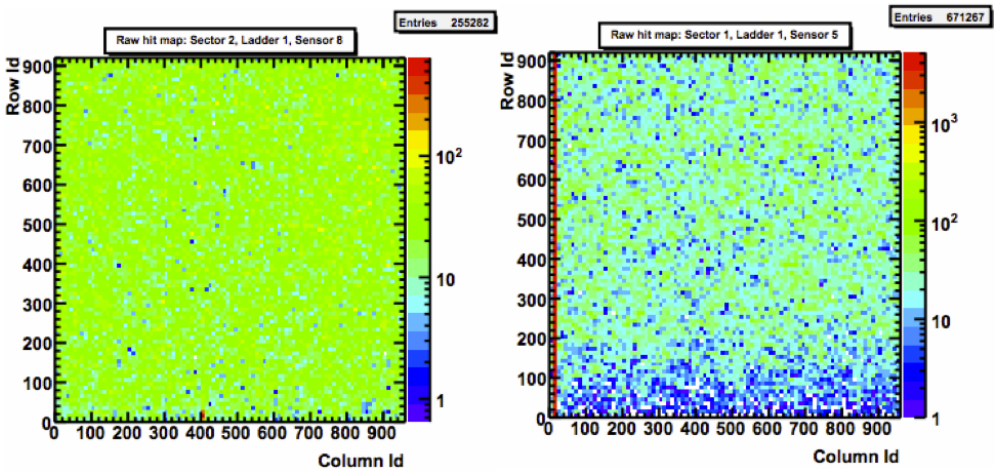


Figure A.2.1: Sample raw hit map for two unmasked sensors

of the detector's efficiency complicated.

Figure A.2.3b shows the number of flagged columns and rows obtained using the criteria reported in the previous section and show considerable improvement, although some outliers remain. However we can note that a change in around 400 flagged columns only represents ∼0.1% of the detector. The number of hot pixels per run is shown in figure A.2.3.

A.3 Cosmic Data Masking

When collecting cosmic data, it is important to note that the signal to noise ratio is greatly reduced given that a single event should record between 4 and 6 hits for particles that cross the entirety of the PXL detector. Unlike the case of Au-Au physics running, there is no substantial difference in the behavior of inner and outer ladders of PXL and so the criteria do not differentiate between these.

When applicable, the name of the constants, defined in StPxlMaskConstants.h (see section 5), have been included to clarify their usage in the masking procedure.

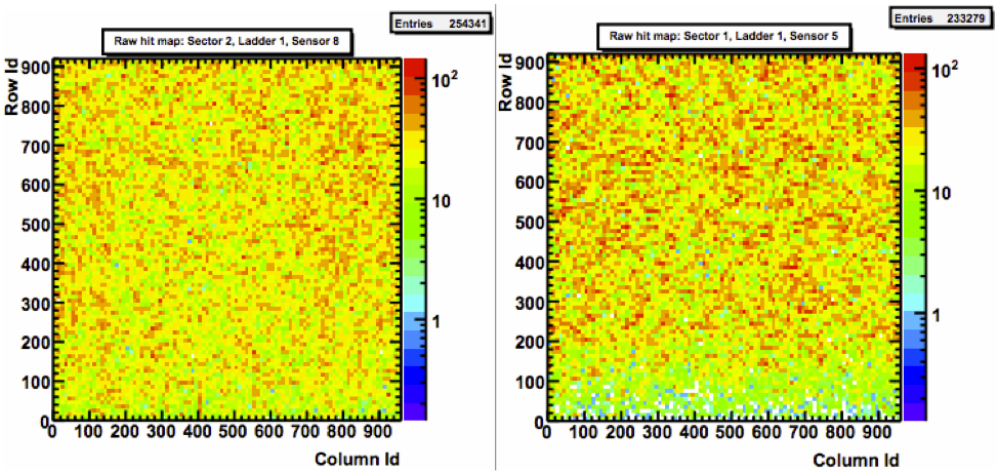


Figure A.2.2: Sample raw hit map for two sensors after masking

Hot Pixels

- Pixel content per event is greater than 0.05

$$\frac{\text{Pixel content}}{\text{No. Events}} > 0.05 = \text{cosmichPix}$$

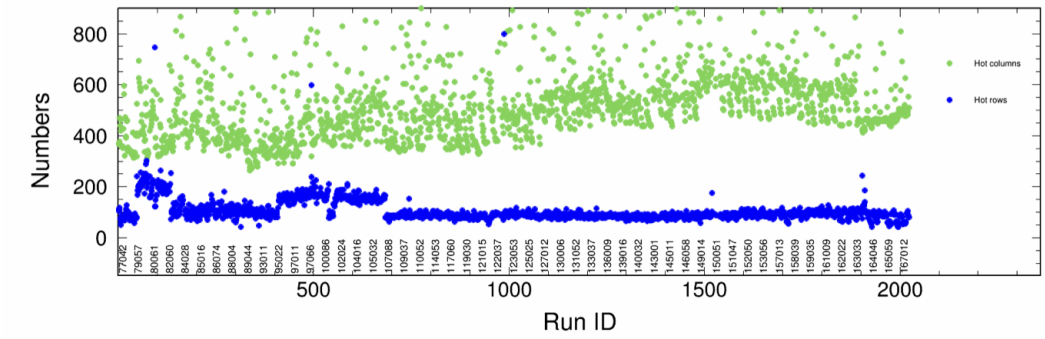
Bad Columns

After masking individual pixels, the following criteria are used to flag either hot or missing columns as a whole:

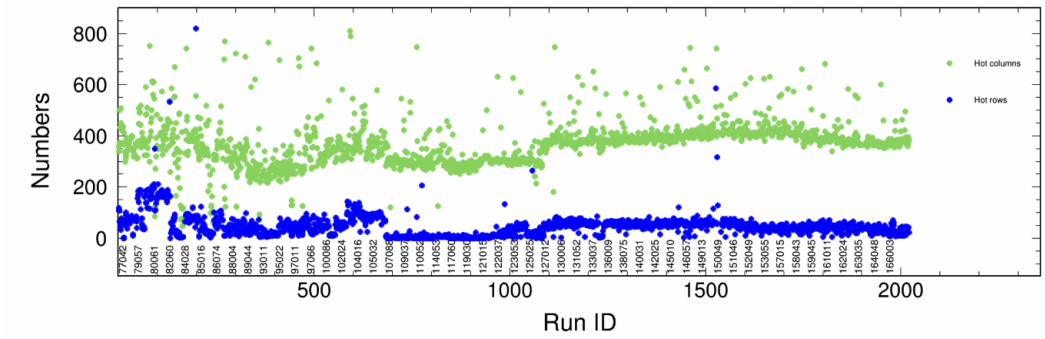
- Column contains more than 200 hot pixels ($\sim 20\%$ of column)
- Column content is roughly 100 times greater than average column content in sensor:

$$\text{Col. content} > 100 \times \frac{\text{Sensor entries}}{1000} = \frac{\text{Sensor entries}}{10} = \frac{\text{Sensor entries}}{\text{hCol}}$$

- Column content is 1000 times greater than expected hits in column. Assuming each cosmic ray crosses entirety of PXL, it should produce 4 hits in the detector.



(a) Number of hot and missing rows and columns for all Au-Au runs obtained during year 2014 using fixed cuts



(b) Number of hot and missing rows and columns for all Au-Au runs obtained during year 2014 using luminosity dependent cut

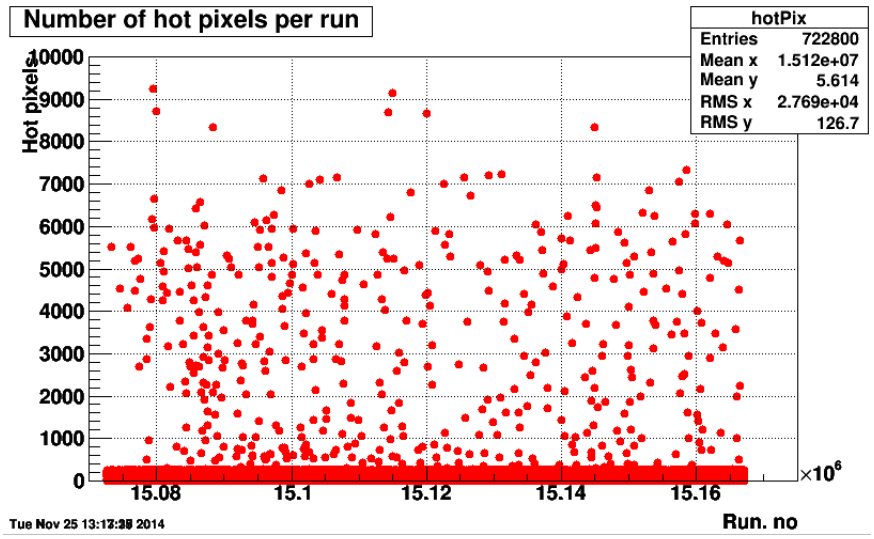


Figure A.2.3: Number of hot pixels for all Au-Au runs obtained during year 2014.

Thus the likelihood of getting a hit in a given sensor is $\sim 1/100$, and since each sensor has 960 columns, then the likelihood of a hit in a given column is $\sim 1/(100 \times 960)$, hence:

$$\frac{\text{Col. content}}{\text{No. events}} > 1000 \times \left(\frac{1}{100} \times \frac{1}{960}\right) = \frac{1}{96}$$

Bad Rows

After masking individual pixels and entire columns, the following criteria are used to flag hot rows:

- Row content is roughly 100 times greater than average column content in sensor:

$$\text{Row content} \quad > \quad 100 \times \frac{\text{Sensor entries}}{1000} = \frac{\text{Sensor entries}}{10} = \frac{\text{Sensor entries}}{\text{hRow}}$$

Sensor Status

Once masking of individual pixels and entire columns/rows, each sensor is classified according with the area of the sensor that was hot/missing. A status between 1

and 10 are used for sensors of varying quality that are to be included in reconstruction while a status above 10 denotes sensors that are rejected for one reason or another. The classification scheme is as follows:

- Good sensor (Flag 1 or status G):

$$0 \ < \text{No. of hot columns and rows} < \ 5 \ (\sim 0.5\% \text{ of sensor})$$

- Good but hot sensor (Flag 2 or status H):

$$5 \ < \text{No. of hot columns and rows} < \ 50 \ (\sim 5\% \text{ of sensor})$$

- Non-uniform sensor (Flag 3 or status U):

$$50 \ < \text{No. of hot columns and rows} < \ 500 \ (\sim 50\% \text{ of sensor})$$

- Low efficiency sensor (Flag 11 or status L):

  After masking hot col/rows, the number of entries per event for the sensor is very low (less than 1). In other words:

$$\frac{\text{No. entries (after masking)}}{\text{No. events}} \ < \ 1 \tag{A.2}$$

- Bad sensor (Flag 12 or status B):

  1. The number of entries per event is very high after masking:

$$\frac{\text{No. entries (after masking)}}{\text{No. events}} \ > \ 1000$$

  2. Roughly half of sensor masked out:

$$\text{No. of hot columns and rows} \ > \ 500 \ (\sim 50\% \text{ of sensor})$$

3. After masking sensor entries are ten times greater than average

$$\text{No. entries (after masking)} > 10 \times \text{Avg.} \tag{A.3}$$

where:

$$\text{Avg.} \quad = \quad \sum_{i=1}^{400} \text{Entries}_i$$

- Dead sensor (Flag 0 or status D):

  Sensor on active sector with no hits.

A.3.1 Performance and results

In order to study the performance of the masking procedure, this section shows a comparison between masked and raw PXL hit distributions obtained from cosmic runs obtained during year 2014. The majority of the plots are obtained from offline PXL monitor maker developed by Dr. Shusu Shi and available online in:
http://portal.nersc.gov/project/star/sss/protected/Run14QA/.
The masking procedure acts directly on the PXL raw hit map output by the monitor maker. Figure A.3.1 we can see the raw hit map, projections onto x and y axis as well as the raw hits as a function of event id for a single sensor of PXL. This sensor displays a cluster of hot pixels as well as an array of overly active columns.
Figure A.3.2 displays the same sensor after masking is applied, looking at the raw hit maps as well as the projections onto columns and rows. Figures A.3.3 and A.3.4 show the number of raw hits per subarray for sensors on sector 4 of PXL before and after the masking, respectively. Drawing your attention to rows around 70-100 in particular, the distribution of raw hits after masking is much more uniform, Figure

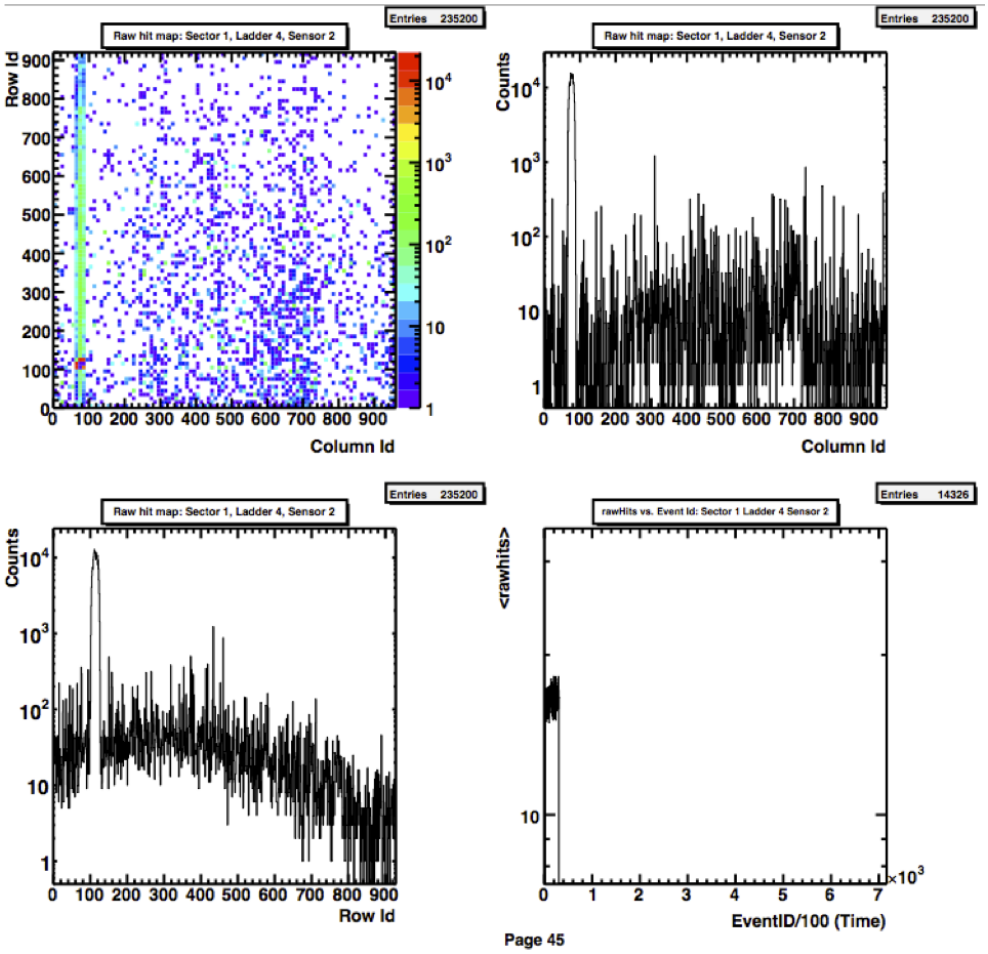


Figure A.3.1: Raw PXL hit distribution Sector 1 Ladder 4 Sensor 2, run 15050257

A.3.5 shows the number of raw hits per sensor normalized by the number of events for all cosmic runs obtained during the year 2014 running period. As we can see, the overall behavior of sensors after the masking is quite stable with an average of 0.6-0.7 hits per sensor per event. Although an order of magnitude greater than expected for perfect sensors (cosmic rays that cross the whole of pixel PXL should result in 4-6 hits and so the number of hits per sensor should be roughly 1/100-1.5/100) this is reasonable enough to obtain good association between the hits and tracks from TPC,

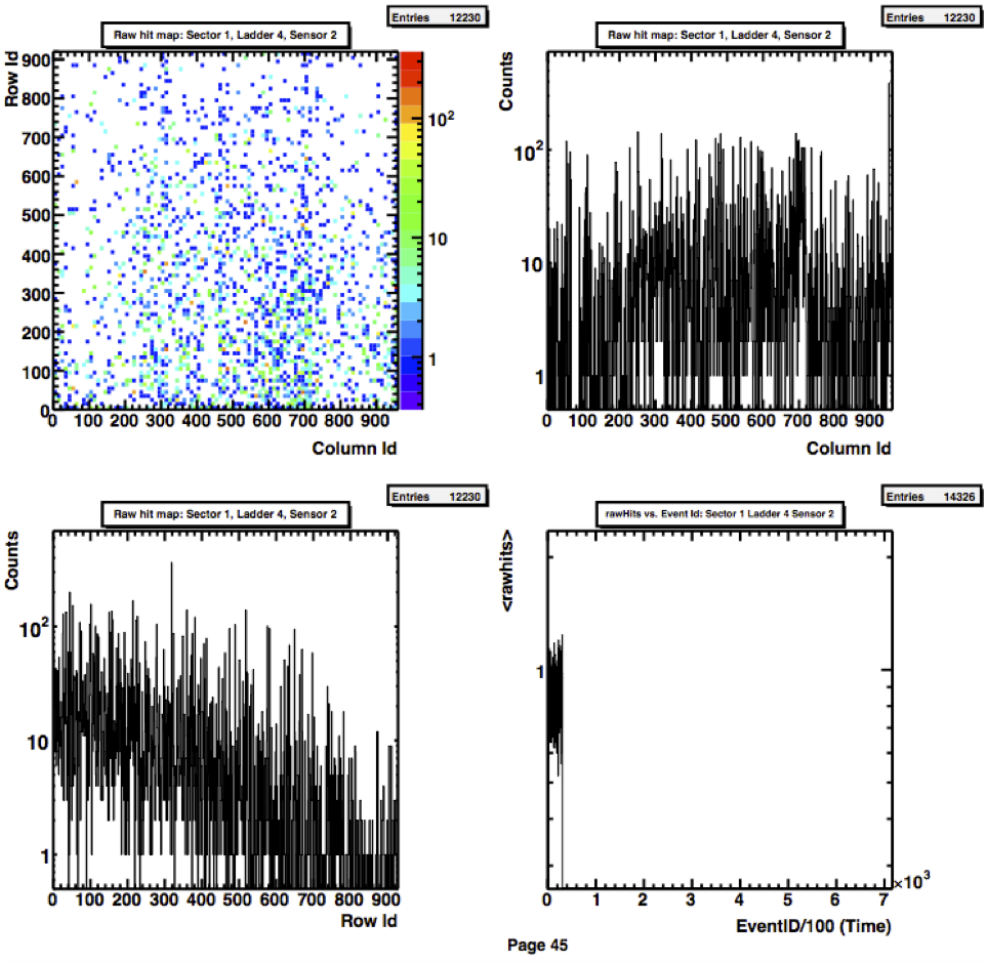


Figure A.3.2: Masked PXL hit distribution Sector 1 Ladder 4 Sensor 2, run 15050257

and further improvement is expected if IST and SST hits are also in tracking.

The peak in the number of hits per event found around days 80-100 has been investigated and is due to a couple of very "hot" sensors such that the established cuts for hot rows or columns are not satisfied. Figure A.3.6 compares one of the misbehaving sensors with another, on the same ladder. This motivated the introduction of a cut to remove these sensors as was discussed in the previous section.

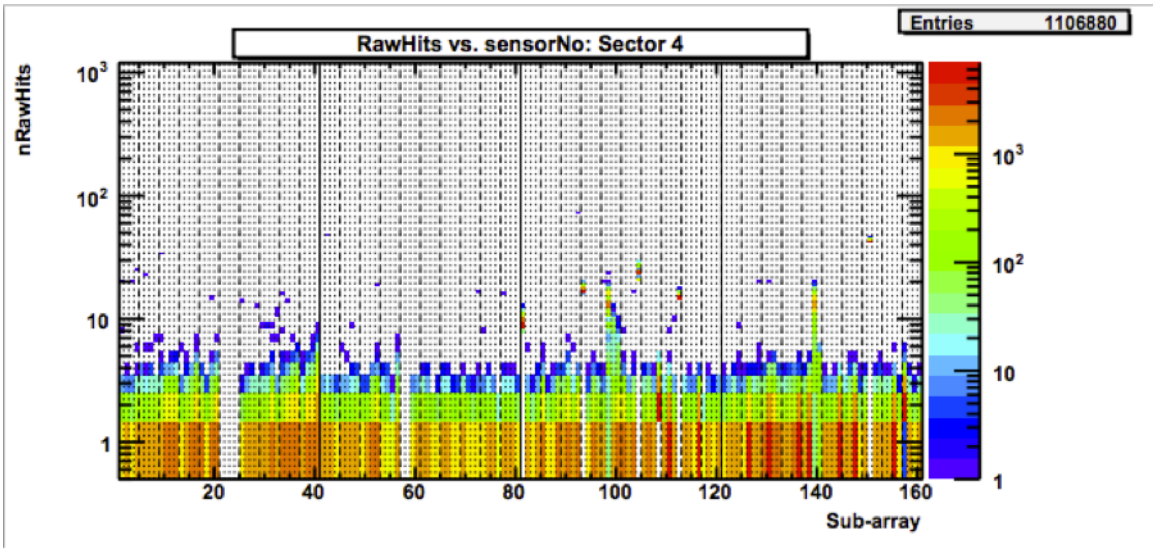


Figure A.3.3: PXL Hits per subarray Sector 4 run 15050257

A.4 Table structure

The information encoded in each of the tables is as follows:

PXL Sensor status

This table assigns a status for each of the 400 sensors in PXL. A status between 1 and 10 is assigned to sensors that are considered to be good and hence should be included in the reconstruction. Values above 10 are assigned to sensors that, for one reason or another, are considered bad and should not be included. The specific criteria used to assign the status to each sensor will be discussed in later sections detailing the definitions in cosmic and physics running.

The coding structure in the sensor status tables is as follows:

$$\text{row.status[sensorId]} \quad = \quad \text{status}$$

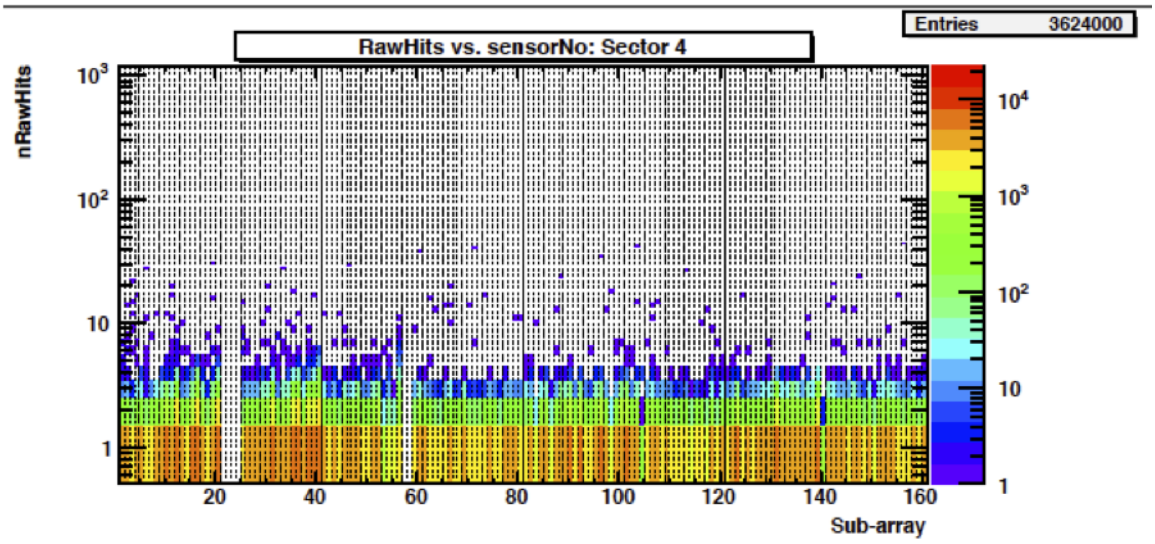


Figure A.3.4: Masked PXL hits per subarray Sector 4 run 15050257

PXL Bad Rows/Columns

This table lists the rows and columns that are flagged as either hot, which should be masked out when reconstructing, or missing. After studying the number of flagged columns and rows, and taking into account memory constraints, a maximum of 10 thousand entries (for the whole detector) are permitted in the table. Only entries from sensors that are considered good are included in this table, since data from sensors with status greater than 10 will be eliminated from the reconstruction.

Furthermore, in the case that more than 10,000 rows and columns are flagged, the sensors are ordered according to the number of hot/missing columns and rows (from most to least) and the table is filled until the cap is reached.

The entries in this table follow the next coding convention:

$$\begin{aligned} \text{row.badRowColumns[entry]} &= 100 \times (10^6 \times \text{isRow} + 10^3 \times \text{sensorId} \\ &\quad + \text{row/column id}) + \text{status} \end{aligned}$$

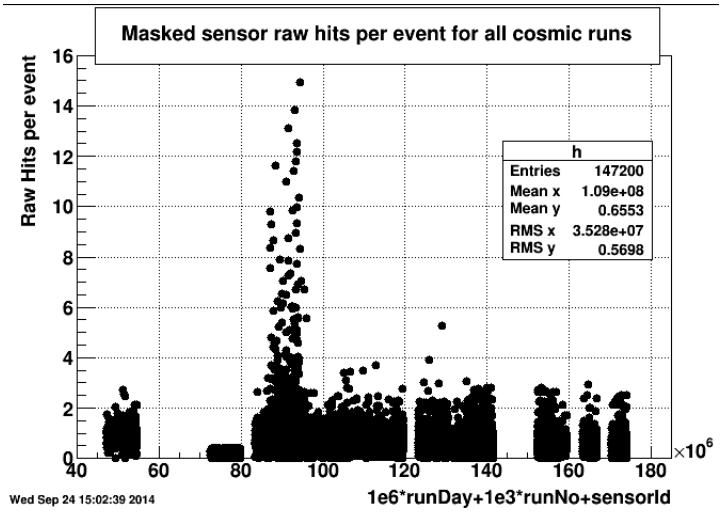
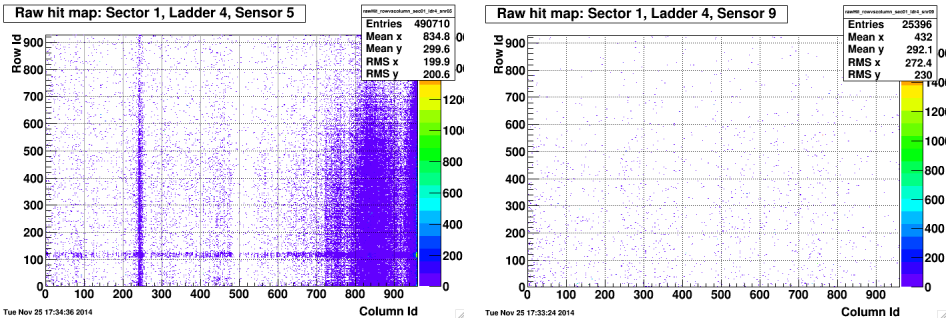


Figure A.3.5: Raw hits per event for all sensors and all runs

isRow can take values 0 or 1 for columns and rows respectively, while status may take values 0 and 2 for rows/columns that are flagged as missing or hot.

PXL Hot pixels

This table encodes the address of individual pixels that are flagged as overly active for the whole detector. Only hot pixels that do not belong to bad sensors or



(a) Sensor with excessive no. of hits per event from day 92 run 71

(b) Sensor displaying expected hit map from day 92, run 71

Figure A.3.6: Comparison between hot and good sensor from run 15092071

bad rows/columns are included in this table and, again, due to memory restrictions, a maximum of 10,000 entries are permitted. As with the bad row/column table, in the case that more than 10k pixels are flagged as hot, the sensors are ordered according to the number of flagged pixels (most to least) and the table is filled until the cap is reached. The coding convention for the pixel address in the table is as follows:

$$\text{row.hotPixel[entry]} \quad = \quad 10^6 \times \text{sensorId} + 10^3 \times \text{row} + \text{column}$$

A.5 Package contents and read me

The directory /star/u/sss/lbl_prod/Cosmic_Data contains the code and scripts to run the StPxlMonMaker. It will generate *.pxlMon.root used as input for the StPxlMaskMaker.

StPxlMonMaker

- The bfc chain options are:

  root4star -b -q 'bfc.C(fistevent,lastevent,"in,pxlRaw,pxlDb,
  event,pxlMon","daqfilename"")'

  The input data file should be STAR daq file.

- For submitting batch jobs, one should use 'submit_runlist.sh'. 'submit_runlist.sh' will submit all batch jobs (run by run) according to the run list stored in 'list_runid'. The directory of the daq files should be specified in file named 'QAroot_generate.sh'.

The directory contains the code and scripts necessary to run the masking code. In order to run and copy the contents of the directory and compile in DEV. The following is a brief description of package contents.

Scripts

- Mask.sh: Script used to mask file. Tables for local masking will be output to "Tables/" directory, write files for online Db will be output to directory "officialDb" and root files used for status tables and other performance checks are output to "run_rootfiles/". Summary.txt files used to compare masking performance are placed in this same directory. Script requires three arguments to run:

  1. File to mask e.g. 15016001 for year 14 day 16 run 1.
  2. Timestamp assigned to beginning of run, this is needed so bcc knows which masking table to pick up. Convention is yyyymmdd.hhmmss e.g. 20140220.120912 codes for Feb 20th 2014 start time 12:09:12.
  3. Running mode: physics or cosmic. By default masking will run in physics mode

- submit_runlist.sh and runAll.sh scripts can be used to submit large batch of jobs. To run you must place a file in directory with list of runs you wish to mask. Each line of the list of runs to mask in the file must have following structure:

  runNo timestamp

  Change line 2 in submit_runlist.sh to indicate which list to use to submit jobs and submit using: csh submit_runlist.sh

- run.con is a template to submit jobs to condor. Replace the contents of line

following Initialdir to your own.

/StRoot/StPxlMaskMaker/:

- StPxlSensor class definition and functions.
- StPxlRun class definitions and functions.
- StPxlMaskConstants.h Contains definitions for necessary constants used during masking procedure:
    1. colMax and rowMax: Define sensors dimensions.
    2. hPix and cosmichPix: Cut used to define hot pixels in physics and cosmic modes respectively.
    3. maxPix: Maximum got pixels allowed in a column.
    4. hRow and hCol: Define cuts used for hot rows and columns respectively.
    5. cosmicAverage: Cut used to define hot columns in terms of average expected hits per event.
    6. cosmicNoRow: Sets average expected this per row in cosmic running to 1000 in order to ignore test that is only used in physics running
    7. mCol: Used for missing column criteria in physics mode.
    8. block: Minimum block size for missing columns.
    9. fileloc: Path to directory where input pxlMon files are located.
- StPxlMasMaker: Masking algorithm, inherits StPxlSensor and StPxlRun classes as well as constant from StPxlMaskCosntants

- MaskFiles.C: Used to load libraries and run masking. Needs three variables as input: run to mask, timestamp for output tables and running mode (either cosmic or physics). This can be called by using Mask.sh script.

/run_rootfiles/

Root files for plots are placed in this directory. Also contains:

- makePlots.C and plotMacro.C: Read ana_runno.root files and produces sensor status and masking summary plots, outputs pdf and root file version to " /run_rootfiles/StatusPlots/" directory (ana.root files can be merged to create one pdf file for all). To run simply "root -b -q 'makePlots.C("filename")'.

In order to run first copy the contents of StRoot to local directory and compile using cons.

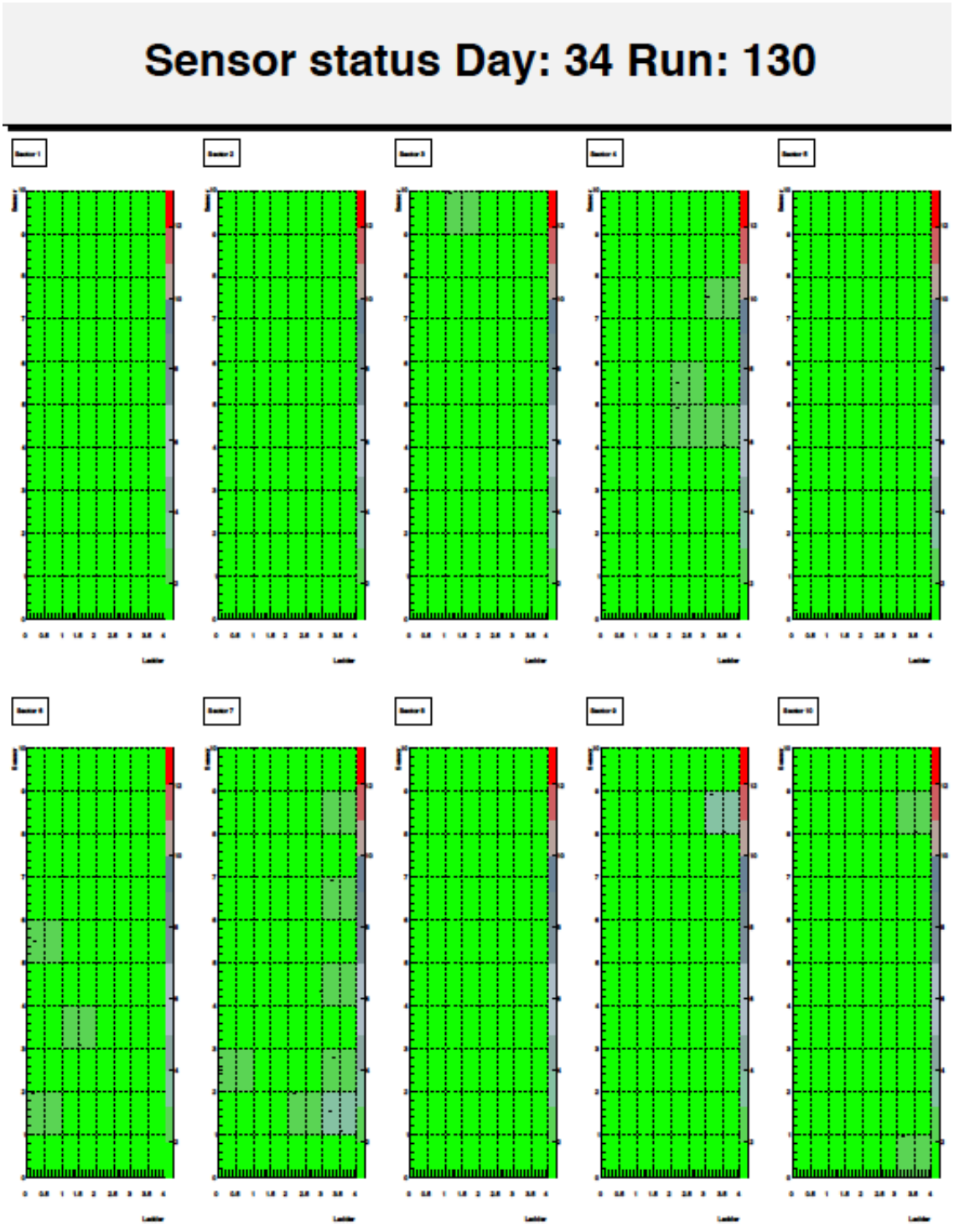


Figure A.5.1: Example of sense status plot produced by makePlot macro

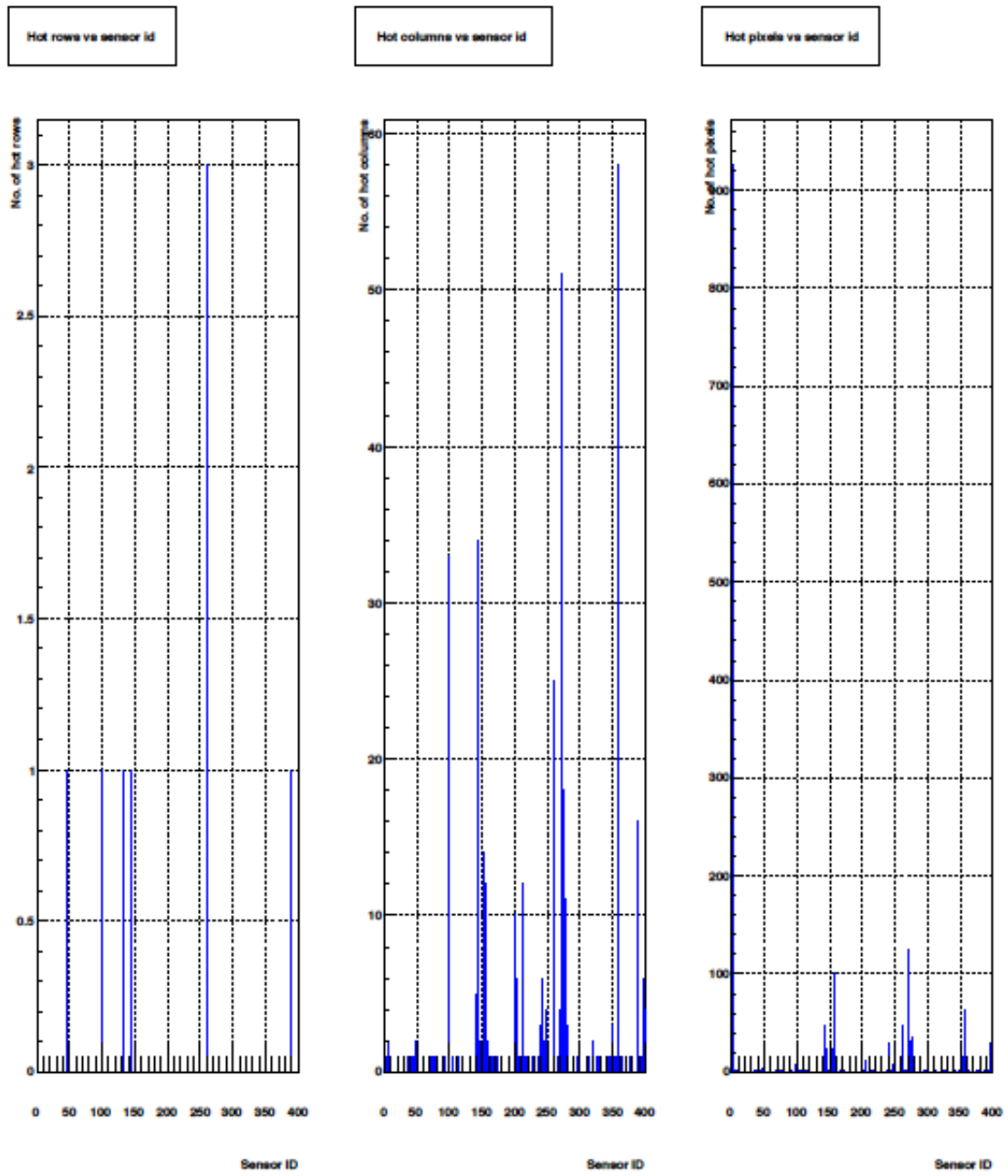


Figure A.5.2: Example of run summary produced by makePlots.C macro

Appendix B

Composite Structure Track Based Alignment

In modern detectors, such as the Heavy Flavor Tracker, it is essential to achieve high precision geometrical calibration to fully exploit the intrinsically high resolution of sensors. For example, the PXL subsystem consists of 2 layers with 400 wafers, each with approximately 1 million active elements (pixels) whose position must be calibrated with an accuracy that is comparable to their resolutions 10-20 μm [37]. However, the assembly precisions typically fall within a range that is an order of magnitude greater than this, and so the placement information must be improved with calibration methods.

In this section we present a track based alignment procedure that can be implemented to calibrate individual sensors as well as composite structures following a well established "Hit and Impact Point" algorithm discussed in [83, 52] to minimize the hit residuals, i.e. the difference between the recorded hit position and the projected track crossing with the sensors.

The algorithm involves a sequence of iterations over an event sample where the tracks are kept static and corrections are calculated through χ^2 minimization and used in the following iteration to refit. The procedure is, overall, computationally economic involving manipulation of small matrices of up 6x6 elements.

B.1 General χ^2 algorithm

To estimate the correction parameters the procedure will, in essence, consist of minimizing the χ^2 distribution of the residuals in terms of 6 parameters: 3 shifts $(\Delta u, \Delta w, \Delta v)$ and 3 rotations $(\Delta\alpha, \Delta\beta, \Delta\gamma)$.

Defining the measured hit as $\mathbf{q}_m = (u_m, 0, v_m)$ and the projected track hit as $\mathbf{q}_\times = (u_\times, 0, v_\times)$ the residual for an individual hit is defined by the 2D vector:

$$\varepsilon = \begin{pmatrix} \varepsilon_u \\ \\ \varepsilon_v \end{pmatrix} = \begin{pmatrix} u_\times - u_m \\ \\ v_\times - v_m \end{pmatrix} \tag{B.1}$$

In terms of which the χ^2 is defined as usual:

$$\chi^2 = \sum_j \varepsilon_j^T \mathbf{V}_j^{-1} \varepsilon_j \tag{B.2}$$

where the sum must be done over the set of associated measured and predicted hits and the matrix $\mathbf{V}_j$ is the covariance matrix associated to each hit.

As will be shown in later sections, the expressions for ε_j are highly non-linear in the correction parameters and so, by defining the vector $\mathbf{p} = (\Delta u, \Delta v, \Delta w, \Delta\alpha, \Delta\beta, \Delta\gamma)$ the generalized (non-linear) solution for χ^2 is obtained through a series of iterative corrections to $\mathbf{p} \to \mathbf{p} - \delta\mathbf{p}$ of the following form:

$$\delta\mathbf{p} = \left[\sum_j \mathbf{J^T}_j \mathbf{V}_j^{-1} \mathbf{J}_j\right]^{-1} \left[\sum_j \mathbf{J^T}_j \mathbf{V}_j^{-1} \varepsilon_j\right] \tag{B.3}$$

The previous expression is given in terms of the Jacobian matrices $\mathbf{J}_j = \nabla_p \varepsilon_j$, and initially the corrections are taken to be null, i.e. $\mathbf{p} = 0$

All that remains is to cast the residuals in a form where the corrections appear explicitly so that the Jacobians can be calculated and used in the algorithm.

B.2 Geometry Transformations and conventions

In the subsequent formulations, the following conventions will be employed: lower case bold $\mathbf{r}$, $\mathbf{g}$ and $\mathbf{q}$ will be used to denote 3D coordinate vectors in global, composite structure "local" and sensor local coordinate systems. Upper case bold $\mathbf{G}$ and $\mathbf{R}$ denote the rotation matrices used to transform from the composite and local systems to global coordinate system respectively.

The vectors $\mathbf{r_0}$ and $\mathbf{g_0}$ are the positions, in global coordinates, of the center of a sensor and the composite structures respectively.

Following STAR convention, the local coordinates $\mathbf{q} = (u, w, v)$ define a right handed coordinate system where w points away from the sensor surface, v points along the beam line (z direction in the global system), and u points in $r\hat{\phi}$. The composite coordinate system $\mathbf{g} = (g_1, g_2, g_3)$ has the same orientation as the global system.

Hence the transformations from global coordinates to each system are given by:

$$\begin{aligned} \mathbf{q} &= \mathbf{R^T}(\mathbf{r} - \mathbf{r_0}) \\ \mathbf{g} &= \mathbf{G^T}(\mathbf{r} - \mathbf{g_0}) \end{aligned} \tag{B.4}$$

In order to align entire sectors, we consider that there is a common misalignment to all ladders on a sector. Assuming that this misalignment is small, it can be corrected by introducing a small rotation matrix $\Delta\mathbf{G}$ and translation $\Delta\mathbf{g}$ such that $\mathbf{g} \rightarrow \Delta\mathbf{G}\mathbf{g} + \Delta\mathbf{g}$.

Hence the corrected transformation is:

$$\begin{aligned} \mathbf{G^T} &\rightarrow \mathbf{G_c}^T = \Delta\mathbf{G}\mathbf{G^T} \\ \mathbf{g}_0 &\rightarrow \mathbf{g}_0^c = \mathbf{g}_0 - \mathbf{G}\Delta\mathbf{G^T}\Delta\mathbf{g} \end{aligned} \tag{B.5}$$

To use this information in the algorithm, we must propagate the effects of this correction to the local "ladder" coordinate system where we can measure the residuals. Since the sector moves as a whole, the transformation that goes from the sector local coordinate system to each ladder remains untouched, and using the initial (uncorrected) geometry we find:

$$\mathbf{q} = \mathbf{A}(\mathbf{g} - \mathbf{a}_0) = \mathbf{R^T G}[\mathbf{g} - \mathbf{G^T}\,(\mathbf{r}_0 - \mathbf{g}_0)] \tag{B.6}$$

Hence by introducing (B.5) we obtain the relevant corrections in the ladder local system:

$$\begin{aligned} \mathbf{R^T} &\rightarrow \mathbf{R_c^T} = \mathbf{R^T G \Delta G G^T} \\ \mathbf{r_0} &\rightarrow \mathbf{r_c} = \mathbf{g_0} - \mathbf{G \Delta G^T \Delta g} + \mathbf{G \Delta G^T G^T}(\mathbf{r_0} - \mathbf{g_0}) \end{aligned} \tag{B.7}$$

With the previous transformations we can express the projected crossing of the trajectory with the sensor plane as a function of the correction parameters. Taking the trajectory to be straight in the vicinity of the sensor plane, it can be parametrized (in the global system):

$$\mathbf{r_s}(h) = \mathbf{r}_\times + h\hat{s} \tag{B.8}$$

where $\mathbf{r}_\times$ is the crossing with the sensor plane, $\hat{s}$ is the track direction and h is a parameter. To calculate the crossing point ($h_\times$) after a correction is applied to the sensor geometry, we can transform to the sensor local coordinate system:

$$\mathbf{q_s}(h) = \mathbf{R_c^T}(\mathbf{r}_\times + h\hat{s} - \mathbf{r_c}) \tag{B.9}$$

And set $\mathbf{q_s}(h_\times) \cdot \hat{w} = 0$ to solve for $h_\times$ on the sensor plane:

$$h_\times = -\frac{\mathbf{R_c^T}(\mathbf{r}_\times - \mathbf{r_c}) \cdot \hat{w}}{\mathbf{R_c^T}\hat{s} \cdot \hat{w}} \tag{B.10}$$

And hence, by substituting back into the expression for $\mathbf{q_s}$ we find the corrected track crossing:

$$\begin{aligned} \mathbf{q}_\times(\mathbf{p}) &= \mathbf{R_c^T}(\mathbf{r}_\times - \mathbf{r_c}) - \frac{\mathbf{R_c^T}(\mathbf{r}_\times - \mathbf{r_c}) \cdot \hat{w}}{\mathbf{R_c^T}\hat{s} \cdot \hat{w}} \mathbf{R_c^T}\hat{s} \\ &= \mathbf{R_c^T}(\mathbf{r}_\times - \mathbf{r_c}) - \frac{[\mathbf{R_c^T}(\mathbf{r}_\times - \mathbf{r_c})]_2}{[\mathbf{R_c^T}\hat{s}]_2} \mathbf{R_c^T}\hat{s} \end{aligned} \tag{B.11}$$

where the subscript 2 is used to indicate the second component of a given vector. Furthermore, it is convenient to note the following simplification:

$$\mathbf{R_c^T}(\mathbf{r}_\times - \mathbf{r_c}) = \mathbf{R_c^T}(\mathbf{r}_\times - \mathbf{g_0}) + \mathbf{R^T G}\Delta\mathbf{g} - \mathbf{R^T}(\mathbf{r_0} - \mathbf{g_0}) \tag{B.12}$$

From here we can find an expression for the elements of the Jacobian matrices for each hit $\mathbf{J_j} = \nabla_\mathbf{p}\varepsilon_j$. This is simplified by the fact that the only dependence on the correction parameters $\mathbf{p} = (\Delta u, \Delta w, \Delta v, \Delta\alpha, \Delta\gamma, \Delta\beta)$ is in the expression for $\mathbf{q}_\times$. After some manipulation (see section B.5) we obtain the following expressions for the derivatives with respect to the three shift parameters p_1, p_2, p_3:

$$\frac{\partial \mathbf{q}_\times}{\partial p_j} = \mathbf{R^T G}\hat{\mathbf{e}}_\mathbf{j} - \frac{[\mathbf{R^T G}\hat{\mathbf{e}}_\mathbf{j}]_2}{[\mathbf{R_c^T}\hat{\mathbf{s}}]_2} \mathbf{R_c^T}\hat{s} \quad , \quad j = 1, 2, 3 \tag{B.13}$$

and the derivatives with respect to the three tilt angles:

$$\frac{\partial \mathbf{q}_\times}{\partial p_j} = \mathbf{D_j}(\mathbf{r}_\times(\mathbf{p}) - \mathbf{g_0}) - [\mathbf{D_j}(\mathbf{r}_\times(\mathbf{p}) - \mathbf{g_0})]_2 \frac{\mathbf{R_c^T}\hat{s}}{[\mathbf{R_c^T}\hat{s}]_2} \quad , \quad j = 4, 5, 6 \tag{B.14}$$

where:

$$\mathbf{D_j} = \frac{\partial \mathbf{R_c^T}}{\partial p_j} = \mathbf{R^T G} \frac{\partial \mathbf{\Delta G}}{\partial p_j} \mathbf{G^T} \tag{B.15}$$

B.3 Method performance: simulations

The alignment method described in previous sections was implemented for the PXL detector sub-assembly of the Heavy Flavor Tracker upgrade for the STAR experiment, and was tested using primary tracks reconstructed by the STAR TPC in

simulation blind tests where whole sector misalignments were introduced in a single sector.

A single sector of PXL consists of 4 ladders with 10 sensors each, three of which sit 8cm away from the beam line and point outward (away from the beam line). The fourth ladder sits at a radius of 2.5 cm and points inward.

Table B.3.1 shows the difference between the calculated correction parameters and the misalignments introduced in the blind test. Comparing the calculated corrections with the introduced misalignments allows for an estimate of the algorithm's performance. However it is worth noting that the pointing resolution of TPC tracks, roughly 1mm [18], is most likely a major source of the observed errors. Similarly, since tracks are kept static in the algorithm, the errors in the calculated correction parameters can be reduced further by repeating the procedure on updated tracks.

	Blind test 1	Alignment result	Error
dx	-750	-710	40
dy	500	507	7
dz	100	118	18
dα	-5	-5	0
dβ	7.4	7.3	0.1
dγ	13	13.3	0.3

Figure B.3.1: Calculated and introduced misalignments. Angles are reported in mrad and shifts in microns

Using the procedure established in [40], the effects of the alignment can be visualized in Figure B.3.2 where plotting and straight-line fitting the global residuals with respect to the corresponding derivative matrices provides information on rotations (slope) and shifts (intercept). Figure B.3.3 shows the convergence of the algorithm

for all six misalignment parameters.

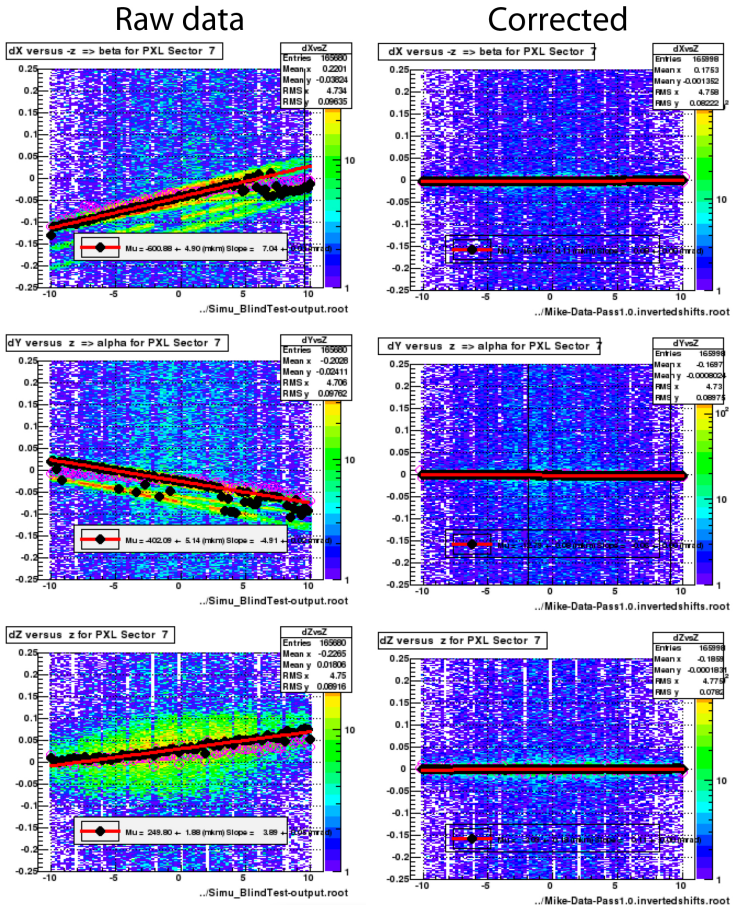


Figure B.3.2: Raw and corrected residuals vs. z for simulations

Three out of the 10 PXL sectors were installed and tested with beam during 2013 run. The alignment procedure was further tested using data obtained during this engineering run and the histogramming was used to verify the alignment. A sample of the results are shown in Figures B.3.4 and B.3.5 .

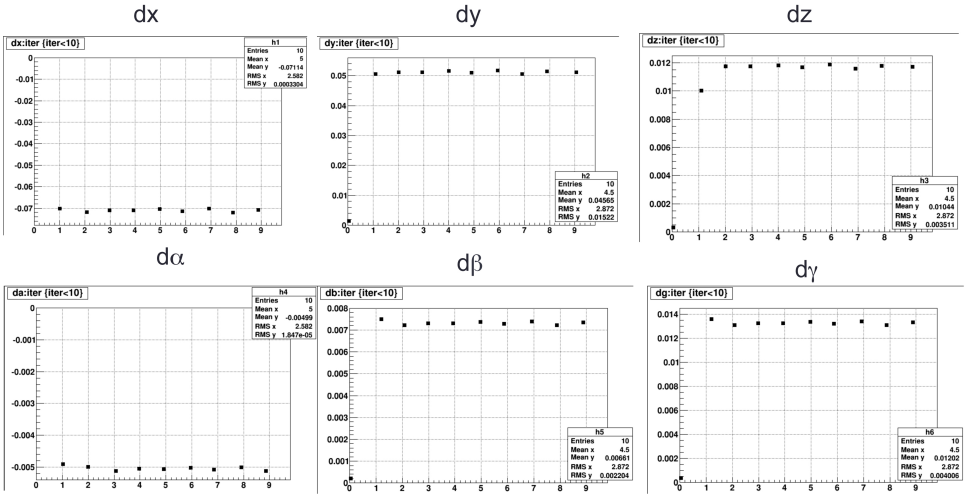


Figure B.3.3: Calculated corrections as a function of algorithm iteration

B.4 Relative alignment for full PXL system

Following the results obtained during the PXL engineering run of 2013, the whole HFT system was installed and used in data taking during 2014. However, pending the calibration of the TPC, the procedure was adapted to align the structures relative to each other using zero field cosmic data obtained during early stages of the run in January and February.

In this environment, straight-line tracks could be used in place of TPC primary tracks, using two hits on separate layers of a single sector of PXL to construct the tracks and then project to the opposite side of PXL in search of a hit-track association. The residual obtained from this projection was used as input for the algorithm.

Corrections were calculated and applied to align different structures of PXL: first the two halves (sectors 1-5 and 6-10) were aligned relative to each other. On top of these corrections the, individual sectors were aligned relative to sector 1 and finally the whole PXL system was aligned relative to the TPC.

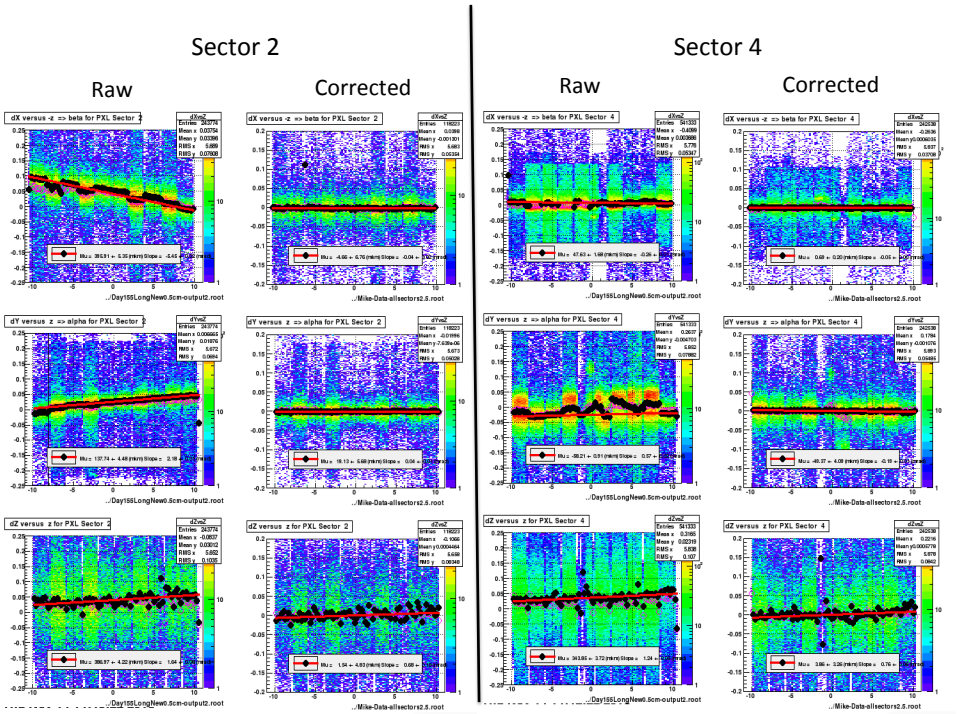


Figure B.3.4: Raw and corrected residuals for run 2013 data for PXL sectors 2 and 4.

B.5 Calculation of Jacobian matrix elements

In this section, we will obtain explicit expressions for the components of the Jacobian matrix $\nabla_p \mathbf{q}_\times$ with respect to the six correction parameters, the simplest of which are the terms involving derivatives with respect to the three shifts. From the expression for $\mathbf{q}_\times$:

$$\mathbf{q}_\times(\mathbf{p}) \;=\; \mathbf{R_c^T}(\mathbf{r}_\times - \mathbf{r_c}) - \frac{[\mathbf{R_c^T}(\mathbf{r}_\times - \mathbf{r_c})]_2}{[\mathbf{R_c^T}\hat{s}]_2}\mathbf{R_c^T}\hat{s} \tag{B.16}$$

We note that the shifts $\Delta u, \Delta w$ and Δw appear only within $\mathbf{r_c}$ in the term $\Delta\mathbf{g}$, so the derivatives with respect to p_j with $j = 1, 2, 3$ can be reduced to:

$$\frac{\partial \mathbf{q}_\times}{\partial p_j} = -\mathbf{R_c^T}\frac{\partial \mathbf{r_c}}{\partial p_j} + \left[\mathbf{R_c^T}\frac{\partial \mathbf{r_c}}{\partial p_j}\right]_2 \frac{\mathbf{R_c^T}\hat{s}}{[\mathbf{R_c^T}\hat{s}]_2} \quad , \quad j = 1, 2, 3 \tag{B.17}$$

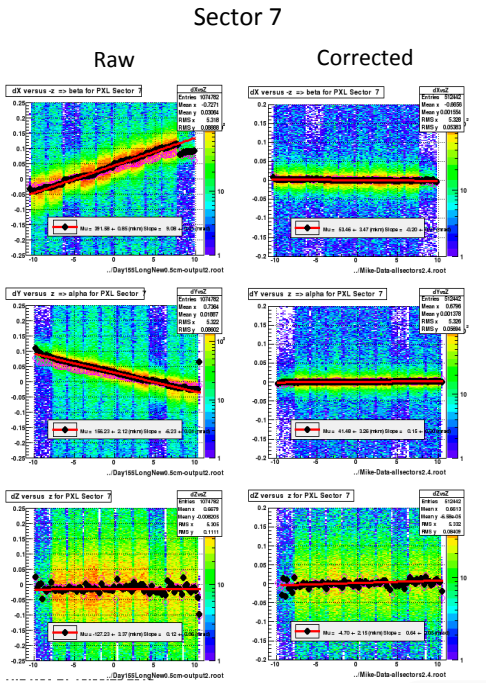


Figure B.3.5: Raw and corrected residuals for run 2013 data forXL sector 7.

and

$$\begin{aligned} \frac{\partial \mathbf{r_c}}{\partial p_j} &= -\mathbf{G}\boldsymbol{\Delta}\mathbf{G}^{\mathbf{T}}\frac{\partial \Delta \mathbf{g}}{\partial p_j} \\ &= -\mathbf{G}\boldsymbol{\Delta}\mathbf{G}^{\mathbf{T}}\hat{\mathbf{e}}_{\mathbf{j}} \quad , \quad j = 1,2,3 \end{aligned} \tag{B.18}$$

and substituting back, together with the expression for $\mathbf{R_c^T} = \mathbf{R^T}\mathbf{G}\Delta\mathbf{G}\mathbf{G^T}$, we obtain the expression for the derivatives of $\mathbf{q}_\times$

$$\frac{\partial \mathbf{q}_\times}{\partial p_j} = \mathbf{R^T}\mathbf{G}\hat{\mathbf{e}}_{\mathbf{j}} - [\mathbf{R^T}\mathbf{G}\hat{\mathbf{e}}_{\mathbf{j}}]_2 \frac{\mathbf{R_c^T}\hat{s}}{[\mathbf{R_c^T}\hat{s}]_2} \quad , \quad j = 1,2,3 \tag{B.19}$$

Now for the derivatives with respect to the tilt angles, we can follow the same approach but noting that the term $\Delta\mathbf{G}$ which contains the correction parameters $\Delta\alpha$, $\Delta\beta$ and

$\Delta\gamma$ appears in both $\mathbf{R_c^T}$ and $\mathbf{r_c}$. However using the relationship (B.12) and denoting:

$$\mathbf{D_j} = \frac{\partial \mathbf{R_c^T}}{\partial p_j} = \mathbf{R^T G} \frac{\partial \Delta \mathbf{G}}{\partial p_j} \mathbf{G^T} \tag{B.20}$$

we have (for j=4,5,6):

$$\begin{aligned} \frac{\partial \mathbf{q}_\times}{\partial p_j} &= \mathbf{D_j}(\mathbf{r}_\times - \mathbf{g_0}) - [\mathbf{D_j}(\mathbf{r}_\times - \mathbf{g_0})]_2 \frac{\mathbf{R_c^T}\hat{s}}{[\mathbf{R_c^T}\hat{s}]_2} \\ &+ \frac{[\mathbf{R_c^T}(\mathbf{r}_\times - \mathbf{r_c})]_2}{[\mathbf{R_c^T}\hat{s}]_2} \left(\frac{[\mathbf{D_j}\hat{s}]_2 \mathbf{R_c^T}\hat{s} - [\mathbf{R_c^T}\hat{s}]_2 \mathbf{D_j}\hat{s}}{[\mathbf{R_c^T}\hat{s}]_2} \right) \end{aligned} \tag{B.21}$$

Now, solving (B.8) for $\hat{s}$

$$\hat{s} = \frac{\mathbf{r}_\times(\mathbf{p}) - \mathbf{r}_\times}{h_\times} = \frac{[\mathbf{R_c^T}\hat{s}]_2}{\mathbf{R_c^T}(\mathbf{r}_\times - \mathbf{r_c})} (\mathbf{r}_\times - \mathbf{r}_\times(\mathbf{p})) \tag{B.22}$$

Note that $\mathbf{r}_\times$ denotes the original track crossing while $\mathbf{r}_\times(\mathbf{p}) = \mathbf{r_s}(h_\times)$, the corrected crossing, and a function of the correction parameters. Substituting into the second term of (B.21) to simplify, we have:

$$\begin{aligned} &\frac{[\mathbf{R_c^T}(\mathbf{r}_\times - \mathbf{r_c})]_2}{[\mathbf{R_c^T}\hat{s}]_2} \left(\frac{[\mathbf{D_j}\hat{s}]_2 \mathbf{R_c^T}\hat{s} - [\mathbf{R_c^T}\hat{s}]_2 \mathbf{D_j}\hat{s}}{[\mathbf{R_c^T}\hat{s}]_2} \right) \\ &= [\mathbf{D_j}(\mathbf{r_x} - \mathbf{r_x}(\mathbf{p}))]_2 \frac{\mathbf{R_c^T}\hat{s}}{[\mathbf{R_c^T}\hat{s}]_2} - \mathbf{D_j}(\mathbf{r}_\times - \mathbf{r}_\times(\mathbf{p})) \end{aligned} \tag{B.23}$$

Finally, by replacing the second term of (B.21) with this result we obtain a simple expression for the derivatives of $\mathbf{q_x}$ with respect to the tilt angles:

$$\frac{\partial \mathbf{q}_\times}{\partial p_j} = \mathbf{D_j}(\mathbf{r}_\times(\mathbf{p}) - \mathbf{g_0}) - [\mathbf{D_j}(\mathbf{r}_\times(\mathbf{p}) - \mathbf{g_0})]_2 \frac{\mathbf{R_c^T}\hat{s}}{[\mathbf{R_c^T}\hat{s}]_2} \quad , \quad j = 4, 5, 6 \tag{B.24}$$

Appendix C

Event Plane Detector Prototype

The observation of hints of a possible transition from high temperature and high density phase, dominated by partonic degrees of freedom, to a phase where the relevant degrees of freedom are those of hadronic matter [8, 21] was an important discovery during the early years at RHIC. Furthermore, several interesting features are expected to appear at larger values of the baryon chemical potential μ_B including a QCD critical point and a first-order phase boundary between the hadronic and partonic phases [30, 39], and motivated an exploration of the QCD phase diagram in the Beam Energy Scan (BES) program carried out at RHIC.

These findings have generated an intense interest and a second phase of the program, BES-II, has been planned for the period between 2019 - 2021 with the goal of discovering the QCD critical point and performing high luminosity scans of the interesting energies revealed in BES-I. To fully achieve these goals a series of detector and accelerator upgrades are now underway for the RHIC facility and the STAR experiment. Amongst the upgrades planned for STAR, a dedicated event plane and centrality detector, the Event Plane Detector (EPD), has been approved and is currently under construction. As well as functioning as a trigger for the experiment, the EPD will provide an independent measurement of both an event's centrality and event plane at high rapidity($2.1 < |\eta| < 5.1$). The latter is crucial to reduce the size of systematic uncertainties due to non-flow in mid-rapidity measurements.

This section will focus on R&D activities related to the design and construction of

the EPD prototype at Lawrence Berkeley National Laboratory.

C.1 Silicon photomultipliers

Based on the physics requirements, area to be covered and pricing, it was decided to use a combination of scintillating plastic and silicon photomultipliers (SiPM) for the EPD detector. Commercial SiPM technology has already been employed in high energy experiments and the list below shows some of the important characteristics of the SiPM's selected for the prototype, showing they can replace traditional photomultipliers with the added advantages of a small device(compact designs) and reduced cost:

- Time of Flight coincidence resolving time $\leq$ 250 ps
- Gain on the order of 10^6
- Linear dependence of gain with voltage bias
- Total quantum efficiency $\geq$ 20% (wavelength dependent)
- Cost on the order of \$20
- Supply voltage $\sim$ 50V
- Not sensitive to magnetic fields
- SiPMs are small devices, allowing for compact designs

As part of the R&D, the SiPM's performance was tested to ensure they were adequate for this application. In particular the following measurements were studied:

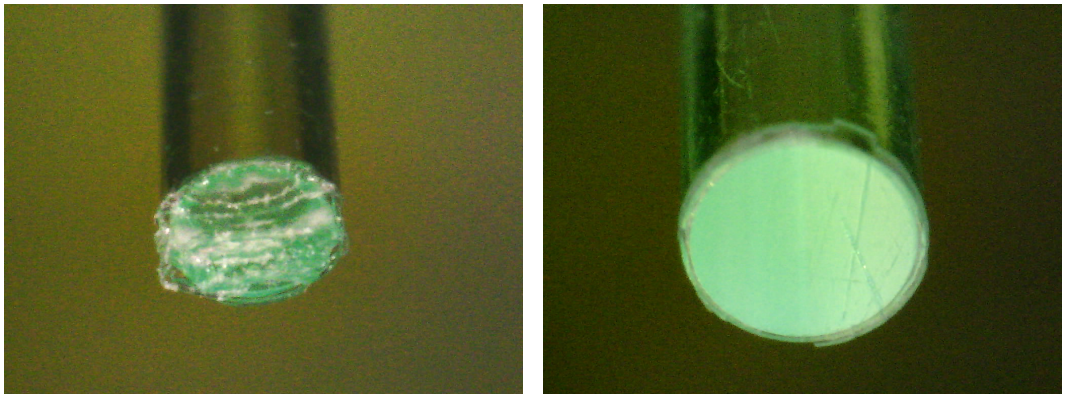
- Efficiency for single Minimum Ionizing Particle (MIP) hits

- Uniformity of pulse area and efficiency as a function of position of hit on a scintillator
- Pulse shapes (rise time and fall time) for MIPs
- Gain vs. bias voltage
- Timing resolution
- Temperature stability

In order to avoid radiation damage to the SiPM's, they will be placed far from the interaction region by coupling the wavelength shifting fibers to optical fibers which will carry the light to the SiPM's.

C.2 Fiber preparation

Kuraray Y-11 wavelength shifting (WLS) fibers were selected in order to collect the light emitted by the detector tiles, shifting the peak wavelength to better match the sensitive range in the SiPM's and finally guide the light out of the detector. Given that the SiPM's must be placed far from the detector and the relatively low attenuation length of the fibers, roughly 400 cm, the WLS fibers are coupled to optical fibers once they have exited the detector. To maximize the optical coupling and transmit as much light as possible, the ends of the cut WLS and optical fibers were polished in a six step procedure using incrementally finer grit polishing sheets ranging from 5 μm down to a grit size of 0.3 μm, till the desired smoothness was achieved. Figure C.2.1 shows a WLS fiber under microscope before and after the polishing steps have been applied with noticeable improvement in the smoothness of the surface.



(a) (b)

Figure C.2.1: Kuraray Y-11(200) wavelength shifting fibers before (left) and after polishing (right).

C.3 Tile design

The tile design was inspired by the barrel Electromagnetic Calorimeter (BEMC) detector in STAR. Eljen EJ-200 scintillating plastic was selected for the body of the detector and was coupled to the SiPM's via optical fibers. In order to best match the peak light detection efficiency, WLS fibers are embedded in the scintillators to both collect the emitted light and shift the light's wavelength towards green. Although the sigma design for the grooves was identified early on as the most likely candidate for the detector, different arrangements were tested at LBNL though ultimately the sigma grooves represented a simple implementation and proved to be capable of detecting single photons.

The WLS fibers exit directly out of the front face of each tile and are coupled to optical fibers that are then directed away from the detector towards the SiPM's which will be positioned near the STAR magnet to shield them from radiation damage coming from fast neutrons.

All the tiles were designed using the SolidWorks® software package. Multiple tiles

were machined out of a single piece of scintillator by machining 90% through the plastic, as was done for the BEMC.

In order to test different tile and groove geometries, a first set of tiles were machined from the scintillating plastic. After polishing the sides of the tiles and the ends of the WLS fiber, to improve reflectivity, the end of the WLS that will be embedded in the scintillator was painted with Eljen EJ-510 reflective paint in order to reflect back photons that were heading in the "wrong" direction. Then the fibers were glued into the grooves of the scintillator using Eljen EJ-500 optical cement for good optical coupling. In order to further ensure that signal photons were contained within the

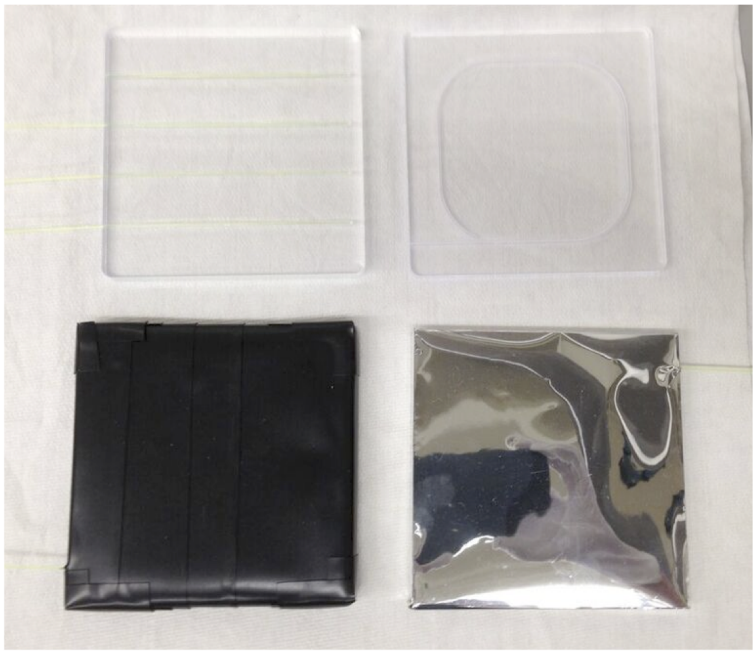


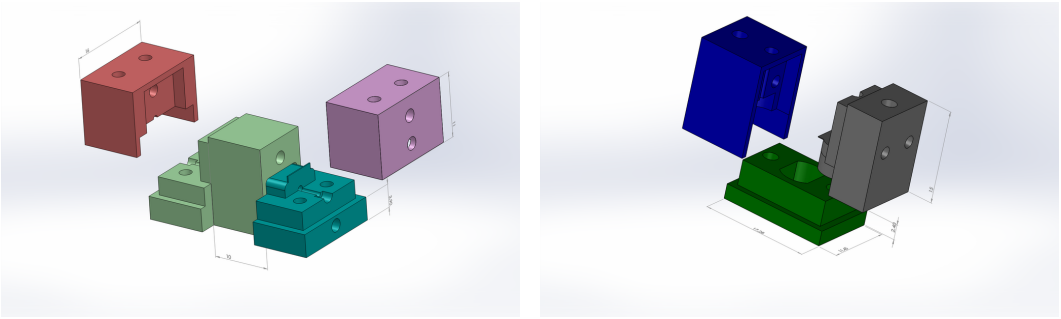
Figure C.3.1: Test tiles for the EPD. The upper right tile shows the sigma groove. The upper left shows a tile design that was discarded. The lower right shows a tile wrapped in mylar, and the lower left shows a tile wrapped in mylar and then covered with black tape.

plastic scintillator, all tiles were tightly wrapped with aluminized mylar and then

again with thick black paper. A template was cut for the mylar that minimized the total surface area of the mylar while completely covering all faces of the tile. The mylar was then laid over the template and cut out with a box cutter for each tile. Any piece of the mylar that would be a fold on the tile was also perforated somewhat so as to ensure sharp edges all around. Figure C.3.1 shows a sample of tile designs and the two step wrapping process.

C.4 Fiber coupling

After the light emitted from the scintillator tiles is collected by the WLS fibers, it must be read out by the SiPM's which must be placed a distance away to protect from radiation damage. To minimize the light loss, the WLS fibers are coupled to transparent optical fibers with a much longer attenuation length. This necessitates establishing good coupling in two locations, the fiber-fiber connection and the fiber-SiPM connection. Simple connectors were designed and built with a 3D printer using black polylactic acid (PLA) plastic, as is shown in figure C.4.1



(a) (b)

Figure C.4.1: WLS to clear fiber connector (left) and fiber to SiPM connector (right) used for the EPD Prototype

C.5 Radiation hardness of optical cement

In order to fix the WLS in place in the grooves as well as to improve the optical coupling to the scintillating plastics, Eljen EJ-500 optical cement was used. However, this brought up the question as to how the optical cement and WLS fibers would respond in a high radiation environment expected during the BES-II program. This particular optical cement had not been previously tested for radiation hardness. However a similar epoxy, Bicron 600, has showed significant radiation damage when exposed to large dose of gamma radiation [80]. Although the dose used in these tests exceeds the expectation for what will be experienced by the EPD, it was deemed necessary to test the radiation hardness of the designed tiles.

The test was conducted at the 88-Inch cyclotron at Lawrence Berkeley National Lab. by constructing five identical tiles containing a fully polished WLS fiber looped in triple layer and held in by about 1.25 mL of EJ-500 epoxy, as shown in figure C.5.1.

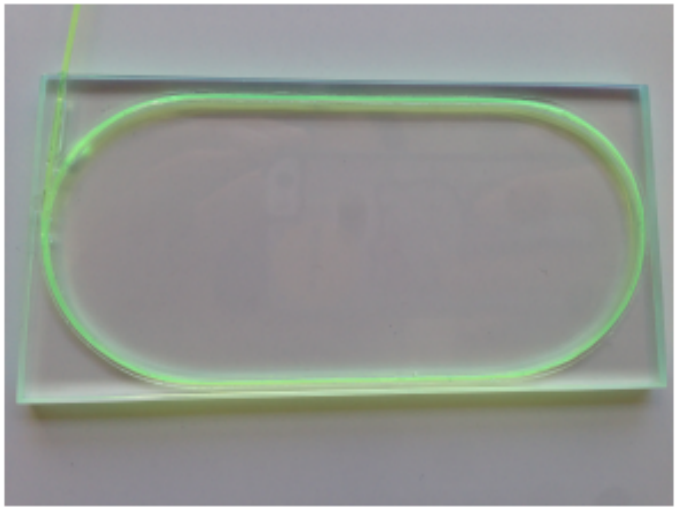


Figure C.5.1: One of 12cm×5.5cm×0.5cm EJ-200 scintillator with a triple layer of Kuraray Y-11 WLS fibers glued with EJ-500 optical cement

The performance of each of the five tiles was tested before irradiation by measuring

the signal amplitudes in cosmic ray events triggered by two other tiles constructed previously and using a trigger threshold of 6 mV for the two reference detectors. The typical signals observed in the tiles were on the order of 40 mV, and the baseline was determined by averaging over roughly 200 measured cosmic events. The signal per tile was also corrected for event-by-event fluctuations in the amount of energy deposited in the scintillators by dividing the tile signal by the average of the trigger detector signals.

The tiles were then placed in a 50 MeV proton beam at one of five levels of fluence determined by the estimated doses expected during the BES-II program of 3×10^{11} particles/cm^2 maximum per year. The performance of the tiles was then tested again once they were deemed safe (no longer activated by the radiation) and the efficiency was then calculated as the ratio of the signal amplitudes before and after irradiation. Table C.5.1 shows the radiation doses and efficiency for the different tiles tested.

There have been studies conducted on the radiation hardness of the Kuraray WLS

	Tile 1	Tile 2	Tile 3	Tile 4	Tile 5
Flux(ions/cm^{2}s)	2.5×10^8	2.5×10^8	2×10^8	6.5×10^7	5×10^7
Fluence(ions/cm^2)	1×10^{12}	5×10^{11}	1×10^{11}	5×10^{10}	1×10^{10}
Dose(kRad)	300	150	30	15	3
Efficiency(%)	70	82	89	97	100

Table C.5.1: Doses deposited per tile and measured efficiency

fibers that show agreement with our result of a 30% loss in detector efficiency, for instance [72] found that after a dose of 650 kRad the fibers had an efficiency of 70%. A second study [47] investigated the attenuation length of Kuraray's 3HF clear fibers and found a a decrease of about 50% after an irradiation dose of roughly 300kRad. These results are summarized in figure C.5.2 and are consistent with a scenario where the efficiency loss is coming mostly from damage in the WLS fibers themselves and

not the optical cement used to couple them to the tile. Furthermore, it is important to note that the largest dose tested corresponds to a dose roughly 3 times the expected value for the entire BES-II suggesting that this should not be a major concern in the detector design.

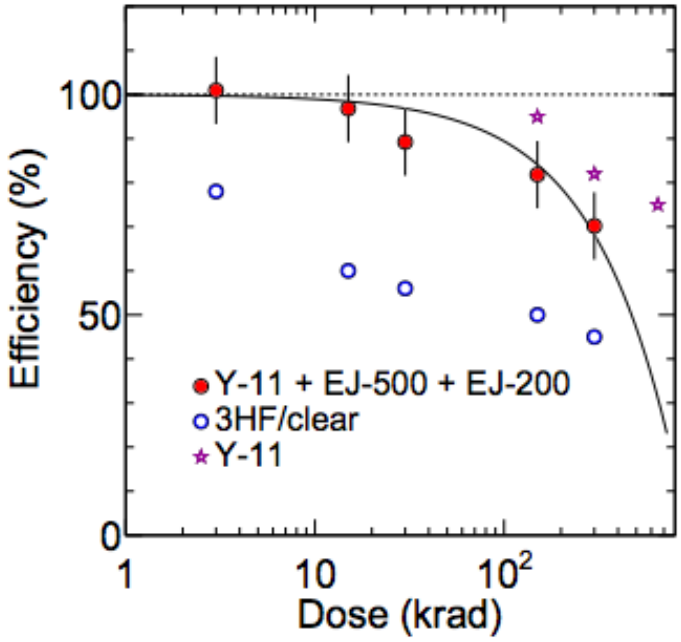


Figure C.5.2: Measured efficiency vs. dose of the assembled detector tiles compared to reported observations in Y-11 WLS and 3HF clear fibers

C.6 EPD prototype design and assembly

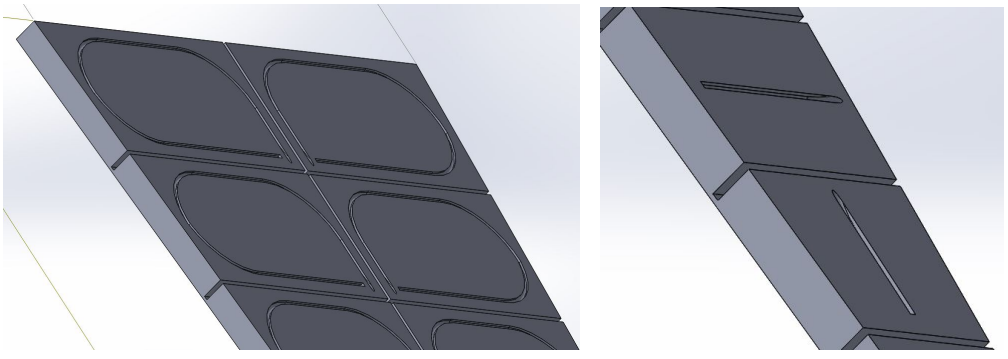
Based on simulations it was determined that the optimal design for the detector would consist of 24 disk sectors at either end of STAR extending radially from the beam pipe and touching side side to side to form a disc. The prototype was designed using 3D computer-aided design software called SolidWorks® and consists of a narrow trapezoid 103.8 cm long made from 1 cm thick scintillator plastic. It is 22.87 cm at its widest and 1.4 cm wide at the bottom edge. Each sector is further divided into 24 pads that are optically separated by machining 90% through the plastic and

then applying optically opaque epoxy. Figure C.6.1 shows the completed prototype design with relevant dimensions. Each of the 24 pads in a sector are machined to



Figure C.6.1: SolidWorks model of the EPD prototype showing dimensions in centimeters.

construct a groove with a depth of 0.16 cm to hold the wavelength shifting fibers used to collect (and shift) the light emitted by the scintillators and guide it away from the detector. The groves in the larger pads (see Fig. C.6.2a) have a sigma shaped groove to maximize the amount of collected light. Smaller tiles in the bottom of the sector are limited by the minimum bending radius of the fibers (∼2.5 cm) so a straight line grove was employed, as illustrated in Fig. C.6.2b. The polished WLS fibers were then



(a) (b)

Figure C.6.2: Tile designs showing σ and straight line groves to accommodate the wavelength shifting fibers.

fixed in the grooves using optical cement that closely matches the refractive index of the scintillating plastics. Reflective paint was applied to the end of the fiber that remains embedded in the detector to increase the amount of light to be collected by the SiPMs.

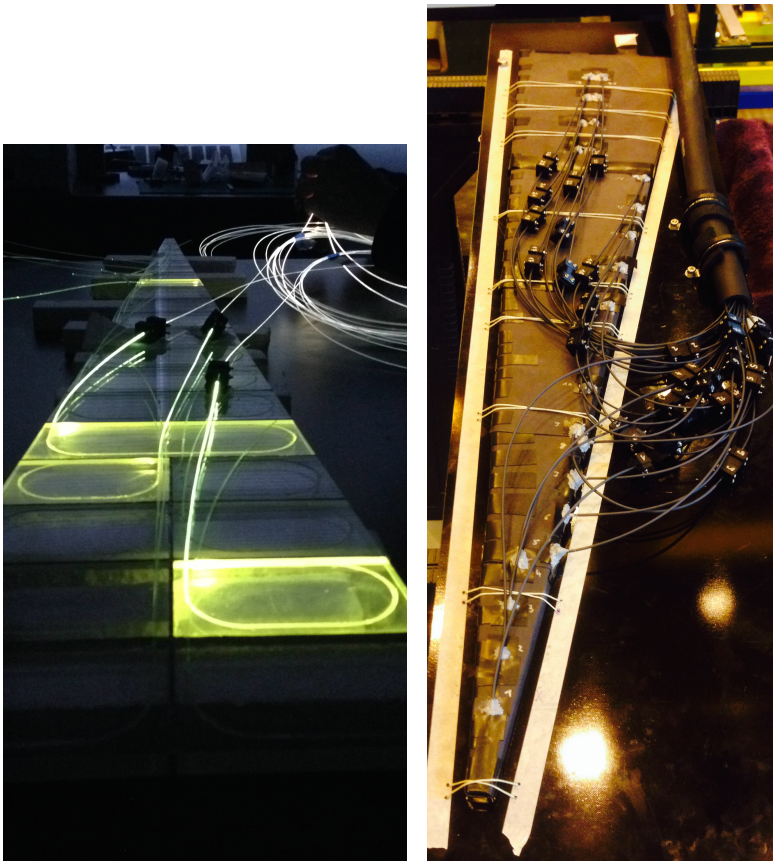
The individual tiles were then optically separated by coating the sides with reflective paint and then filling the machined-out channel with epoxy to preserve the mechanical robustness. Figure C.7.1a shows a test of the optical isolation where light was shone into individual fibers.

After hardening, the entire sector was covered in mylar and black paper for light tightness, as was discussed in the previous section.

C.7 Prototype installation

After the EPD was assembled at LBNL, it was sent to Brookhaven National Lab for installation. At this time, the shrink tube necessary for light-tightness was added to the WLS fibers that protruded from the EPD. This was done via a heat gun. Next the WLS and clear optical fibers were connected. The 24 clear optical fibers were put into a single large black tube for light tightness. The ends that protruded from this tube were also covered in shrink tubing. The final assembly can be seen in Figure C.7.1b.

The prototype, consisting of full sector with 24 channels, was installed before the start of run 16. Additionally, timing information was added to 8 of the channels, selected to evaluate different tile sizes and fiber geometries and their feasibility for triggering. The EPD prototype started to record data on the 22nd day of the run. At this point, the EPD was incorporated in the DAQ files so that the data is accessible



(a) (b)

Figure C.7.1: On the left is the light test done for the assembled prototype, where light was shined into the fiber optics. On the right is the finished EPD prototype.

to all. Additionally, the EPD was included in the STAR pedestal runs, which allowed the STAR software frame to subtract the pedestals from the data.

The data taken with the EPD prototype is currently being analyzed with generally good results. However due to time constraints I had to scale back my activities on the EPD project and was not involved in the analysis of collected results and the re-design for the final detector. The details on these activities not covered here can be found in the STAR EPD construction proposal [17].

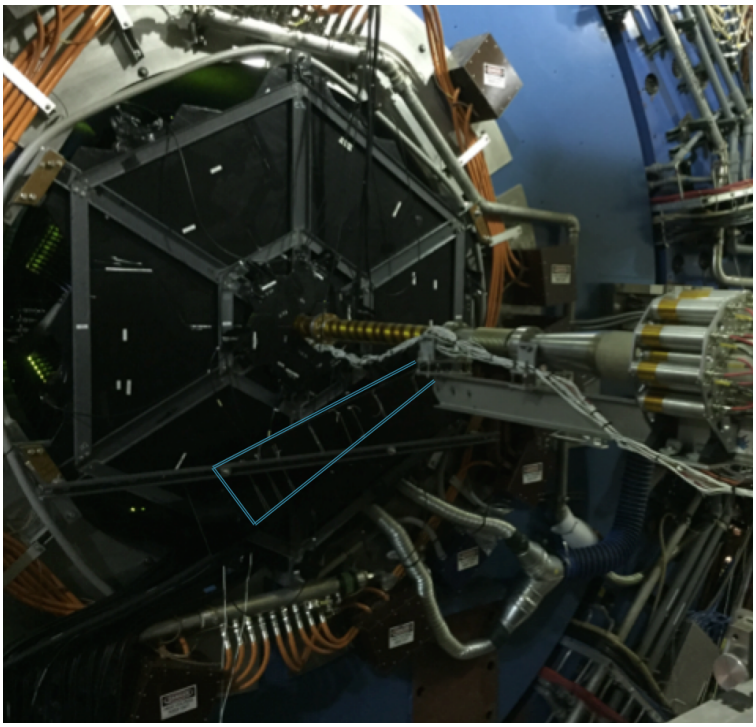


Figure C.7.2: The installation of the EPD prototype in 2016. The blue lines are drawn into the photograph in order to guide the eye.

Bibliography

[1] G. Aad et al. "Observation of a new particle in the search for the Standard Model Higgs boson with the ATLAS detector at the LHC". In: *Physics Letters B* 716.1 (2012), pp. 1 –29. ISSN: 0370-2693. DOI: http://dx.doi.org/10.1016/j.physletb.2012.08.020. URL: http://www.sciencedirect.com/science/article/pii/S037026931200857X.

[2] B. Abelev et al. "D Meson Elliptic Flow in Noncentral Pb-Pb Collisions at $\sqrt{s_{NN}} = 2.76$ TeV". In: *Phys. Rev. Lett.* 111 (10 2013), p. 102301. DOI: 10.1103/PhysRevLett.111.102301. URL: http://link.aps.org/doi/10.1103/PhysRevLett.111.102301.

[3] B. I. Abelev et al. "Centrality dependence of charged hadron and strange hadron elliptic flow from $\sqrt{s_{NN}} = 200$ GeV Au+Au collisions". In: *Phys. Rev. C* 77 (5 2008), p. 054901. DOI: 10.1103/PhysRevC.77.054901. URL: http://link.aps.org/doi/10.1103/PhysRevC.77.054901.

[4] L. Adamczyk et al. "Centrality and Transverse Momentum Dependence of Elliptic Flow of Multistrange Hadrons and ϕ meson in Au + Au Collisions at $\sqrt{s_{NN}} = 200$ GeV". In: *Phys. Rev. Lett.* 116 (6 2016), p. 062301. DOI: 10.1103/PhysRevLett.116.062301. URL: http://link.aps.org/doi/10.1103/PhysRevLett.116.062301.

[5] L. Adamczyk et al. "Observation of D^0 Meson Nuclear Modifications in Au+Au Collisions at $\sqrt{s_{NN}} = 200$ GeV". In: *Phys. Rev. Lett.* 113 (14 2014), p. 142301. DOI: 10.1103/PhysRevLett.113.142301. URL: http://link.aps.org/doi/10.1103/PhysRevLett.113.142301.

[6] L. Adamczyk et al. "Observation of D^0 Meson Nuclear Modifications in Au+Au Collisions at $\sqrt{s_{\mathrm{NN}}} = 200$ GeV". In: *Phys. Rev. Lett.* 113 (14 2014), p. 142301. DOI: 10.1103/PhysRevLett.113.142301. URL: http://link.aps.org/doi/10.1103/PhysRevLett.113.142301.

[7] J. Adams et al. "Azimuthal Anisotropy and Correlations at Large Transverse Momenta in $p + p$ and Au + Au Collisions at $\sqrt{s_{NN}} = 200$ GeV". In: *Phys. Rev. Lett.* 93 (25 2004), p. 252301. DOI: 10.1103/PhysRevLett.93.252301. URL: http://link.aps.org/doi/10.1103/PhysRevLett.93.252301.

[8] J. Adams et al. "Experimental and theoretical challenges in the search for the quark-gluon plasma: The STAR Collaboration's critical assessment of the evidence from RHIC collisions". In: *Nuclear Physics A* 757.1-2 (2005). First Three Years of Operation of RHIC, pp. 102 –183. ISSN: 0375-9474. DOI: http://dx.doi.org/10.1016/j.nuclphysa.2005.03.085. URL: http://www.sciencedirect.com/science/article/pii/S0375947405005294.

[9] J. Adams et al. "Heavy-flavour and quarkonium production in the LHC era: from proton–proton to heavy-ion collisions". In: *The European Physical Journal C* 76.3 (2016), pp. 1–151. ISSN: 1434-6052. DOI: 10.1140/epjc/s10052-015-3819-5. URL: http://dx.doi.org/10.1140/epjc/s10052-015-3819-5.

[10] J. Adams et al. "Transverse momentum dependence of D-meson production in Pb-Pb collisions at $\sqrt{s_{NN}}$ = 2.76 TeV". In: *Journal of High Energy Physics* 2016.3 (2016), pp. 1–43. ISSN: 1029-8479. DOI: 10.1007/JHEP03(2016)081. URL: http://dx.doi.org/10.1007/JHEP03(2016)081.

[11] A. Adare et al. "Suppression Pattern of Neutral Pions at High Transverse Momentum in Au+Au Collisions at $\sqrt{s_{NN}} = 200$ GeV and Constraints on Medium Transport Coefficients". In: *Phys. Rev. Lett.* 101 (23 2008), p. 232301. DOI: 10.1103/PhysRevLett.101.232301. URL: http://link.aps.org/doi/10.1103/PhysRevLett.101.232301.

[12] K. Adcox et al. "Formation of dense partonic matter in relativistic nucleus-nucleus collisions at RHIC: Experimental evaluation by the PHENIX Collaboration". In: *Nuclear Physics A* 757.1-2 (2005). First Three Years of Operation of RHIC, pp. 184 –283. ISSN: 0375-9474. DOI: http://dx.doi.org/10.1016/j.nuclphysa.2005.03.086. URL: http://www.sciencedirect.com/science/article/pii/S0375947405005300.

[13] C. Adler et al. "Elliptic flow from two- and four-particle correlations in Au+Au collisions at $\sqrt{s_{\mathrm{NN}}}$ = 130GeV". In: *Phys. Rev. C* 66 (3 2002), p. 034904. DOI: 10.1103/PhysRevC.66.034904. URL: http://link.aps.org/doi/10.1103/PhysRevC.66.034904.

[14] S. S. Adler et al. "Systematic studies of the centrality and $\sqrt{s_{NN}}$ dependence of the $dE_T/d\eta$ and $dN_{\mathrm{ch}}/d\eta$ in heavy ion collisions at midrapidity". In: *Phys. Rev. C* 71 (3 2005), p. 034908. DOI: 10.1103/PhysRevC.71.034908. URL: http://link.aps.org/doi/10.1103/PhysRevC.71.034908.

[15] W. M. Alberico et al. “Heavy flavors in AA collisions: production, transport and final spectra”. In: *The European Physical Journal C* 73.7 (2013), pp. 1–15. ISSN: 1434-6052. DOI: 10.1140/epjc/s10052-013-2481-z. URL: http://dx.doi.org/10.1140/epjc/s10052-013-2481-z.

[16] W. M. Alberico et al. “Heavy-flavour spectra in high-energy nucleus–nucleus collisions”. In: *The European Physical Journal C* 71.6 (2011), pp. 1–21. ISSN: 1434-6052. DOI: 10.1140/epjc/s10052-011-1666-6. URL: http://dx.doi.org/10.1140/epjc/s10052-011-1666-6.

[17] *An Event Plane Detector for STAR*. 2016. URL: https://drupal.star.bnl.gov/STAR/system/files/EPD_Construction_Proposal.pdf.

[18] M. Anderson et al. “The Star time projection chamber: A Unique tool for studying high multiplicity events at RHIC”. In: *Nucl. Instrum. Meth.* A499 (2003), pp. 659–678. DOI: 10.1016/S0168-9002(02)01964-2. arXiv: nucl-ex/0301015 [nucl-ex].

[19] Federico Antinori et al. “Hard Probes 2012 Recent results on heavy quark quenching in ultrarelativistic heavy ion collisions: the impact of coherent gluon radiation”. In: *Nuclear Physics A* 910 (2013), pp. 301 –305. ISSN: 0375-9474. DOI: http://dx.doi.org/10.1016/j.nuclphysa.2013.02.020. URL: http://www.sciencedirect.com/science/article/pii/S037594741300136X.

[20] L. Arnold et al. “The STAR silicon strip detector (SSD)”. In: *Nuclear Instruments and Methods in Physics Research Section A: Accelerators, Spectrometers, Detectors and Associated Equipment* 499.2,Äì3 (2003). The Relativistic Heavy Ion Collider Project: RHIC and its Detectors, pp. 652 –658. ISSN: 0168-9002.

DOI: http://dx.doi.org/10.1016/S0168-9002(02)01963-0. URL: http://www.sciencedirect.com/science/article/pii/S0168900202019630.

[21] I. Arsene et al. "First Three Years of Operation of RHIC Quark-Äìgluon plasma and color glass condensate at RHIC? The perspective from the BRAHMS experiment". In: *Nuclear Physics A* 757.1 (2005), pp. 1 –27. ISSN: 0375-9474. DOI: http://dx.doi.org/10.1016/j.nuclphysa.2005.02.130. URL: http://www.sciencedirect.com/science/article/pii/S0375947405002770.

[22] I. Arsene et al. "Quark-Äìgluon plasma and color glass condensate at RHIC? The perspective from the BRAHMS experiment". In: *Nuclear Physics A* 757.1-2 (2005). First Three Years of Operation of RHIC, pp. 1 –27. ISSN: 0375-9474. DOI: http://dx.doi.org/10.1016/j.nuclphysa.2005.02.130. URL: http://www.sciencedirect.com/science/article/pii/S0375947405002770.

[23] B.B. Back et al. "The PHOBOS perspective on discoveries at RHIC". In: *Nuclear Physics A* 757.1-2 (2005). First Three Years of Operation of RHIC, pp. 28–101. ISSN: 0375-9474. DOI: http://dx.doi.org/10.1016/j.nuclphysa.2005.03.084. URL: http://www.sciencedirect.com/science/article/pii/S0375947405005282.

[24] R. Baier et al. "Radiative energy loss of high energy quarks and gluons in a finite-volume quark-gluon plasma". In: *Nuclear Physics B* 483.1 (1997), pp. 291 –320. ISSN: 0550-3213. DOI: http://dx.doi.org/10.1016/S0550-3213(96)00553-6. URL: http://www.sciencedirect.com/science/article/pii/S0550321396005536.

[25] Debasish Banerjee et al. "Heavy quark momentum diffusion coefficient from lattice QCD". In: *Phys. Rev. D* 85 (1 2012), p. 014510. DOI: 10.1103/PhysRevD.85.014510. URL: http://link.aps.org/doi/10.1103/PhysRevD.85.014510.

[26] J. Barrette et al. "Energy and charged particle flow in 10.8A GeV/c Au+Au collisions". In: *Phys. Rev. C* 55 (3 1997), pp. 1420–1430. DOI: 10.1103/PhysRevC.55.1420. URL: http://link.aps.org/doi/10.1103/PhysRevC.55.1420.

[27] J. Barrette et al. "Proton and pion production relative to the reaction plane in Au + Au collisions at 11A GeV/c". In: *Phys. Rev. C* 56 (6 1997), pp. 3254–3264. DOI: 10.1103/PhysRevC.56.3254. URL: http://link.aps.org/doi/10.1103/PhysRevC.56.3254.

[28] J. Beringer et al. "Review of Particle Physics". In: *Phys. Rev. D* 86 (1 2012), p. 010001. DOI: 10.1103/PhysRevD.86.010001. URL: http://link.aps.org/doi/10.1103/PhysRevD.86.010001.

[29] S. Bethke. "Determination of the QCD coupling α_s". In: *J. Phys.* G26 (2000), R27. DOI: 10.1088/0954-3899/26/7/201. arXiv: hep-ex/0004021 [hep-ex].

[30] E. S. Bowman and J. I. Kapusta. "Critical points in the linear σ model with quarks". In: *Phys. Rev. C* 79 (1 2009), p. 015202. DOI: 10.1103/PhysRevC.79.015202. URL: http://link.aps.org/doi/10.1103/PhysRevC.79.015202.

[31] Eric Braaten and Robert D. Pisarski. "Soft amplitudes in hot gauge theories: A general analysis". In: *Nuclear Physics B* 337.3 (1990), pp. 569 –634. ISSN: 0550-3213. DOI: http://dx.doi.org/10.1016/0550-3213(90)90508-B. URL: http://www.sciencedirect.com/science/article/pii/055032139090508B.

[32] Stanley J. Brodsky and Paul Hoyer. "A bound on the energy loss of partons in nuclei". In: *Physics Letters B* 298.1 (1993), pp. 165 –170. ISSN: 0370-2693. DOI: http://dx.doi.org/10.1016/0370-2693(93)91724-2. URL: http://www.sciencedirect.com/science/article/pii/0370269393917242.

[33] Matteo Cacciari, Mario Greco, and Paolo Nason. "The p_T spectrum in heavy-flavour hadroproduction". In: *Journal of High Energy Physics* 1998.05 (1998), p. 007. URL: http://stacks.iop.org/1126-6708/1998/i=05/a=007.

[34] Shanshan Cao, Guang-You Qin, and Steffen A. Bass. "Energy loss, hadronization, and hadronic interactions of heavy flavors in relativistic heavy-ion collisions". In: *Phys. Rev. C* 92 (2 2015), p. 024907. DOI: 10.1103/PhysRevC.92.024907. URL: http://link.aps.org/doi/10.1103/PhysRevC.92.024907.

[35] Shanshan Cao, Guang-You Qin, and Steffen A. Bass. "Heavy-quark dynamics and hadronization in ultrarelativistic heavy-ion collisions: Collisional versus radiative energy loss". In: *Phys. Rev. C* 88 (4 2013), p. 044907. DOI: 10.1103/PhysRevC.88.044907. URL: http://link.aps.org/doi/10.1103/PhysRevC.88.044907.

[36] S. Chatrchyan et al. "Observation of a new boson at a mass of 125 GeV with the CMS experiment at the LHC". In: *Physics Letters B* 716.1 (2012), pp. 30 –61. ISSN: 0370-2693. DOI: http://dx.doi.org/10.1016/j.physletb.2012.08.021. URL: http://www.sciencedirect.com/science/article/pii/S0370269312008581.

[37] G. Contin et al. “The MAPS based PXL vertex detector for the STAR experiment”. In: *Journal of Instrumentation* 10.03 (2015), p. C03026. URL: http://stacks.iop.org/1748-0221/10/i=03/a=C03026.

[38] H-T Ding et al. “Heavy quark diffusion from lattice QCD spectral functions”. In: *Journal of Physics G: Nuclear and Particle Physics* 38.12 (2011), p. 124070. URL: http://stacks.iop.org/0954-3899/38/i=12/a=124070.

[39] Shinji Ejiri. “Canonical partition function and finite density phase transition in lattice QCD”. In: *Phys. Rev. D* 78 (7 2008), p. 074507. DOI: 10.1103/PhysRevD.78.074507. URL: http://link.aps.org/doi/10.1103/PhysRevD.78.074507.

[40] Y V Fisyak et al. “Overview of the inner silicon detector alignment procedure and techniques in the RHIC/STAR experiment”. In: *Journal of Physics: Conference Series* 119.3 (2008), p. 032017. URL: http://stacks.iop.org/1742-6596/119/i=3/a=032017.

[41] R. Frühwirth. “Application of Kalman filtering to track and vertex fitting”. In: *Nuclear Instruments and Methods in Physics Research Section A: Accelerators, Spectrometers, Detectors and Associated Equipment* 262.2,Äì3 (1987), pp. 444 –450. ISSN: 0168-9002. DOI: http://dx.doi.org/10.1016/0168-9002(87)90887-4. URL: http://www.sciencedirect.com/science/article/pii/0168900287908874.

[42] R. Frühwirth et al. “Vertex reconstruction and track bundling at the LEP collider using robust algorithms”. In: *Computer Physics Communications* 96.2-3 (1996), pp. 189 –208. ISSN: 0010-4655. DOI: http://dx.doi.org/10.1016/

0010-4655(96)00040-9. URL: http://www.sciencedirect.com/science/article/pii/0010465596000409.

[43] P. B. Gossiaux and J. Aichelin. "Toward an understanding of the single electron data measured at the BNL Relativistic Heavy Ion Collider (RHIC)". In: *Phys. Rev. C* 78 (1 2008), p. 014904. DOI: 10.1103/PhysRevC.78.014904. URL: http://link.aps.org/doi/10.1103/PhysRevC.78.014904.

[44] P. B. Gossiaux, R. Bierkandt, and J. Aichelin. "Tomography of quark gluon plasma at energies available at the BNL Relativistic Heavy Ion Collider (RHIC) and the CERN Large Hadron Collider (LHC)". In: *Phys. Rev. C* 79 (4 2009), p. 044906. DOI: 10.1103/PhysRevC.79.044906. URL: http://link.aps.org/doi/10.1103/PhysRevC.79.044906.

[45] Steven S. Gubser. "Symmetry constraints on generalizations of Bjorken flow". In: *Phys. Rev. D* 82 (8 2010), p. 085027. DOI: 10.1103/PhysRevD.82.085027. URL: http://link.aps.org/doi/10.1103/PhysRevD.82.085027.

[46] Miklos Gyulassy and Xin-Nian Wang. "HIJING 1.0: A Monte Carlo program for parton and particle production in high energy hadronic and nuclear collisions". In: *Computer Physics Communications* 83.2 (1994), pp. 307 –331. ISSN: 0010-4655. DOI: http://dx.doi.org/10.1016/0010-4655(94)90057-4. URL: http://www.sciencedirect.com/science/article/pii/0010465594900574.

[47] K. Hara et al. "Radiation hardness and mechanical durability of Kuraray optical fibers". In: *Nuclear Instruments and Methods in Physics Research Section A: Accelerators, Spectrometers, Detectors and Associated Equipment* 411.1 (1998), pp. 31 –40. ISSN: 0168-9002. DOI: http://dx.doi.org/10.1016/S0168-

9002(98)00281-2. URL: http://www.sciencedirect.com/science/article/pii/S0168900298002812.

[48] C. Hu-Guo et al. "First reticule size MAPS with digital output and integrated zero suppression for the EUDET-JRA1 beam telescope". In: *Nucl. Instrum. Meth.* A623 (2010), pp. 480–482. DOI: 10.1016/j.nima.2010.03.043.

[49] Peter Jacobs and Xin-Nian Wang. "Matter in extremis: ultrarelativistic nuclear collisions at RHIC". In: *Progress in Particle and Nuclear Physics* 54.2 (2005), pp. 443 –534. ISSN: 0146-6410. DOI: http://dx.doi.org/10.1016/j.ppnp.2004.09.001. URL: http://www.sciencedirect.com/science/article/pii/S0146641004001097.

[50] F. James and M. Roos. "Minuit - a system for function minimization and analysis of the parameter errors and correlations". In: *Computer Physics Communications* 10.6 (1975), pp. 343 –367. ISSN: 0010-4655. DOI: http://dx.doi.org/10.1016/0010-4655(75)90039-9. URL: http://www.sciencedirect.com/science/article/pii/0010465575900399.

[51] Olive K.A. et al. "2015 Review of Particle Physics". In: *Chin. Phys. C* 38 (090001 2015). URL: http://http://pdg.lbl.gov/.

[52] V. Karimaki et al. "Sensor alignment by tracks". In: *eConf* C0303241 (2003), TULT008. arXiv: physics/0306034 [physics].

[53] F. Karsch. "Lattice results on QCD thermodynamics". In: *Nuclear Physics A* 698.1-Äì4 (2002). 15th Int. Conf. on Ultra-Relativistic Nucleus-Nucleus Collisions (Quark Matter 2001), pp. 199 –208. ISSN: 0375-9474. DOI: http://dx.doi.

org/10.1016/S0375-9474(01)01365-3. URL: http://www.sciencedirect.com/science/article/pii/S0375947401013653.

[54] Peter F. Kolb and Ulrich Heinz. "Emission angle dependent HBT at RHIC and beyond". In: *Nuclear Physics A* 715 (2003). Quark Matter 2002 Proceedings of the 16th International Conference on Ultra-Relativistic Nucleus-Nucleus Collisions, pp. 653c –656c. ISSN: 0375-9474. DOI: http://dx.doi.org/10.1016/S0375-9474(02)01554-3. URL: http://www.sciencedirect.com/science/article/pii/S0375947402015543.

[55] Peter F. Kolb and Ralf Rapp. "Transverse flow and hadrochemistry in Au + Au collisions at $\sqrt{s_{\mathrm{NN}}} = 200\mathrm{GeV}$". In: *Phys. Rev. C* 67 (4 2003), p. 044903. DOI: 10.1103/PhysRevC.67.044903. URL: http://link.aps.org/doi/10.1103/PhysRevC.67.044903.

[56] Peter F. Kolb, Josef Sollfrank, and Ulrich Heinz. "Anisotropic transverse flow and the quark-hadron phase transition". In: *Phys. Rev. C* 62 (5 2000), p. 054909. DOI: 10.1103/PhysRevC.62.054909. URL: http://link.aps.org/doi/10.1103/PhysRevC.62.054909.

[57] W.J. Llope. "Multigap RPCs in the STAR experiment at RHIC". In: *Nuclear Instruments and Methods in Physics Research Section A: Accelerators, Spectrometers, Detectors and Associated Equipment* 661, Supplement 1 (2012). X. Workshop on Resistive Plate Chambers and Related Detectors (RPC 2010), S110 –S113. ISSN: 0168-9002. DOI: http://dx.doi.org/10.1016/j.nima.2010.07.086. URL: http://www.sciencedirect.com/science/article/pii/S0168900210017006.

[58] W.J. Llope et al. "The STAR Vertex Position Detector". In: *Nuclear Instruments and Methods in Physics Research Section A: Accelerators, Spectrometers, Detectors and Associated Equipment* 759 (2014), pp. 23 –28. ISSN: 0168-9002. DOI: http://dx.doi.org/10.1016/j.nima.2014.04.080. URL: http://www.sciencedirect.com/science/article/pii/S0168900214004938.

[59] Matthew Luzum and Paul Romatschke. "Conformal relativistic viscous hydrodynamics: Applications to RHIC results at $\sqrt{s_{NN}} = 200$ GeV". In: *Phys. Rev. C* 78 (3 2008), p. 034915. DOI: 10.1103/PhysRevC.78.034915. URL: http://link.aps.org/doi/10.1103/PhysRevC.78.034915.

[60] *Masking in year 2014*. 2014. URL: https://drupal.star.bnl.gov/STAR/blog/mlomnitz/masking-studies-22-march-2014-0.

[61] Hiroshi Masui and Alexander Schmah. "Event plane resolution correction for azimuthal anisotropy in wide centrality bins". In: *ePrint arXiv:1506.07605* (2012).

[62] M.L. Miller et al. "Glauber Modeling in High-Energy Nuclear Collisions". In: *Annual Review of Nuclear and Particle Science* 57 (2007). DOI: 10.1146/annurev.nucl.57.090506.123020.

[63] Guy D. Moore and Derek Teaney. "How much do heavy quarks thermalize in a heavy ion collision?" In: *Phys. Rev. C* 71 (6 2005), p. 064904. DOI: 10.1103/PhysRevC.71.064904. URL: http://link.aps.org/doi/10.1103/PhysRevC.71.064904.

[64] Marlene Nahrgang et al. "Elliptic and triangular flow of heavy flavor in heavy-ion collisions". In: *Phys. Rev. C* 91 (1 2015), p. 014904. DOI: 10.1103/PhysRevC.91.014904. URL: http://link.aps.org/doi/10.1103/PhysRevC.91.014904.

[65] Yongseok Oh et al. "Ratios of heavy baryons to heavy mesons in relativistic nucleus-nucleus collisions". In: *Phys. Rev. C* 79 (4 2009), p. 044905. DOI: 10.1103/PhysRevC.79.044905. URL: http://link.aps.org/doi/10.1103/PhysRevC.79.044905.

[66] K. A. Olive et al. "Review of Particle Physics". In: *Chin. Phys.* C38 (2014), p. 090001. DOI: 10.1088/1674-1137/38/9/090001.

[67] Long-Gang Pang et al. "Analytical and numerical Gubser solutions of the second-order hydrodynamics". In: *Phys. Rev. D* 91 (7 2015), p. 074027. DOI: 10.1103/PhysRevD.91.074027. URL: http://link.aps.org/doi/10.1103/PhysRevD.91.074027.

[68] A. M. Poskanzer and S. A. Voloshin. "Methods for analyzing anisotropic flow in relativistic nuclear collisions". In: *Phys. Rev. C* 58 (3 1998), pp. 1671–1678. DOI: 10.1103/PhysRevC.58.1671. URL: http://link.aps.org/doi/10.1103/PhysRevC.58.1671.

[69] Scott Pratt. "Resolving the Hanbury Brown˘Twiss Puzzle in Relativistic Heavy Ion Collisions". In: *Phys. Rev. Lett.* 102 (23 2009), p. 232301. DOI: 10.1103/PhysRevLett.102.232301. URL: http://link.aps.org/doi/10.1103/PhysRevLett.102.232301.

[70] Hao Qiu. "{STAR} heavy flavor tracker". In: *Nuclear Physics A* 931 (2014). QUARK MATTER 2014XXIV INTERNATIONAL CONFERENCE ON ULTRARELATIVISTIC NUCLEUS-NUCLEUS COLLISIONS, pp. 1141 –1146. ISSN: 0375-9474. DOI: http://dx.doi.org/10.1016/j.nuclphysa.2014.

08.056. URL: http://www.sciencedirect.com/science/article/pii/S0375947414003157.

[71] Zhi Qiu, Chun Shen, and Ulrich Heinz. "Hydrodynamic elliptic and triangular flow in Pb+ÄìPb collisions at $\sqrt{s_{NN}} = 2.76$ TeV". In: *Physics Letters B* 707.1 (2012), pp. 151 –155. ISSN: 0370-2693. DOI: http://dx.doi.org/10.1016/j.physletb.2011.12.041. URL: http://www.sciencedirect.com/science/article/pii/S0370269311014985.

[72] *Radiation damage for the Hodoscope*. 2012. URL: http://www2.ph.ed.ac.uk/~s0678696/neutron_damage.pdf.

[73] L. Ravagli and R. Rapp. "Quark coalescence based on a transport equation". In: *Physics Letters B* 655.3-4 (2007), pp. 126 –131. ISSN: 0370-2693. DOI: http://dx.doi.org/10.1016/j.physletb.2007.07.043. URL: http://www.sciencedirect.com/science/article/pii/S0370269307008854.

[74] F. Riek and R. Rapp. "Quarkonia and heavy-quark relaxation times in the quark-gluon plasma". In: *Phys. Rev. C* 82 (3 2010), p. 035201. DOI: 10.1103/PhysRevC.82.035201. URL: http://link.aps.org/doi/10.1103/PhysRevC.82.035201.

[75] F Riek and R Rapp. "Selfconsistent evaluation of charm and charmonium in the quark-gluon plasma". In: *New Journal of Physics* 13.4 (2011), p. 045007. URL: http://stacks.iop.org/1367-2630/13/i=4/a=045007.

[76] K Schweda. "Prompt production of D mesons with ALICE at the LHC". In: *ePrint arXiv:1402.1370* (2014).

[77] Taesoo Song et al. “Tomography of the quark-gluon plasma by charm quarks”. In: *Phys. Rev. C* 92 (1 2015), p. 014910. DOI: 10.1103/PhysRevC.92.014910. URL: http://link.aps.org/doi/10.1103/PhysRevC.92.014910.

[78] *STAR images*. https://drupal.star.bnl.gov/STAR/book/export/html/7278.

[79] Michael Strickland. “Anisotropic Hydrodynamics: Three lectures”. In: *Acta Phys. Polon.* B45.12 (2014), pp. 2355–2394. DOI: 10.5506/APhysPolB.45.2355. arXiv: 1410.5786 [nucl-th].

[80] M Haering T Kirn D Schmitz and W Schulz. “Absorption length, radiation hardness and ageing of different optical glues”. In: *CMS-NOTE* 003 (1999).

[81] R. Thomas, B. Kämpfer, and G. Soff. “Gluon emission of heavy quarks: Dead cone effect”. In: *Acta Physica Hungarica Series A, Heavy Ion Physics* 22.1 (2005), pp. 83–91. ISSN: 1588-2675. DOI: 10.1556/APH.22.2005.1-2.9. URL: http://dx.doi.org/10.1556/APH.22.2005.1-2.9.

[82] Sjöstrand Torbjörn, Mrenna Stephen, and Skands Peter. “PYTHIA 6.4 physics and manual”. In: *Journal of High Energy Physics* 2006.05 (2006), p. 026. URL: http://stacks.iop.org/1126-6708/2006/i=05/a=026.

[83] T. Lampen V. Karimaki and F.P. Schilling. “The HIP algorithm for track based alignment”. In: *CMS-NOTE* 18 (2006). URL: http://cdsweb.cern.ch/record/926537?ln=en.

[84] Xin-Nian Wang. “A pQCD-based approach to parton production and equilibration in high-energy nuclear collisions”. In: *Physics Reports* 280.5-6 (1997), pp. 287 –371. ISSN: 0370-1573. DOI: http://dx.doi.org/10.1016/S0370-

1573(96)00022-1. URL: http://www.sciencedirect.com/science/article/pii/S0370157396000221.

[85] Xin-Nian Wang. "Systematic study of high p_T hadron spectra in pp, pA, and AA collisions at ultrarelativistic energies". In: *Phys. Rev. C* 61 (6 2000), p. 064910. DOI: 10.1103/PhysRevC.61.064910. URL: http://link.aps.org/doi/10.1103/PhysRevC.61.064910.

[86] Xin-Nian Wang, Miklos Gyulassy, and Michael Plümer. "Landau-Pomeranchuk-Migdal effect in QCD and radiative energy loss in a quark-gluon plasma". In: *Phys. Rev. D* 51 (7 1995), pp. 3436–3446. DOI: 10.1103/PhysRevD.51.3436. URL: http://link.aps.org/doi/10.1103/PhysRevD.51.3436.

[87] K. Werner et al. "Analyzing radial flow features in p-Pb and p-p collisions at several TeV by studying identified-particle production with the event generator EPOS3". In: *Phys. Rev. C* 89 (6 2014), p. 064903. DOI: 10.1103/PhysRevC.89.064903. URL: http://link.aps.org/doi/10.1103/PhysRevC.89.064903.

[88] X. Zhu et al. "Correlations as a sensitive probe for thermalization in high energy nuclear collisions". In: *Physics Letters B* 647.5-6 (2007), pp. 366 –370. ISSN: 0370-2693. DOI: http://dx.doi.org/10.1016/j.physletb.2007.01.072. URL: http://www.sciencedirect.com/science/article/pii/S0370269307002316.